A FINITE ELEMENT FRETTING ANALYSIS OF CYLINDRICAL AND SPHERICAL CONTACTS AT ROOM AND HIGH TEMPERATURES

A Dissertation
Presented to
The Academic Faculty

by

Huaidong Yang

In Partial Fulfillment
of the Requirements for the Degree
Doctor of Philosophy in the
George W. Woodruff School of Mechanical Engineering

Georgia Institute of Technology
December 2020

A FINITE ELEMENT FRETTING ANALYSIS OF CYLINDRICAL AND SPHERICAL CONTACTS AT ROOM AND HIGH TEMPERATURES

Approved by:

Dr. Itzhak Green, Advisor
School of Mechanical Engineering
Georgia Institute of Technology

Dr. Richard W. Neu
School of Materials Science and Engineering
Georgia Institute of Technology

Dr. Jeffrey L. Streator
School of Mechanical Engineering
Georgia Institute of Technology

Dr. Robert L.Jackson
Department of Mechanical Engineering
Auburn University

Dr. Michael Varenberg
School of Mechanical Engineering
Georgia Institute of Technology

Date Approved: [October 27, 2020]

ACKNOLEDGEMENTS

I must thank Professor Itzhak Green for offering me the opportunity to start my research journey in the tribological world. As an advisor, he has always been kind, helpful and supportive not only in my research but also in my personal life. I am sincerely grateful to the remaining members of my thesis reading committee: Professor Richard Neu, Professor Jeffrey Streator, Professor Robert Jackson, and Professor Michael Varenberg for their efforts in reviewing this thesis work and their insights and clarifying remarks. Especially, I would like to thank Professor Michael Varenberg for offering me the chance to conduct reciprocal sliding experiments. I would like also to thank Professor Jeffrey Streator for the useful discussions on the adhesion model.

I am also very grateful to Department of Energy for funding Project 2506U87, Award RH452. Additionally, I would like to extend my thanks to Department of Mechanical Engineering, especially, Dr. Wayne Whiteman, Dr. David Torello and Dr. David Smith for offering the graduate teaching assistant opportunity. These supports guaranteed me to devote myself to the completion of the work in this dissertation.

I must also say thanks to all the visiting scholars, Dr. Joan Josep Roa Rovira and Yasmin Alejandr Maril Millan in our Lab. We had a good time working on the tribological contact research and published papers. Thanks to Professor Farshid Sadeghi, Professor Jacob Eapen, and their Ph.D. students Arman Ahmadi and Ahmed Darwish for coworking with us on the Department of Energy project.

I would express my sincere appreciation to friends in Georgia Institute of Technology. Firstly, thanks to the tribology family, Dr. Yingdan Wu, Ye Qi, Jaekang Kim, and Yuan Gao. Yingdan has always been a good roommate, a good classmate, and a good friend. Congratulates to his early Ph.D. graduation. Thanks for his great help and understanding not only on the course work but also on the personal life. Ye Qi is a kind senior sister, who is an original member of our Friday Evening Entertainment. Additionally, I am thankful to the rest members of our Friday Evening Entertainment, Xiaofeng Liu, Zhuangdi Xu, Jiangpeng Pan, Congshi Zou, Xin Xing, and Yuening Tang. Friday was the life power especially when I was stuck in research. Thanks to the badminton friends, Yamin Zhang, Xiaofeng Liu, Congshi Zou, Brian Huang, Dr. Yixuan Feng, Dr. Wei Li, and Juntao Wang, who have made the Ph.D. life more delightful. Thanks to friends in mechanical engineering, Chong Ye, Haiqi Wen, Yutong Guo, Yiwei Xia, Nguyen, Vinh, and Mu Lve. Thanks to my roommates, Jiangpeng Pan, Yingdan Wu, Zixiao Wang, Chenan Ni, Yuan Gao, Sicheng Wang for the pleasant time spent together. Especially, I am thankful to Sicheng Wang. I cannot imagine how I can go through all this Ph.D. journey without him.

Finally, I wish to express my deepest gratefulness to my family for their endless love and support. My parents, Chunhui Tu and Changlin Yang have always been giving me love no matter who I am, or no matter what I have done. It is so lucky to be their son, and so proud to have them be my parents. Thanks to grandmas, Chunling Sun and Zhimin Shen, and grandpas, Chunrong Yang and Xinkang Tu, for an incredibly happy childhood. I wish Yeye, Nainai, and Waigong could share the happiness of this graduation, and I am sure that you would be proud of me. Thanks for aunts, Xiue Yang and Xiuhua Yang, and all the other family members. The big family I grew up is always the strong support of my life.

TABLE OF CONTENTS

LIST OF TABLES

LIST OF FIGURES

NOMENCLATURE

A	contact area
A_c	critical contact area
a	contact radius
a_c	critical contact radius
b	half contact width
b_c	critical half contact width
C	Poisson's ratio parameter
c	stick half contact width
E	elastic modulus
E_1	elastic modulus of the upper body
E_2	elastic modulus of the bottom body
E'	equivalent elastic modulus, Eq.3-3
G	shear modulus
H	material hardness
I	second moment of area for bending
K	dimensionless wear coefficient
L	transverse length along the cylindrical contact
M_0/L	moment on the tip of the half-cylinder per unit length
p_0	maximum contact pressure
p_{0c}	critical maximum contact pressure
P/L	normal force per unit length
P_c/L	critical normal force per unit length

P	normal force
P_c	critical normal force
P_w	worst normal force which generates the largest wear volume
P^*	normalized normal force, P/P_c
q	tangential traction, $q=q'+q''$
q'	tangential traction at slip region, $\mu p(x)$
q''	tangential traction at stick region
Q/L	tangential force per unit length
Q	tangential force
R	radius of cylinder or sphere
s	local sliding distance
S	oscillatory sliding amplitude
s_0	local sliding distance at the initiation of the gross slip
S_n	nominal sliding distance
S_n^*	normalized nominal sliding distance, S_n/ω_c
S_y	yield strength
S_{sy}	shear strength
$\bar{u}$	tangential displacement on the surface of a half elastic space
U_c	critical elastic strain energy
v	local wear volume
V	wear volume
V_0	wear volume at the initiation of the gross slip
V_c	critical wear volume
V^*	normalized wear volume, V/V_c
δ	horizontal displacement

δ^* normalized horizontal displacement, δ/ω_c

δ_i initial gross slip distance

δ_{i1} the deflection of the half-cylinder at the initiation of the gross slip

δ_{i2} the displacement of the stick region at the initiation of the gross slip

Δ the deflection of the half-cylinder

Δx compressive displacement of the two sides of the block in the case of pre-stress

Δy displacement of the top side of the block in the case of pre-stress

μ coefficient of friction

μ_e effective coefficient of friction

ω interference

ω_c critical interference

ω^* normalized interference, ω/ω_c

ω' interference in the case of pre-stress

ϕ angle of the mid-surface of beam

ν_1 Poisson's ratio of the upper body

ν_2 Poisson's ratio of the bottom body

σ_x normal stress in the X direction

σ_y normal stress in the Y direction

σ_e equivalent von-Mises stress

ε_p equivalent plastic strain

ε_x normal strain in the X direction

ε_y normal strain in the Y direction

SUMMARY

Fretting can be considered as a small amplitude cyclic relative motion. Nuclear reactors are designed to operate at high temperatures as it results in substantial improvements of thermal efficiency. The structural and in-core components of a high/very high temperature gas cooled reactors (HTGR/VHTRs) are exposed to this high temperature environment. In components such as valve stems and seats, control rod drive mechanisms, fuel handling mechanisms, and helium circulators, fretting wear and fretting fatigue can significantly reduce the operational lifetime of these components. Inconel 617 and Incoloy 800H are nickel-based alloys, commonly used materials in HTGR/VHTRs. These alloys possess excellent high temperature corrosion, strength, and oxidation resistance properties. The fretting contact behaviors between these two alloys in room and high temperatures are investigated to obtain fundamental knowledge of fretting wear and fretting fatigue mechanisms.

The purpose of this work is to understand the physical phenomena of the fretting system. It is desirable to model a numerical model for the fretting system and do the stress strain analysis at and under the contacting interface, which helped understand the mechanisms of fretting wear and fretting fatigue. It is also desirable to develop analytical and semi-analytical solutions for fretting wear volume, which helped understand the relation between wear volume, normal load, amplitude, and material properties during the fretting motion. The understanding of the physical phenomena of fretting, in turn, may lead to mitigation methods which alleviate the fretting damage. Thus, the objective of this research is to

model the fretting system, identify its physical phenomena, and propose mitigation methods to reduce the fretting damage.

In previous models, a predetermined constant COF is applied at the interface to simulate frictional contact. A tentative fretting adhesion model is built herein, where the COF is replaced with effect of adhesion. It builds a comprehensive adhesion model by finite elements (FEA) for a deformable hemisphere subject to fretting. The normal direction adhesion contact is based on the classic JKR model. The tangential resistance is based on the definition of the shear strength and the surface free energy. That is manifested into interfacial bilinear springs where detachment or reattachment of the two contacting surfaces occur when the springs "break" or "snap-back" at the interface. The tangential resistance effect is robust, that is, it is not influenced by the choice of meshing or the spring settings.

This work provides systematic results for the stress-strain analysis, junction growth, fretting loop, and depression marks at the bottom body for different material pairs. The results are normalized, which are verified to be effective to be applied to different dimensions (microscopically and macroscopically). Based on the locations of largest von-Mises stress and plastic strains, and the relation between the wear volume and the loading conditions, the mechanisms of fretting wear and fretting fatigue are thoroughly investigated.

Also, a notable contribution of this work is derivation of the analytical solutions for different fretting models in the elastic regime. In the 2D cylindrical contact, the relation between the interference and normal load for a deformable half cylinder and a flat block is

derived. In the 2D and 3D wear models, the initial gross slip distance for frictional contact is derived for unidirectional sliding, and the wear volume during the partial slip condition is also derived. Based on the two derivations, the wear volume for one general cycle of fretting motion is derived.

Lastly, a novel fretting adhesion model is built, where the COF is replaced with the effect of adhesion. For the first time, a comprehensive adhesion model is devised for contact with traction resistance considering both the normal and tangential direction adhesion effects. The normal direction adhesion contact is based on the classic JKR model. The tangential resistance is based on the definition of the shear strength and the surface free energy. This model is a substitute to the assignment of a predetermined COF. That is a giant leap in the FEA “frictional” contact modelling.

CHAPTER 1. INTRODUCTION

1.1 Problem Motivation

Fretting can be considered as a small amplitude cyclic relative motion [1]. The loading condition in fretting is an oscillatory tangential load compounded with a normal load. It occurs in assemblies of engineering elements with the existence of vibration, cyclic loading or cyclic temperature changes, as well as bearing races and shafts, electrical contacts, reactor elements, turbine engine disks [2-5], etc. Three different regimes of fretting are observed according to the types of the contact conditions: stick, mixed stick-slip, and gross slip [6]. The stick conditions correspond to low fretting damage. The mixed stick-slip conditions mainly result in fatigue crack formation, while the gross slip conditions are mainly responsible for wear [1]. In particular, fretting damage can significantly reduce the operational lifetime of components in nuclear reactors [7].

Nuclear reactors are designed to operate at high temperatures as it results in substantial improvements of thermal efficiency [8, 9]. The structural and in-core components of a high/very high temperature gas cooled reactors (HTGR/VHTRs) are exposed to this high temperature environment. In components such as valve stems and seats, control rod drive mechanisms, fuel handling mechanisms, and helium circulators, fretting wear and fretting fatigue can significantly reduce the operational lifetime of these components.

Inconel 617 and Incoloy 800H are nickel-based alloys, commonly used materials in HTGR/VHTRs. These alloys possess excellent high temperature corrosion, strength, and oxidation resistance properties. The fretting contact behaviors between these two alloys in

room and high temperatures are investigated to obtain fundamental knowledge of fretting wear and fretting fatigue mechanisms. Additionally, based on the fundamental knowledge of fretting, mitigation schemes for fretting damage are proposed. For reference, in some cases, steel and copper will also be considered herein. The results in this thesis work is also a foundation for the experimental work done by a group at Purdue University.

1.2 Objective

The purpose of this work is to understand the physical phenomena of the fretting system. It is desirable to model a numerical model for the fretting system and do the stress strain analysis at and under the contacting interface, which helped understand the mechanisms of fretting wear and fretting fatigue. It is also desirable to develop analytical and semi-analytical solutions for fretting wear volume, which helped understand the relation between wear volume, normal load, amplitude, and material properties during the fretting motion. The understanding of the physical phenomena of fretting, in turn, may lead to mitigation methods which alleviate the fretting damage. Thus, the objective of this research is to model the fretting system, identify its physical phenomena, and propose mitigation methods to reduce the fretting damage.

1.3 Methodology

It is proposed to investigate, by analytical and finite element methods, the fretting behavior between identical material pairs (this is investigated in Chapter 3) and dissimilar material pairs (this is investigated in Chapter 4). The identical material pairs include steel on steel, copper on copper, and Inconel 617 on Inconel 617. The dissimilar material pairs include

Inconel 617 on Incoloy 800H at 20C and 800C. For brevity, the material pairs are designated in a compact way. For instance, steel on steel is designated as “steel/steel”.

The hemispherical and cylindrical contacts are two classical contact models to investigate contact mechanics, following the original work by Hertz. In this thesis work, these two geometries are likewise used to investigate the fretting phenomenon.

The finite element fretting models are built in ANSYS 17.1. Firstly, the 2D (plane-strain) models were built. There are two loading conditions, displacement-controlled and force-controlled both with respect to the normal direction. As shown in Fig.1-1, the fretting contact is between a deformable half cylinder and a deformable flat block. As shown in Fig.1-1a, the displacement-controlled model’s inputs are interference, ω, and oscillatory tangential displacement, δ, being applied to the top surface of the half cylinder. As shown in Fig.1-1b, a simulated rigid plate is placed on top of the half cylinder to prevent rotation about the Z-axis in force-controlled model. Its inputs are normal load P, being applied to the top surface of the rigid plate, and oscillatory tangential displacement, δ, being applied to the top surface of the half cylinder. Then, the 3D spherical contact models are built. Similar to the 2D case, there are displacement-controlled and force-controlled models. As shown in Fig.1-2, the fretting contact is between a deformable hemisphere and a deformable flat block. To reduce the computation effort, we take advantage of the symmetric fretting loading about XZ plane. The model is cut in half as a quarter sphere in contact with a half flat block. As shown in Fig.1-2a, the displacement-controlled model’s inputs are interference, ω, and oscillatory tangential displacement, δ, being applied to the top surface of the hemisphere. As shown in Fig.1-2b, a simulated rigid plate is placed on top of the half cylinder to prevent rotation about the Z-axis in force-controlled model. Its

inputs are normal load P, being applied to the top surface of the rigid plate, and oscillatory tangential displacement, δ, being applied to the top surface of the hemisphere. Different coefficient of frictions (COFs) are applied to the interface to simulate the frictional contact. The evolutions of von-Mises stresses, plastic strains, junction growth, friction force, wear volume will be investigated. A scheme of results normalization is proposed for different material pairs.

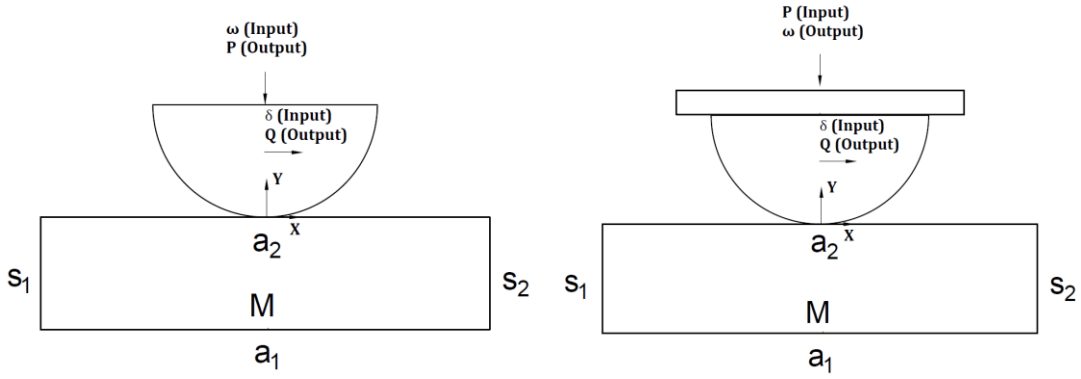

(a) Displacement-controlled condition (b) Force-controlled condition

Figure 1-1. Schematic of 2D plane-strain cylindrical contact model

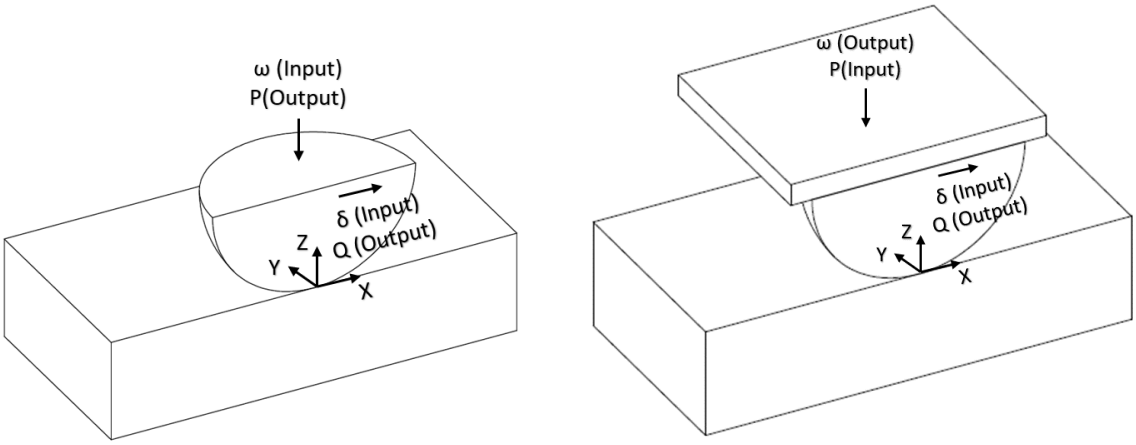

(a) Displacement-controlled condition (b) Force-controlled condition

Figure 1-2. Schematic of 3D spherical contact model

The fretting wear model is based on the force-controlled models, Fig.1-1b and Fig.1-2b (this is investigated in Chapter 5). The Archard wear model [10] are applied to the interface. The wear volume for a general cycle of fretting under elastic contact is derived in 2D case by semi-analytical solutions and it is derived in 3D case by analytical solutions.

To mitigate the damage during fretting, two main properties are focused on: plastic strain and wear volume (this is investigated in Chapter 6). The plastic strain represents the plastic deformation in the bulk material, which will decrease the life of the component. The wear volume represents permanent material removal at the interface, which will also decrease the life of the component. A designed pre-stress scheme is shown to reduce the plastic strain, while the analytical solutions derived in the fretting wear model helps determine loading condition which avoids maximizing fretting wear volume.

In the previous models, predetermined constant COF are applied at the interface to simulate frictional contact. By keeping the COF constant, the influence of COF on stress-strain

distribution, junction growth, depression marks, and fretting loops can be isolated and investigated for various levels of COF cases. However, the FEA models herein are not restricted to just constant COFs, as they are capable of handling non-constant COF just as well.

A tentative fretting adhesion model is built herein, where the COF is replaced with effect of adhesion (this is investigated in Chapter 7). It builds a comprehensive adhesion model by finite elements (FEA) for a deformable hemisphere subject to fretting. The normal direction adhesion contact is based on the classic JKR model. The tangential resistance is based on the definition of the shear strength and the surface free energy. That is manifested into interfacial bilinear springs where detachment or reattachment of the two contacting surfaces occur when the springs "break" or "snap-back" at the interface. The tangential resistance effect is robust, that is, it is not influenced by the choice of meshing or the spring settings.

1.4 Significant Contributions

This work provides systematic results for the stress-strain analysis, junction growth, fretting loop, and depression marks at the bottom body for different material pairs. The results are normalized, which are verified to be effective to be applied to different dimensions (microscopically and macroscopically). However, the results are only applicable for contacts that are above the range of roughness. Based on the locations of largest von-Mises stress and plastic strains, and the relation between the wear volume and the loading conditions, the mechanisms of fretting wear and fretting fatigue are thoroughly investigated.

Also, a notable contribution of this work is derivation of the analytical solutions for different fretting models in the elastic regime. In the 2D cylindrical contact, the relation between the interference and normal load for a deformable half cylinder and a flat block is derived. In the 2D and 3D wear models, the initial gross slip distance for frictional contact is derived for unidirectional sliding, and the wear volume during the partial slip condition is also derived. Based on the two derivations, the wear volume for one general cycle of fretting motion is derived.

Lastly, a novel fretting adhesion model is built, where the COF is replaced with the effect of adhesion. For the first time, a comprehensive adhesion model is devised for contact with traction resistance considering both the normal and tangential direction adhesion effects. The normal direction adhesion contact is based on the classic JKR model. The tangential resistance is based on the definition of the shear strength and the surface free energy. This model is a substitute to the assignment of a predetermined COF. That is a giant leap in the FEA “frictional” contact modelling.

CHAPTER 2. LITERATURE REVIEW

2.1 Sliding Contact

Frictional sliding contact analysis lays the foundation of fretting. The theoretical frictional sliding contact analysis is addressed by Johnson [11]. He provides elastic solutions of contact pressure, tangential force and deformation on the contacting surfaces, addressing both cylindrical and spherical contacts in situations of partial and gross slip. Additionally, Cattaneo [12] and Mindlin [13] address the stress distribution of the surface and subsurface for spherical partial slip. The complete stress field of spherical sliding contacts is further developed by Goodman and Hamilton [14]. The cylindrical plane strain contact is investigated by Adams [15], considering stick, partial slip and sliding. The analytical solution for the local slip distance under a Hertzian pressure with a constant coefficient of friction is recorded for 3D spherical contact by Popov and Heß [16] . However, the solution for the cylindrical line contact for fretting is not available.

The experiments conducted by Courtney-Pratt and Eisner[17] may be of the earliest studies related to the reciprocal frictional sliding phenomenon. They examine the underlying phase of the oscillatory tangential loading applied at the contact between a metallic sphere and metallic flat surfaces. The hysteresis loops of tangential force and the junction growth are indicated by the difference in the electrical conductance. Junction growth is also found by Parker and Hatch [18], and by Tabor [19].

The elastic-plastic and fully plastic spherical contacts in strictly normal loading have been studied in great details, using the finite element analysis (FEA) method [20-22].The elastic-

plastic cylindrical contact in plane stress is recently done by Sharma [23]. However, when the tangential force is introduced under normal load, only a few attempts to analyze the contact have been made. Brizmer et al. [24] use FEA to investigate the spherical contact under the fully stick condition with tangential load. Junction growth is reported. Chang and Zhang [25] model their contact without fully stick conditions and apply static frictional coefficient. Similar results of junction growth are found in the elastic-plastic regime. In the model by Holmberg *et al.* [26], of a rigid sphere pressed against elastic-plastic flat surfaces, ploughing and pileups are apparent in the results. The work by Boucly et al. [27] presents a semi-analytical method for the tridimensional elastic-plastic sliding contact between two interfering hemispherical asperities using either a load-driven or a displacement-driven algorithms. Pile-up induced by the permanent deformation of the bodies due to their relative motion is evident. A similar pile-up phenomenon is also present in the current work.

2.2 Fretting

The very first research work about fretting, to the best of the author's knowledge, is done by Tomlinson et al. [28],where the terminology "fretting corrosion" is coined. After that Vingsbo and Söderberg [6] found the fretting map, which sort fretting into stick, mixed stick-slip, and gross slip regimes. Under a certain normal load, the contact status goes from stick, to partial slip, and gross slip with the increase of the tangential displacement. A mixed fretting regime is then found by Zhou and Vincent [29, 30]. It can be identified from the fretting loop evolution, which varies its shape during thousands of fretting cyclic loadings. Varenberg et al. [1] define a slip index to determine the different fretting regimes.

Fretting wear and fretting fatigue have been the two main fretting damages. Fretting wear is the main cause of component failure in gross slip regime, which has been investigated by Waterhouse [31], McColl et al.[32], Fouvry [33], and Blanchard et al.[34]. Fretting fatigue is the main case of component failure in partial slip regime, which has been studied by Waterhouse [35], Hills [36], and Szolwinski. [37]. Fouvry, Kapsa, and Vincent deliver the quantification criteria for different regime of fretting wear and fretting fatigue [38]. Neu et al. [39] build nucleation models to predict fretting fatigue. Later, fretting damage (wear and fatigue) is investigated by increasing the number of loading cycles to the order of thousands or even millions [40-44]. Coatings and lubricant conditions are found to mitigate fretting damage in these works. References [45-47] focus on the fretting damage for materials applied in the steam generator, including Inconel 600, Inconel 690 and Incoloy 800.

Gordelier and Chivers suggest a method of categorizing fretting by the loading conditions [48], i.e., displacement-controlled or force-controlled fretting. While practical situations may be a combination of these two loading conditions. The outcomes of these two conditions are different in wear tests according to Mohrbacher et.al [49]. Displacement-controlled fretting in normal direction is applicable to conditions when the contacting elements are confined within prescribed spaces, such as prosthetic knee joints [50-52], bolted joints, interference (press) fits [53, 54], and cutting tools in machining [55].Force-controlled fretting in normal direction is more prevalent, which occurs in bolting [56], electrical connectors [57], and steam generators[58].

The numerical work on fretting developed with the development of the finite element analysis. Parallel cylindrical fretting contact are reported in [59, 60]. Specifically, the

Gupta et al. model [59] consists of a meager 285 elements which is limited by the computational memory typically available in 1993. Ghosh et al. [60] simulate fretting wear of Hertzian line contact in partial slip. However, by applying the same level of mesh density as in the previous two models (FEA repeated herein), the theoretical predictions in Green's work [61] could not be met. With current computing capabilities, the accuracy of these results can be improved considerably and that is one of the aims of this work. Mei et al. [7] investigate the cylindrical fretting wear via FEA for Inconel 690 Alloy, which is a material used for steam generator in nuclear power plants. However, the stress field distribution, the effects of the COF, normal load and plastic deformation are not considered.

The 3D fretting contacts are studied in [62, 63]. Both works model the contact between a rigid flat and a deformable hemisphere. Zolotarevskiy *et al.* [62] focus on the full stick and force-controlled conditions. The evolution of the tangential load and the shake down phenomenon are reported. Shi *et al.* [63] focus on the partial slip condition with both force-controlled and displacement-controlled loadings. Junction growth and shake down are investigated. However, sliding and gross slip conditions, or depression marks on the flat are excluded from these two analyses.

2.3 Adhesion in Tribological Contacts

Friction is a complex phenomenon that is influenced by various effects such as contamination, elastic and plastic deformations, roughness, and adhesion, among others [64]. The first work that relates adhesion to friction can possibly be traced back to Desaguliers in 18th century [65]. An adhesion model is developed by Bowden and Tabor, who propose the "plastic junction" concept, which means that adhesion can exhibit

tangential resistance by forming a plastic junction at interface [66]. The study in the current work focuses on the modelling of such a tangential resistance by employing interfacial bilinear springs to represent the adhesion effect between metallic contacts, while all that is under fretting conditions. Adhesion is the only physical bond between the surfaces, where an arbitrary "coefficient of friction" is never imposed in the model.

The study of metal-to-metal adhesion can be traced back to 1963 to the work by Keller[67]. When two metallic surfaces are brought to be close enough, the atomic level attractive force can increase significantly, which encapsulates the adhesion effect. Metallic adhesion can influence the process of friction [68], wear[69], and fatigue[70] when the contact is considered microscopic.

Johnson, Kendall, and Robert add the adhesion effect to the Hertzian contact solution in the normal direction in their venerable JKR model [71]. It is based on the balance between the stored elastic energy and the loss of surface energy. The limitation of that model is that adhesion is assumed active only inside the area of contact. An alternative adhesion model, the DMT model, was later developed by Derjaguin, Muller, and Toporov [72]. The DMT model includes the adhesion effect both inside and outside of the area of contact. However, the JKR and DMT models are at odds with each other. Tabor [73], and later Maugis [74] solve this contradiction by showing that JKR model applies for large and compliant contacting bodies while DMT model applies for stiff contacting bodies. They develop, respectively, the Tabor or Maugis parameters to determine whether a contact is more suitable for the JKR or the DMT model. Later, a numerical model based on these two classic adhesion models is incorporated in a finite element analysis (FEA) software to study the loading and unloading behavior of the adhesion in normal contact[75]. Du *et al.* include

plasticity in the loading-unloading adhesion model[76]. However, in all of the above studies, adhesion is considered only in the normal direction. In other words, the models do not consider a tangential direction strength.

Adhesion has been observed experimentally to be related to friction [77]. According to Bowden and Tabor[66], the friction force is proposed to be directly proportional to the contact area and the shear strength of the material. In order to understand the mechanism of contact behavior in the microscopic level, the atomic force microscopic (AFM) was developed in 1986 by Binning *et al* [78]. Since then, the AFM has regularly been used to test the relationship between the friction force and the contact area microscopically [79-81]. The contact areas based on the JKR, DMT, or the Maugis models are found to be proportional to the friction force obtained in the AFM experiment. However, theoretical and numerical works of combing sliding friction and adhesion are scarce.

Theoretical and numerical works that do consider friction as an effect of adhesion are those by Johnson [65] and Popov *et al* [82]. The theoretical model built by Johnson [65] is based on fracture mechanics, which is complicated to be implemented in numerical simulations. Only some preliminary elastic results are generated in that work. The model built by Popov *et al* [82] is based on the method of dimensionality reduction. It studies the contact between a rigid sphere and an elastic flat surface. Linear elastic springs are used to generate tangential resistance effect caused by adhesion. They use the surface energy and shear modulus to define the elastic spring stiffness and maximum elongation of the springs. But the tangential resistance can only be generated for rotational motion since the model is axisymmetric. Moreover, if the model is extended to three dimensions, an issue arises where the results change with the size of the mesh at the interface.

CHAPTER 3. FRETTING BETWEEN IDENTICAL MATERIAL PAIRS

In this chapter, the fretting analyses for plane strain cylindrical and spherical contacts with no wear or adhesion effects are presented between identical material pairs. Two different loading condition models are built. One is displacement-controlled in both vertical and horizontal directions. The other one is force-controlled in vertical direction and displacement-controlled in horizontal direction, which is called as "force-controlled model" later for brevity. The models built in this chapter are capable of executing analyses in both elastic and elastic plastic regimes. The distribution of von-Mises stress, plastic strain, junction growth, depression mark on the block, and work done to the system are discussed. The models and results presented in this chapter are published in Ref. [83] for the 2D case, and Ref. [84] for the 3D case.

3.1 Cylindrical Plane Strain Fretting Contact

The cylindrical plane strain fretting model is built in the 2D condition. The model is first verified in elastic normal contact condition by theoretical equations and then verified in elastic-plastic fretting contact condition by mesh convergence. The material pair is steel/steel. The stress-strain analysis, mechanism of junction growth, the fretting loop, and the depression mark on the block are discussed.

3.1.1 The Cylindrical Contact Model

The 2D displacement-controlled model is shown in Figure 3-1a, which is a half cylinder of a radius R=0.5m rubbing against a 4RxR block. Both half cylinder and the block are deformable. In the figure, the axes of X and Y are shown where the origin is located at the

contact point. It is noted that referring motion to the “right” or “left” indicate motion in the positive or negative X axis, respectively.

As shown in Fig.3-1b, the cylinder radius is R; block dimensions are given in terms of that radius, and this is maintained throughout this work. The fretting model is now introduced. First, a vertical displacement, ω, on the top of the half cylinder is applied. That is referred to as the interference. While keeping the interference constant, horizontal oscillations, δ, are then applied to simulate the fretting motion. That is, the top of the half cylinder is forced to displace a certain distance to the right and then back to the left passing the origin position, continuing the same distance to the left, before returning back to the origin – that constitutes one cycle of loading. The procedure is performed quasi-statically, taking 40 load steps to complete one cycle.

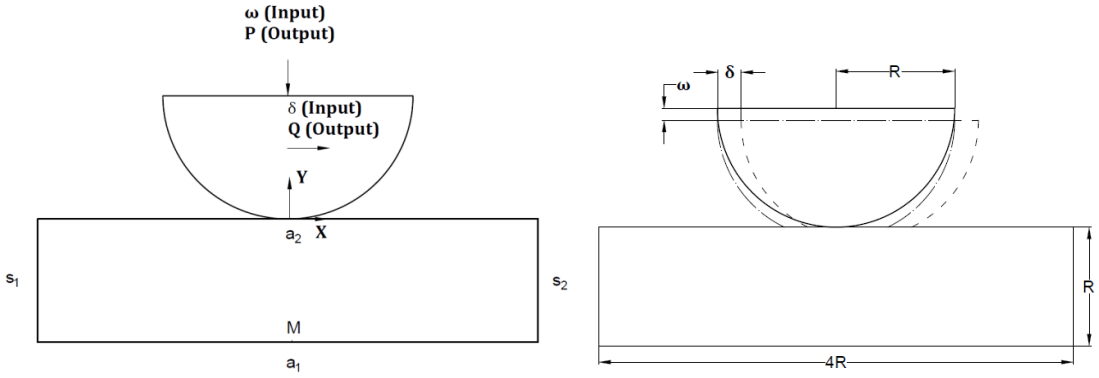

(a) Displacement-controlled inputs, and reaction output (b) Cylinder-block dimensions and displacement directions

Figure 3-1. Schematic of a half-cylinder in contact with a flat block, along with the loading definitions for displacement-controlled loading condition.

The 2D force-controlled model is shown in Fig.3-2. The difference between the displacement-controlled model and the force-controlled model is that the input in the Y direction is interference, ω, in the displacement-controlled model, while it is normal load, P, in the force-controlled model. To enforce a uniform downward displacement at the top surface of the half-cylinder, a simulated rigid plate with sufficient large elastic modulus (2×10^{10} GPa) is positioned on the top. The interface between the rigid plate and the half cylinder is made frictionless, as the rigid plate role is to prevent rotation of the half-cylinder at its upper boundary. The input of the oscillation in the X direction is the same as that in the displacement-controlled model.

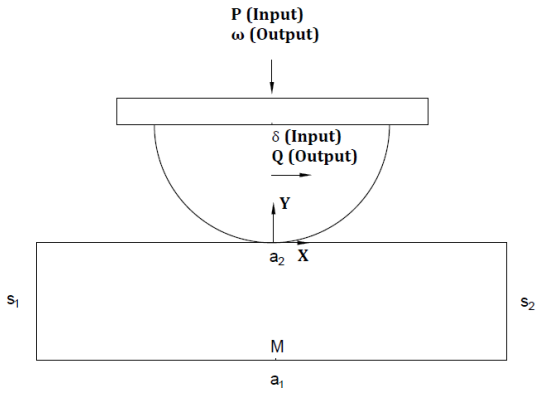

Figure 3-2. Schematic of a half-cylinder in contact with a flat block, along with the loading definitions for force-controlled loading condition.

The materials of the half cylinder and block are set to identical material pair: steel/steel[61]. The material properties are summarized in Table 3-1. The parameter C(ν) represents the ratio between the maximum pressure and the maximum von Mises stress in normal elastic contact in 2D plane-strain case as given by Green [61]. The elastic-perfectly plastic behavior is used in the FEA.

Table 3-1. Material properties for cylindrical fretting model

Material	Elastic Modulus[GPa] E	Yielding Strength[MPa] S_y	Poisson Ratio ν	C(ν)	$C \cdot S_y$ [MPa]
Steel	200.0	912	0.32	1.818	1657

In an elastic contact regime, the solution of the 2D plane strain cylindrical contact is given by the Hertzian contact model. Under a total load per unit length, *P/L*, the maximum pressure, p_0, is located at the center of the contact [11]:

$$p_0 = \frac{2P}{\pi bL} \tag{3-1}$$

The half-width of the contact, b, is given by:

$$b = \left(\frac{4PR}{\pi LE^{'}} \right)^{\frac{1}{2}} \tag{3-2}$$

where E' is the equivalent elastic modulus is:

$$\frac{1}{E^{'}} = \frac{1-\nu_1^2}{E_1} + \frac{1-\nu_2^2}{E_2} \tag{3-3}$$

The interference of a half cylinder in contact with a block, whose depth is *d=R*, is derived in Appendix A, Eq. A-8:

$$\omega = \frac{P/L}{2\pi E^{'}} \left\{ 2\ln\left(\frac{2\pi RE^{'}}{P/L}\right) - \frac{1}{1-\nu} \right\} \tag{3-4}$$

At the onset of yielding $\sigma_{e-\max} = S_y$, for contact between identical materials, the product C^*S_y determines the maximum contact pressure, p_0, at which the material yields first. For cylindrical contact as given by Green [61], C(υ)=1.164+2.975 υ -2.906 υ^2, for υ >0.1938. Hence, at yielding onset, p_o is replaced by the product,

$$p_{0c} = CS_y \tag{3-5}$$

to provide the critical parameters. These values are used to calculate the critical half contact width, b_c , and the critical load per unit length, P_c/L , according to [61]:

$$b_c = \frac{2RCS_y}{E'} \tag{3-6}$$

$$\frac{P_c}{L} = \frac{\pi R(CS_y)^2}{E'} \tag{3-7}$$

By subsisting Eq.3-7 into Eq.3-4, the critical interference is:

$$\omega_c = \frac{R}{2}\left(\frac{CS_y}{E'}\right)^2\left[4\ln\left(\frac{\sqrt{2}E'}{CS_y}\right) - \frac{1}{1-\upsilon}\right] \tag{3-8}$$

For the material properties listed in Table 3-1 and the depth of the block ($d=R$) herein, the critical interference, the critical load per unit length, and the critical half contact width are given in Table3-2. The critical values, ω_c, b_c, P_c/L are used to normalize the forthcoming room and high temperature results, respectively.

Table 3-2. The critical values (onset of plasticity) for steel/steel plane strain case

Cylinder Material	Block Material	Critical Interference ω_c [μm]	Critical Load per Unit Length P_c/L [MN/m]	Critical Half Contact Width b_c [mm]
Steel	Steel	927	38.7	14.9

In this work, the values of the vertical interference are integer multiples of the critical one, namely $1*\omega_c$, $2*\omega_c$, $3*\omega_c$, etc. The amplitude of the horizontal displacement is always kept being equal to the critical interference, $1*\omega_c$. In this way, the results are readily nondimensionalized and they can be applied to both macroscopic and microscopic contacts. In the displacement-controlled simulation, the vertical interference and the horizontal displacement, ω and δ, are the inputs, while the normal and tangential forces at

the contact, P and Q, are outputs. In the force-controlled simulation, the normal force and the horizontal displacement, P and δ, are the inputs, while the interference and tangential forces at the contact, ω and Q, are outputs.

3.1.2 Mesh Convergence of Cylindrical Contact Model

A 2D plain strain element (PLANE183) is used in ANSYS 17.1 to model the contact. Taking the displacement-controlled model of steel/steel for instance (shown in Fig. 3-3), the total mesh consists of 66383 elements, where the mesh in contact area is refined with the element length size of $8*10^{-5}$R. One hundred contact elements are defined on each side of contact. Stiff springs are attached to these elements and activated once penetration is incipient. This is intrinsically handled by the ANSYS contact and target elements, CONTA172 and TARGE169, respectively. For different material pairs, the critical contact widths are different, which generate different total number of mesh elements. However, one hundred contact elements are maintained for each model, when the normal load reaches P_c/L.

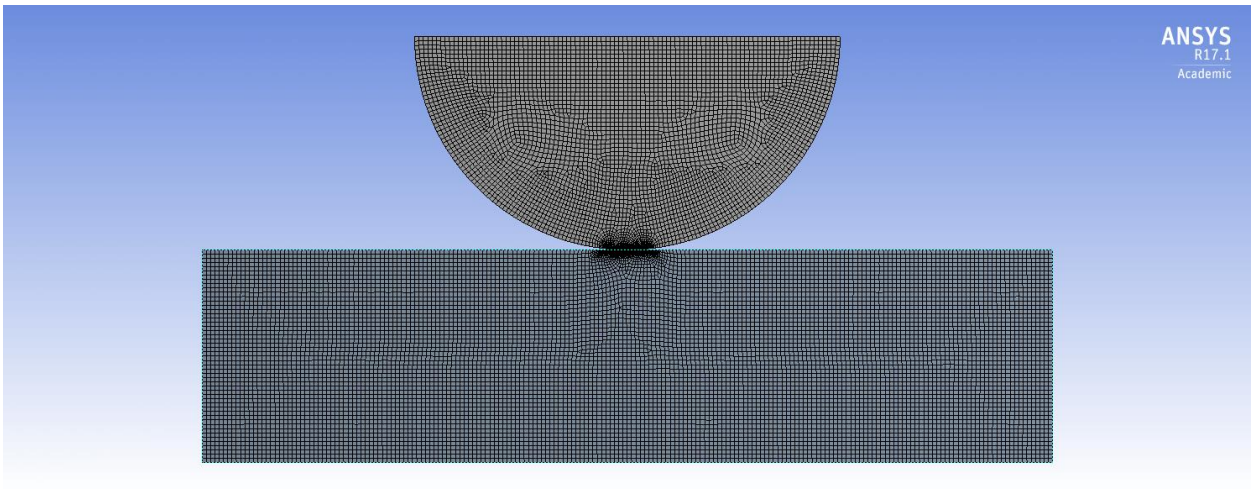

Figure 3-3. Finite element model in ANSYS 17.1 for plane strain steel/steel case.

To validate the model, mesh convergence is first performed for the elastic contact (interference ranges from $0.2*\omega_c$ to $1*\omega_c$), and the results are compared with those from Hertz contact solution. For the comparison ω/ω_c is the input, ω_c is calculated by Eq.3-8, and thus ω is imposed in the FEA. The theoretical load per length, P/L, is solved from Eq. 3-4, while in the FEA simulation P/L is a reaction output. From the entire interference range examined in Table 3-3, for *d/R=1*, the load per unit length differs by a maximum of 0.47%, the contact width by 2.17%, the maximum contact pressure by 1.57%, and the maximum von-Mises stress by 1.09%. Additional comparisons are also given in the Appendix A for different block sizes at the critical interference. With such outstanding agreement between theoretical and FEA results, the model and mesh converge have been established in the elastic regime.

In addition, as there is no closed-form solution for elastic-plastic contacts under the combined load of normal and tangential loads. For such cases, the elements of the mesh are iteratively refined by a factor of two until there is less than one percent difference in the contact width between iterations. Additionally, the region in contact is always confined within the refined mesh.

Table 3-3. Comparison of selected values between theoretical predictions and FEA results for a half-cylinder of radius, R, in elastic contact with a 4RxR block (ω ranges from 0.2*ω_c to 1* ω_c).

Input	Theoretical Predictions					FEA Results							
ω/ω_c	ω [mm]	b [mm]	P/L [MN/m]	p_0 [GPa]	σ_{emax}[GPa]	b [mm]	% dif	P/L [MN/m]	%dif	p_0 [GPa]	%dif	σ_{emax}[GPa]	%dif
0.2	0.1854	6.03	6.36	0.672	0.3693	6.04	-0.41	6.33	-0.43	0.661	-1.57	0.3675	-0.50
0.6	0.5562	11.15	21.75	1.242	0.6830	11.20	0.48	21.65	-0.47	1.231	-0.86	0.6904	1.09
1	0.9266	14.88	38.73	1.657	0.9115	15.20	2.17	38.56	-0.43	1.645	-0.75	0.9122	0.08

The mesh convergence procedure for other material pairs under displacement-controlled loading condition is the same as the one shown above. However, the mesh convergence for the force-controlled model is somewhat different. The input is normal load per unit length, P/L. Based on P/L, the interference, ω, can be obtained from Eq. 3-4. The remaining portion of the model is the same as that in displacement-controlled model. For all the cases in this work, the difference between the theoretical value and FEA value is below 3% for normal elastic condition, and the elements of the mesh are iteratively refined by a factor of two until there is less than one percent difference in the contact width between iterations.

3.1.3 Loading Steps in Cylindrical Contact Model

The results for the displacement-controlled and the force-controlled models have similar trends. For brevity in this chapter, all results are for the displacement-controlled model unless otherwise noted. The following results are reported for specific boundary conditions applied on the block (shown in Fig.3-1a): The base of the block, a_1, is fixed in both the X and Y directions, and the other three sides of the block (a_2, s_1, and s_2) are free. The effects

of other boundary conditions are discussed in Appendix B. The results of the finite element model are presented using the normalized vertical interference, $\omega^* = \frac{\omega}{\omega_c}$, ranging from 0.7 (initially inducing a purely elastic regime) to 3 (initially inducing an elastic-plastic regime [85] , where the plasticity reaches the surface). Four different frictional coefficients are imposed at the contact interface, 0.1, 0.3, 0.45, and 1. In order to describe the oscillatory horizontal displacement, load steps are used. As shown in Fig.3-4, Step 0 represents the start of horizontal load just after the vertical interference is applied. Each step increment represents a sliding distance of $0.1* \omega_c$. It takes 40 steps to complete one cycle of loading. Due to the computational burden (20 hours for a single simulation on a 3GHz Intel Xeon PC Workstation), the maximum number of horizontal displacement cycles investigated in this work is set to six.

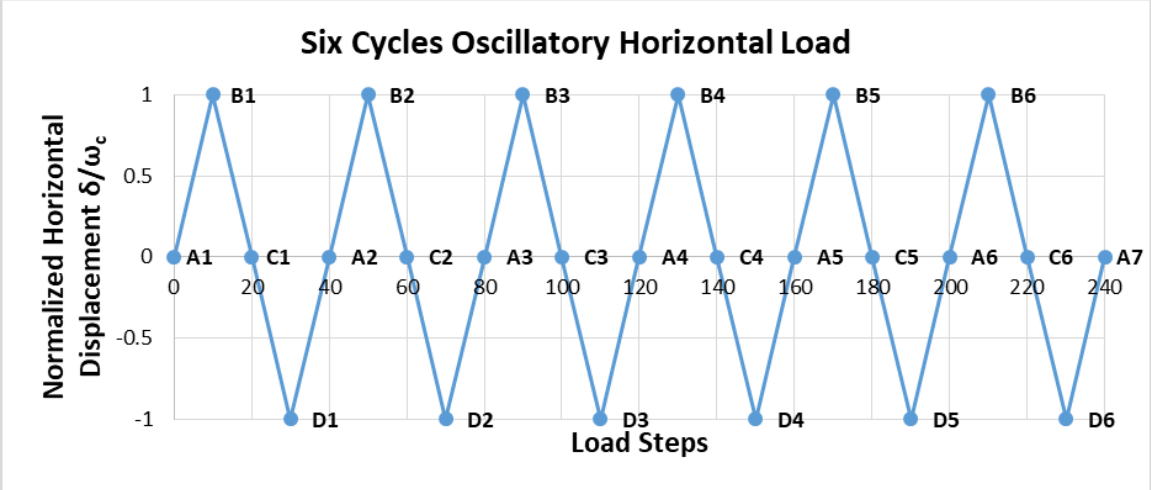

Figure 3-4. Loading steps of six cycles oscillatory horizontal for plane strain case.

The following convention of notation is used to signify the location and the cycle number. Points (A,B,C,D) signify, respectively, $\delta = (0,1,0,-1)\omega_c$, and n=1,2,…,6 specifies the cycle number. For example, A_4 represents the inception of the fourth cycle, where $\delta = 0 * \omega_c$.

3.1.4 The Distribution of von-Mises Stresses

Figure 3-5 shows the progression of von-Mises stress at $1^* \omega_c$ interference with μ=1 applied at the contact interface for steel/steel. The color coding in each picture is maintained to the same scale. The highest intensity red color indicates the maximum von-Mises stress. The next two parameters are used to identify the horizontal load step. The first parameter represents the horizontal displacement, and the second parameter indicates at which branch of the cycle the displacement is approached. For example, Fig.3-5a through Fig.3-5g represent the horizontal displacement of the cylinder, δ= (0, 0.1, 0.3, 0.5, 0.6, 0.7, 1)* ω_c, respectively, in branch A_1-B_1 (defined in Fig.3-4). Since the von-Mises stress distributions in the cylinder and the block appear as mirror images, only the progressions of the von-Mises stresses on the cylinder are discussed in the following.

At the very beginning, before horizontal displacement commences, the distribution of the von-Mises stress (shown in Fig.3-5a) solely represents a normal contact. The area with large von-Mises stresses is located under the surface for $\nu > 0.1938$, in agreement with Green [61]. In this case, Fig.3-5a, there is one point in each body reaching the yield strength. Then the cylinder is forced to slide to the right (i.e., in the positive X direction). Depending on the value of the COF, the status of the contact region is gross sliding when μ=0.1 and 0.3, partial stick and partial slip when μ=0.45, or fully stick when μ=1, as indicated by ANSYS. The region of large von-Mises stresses under the contacting surface is skewed to the left (Fig.3-5b) due to the introduction of a tangential force acting in the direction opposite to the relative horizontal displacement. Then another two regions of large von-Mises stresses appear at the two edges of the contact (Fig.3-5c). Afterwards, the left plastic region merges with the one under surface (Fig.3-5d) and then the two combined

merge with the right one (Fig.3-5e). As the cylinder moves further to the right, the region is stretched in the x-direction (Fig.3-5f) until it reaches the amplitude of the displacement, $1 * \omega_c$, (Fig.3-5g). It is apparent that large von-Mises stresses appear at the edge of the contact. Then the displacement is forced back to the left (i.e., in the negative X direction) and shakedown occurs (Fig.3-5h). In other words, the von-Mises stress decreases suddenly because of the change in the direction of the tangential force. As it displaces further to the left, the von-Mises stress keeps decreasing, and the region of large von-Mises stresses starts to show up again at the two edges of the contact area (Fig.3-5i-Fig.3-5j). The area with large von-Mises stresses keeps growing and being stretched (Fig.3-5k-Fig.3-5l) until it reaches $-1 * \omega_c$, where it has a mirror image shape similar to that of the case at $1 * \omega_c$ (Fig.3-5g). Another shakedown takes place as the displacement is forced to the right (Fig.3-5m). Finally, the cylinder moves back to $0 * \omega_c$ and that completes one cycle of loading (Fig.3-5n). The large von-Mises stress appears at the two edges of the contact again. The simulation continues for another five cycles. As shown in (Fig.3-5o), the large von-Mises stress stays there after six cycles of load. The development of the von-Mises stresses is also investigated for other interference cases of $0.7 * \omega_c$, $2 * \omega_c$, and $3 * \omega_c$, but the trends remain the same as for the case of $1 * \omega_c$ (of course, having larger plastic regions as the interference increases). For brevity, these results are not reported. From the evolution of von-Mises stress above, a conclusion can be drawn that during the oscillatory tangential loading, the two contact edges tend to experience the largest von-Mises stress. It is, therefore, postulated that cracks and fatigue are most likely to initiate and propagate at the contact edges for frictional contact.

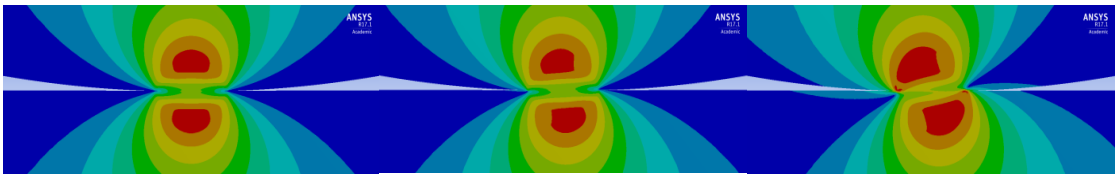

(a) $0 * \omega_c$ at A1-B1 (b) $0.1 * \omega_c$ at A1-B1 (c) $0.3 * \omega_c$ at A1-B1

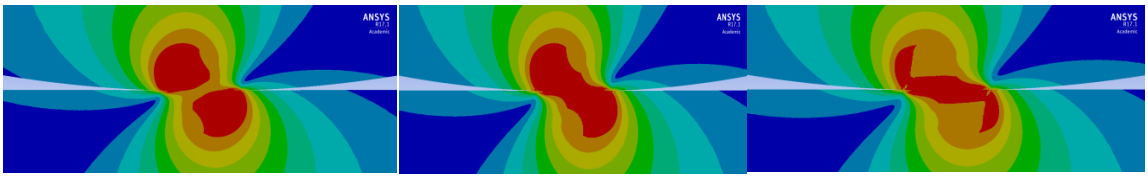

(d) $0.5 * \omega_c$ at A1-B1 (e) $0.6 * \omega_c$ at A1-B1 (f) $0.7 * \omega_c$ at A1-B1

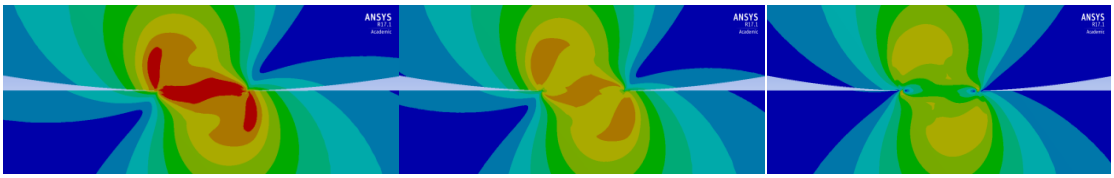

(g) $1 * \omega_c$ at A1-B1 (h) $0.9 * \omega_c$ at B1-C1 (i) $0.5 * \omega_c$ at B1-C1

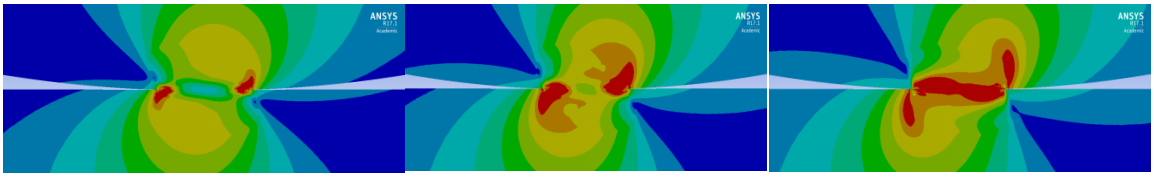

(j) $0 * \omega_c$ at B1-C1 (k) $-0.2 * \omega_c$ at C1-D1 (l) $-1 * \omega_c$ at C1-D1

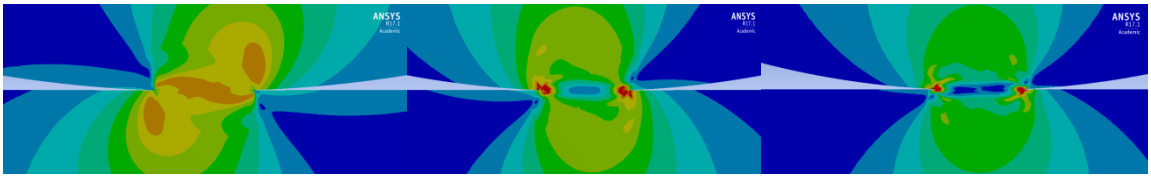

(m) $-0.9 * \omega_c$ at D1-A2 (n) $0 * \omega_c$ at D1-A2 (o) $0 * \omega_c$ at D6-A7

Figure 3-5. Evolution of von-Mises stresses at 1*ω_c vertical interference during the first cycle (a)-(n) and the last point (o) at the end of six cycles of horizontal loading with μ=1 for steel/steel.

3.1.5 The Distribution of Plastic Strain

When the von-Mises stresses reach the yield strength and fretting is in the elastic-plastic regime, there are plastic strains in the contacting bodies which are indicated by the equivalent plastic strain, ε_p. Fig.3-6 shows the distribution of ε_p at the region of contact after three cycles of horizontal loading have completed, at different interferences and COFs for steel/steel. In all the three cases, the maximum ε_p is located at the two edges of contact, which coincides with the location of the maximum von-Mises stress. That is consistent with the direct correspondence between stress and strain. It can be further explained by the pileup (discussed further in Section 3.1.8) on the surface of the block.

Fig.3-6a illustrates the plastic strain distribution at $0.7 * \omega_c$ interference with μ=1. Although there is no plastic strain under surface after the just normal loading (i.e., a pure elastic regime), the introduction of the tangential force spawns plastic strains that are confined near the contacting surfaces. This also gives rise to friction-induced work. When the interference increases to $1* \omega_c$ (the limit of the elastic regime in normal loading), as shown in Fig.3-6b, the plastic strains increase because of the increase of the normal force caused by the larger interference. As the interference increases further to $3 * \omega_c$ (Fig.3-6c), the plastic strain distributions change. Since the region under the surface reaches plasticity in a much larger area (details provided by Jackson and Green [21]), the plastic strain spreads to a deeper and wider region under the surface. Consequently, the larger region absorbs the damage manifested by a deeper depression mark. As a result, the maximum ε_p (located at the edges) is relatively smaller at larger interference. In other words, as the contact produces more permanent damage, there is less plastic strain at the edges, i.e., at

the location where the failure, as postulated in Section 3.1.3.1, is most likely to show up. Evident from the maximum values in Fig5.c (μ=1) and Fig5.d (μ=0.3), the plastic strain decreases with the drop of the COF, especially at the edges.

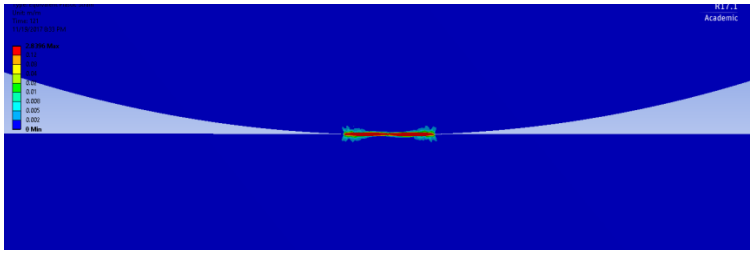

(a) $0.7 * \omega_c$ interference, μ=1, maximum ε_p=2.84

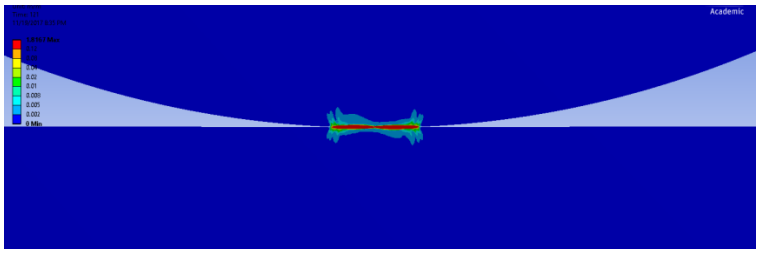

(b) $1 * \omega_c$ interference, μ=1, maximum ε_p=1.82

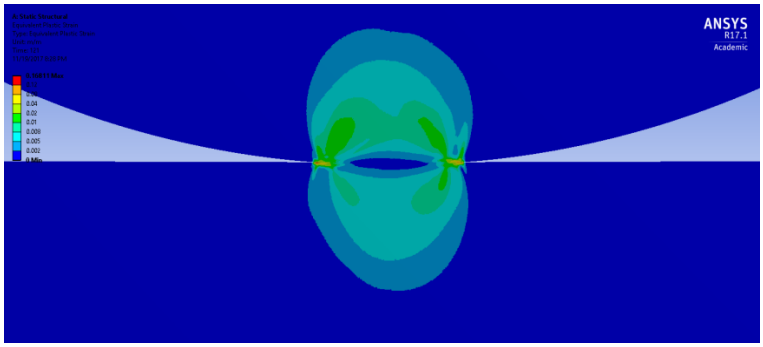

(c) $3 * \omega_c$ interference, μ=1, maximum ε_p=0.17

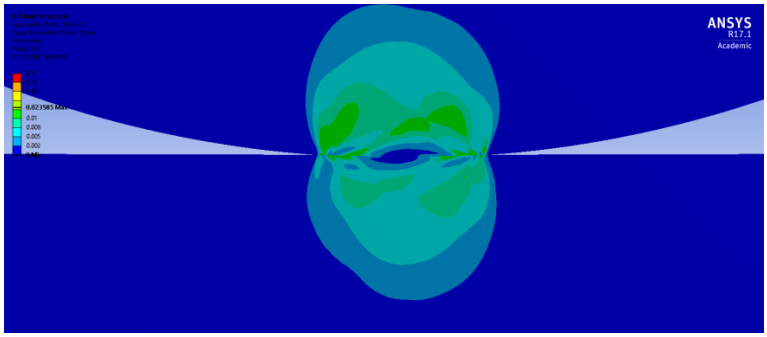

(d) $3 * \omega_c$ interference, μ=0.3, maximum ε_p=0.024

Figure 3-6. The distribution of the equivalent plastic strain after three cycles of horizontal load near the contacting area for steel/steel.

In order to understand the progression of plastic strain, the distribution of ε_p on the contacting surfaces after each horizontal loading cycle is investigated. Fig.3-7 represents the evolution of the ε_p on the surface of the half cylinder during the six cycles of horizontal load at 1*ω_c interference with μ=1. The abscissa is the horizontal position on the surface normalized by the critical half contact width, b_c (as defined and reported above). As shown in Fig.3-7, the plastic strain keeps increasing after each cycle of loading. Additionally, the maximum ε_p stays at the right edge of the contact (due to junction growth as discussed in Section 3.1.6, where the edges of contact keep moving laterally outward after each cycle). This phenomenon could be attributed to the decrease of the normal force required to keep the interference. As the oscillatory sliding motion proceeds, the tip of the cylinder keeps being flattened and the normal force required to maintain the same interference continues to decrease. Since, at the very beginning of the horizontal load, the cylinder moves to the right first, the right edge of the contact experiences deformation caused by the pileup (or the abrupt change of the curvature) on the surface of the block under a larger normal force. As the cylinder returns to the left, under a smaller normal force, the deformation on the left edge of the contact is less than that on the right. Consequently, the ε_p is relatively larger on the right edges which is located in the same direction as the initial horizontal motion of the cylinder. The observed directional affect is consistent with the initial direction of motion in the current simulation.

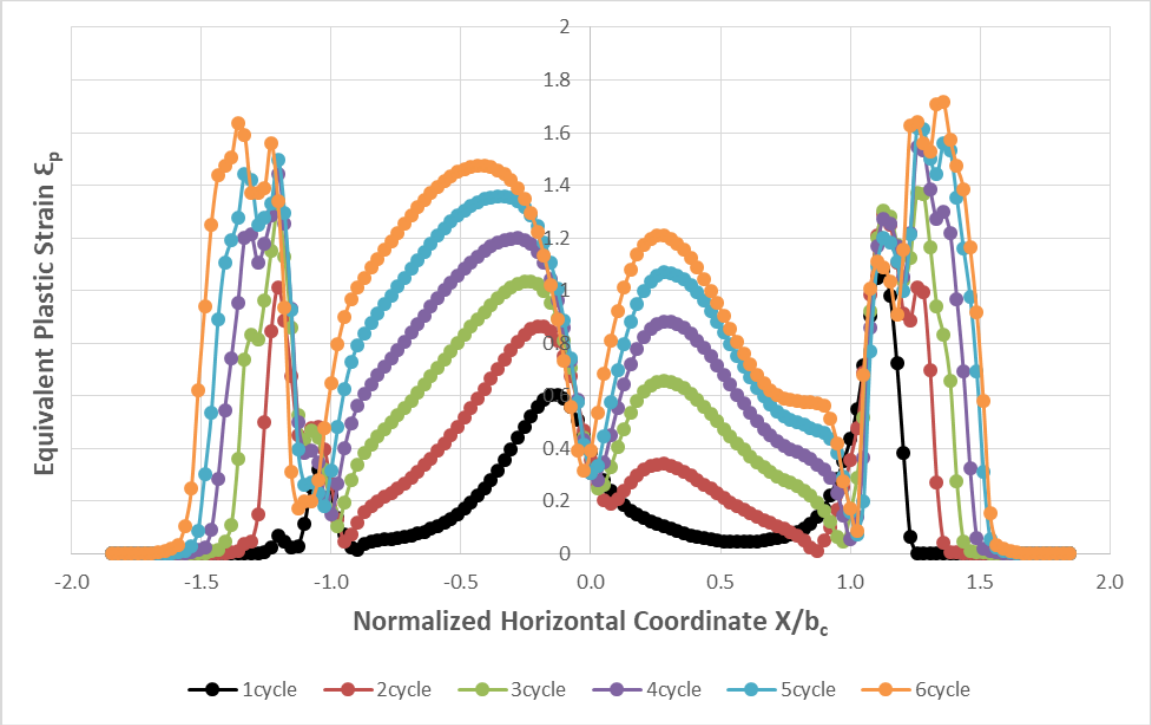

Figure 3-7. The distribution of the equivalent plastic strain on the contacting surface of the cylinder at 1*ω_c interference with μ=1 for steel/steel.

3.1.6 Junction Growth

The junction growth, i.e. the increase of the contact area, is observed during the oscillatory horizontal motion for displacement-controlled analysis performed in this work. Fig.3-8 shows the development of the half contact width, normalized by the critical half contact width, during the six cycles of horizontal displacement at $1 * \omega_c$ interference for frictional (μ=1) and frictionless contacts. When μ=1, the frictional contact area keeps increasing, where it tends to stabilize after sufficient cycles of load. But for frictionless contact, the area remains constant. The explanation is that the introduction of the friction force produces plasticity on the contacting surface and consequently increases the contacting width. However, without friction, there is no plastic region on the surface at $1 * \omega_c$ interference, and no plastic strain is caused so that there is no junction growth. To study

the effect of the COF on the junction growth, different COFs are applied to the model at the same interference. Fig.3-9 shows the development of half contact width at $3 * \omega_c$ interference during three cycles of load. Two conclusions are drawn from the above observation. First, the magnitude of the junction growth increases with the COF. The explanation is that the small COF introduces small tangential force, which causes less plastic deformation on the surface so that less junction growth is generated. Second, the rate of stabilization decreases as the COF increases, because the normal force keeps decreasing during sliding and the von-Mises stress on the surface decreases faster with smaller COF. Consequently, in the cases with smaller COFs, the von-Mises stress on the surface falls below the yield strength earlier so that the junction growth stabilizes earlier.

The junction growth is also found even at $0.7 * \omega_c$ interference, but that is combined with fretting (sliding motion) under a COF of μ=1. Since there is plastic strain at the interface, it is reasonable to expect junction growth. And indeed, there is a 9.7% increase in the contact width after one cycle of horizontal loading.

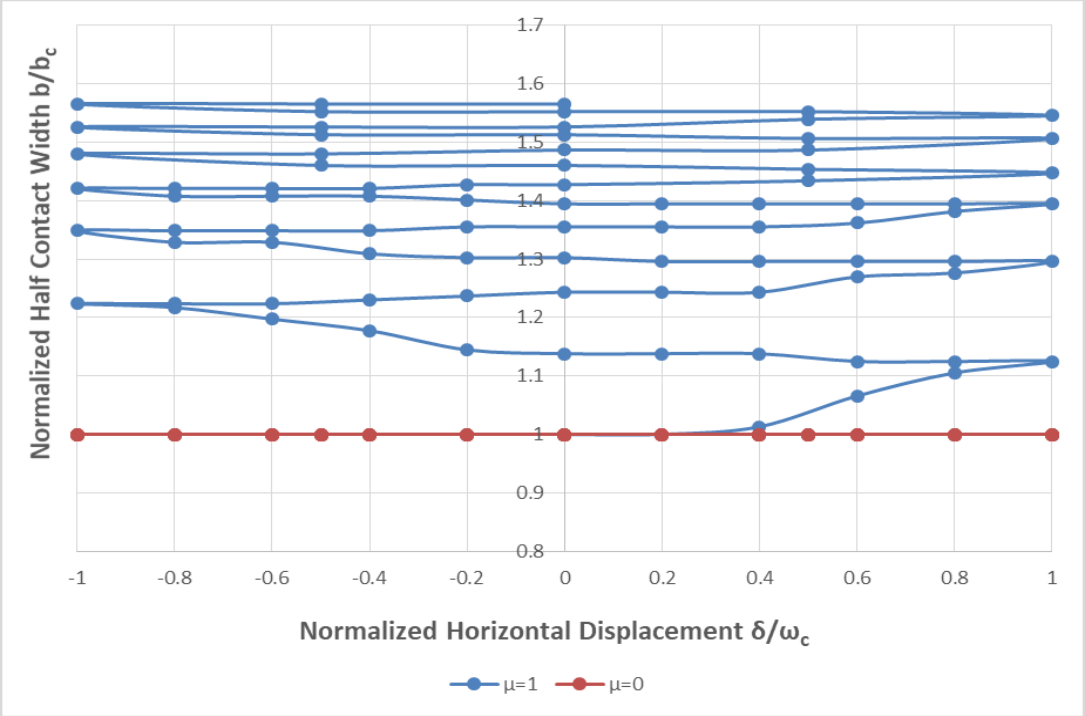

Figure 3-8. The development of junction growth at 1*ω$_c$ interference for fictional and frictionless contacts during six cycles of load for steel/steel.

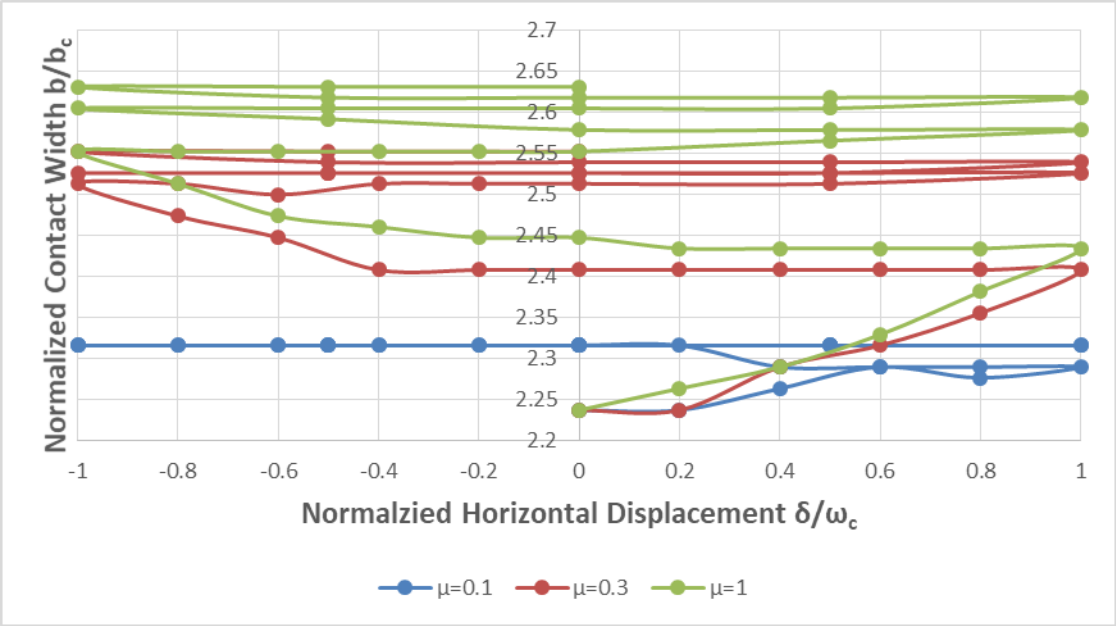

Figure 3-9. The development of junction growth at 3*ω$_c$ interference with different COFs during three cycles of load for steel/steel.

3.1.7 The Evolution of Tangential Force per Unit Length

As the fretting motion proceeds, the output of the tangential force per unit length, Q/L, is recorded. Even with μ=0, it is found that $Q/L \neq 0$. Take the steel/steel case for instance, the absolute Q/L at $1* \omega_c$ interference, with μ=0, ranges from 0 to 573N/m during the first cycle of the horizontal loading. It is noted, however, that the maximum value of Q/L = 573N/m, by comparison to $P_c/L=3.873\times 10^7$ N/m, (i.e., $Q/P_c=1.5x10^{-5}$), is minute. It is caused by numerical round-off errors, and effectively it verifies a frictionless case. In contrast, at $1 * \omega_c$ interference and with μ=1, the absolute Q/L ranges from 0 to $1.79*10^7$N/m during the first cycle of the horizontal loading. Fig.3-10 shows the development of the Q/L, normalized by critical normal load per unit length P_c/L, during six cycles of loading at $1* \omega_c$ interference with μ=1. The evolution of the traction force in Fig.3-10 begins to stabilize after the first one quarter of the cycle. The stabilized curve is the typical fretting loop at the initial few cycles of loading (also reported by Walvekar [86]). The enclosed area represents the energy loss caused during the fretting motion. It is evident that the maximum tangential force increases as fretting proceeds. It is caused by the cumulative plastic deformation on the contacting surfaces.

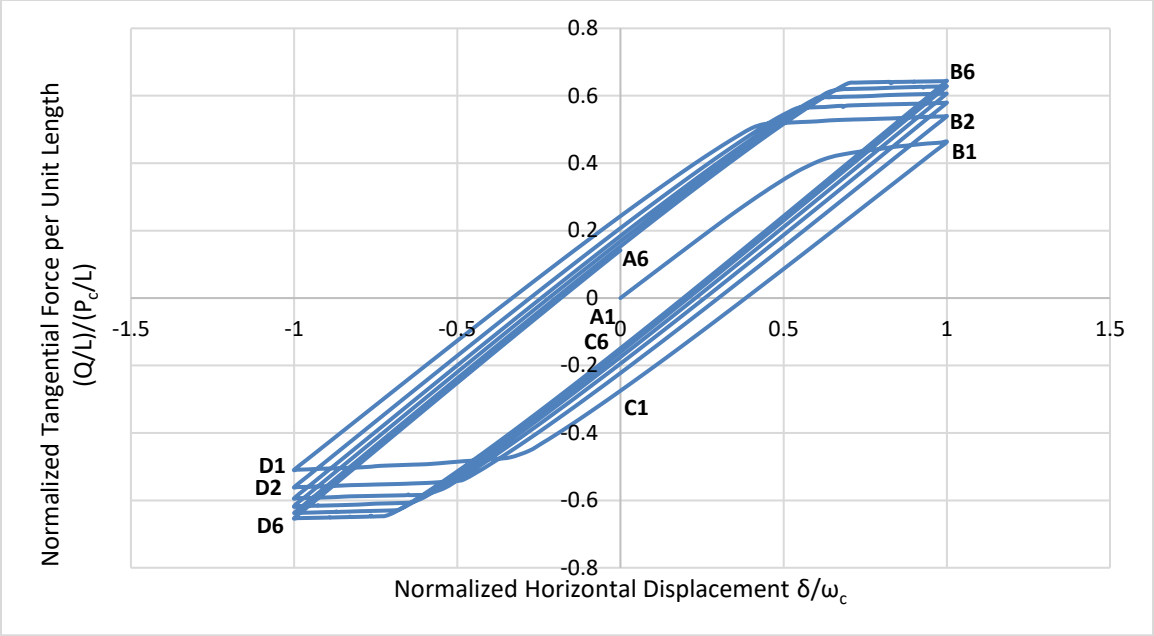

Figure 3-10. The development of tangential force at 1*ω_c interference with μ=1 during six cycles of load for steel/steel.

3.1.8 Depression Marks on the Block

As the fretting motion proceeds, a depression mark is generated at the surface of the flat block. The depression mark can be visualized by the deformed curve of that surface. Fig.3-11 shows the deformed curve at $1* \omega_c$ interference with μ=1 just after the interference is applied. The curve is identical in shape to that of an elastic half-space with line loading, as given by Johnson [11], except that the displacement is infinite at the origin by Johnson while it is finite in the current model. When the curve near the contact is zoomed in (see the inset in Fig.3-11), the indentation caused by the interference becomes clearly visible.

The depression mark grows during the oscillatory horizontal loading. Fig.3-12 depicts the deformed curves of the surface of the contact region at $3* \omega_c$ interference with μ=0.1 (gross sliding), μ=0.45 (partial slip and partial stick), and μ=1 (fully stick) after three cycles of

loading. For μ=0.1, the depression is the shallowest. For μ=0.45, the depression is deeper and wider, but the center part of the surface is dragged somewhat upwards by the lateral motion. The change of the curvature at the inflection point (the position of the edge of the contact) is more pronounced. For μ=1, the trends mentioned above are intensified, and pileup shows up near the inflection point of the curve. According to the results above, the pileup will occur at the edges of the indentation with a sufficiently large COF, especially in the case of the fully stick. The abrupt change of the curvature or pileup will further produce the large von-Mises stress and plastic deformation at the corresponding position of the contact.

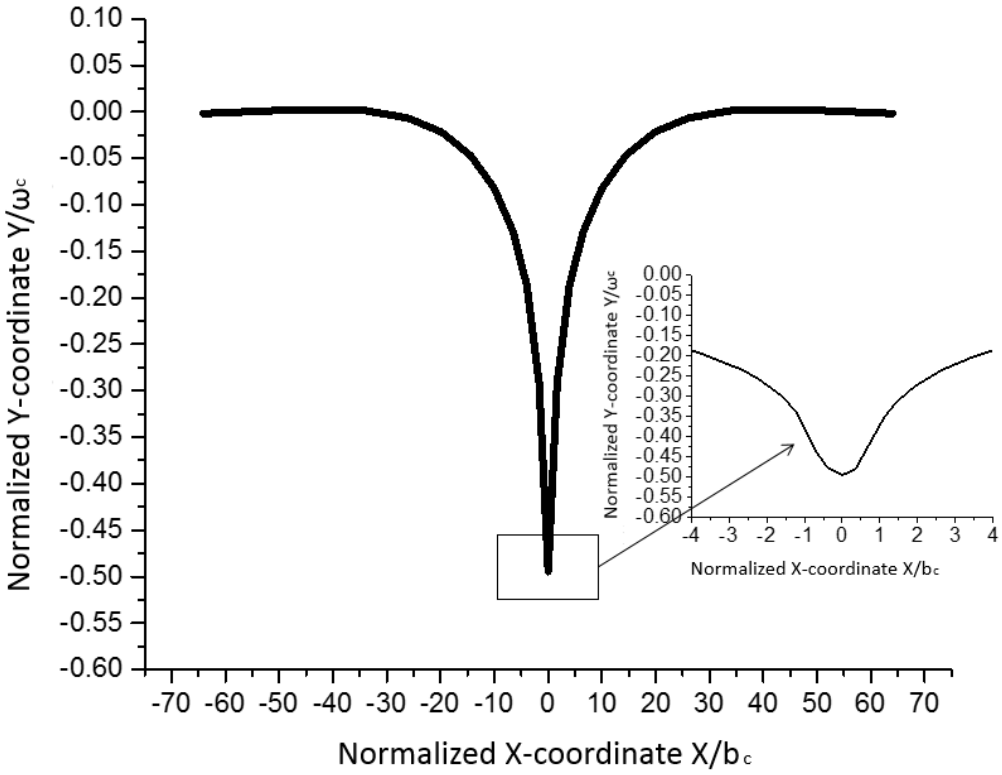

Figure 3-11. The curve of the surface of the block after 1*ω_c interference for steel/steel.

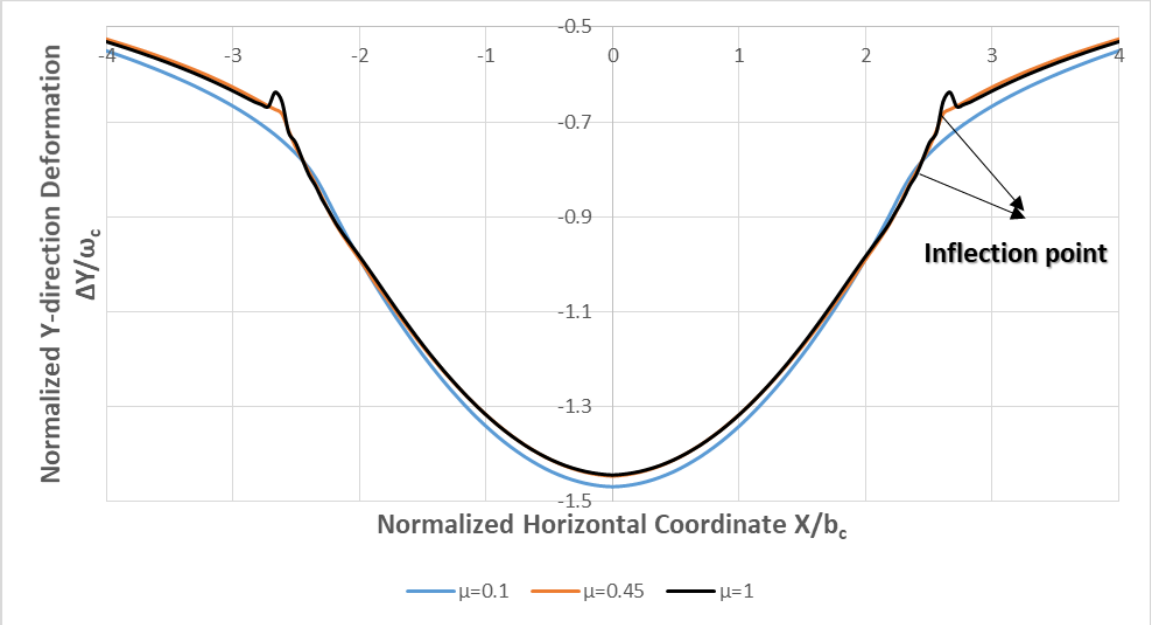

Figure 3-12. The depression marks on the surface of the block at 3*ω_c interference after three cycles of load for steel/steel.

3.1.9 Conclusion

The 2D plane strain fretting model is a half cylinder in contact with a block. The materials of the two bodies are set to the same elastic-perfectly plastic steel. The fretting model is displacement-controlled, where it is loaded with an interference first, and then a reciprocating horizontal displacement is applied to the top of the half cylinder. Different COFs are used in the model.

Five aspects of the fretting model are studied in this work: the progression of the von-Mises stress distribution, the evolution of the plastic strain, the junction growth, the development of tangential force, and the depression marks on the surface of the block. During the oscillatory tangential loading, the two contact edges tend to experience the largest von-

Mises stress. It is, therefore, postulated that cracks and fatigue are most likely to initiate and propagate at the contact edges. Likewise, the largest plastic strain shows up at the edges, too. These two phenomena are caused by the abrupt change of the curvature at the edges of the indentation on the surface. When the COF is large enough to reach the fully stick condition, pileup will appear at the position of the abrupt change, which will intensify the phenomena. The plastic deformation on the surface of the cylinder is not perfectly symmetric about the origin point, where it is slightly larger on the right, which is the direction of the initial motion. This is attributed to the decreasing normal force necessary to maintain a prescribed interference. Also, on the right edge, material pileup is larger under a larger normal reaction force relative to the left edge. Due to the plastic deformation of the surfaces, junction growth is found. The magnitude of the junction growth increases with the COFs, while the rate of the convergence of the growth decreases with the COFs. The behavior of the junction growth is found to agree qualitatively with the experimental results [17, 18] . Also, larger COF introduces larger tangential forces, which results in larger von-Mises stresses. The fretting loop (i.e., the development of the tangential force versus fretting motion) for the initial few cycles of loading is likewise found, where the enclosed area indicates the energy loss. That loop is similar to that found experimentally by Courtney-Pratt and Eisner [17].

3.2 Spherical Contact Model

The spherical fretting condition necessitates a 3D model. The model is first verified in elastic normal contact conditions against theoretical equations and then verified in elastic-plastic fretting contact condition by mesh convergence. The material pair is first set to steel/steel. The stress-strain analysis, mechanism of junction growth, and the fretting loop are discussed. Later, copper is used also to explore generalization of the results by using a normalization scheme. It will be discussed in Section 4.3.

3.2.1 The Spherical Fretting Contact Model

The displacement-controlled fretting model represents contact between an oscillating hemisphere and a stationary flat block (Fig.3-13). In order to take advantage of the symmetry of the problem, the hemisphere and the block are cut in half along the vertical plane. As shown in Fig.3-13a, a quarter sphere with radius R=0.5 m is in contact with a 4R×2R×R block. The coordinate system is shown in Figs.3-13b and 3-13c. For brevity, the positive and negative X directions are implicitly represented by “right” and “left.”

Roller boundary conditions of no displacement normal to the plane are applied to the vertically cut plane of the quarter sphere (due to the symmetry with respect to XY plane) and to all the five faces of the block, except to the top face (the XZ plane), which is free to deform in all directions. Such boundary conditions make the block behave as an elastic half space due to the Saint Venant principal, as discussed later.

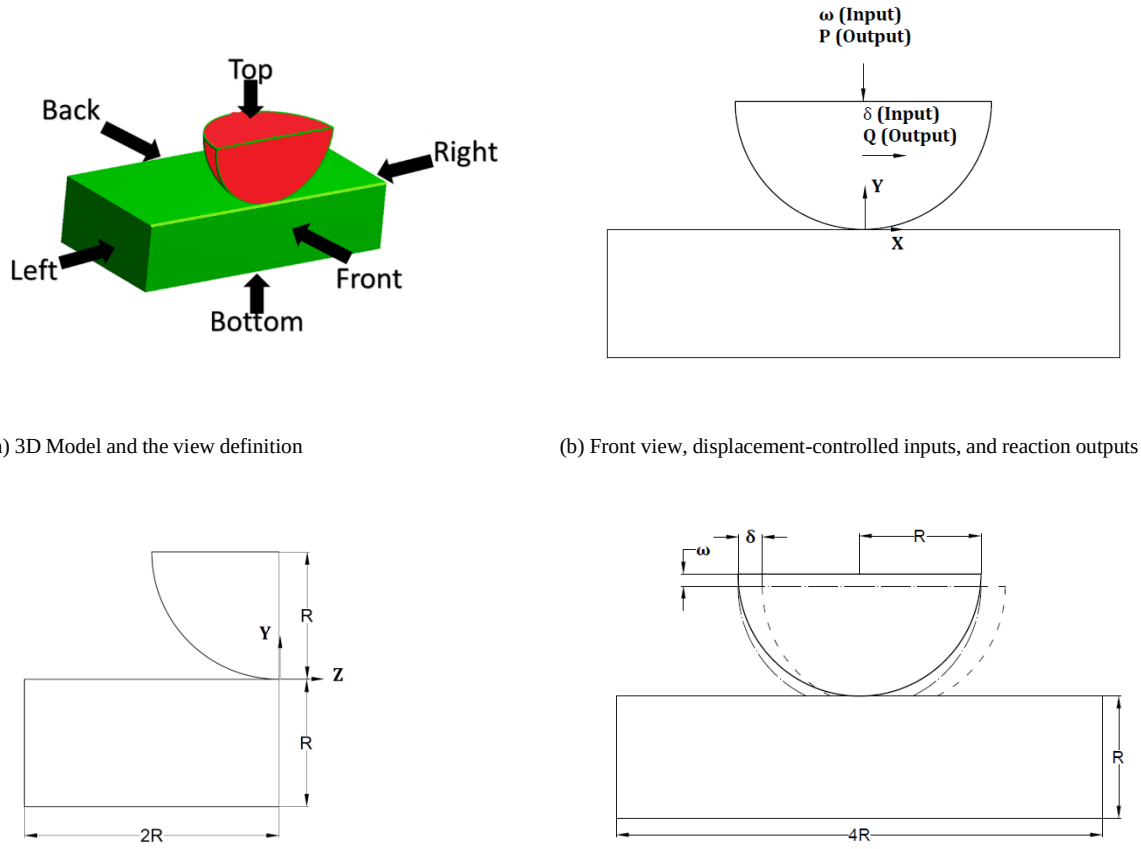

(a) 3D Model and the view definition

(b) Front view, displacement-controlled inputs, and reaction outputs

(c) Side view of the model

(d) Front view, sphere-block dimensions and displacement directions

Figure 3-13. Schematic of a ¼ sphere in contact with a flat block, along with the loading definitions for displacement-controlled steel/steel model.

The 3D force-controlled model is shown in Figure 3-14. The difference between the displacement-controlled model and the force-controlled model is that the input in the Y direction is interference, ω, in the displacement-controlled model, while it is normal load, P, in the force-controlled model. To enforce a uniform downward displacement at the top surface of the half-cylinder, a simulated rigid plate with sufficient large elastic modulus (2×10^{15} GPa) is positioned on the top. The interface between the rigid plate and the half cylinder is made frictionless, as the rigid plate role is to prevent rotation of the half-cylinder at its upper boundary. The input of the oscillation in the X direction is the same as that in the displacement-controlled model.

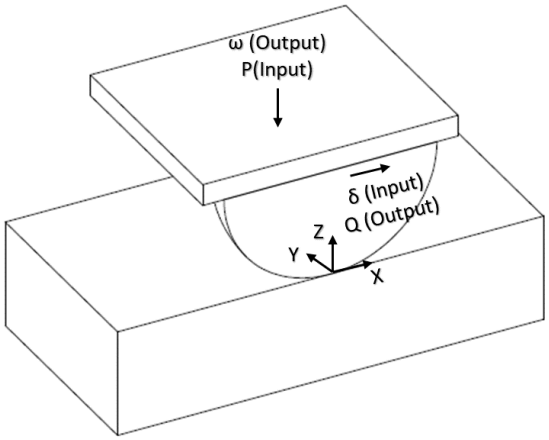

Figure 3-14. Schematic of a ¼ sphere in contact with a flat block for force-controlled steel/steel model.

The hemisphere and the block are set to possess identical material properties, steel/steel. The material properties are listed in Table 3-4. The parameter C(ν) represents the ratio between the maximum pressure and the maximum von Mises stress in normal elastic contact in 3D plane-strain case as given by Green [61]. Both materials are assumed to possess a 1% strain hardening based on the elastic modulus. That amount of the tangential modulus is verified not to significantly affect the FEA results, yet it improves the convergence times in ANSYS. The code ABAQUS is used too on select cases just to verify result. Adhesion is not considered in this chapter.

Table 3-4. Material properties for spherical fretting model steel/steel and copper/copper [87].

Material	Elastic Modulus[GPa] E	Yielding Strength[MPa] S_y	Poisson Ratio ν	C(ν)	$C \cdot S_y$ [MPa]
Steel	200	912	0.32	1.639	1494
Copper	115	124	0.34	1.662	206

In the regime of static elastic normal contact, the Hertzian theory gives the solution to the 3D spherical contact [11]. Given a normal load, P, the contact radius, a, is obtained by,

$$a = \left(\frac{3PR}{4E'} \right)^{\frac{1}{3}} \tag{3-9}$$

E' is the equivalent elastic modulus:

$$\frac{1}{E'} = \frac{1-\nu_1^2}{E_1} + \frac{1-\nu_2^2}{E_2} \tag{3-10}$$

Since the material properties of the hemisphere and block are the same, herein, $E_1=E_2=E$, and $\nu_1=\nu_2=\nu$. The maximum contact pressure, p_0, and the interference, ω, are given by Eqs.3-11 and 3-12:

$$p_0 = \frac{3P}{2\pi a^2} \tag{3-11}$$

$$\omega = \left(\frac{\pi p_0}{2E'}\right)^2 R \tag{3-12}$$

According to Green [61], the ratio between the maximum pressure and the maximum von Mises stress in normal elastic contact is defined by $C(\nu) = p_o / \sigma_{e-\max}$, where C(ν)=1.30075+0.87825 ν +0.54373 ν^2 . At the onset of yielding, the distortion energy theory asserts that $\sigma_{e-\max} = S_y$. The critical maximum pressure, $P_{0c,}$ is, therefore, replaced by the product $C(\nu)S_y$, to establish critical values via Eq.3-9, Eq3-10, Eq.3-11 and Eq.3-12. The critical contact radius, a_c, the critical load, P_c, the critical interference, ω_c, and the critical elastic strain energy, U_c, at which the maximum von-Mises stress reaches the yield strength, S_y, are derive in [61],

$$a_c = \frac{\pi C S_y R}{2E'} \tag{3-13}$$

$$P_c = \frac{(\pi C S_y)^3 R^2}{6E'^2} \tag{3-14}$$

$$\omega_c = \left(\frac{\pi C S_y}{2E'}\right)^2 R \tag{3-15}$$

$$U_c = \frac{(\pi C S_y)^5 R^3}{60E'^4} \tag{3-16}$$

Note that C(ν) and S_y always appear together as a single product term representing a combined material property. By substituting the material properties of Table 3-4 in Eq.3-9, Eq.3-11, and Eq.3-12, the said critical parameters are obtained, and are listed in Table 3-5. The critical contact area is calculated based on a_c, $A_c=\pi a_c^2$. These critical values are subsequently used to normalize (i.e., generalize) results within this work. This is significant because, as noted, the critical values differ by one, two, or three orders of magnitudes.

Table 3-5. The critical values (onset of plasticity) for spherical contact cases

Sphere Material	Block Material	Critical Interference ω_c [μm]	Critical Load P_c [kN]	Critical Elastic Strain Energy U_c [J]	Critical Contact Radius a_c [mm]	Critical Contact Area A_c [mm^2]
Steel	Steel	222	347	14.9	10.5	346.4
Copper	Copper	12.4	2.68	0.013	2.49	19.48

The scheme of normalization in this work is achieved by utilizing the normalized interference, namely $1*\omega_c$, $2*\omega_c$, $3*\omega_c$, while keeping the amplitude of the horizontal displacement $1*\omega_c$ constant throughout. It allows the results to be applied to the practical situations both microscopically and macroscopically.

3.2.2 Mesh Convergence of Spherical Contact Model

Elements Solid 186 and Solid 187 are used to mesh the model in ANSYS 17.1 (shown in Fig.2). There are 161830 elements. The size of the refined mesh in the contact area is $5*10^{-4}$m. Approximately six thousand contact elements (CONTA174 and TARGE170) on each side of the contact are used to simulate frictionless and frictional contacts.

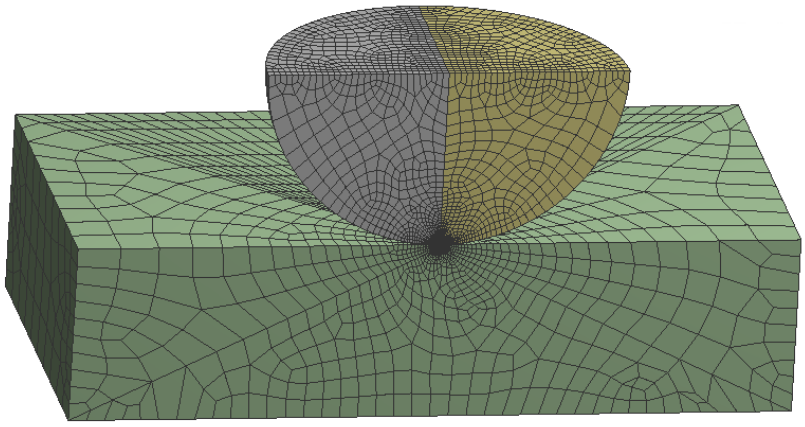

Figure 3-15. Finite element model in ANSYS 17.1 for spherical steel/steel case.

In order to validate the model, the mesh convergence is first performed in the regime of elastic contact for which a closed-form Hertzian solution exists [11], and the results are then compared. The following results are shown for contacts between identical steels. The same procedure is performed for the contact between an identical pair of copper with similar outcomes and for brevity these are omitted.

With the input of ω/ω_c, the interference, ω, is obtained using the aforementioned $\omega_c=0.222mm$. By substituting ω into Eq.3-12, the maximum contact pressure, p_0, is obtained, and by using Eq.3-9 and Eq.3-11, the total load applied to the contact, P, and contact radius, a, are then calculated. In the FEA simulation, with the input of the interference, ω, the total of the normal reaction force at the bottom of the block, P, the maximum contact pressure on the contacting region, p_0, and the radius of the contacting region, a, are extracted from ANSYS. The results are shown in Table 3 for steel-on-steel normal contact. Varying ω/ω_c from *0.2* to the onset of plasticity, $\omega/\omega_c=1$, the load differs by a maximum of *2.28%*, contact radius *3.70%* and maximum contact pressure *4.07%*. The difference is higher when the interference is lower because extremely fine meshes are needed at lower interferences to capture the contact. However, the results are rather accurate about the $1*\omega_c$ interference and above. Therefore, the model and mesh converge using ANSYS have been established. It is noted that for verification purposes a similar model is executed using ABAQUS with practically identical results, with similar execution times.

Table 3-6. Comparison of selected values between theoretical predictions and FEA results for a hemisphere of radius, R, in an elastic contact with a 4Rx4RxR block.

Input	Theoretical Predictions					FEA Results							
ω/ω_c	ω [mm]	a [mm]	P [kN]	p_0 [GPa]	σ_{emax}[GPa]	a [mm]	% dif	P [kN]	%dif	p_0 [GPa]	%dif	σ_{emax}[GPa]	%dif
0.2	0.044	4.71	31.0	0.668	0.408	4.88	3.70	30.3	-2.28	0.641	-4.07	0.393	-3.66
0.6	0.133	8.16	161	1.157	0.706	8.28	1.55	160	-0.82	1.147	-0.91	0.690	-2.33
1	0.222	10.53	347	1.494	0.911	10.6	0.65	344	-0.77	1.487	-0.47	0.899	-1.35

Since, for elastic-plastic contacts under combined normal and tangential loads, there is no closed-form solution, in that regime the elements of the mesh are iteratively refined by a factor of two until there is less than two percent difference in the contact radius between iterations.

The mesh convergence procedure for other material pairs under displacement-controlled loading condition is same as the one shown above. However, the mesh convergence for the force-controlled model is somewhat different. The input is normal load per unit length, P/L. Based on P/L, the interference, ω, can be obtained from Eq. 3-12. The rest part is the same as that in displacement-controlled model. For all the cases in this work, the difference between the theoretical value and FEA value is below 3% for normal elastic condition, and the elements of the mesh are iteratively refined by a factor of two until there is less than one percent difference in the contact area between iterations.

3.2.3 Loading Steps in Spherical Contact Model

The results for displacement-controlled and force-controlled model are in similar trends. For brevity, all results are for displacement-controlled model in this chapter unless

otherwise noted. The results of the model described above are presented for normalized vertical interference, $\omega^* = \frac{\omega}{\omega_c}$, ranging from 1 (the limit of the elastic regime) to 3 (in the elastic-plastic regime). Three different COFs are applied, 0, 0.3 and 1. According to the wear control handbook by Peterson and Winer [88], a COF=0.3 is "typical" for metallic surface in dry contact, where a COF=1 represents a high value. Therefore, with COFs=0, 0.3, and 1, the contact conditions range from "frictionless" through "typical" to "high." As shown in Fig.3-16, load steps are used to impose the oscillatory horizontal displacement and extract results of the intermediate state. Step 0 corresponds to the loading condition where the normal interference has been just applied before the hemisphere is about to move horizontally. Each cycle of the horizontal displacement is achieved by 40 loading steps. The maximum number of cycles of the oscillatory horizontal displacement is three, because of the vast computational effort (132 hours for a single case on a 4 cores 3GHz PC with a Xeon CPU).

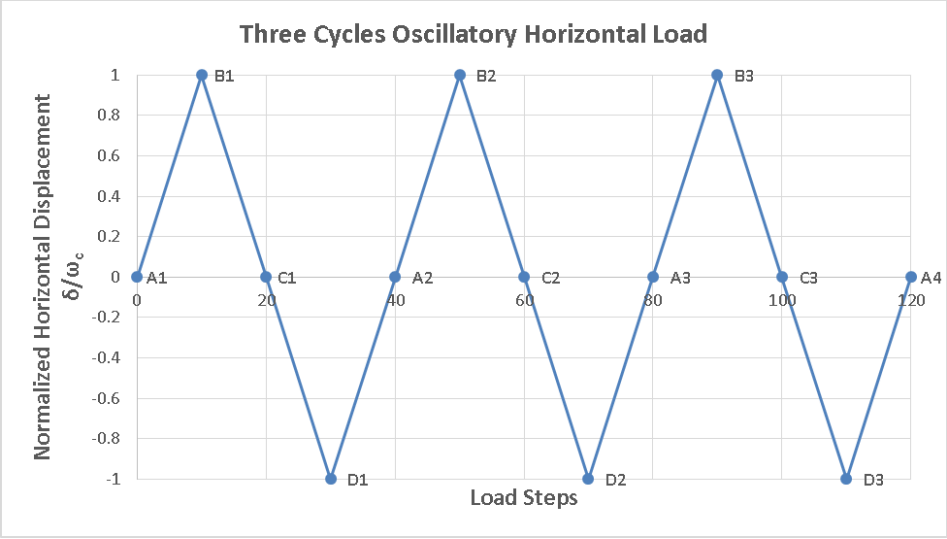

Figure 3-16. Loading steps of three cycles oscillatory horizontal for plane strain case.

In order to describe the location and the cycle number explicitly, the following convention of notation is utilized. Points (A,B,C,D) represent, respectively, $\delta = (0,1,0,-1)\omega_c$, and the cycle number is specified by n=1,2,3. For instance, A_2 corresponds to the end of the first cycle, where $\delta = 0 * \omega_c$.

3.2.4 The Distribution of von-Mises Stress

Figure 3-17 shows the evolution of the von-Mises stress during three cycles of the horizontal loading at $1*\omega_c$ with $\mu = 0.3$. Each picture is held at the same color-coding scale with the highest intensity of red color representing the largest von-Mises stress. The first parameter describes the view from which the distribution of the von-Mises stress is given, corresponding to the views defined in Fig.3-13a. The next two parameters are used to identify the horizontal load step, as discussed above. For example, Fig.3-17a through Fig.3-17c represent the horizontal displacement of the sphere, $\delta = (0, 0.2, 1) * \omega_c$, respectively, in branch A1-B1 (defined in Fig.3-16) from the front view. Since the von-Mises stress distributions in the hemisphere and the block appear as mirror images with very slight difference (caused by the geometry dissimilarity), only the progressions of the von-Mises stresses in the hemisphere are discussed in the following.

In order to analyze the von-Mises stress under the contacting surface (where plasticity is first to appear), the distributions of the von-Mises stress in the cut plane of the front view are shown through Fig.3-17a to Fig.3-17h. At the beginning, as shown in Fig.3-17a, there is only one point under the contacting surface reaching the yield strength in the sphere after $1*\omega_c$ interference is just applied. It agrees with the prediction by Green [61]. Then the hemisphere starts to move to the right as shown in Fig.3-17b. The region with large von-

Mises stresses in the hemisphere increases due to the introduction of the resisting tangential force. In Fig.3-17c, the hemisphere reaches the rightmost position, where von-Mises stress on the contacting surface increases as another effect of the tangential force. Then, the hemisphere turns back to the left, where the shakedown phenomenon is observed, as shown in Fig.3-17d, where plasticity disappears, leaving only an elastic state. As the hemisphere slides further to the left, the largest von-Mises stresses reappear under the contacting surface (Fig.3-17e). The distribution of the von-Mises stress stabilizes after the sphere passes the origin and keeps that pattern until the hemisphere reaches the leftmost position (Fig.3-17f). As the hemisphere turns back to the right, another shakedown appears (Fig.3-17g). Then the largest von-Mises stresses again reappear under the contacting surface as the hemisphere moves back to the origin (Fig.3-17h), finishing one cycle of horizontal loading. The evolution of the von-Mises stresses remains the same for the second and the third cycle, with the same distributions of von-Mises stress at A2, A3, and A4, as shown by ANSYS.

In addition to the front view, the bottom view of the distribution of the von-Mises stresses showing the contacting surface of the hemisphere is shown in Fig.3-17i. Since the COF is relative small, the von-Mises stress on the contacting surface is smaller than that under the surface in the bulk material, and never reaches the yield strength during oscillatory horizontal loading (indicated by Fig.3-17i, the evolutions of the other bottom views are omitted for brevity). For this case of $1*\omega_c$ and $\mu=0.3$, the largest von-Mises stress shows up always under the surface, where the cracks and fatigue are most likely to initiate and propagate.

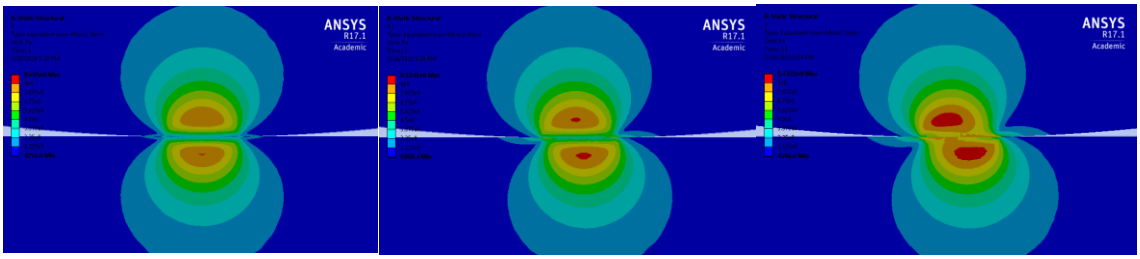

(a) Front view, 0*ω_c at A1-B1 (b) Front view, 0.2*ω_c at A1-B1 (c) Front view, 1*ω_c at A1-B1

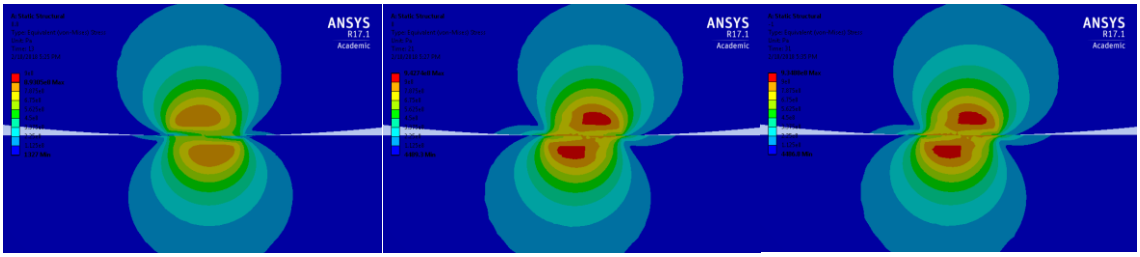

(d) Front view, 0.8*ω_c at B1-C1 (e) Front view, 0*ω_c at B1-C1 (f) Front view, -1*ω_c at C1-D1

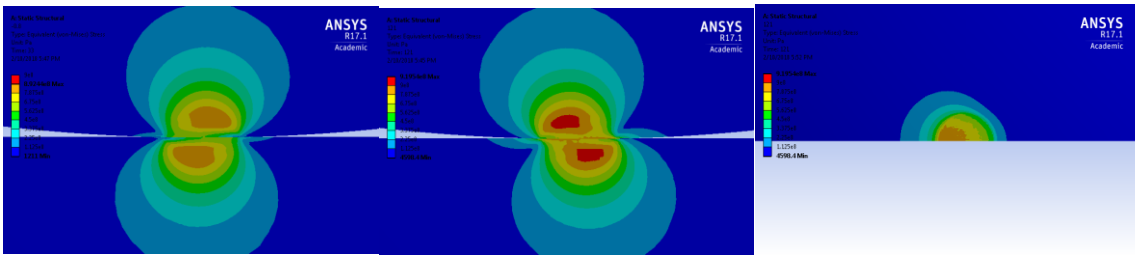

(g) Front view, -0.8*ω_c at D1-A2 (h) Front view, 0*ω_c at A2 (i) Bottom view,0*ω_c at A4

Figure 3-17. The evolution of von-Mises stresses during three cycles of horizontal loading at 1* ω_c interference with μ=0.3 for steel/steel.

However, as the COF increases, different evolutions of the von-Mises stresses show up. Figure 3-18 depicts the evolution of the von-Mises stress during three cycles of the horizontal loading at 1*ω_c with μ=1. As shown in the front view, Fig.3-18a, after three cycles of loading, the largest von-Mises stress appears at the edges of the contact. In order to analyze the von-Mises stress on the contacting surface, the bottom views of the von-Mises stress distribution in the hemisphere are shown in through Fig.3-18b to Fig.3-18l.

At the very being beginning just after the vertical interference is applied, the von-Mises stress on the surface, as shown in Fig.3-18b, is relatively small, since the tangential force has not been introduced yet. Then the hemisphere moves to the right. In Fig.3-18c, The large von-Mises stresses form “rings” at the contacting edges. As the hemisphere slides further to the right, the “rings” spread to the center until the whole contacting area is covered by the large von-Mises stresses (Fig.3-18d). This is caused by continued accumulation of plastic deformation. After reaching the rightmost position (Fig.3-18d), the hemisphere turns back to the left (Fig.3-18e), where shakedown is apparent. As the sphere slides to the left further, the “ring” of large von-Mises stresses appears at the edges of the contact again (from Fig.3-18f to Fig.3-18h). When the hemisphere reaches the leftmost position, the whole contacting area is covered by the large von-Mises stresses (Fig.3-18i). Seemingly, Fig.3-18d and Fig.3-18i are mirror images at the two extreme side positions. Then the hemisphere turns back to the right, and another shakedown appears (Fig.3-18j). As the hemisphere returns to the origin (Fig.3-18k), the “rings” of large von-Mises stresses show up at the contacting edges again. Comparing the distributions of von-Mises stresses at the end of the first cycle and third cycle, the “rings” of large von-Mises stress are stretched in the X direction, which indicates the stretching of the contacting area (discussed in Section 3.2.6). In this case, once the fretting motion commences, the largest von-Mises stress stays at the edges of the contacting area, where cracking and fatigue are most likely to initiate and propagate.

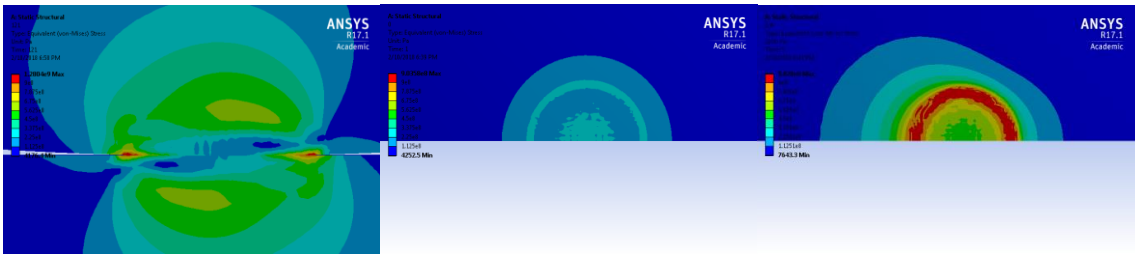

(a) Front view, 0*ω_c at A4 (b) Bottom view, 0*ω_c at A1 (c) Bottom view,0.4*ω_c at A1-B1

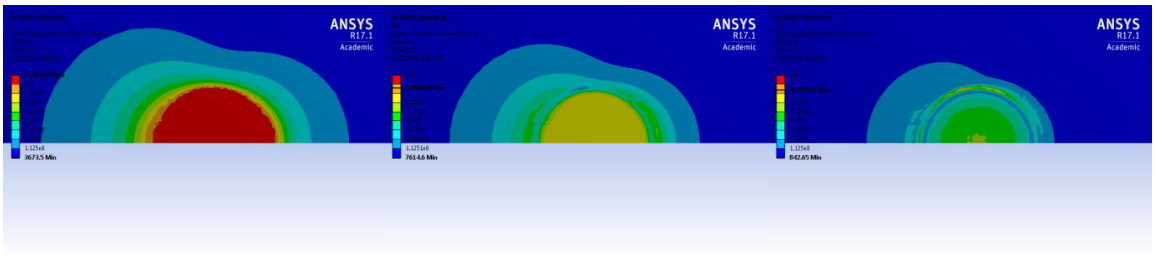

(d) Bottom view, 1*ω_c at A1-B1 (e) Bottom view, 0.8*ω_c at B1-C1 (f) Bottom view,0.6*ω_c at B1-C1

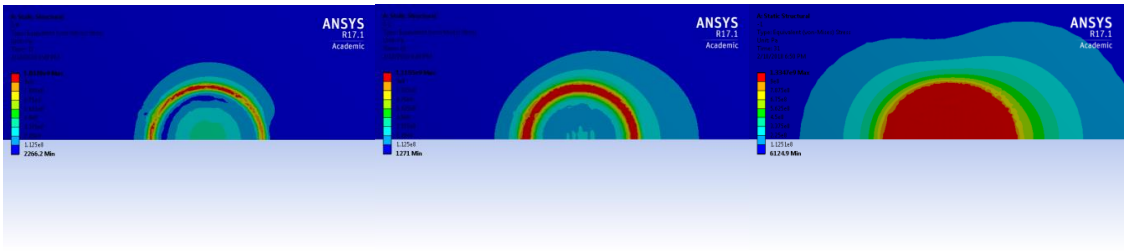

(g) Bottom view, 0.4*ω_c at B1-C1 (h) Bottom view, 0.2*ω_c at B1-C1 (i) Bottom view,-1*ω_c at C1-D1

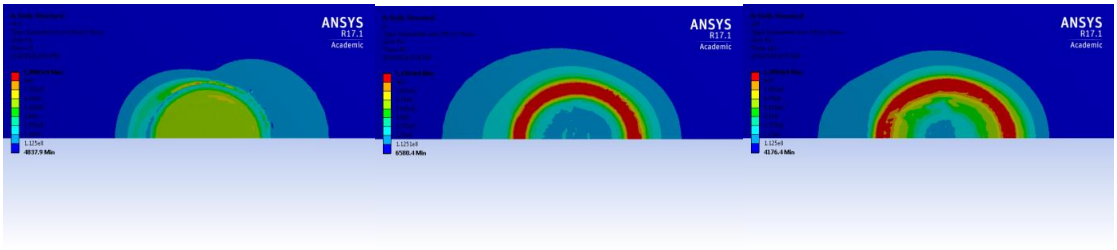

(j) Bottom view, -0.6*ω_c at C1-D1 (k) Bottom view, 0*ω_c at A2 (l) Bottom view,0*ω_c at A4

Figure 3-18. The evolution of von-Mises stresses during three cycles of horizontal loading at 1* ω_c interference with μ=1 for steel/steel.

A conclusion can be drawn that, with small COF, the largest von-Mises stress is located under the surface, while with sufficient large COF, the largest von-Mises stress shows up at the contacting surface and is located at the edge of the contact.

3.2.5 The Distribution of Plastic Strain

With the von-Mises stress reaching the yield strength, there are equivalent plastic strains, ε_p, appearing in the model. Figure 3-19 shows the evolution of the plastic strain at 1* ω_c interference with μ=1 for three cycles of horizontal loading. Fig.3-19 depicts the front view of the distribution of ε_p at the end of the third cycle. Evidently, the large plastic strains are located at the surface of the contact. To track the evolution of the plastic strain on the contacting surface, the bottom of the hemisphere during the fretting is shown from Fig.3-19b to Fig.3-19h. There is no plastic strain shown on the bottom surface until the hemisphere slides 0.4* ω_c to the right (Fig.3-19b), where the earliest plastic strain appears at the edge of the contact. As the hemisphere moves further to the right, the plastic strain gradually forms a "ring" at the edges of the contact (Fig.3-19c-Fig.3-19e). This "ring" stays there at the end of the first cycle, and it is stretched in the X direction just as the distribution of the von-Mises stresses do in Section 3.2.4. As the fretting motion proceeds, the "ring" of the plastic strain remains at the edges of the contact (Fig.3-19f and Fig.3-19g), with multiple peaks, which are caused by the oscillatory motion.

The plastic strain is not found on the contacting surface for the above case when the COF drops to 0.3. Instead, there is only slight plastic strain under the surface (ε_{pmax}=0.001 at loading step A_4) compared with that of the case of COF=1 (ε_{pmax}=0.1 at loading step A_4).

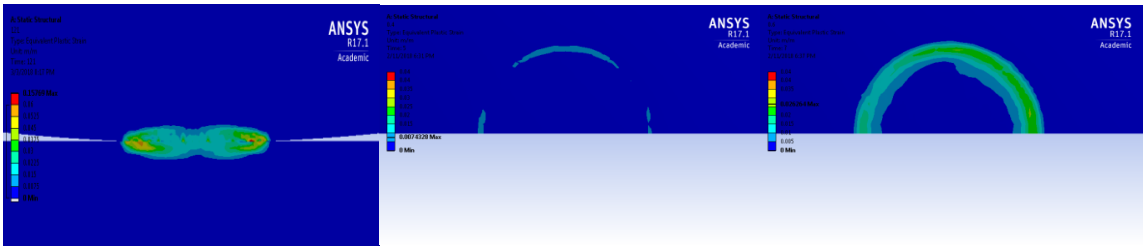

(a) Front view, 0*ω_c at A4 (b) Bottom view, 0.4* ω_c at A1-B1 (c) Bottom view, 0.6* ω_c at A1-B1

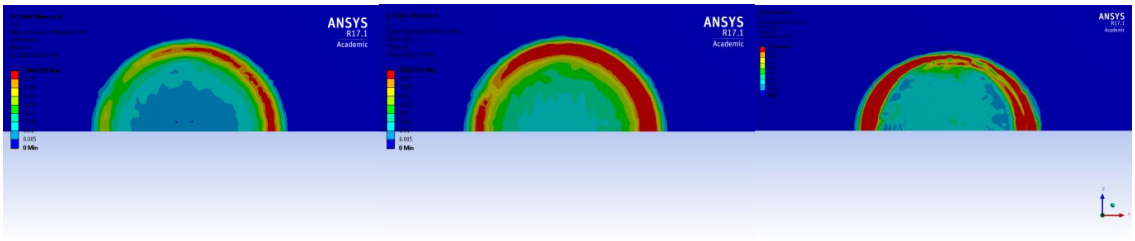

(d) Bottom view, 0.8* ω_c at A1-B1 (e) Bottom view, 1* ω_c at B1 (f) Bottom view, 0* ω_c at A2

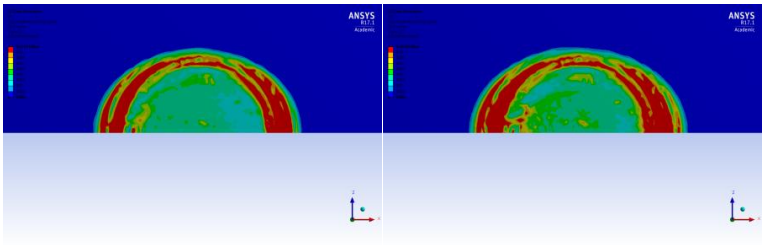

(g) Bottom view, 0* ω_c at A3 (h) Bottom view, 0* ω_c at A4

Figure 3-19. The evolution of equivalent plastic strain during three cycles of horizontal loading at 1* ω_c interference with μ=1 for steel/steel.

3.2.6 Junction Growth

During the fretting motion, the contact area is found to increase in some cases, which is known as the junction growth. Figure 3-20 shows the schematics of the contact region at 1*ω_c with μ=1. The red color represents the region at the loading step A_1, i.e., at the beginning of the loading. The blue color represents the region at the loading step A_4, i.e., at the end of the three cycles of loading. In the figure, the contact region grows radially.

However, the growth in the X direction is larger than that in the Z direction, which stretches the contact region in the X direction. It is corresponding to the stretch of the distribution of von-Mises stresses and plastic strains in the X direction (Section 3.2.4 and 3.2.5).

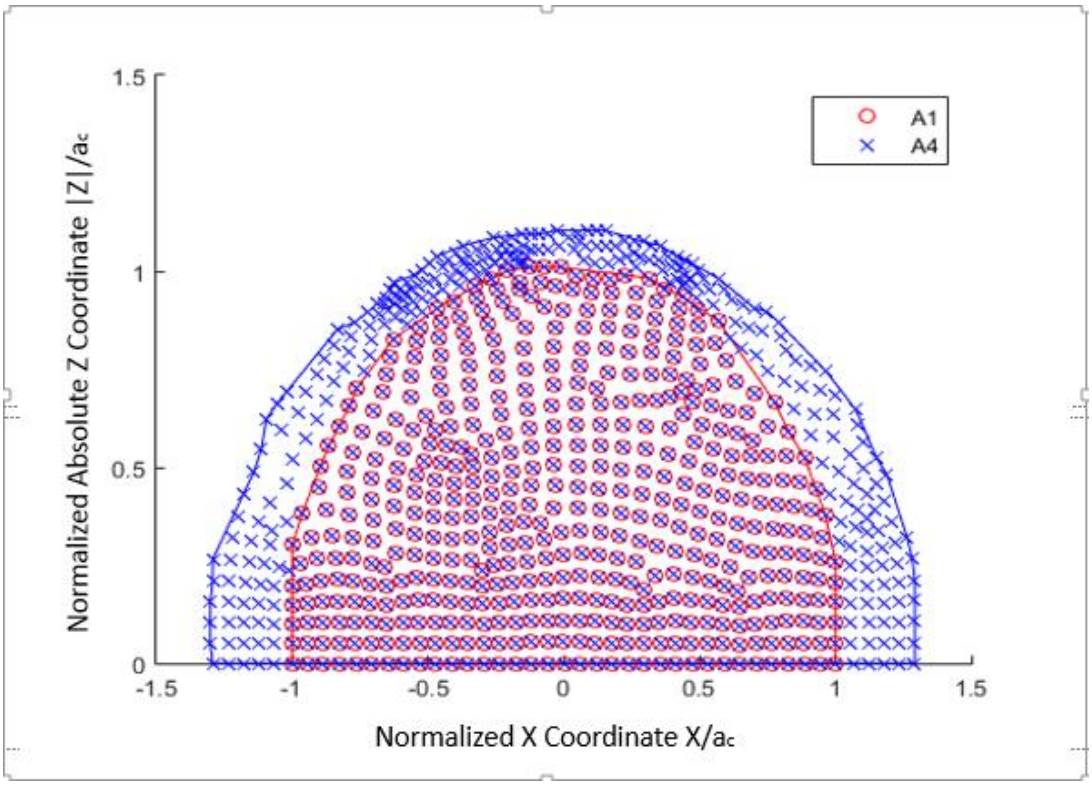

Figure 3-20. The schematics of the contact zone at the beginning and ending of the three cycles (A4) of loading at 1*ω_c with μ=1 for steel/steel.

In order to calculate the contact area, the trapezoidal rule is utilized to integrate the discretized data as shown in Fig.3-20. Figure 3-21 shows the evolutions of the contact area at 1*ω_c with μ=0.3 and μ=1 during three cycles of horizontal loading. When the COF is small (μ=0.3), the von-Mises stress on the contacting surface never reaches the yield strength (Section 3.2.4), which introduces no plastic deformation on the surface (Section 3.2.5). As a result, there is no junction growth at 1*ω_c with μ=0.3. However, as the COF increases to μ=1, the tangential force introduces plastic strain on the surface (Section

3.2.5), which eventually causes the junction growth, as shown in Fig.3-20. The junction growth continues during three cycles of loading, and it tends to stabilize after sufficient cycles.

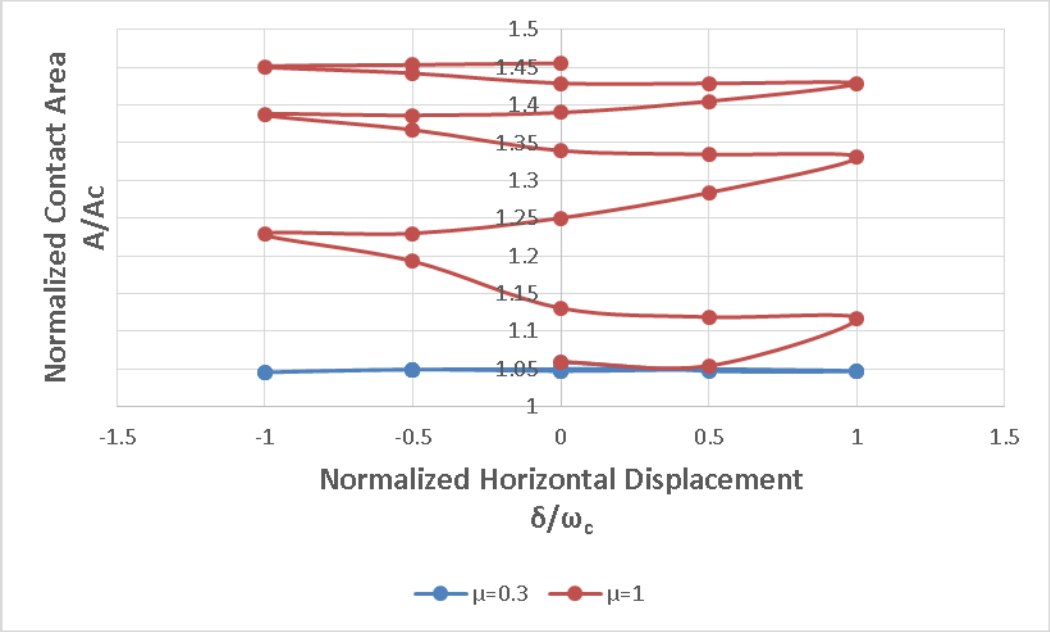

Figure 3-21. The evolution of junction growth at 1*ω_c with μ=0.3 and μ=1 during three cycles of horizontal loading for steel/steel.

3.2.7 Depression Marks on the Surfaces of the block

Figure 3-22 shows the profile of the contacting region of the block after three cycles of horizontal loading while the vertical interference is still maintained at 1*ω_c with μ=1 at location A4. There are pileups at the edges of the contact (see also the inset). This is due to the plasticity on the surface, introduced by the friction force. When the COF decreases to μ=0.3 with the same interference 1*ω_c, there is no pileup after three cycles of horizontal loading, as shown in Fig.3-23. It can be explained by the absence of plastic strain at the surface, as indicated in Section 3.2.5. When the interference increases to 3*ω_c with the

COF of μ=1, the pileups show up again (Fig.3-24), but they are not as pronounced as those for 1*ω_c interference (Fig.3-22). The explanation is as follows. First, it should be noted that ANSYS provides specific information regarding the status of the contact, i.e., whether it is in full stick, partial slip, or gross slip. Thus, as the hemisphere starts to move from the original contact position, the contact status is in full stick at first, but then it goes into partial slip, and finally it transitions to gross slip (i.e., when the local tangential stress reaches the value of COF*normal-pressure). For the cases with pileups, the contact status is full stick at the rightmost and leftmost positions. The horizontal displacement applied on the top surface of the hemisphere causes in general an elastic deformation of the bulk material and the displacement of the stick region. The smaller the displacement of the stick region is, less pronounced the depression mark is. With a larger interference, the stick area is more firmly fixed, and it displaces less. Therefore, the larger interferences introduce less pronounced depression marks with the same COF.

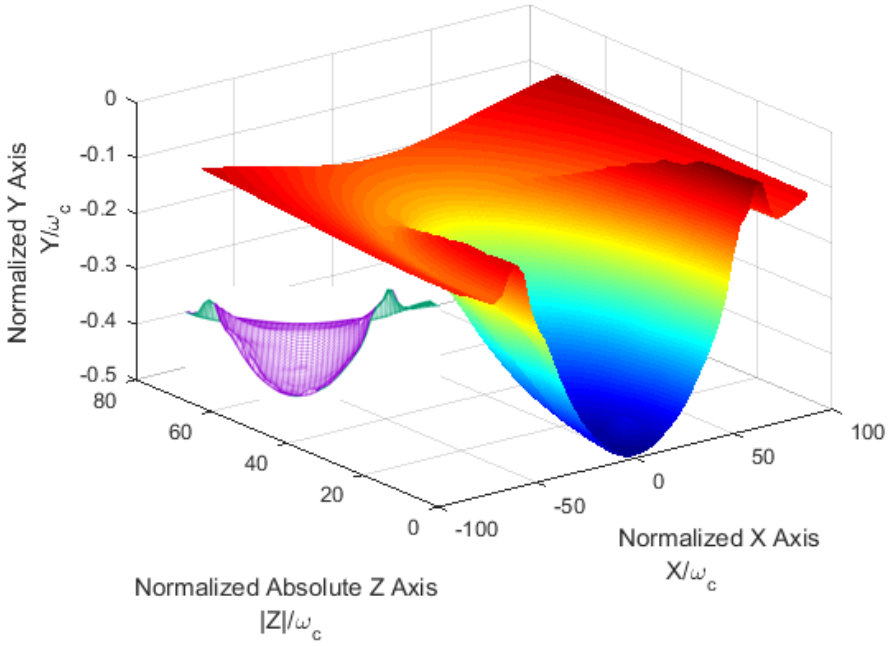

Figure 3-22. The surface profile of the contacting region of the block at 1*ω_c after three cycles of horizontal loading with μ=1 for steel/steel.

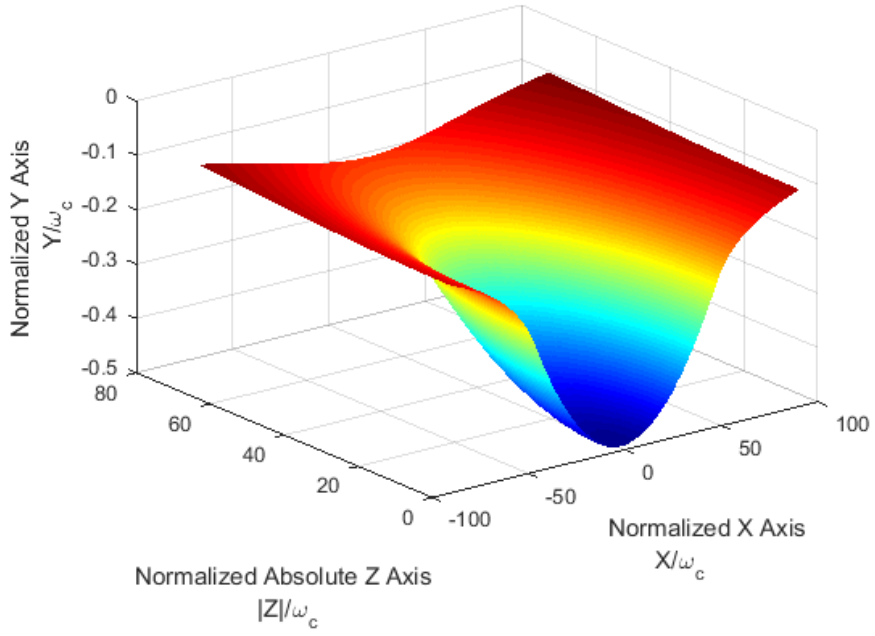

Figure 3-23. The surface profile of the contacting region of the block at 1*ω_c after three cycles of horizontal loading with μ=0.3 for steel/steel.

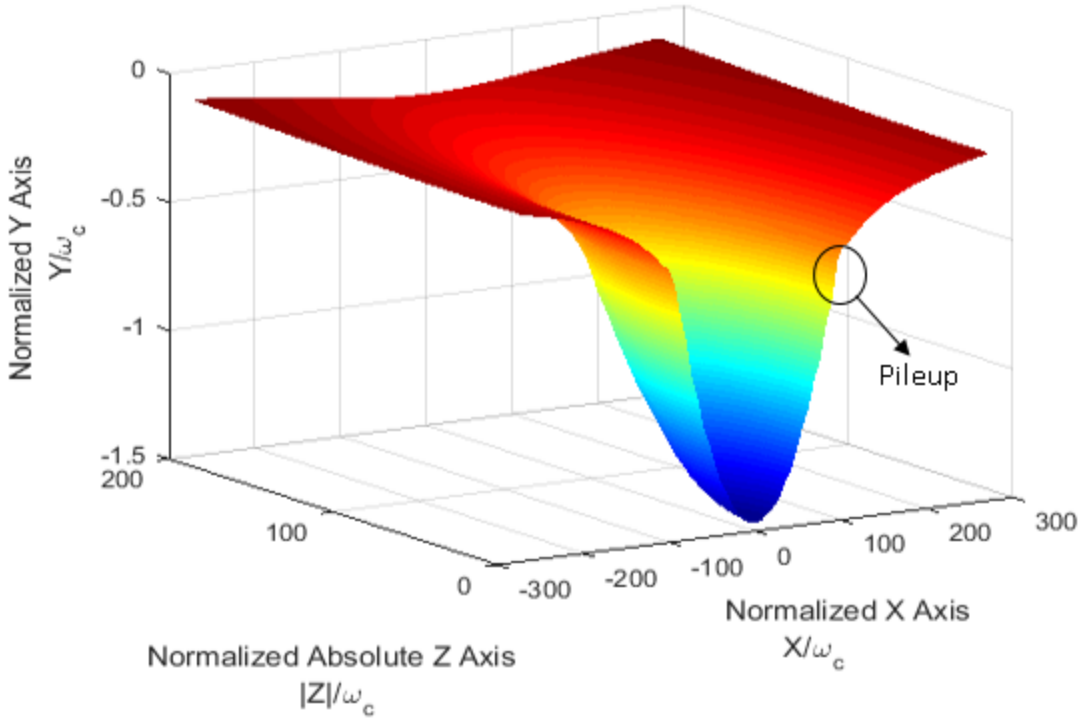

Figure 3-24. The surface profile of the contacting region of the block at 3*ω_c after three cycles of horizontal loading with μ=1 for steel/steel.

3.2.8 The Evolution of the Tangential Force

Figure 3-25 shows the evolution of the tangential force during three cycles of horizontal loading with μ=1 at 1*ω_c interference. The tangential force (or traction), Q, is extracted from ANSYS similar to the normal force, *P*. Specifically, the reaction forces on the top surface of the hemisphere are summed up in the horizontal direction, and designated as Q, to be the active force necessary to displace the hemisphere as prescribed. That force, Q, is normalized by the critical load, P_c. As shown in Fig.3-25, the normalized tangential force, Q/P_c, tends to stabilize after the first quarter of the cycle. The evolution has the similar trend of the initial few cycles of the fretting loop as reported in [86]. The enclosed area represents the work consumption during the fretting motion. The maximum normalized

tangential load increases after each cycle, and tends to reach the COF applied, μ=1. It is relative smaller than the applied COF due to the partial slip and partial stick contact conditions occurring at the rightmost and leftmost positions.

When the COF decreases to 0.3, the evolution of the normalized tangential force is shown in Fig.3-26 (see the loop). The loop stabilizes after the first quarter of the cycle. The evolutions of the second and the third cycles are the same, which means the fretting motion has stabilized after two cycles. Additionally, the maximum normalized tangential force, which quantitatively equals to the effective COF (μ_e=Q/P_c), stabilizes at the value of the COF applied, μ=0.3. It is attributed to the full slip contact conditions (indicated by ANSYS) at the rightmost and leftmost positions.

The frictionless evolution of the tangential force at 1*ω_c is also shown in Fig.3-26 (see the horizontal line). In that case, the tangential force is always zero, which means that the elastic resistance caused by the indentation is subtle. The frictionless evolutions of the tangential force are also investigated at different interferences. The tangential force stays at zero even when the interference is extended to 10* ω_c. The explanation is that since the two bodies are made of the same material, the sphere is geometrically, i.e. structurally, weaker than the block. The sphere then is deformed more, so that there is no effective plowing during the fretting motion, which leads to the zero tangential force. Therefore, when friction is present, the tangential force is generated by the frictional traction at the interface.

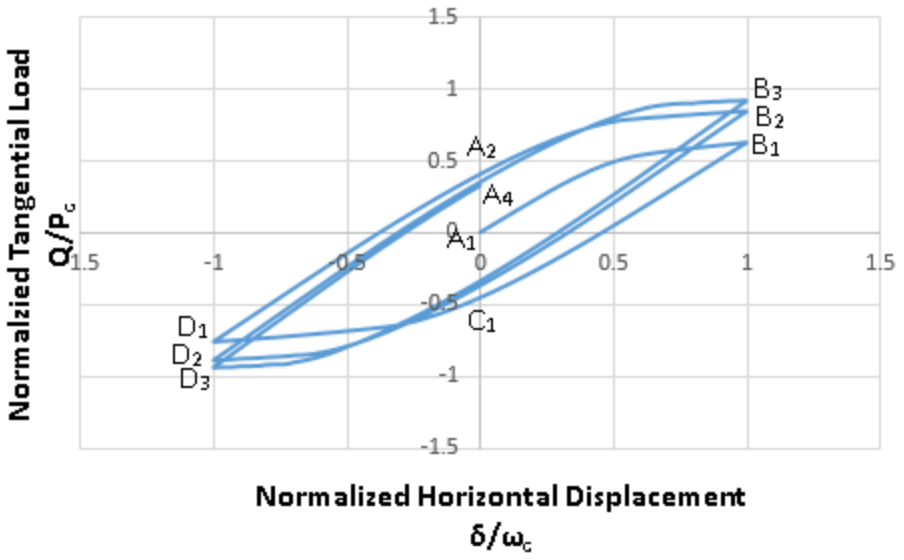

Figure 3-25. The evolution of the tangential force during three cycles of horizontal loading at 1*ω_c with μ=1 for steel/steel.

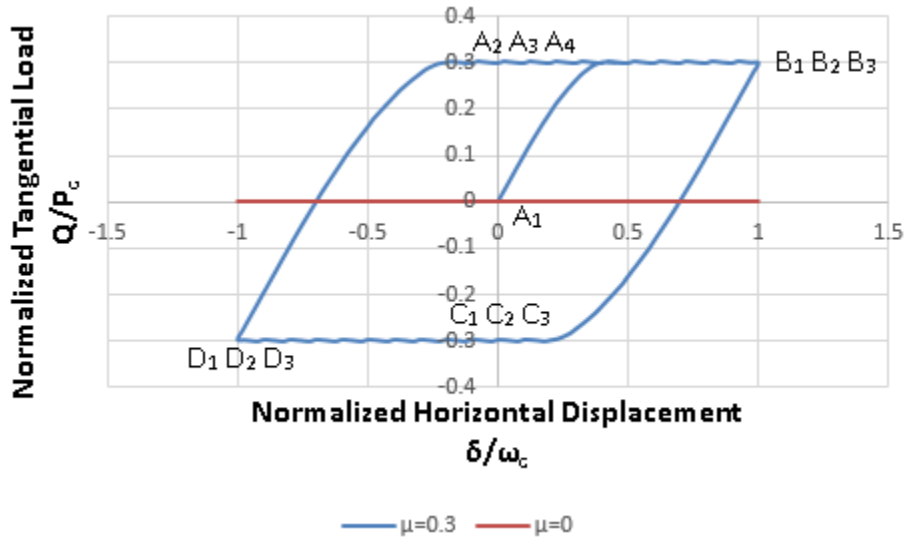

Figure 3-26. The evolution of the tangential force during three cycles of horizontal loading at 1*ω_c with μ=0.3 and μ=0 for steel/steel

3.2.9 The Work Done to the System

As shown in Section 3.2.8, the area under hysteresis curve of the tangential force represents the work invested into the system (Fig.3-25 and Fig.3-26). Considering loading as quasi-static, the kinetic energy is not considered. Therefore, the work transfers to three kinds of energy: elastic strain energy, plastic strain energy, frictional energy dissipation.

The work, U, is derived by Eq.3-16, where Q is the active tangential force applied on the top surface of the hemisphere to impose δ, which is the horizontal displacement of the hemisphere top surface. The trapezoidal rule is utilized to integrate the discretized data extracted from ANSYS.

$$U = \int Q \, d\delta \tag{3-16}$$

Figure 3-27 shows the evolution of the total work done to the system at $3*\omega_c$ during three cycles of loading with different COFs. The work is normalized by the critical work, U_c=30.789J (see Table 3-5). The sliding distance represents the absolute distance the hemisphere passes, and the corresponding fretting motion position is shown. Note that additional COFs cases are added here, including 0.001, 0.05, 0.08, 0.1, and 10. Taking the work evolution with μ=0.3 as an example, the work increases during the sliding of the hemisphere first to the right, which contains the three work forms discussed above. As the hemisphere turns back to the left at B_1, the work drops because of the release of the elastic strain energy, which is further verified by the shakedown phenomenon in Section 3.2.3.1. When the hemisphere approaches the origin at C_1, the effect of the elastic strain energy is overshadowed by the dissipation of frictional and plastic effects. The work starts to increase again until another shakedown occurring at D_1. The fluctuating nature of the

evolution is caused by the restoration (i.e., release) of elastic strain energy, and the cumulative increase of the evolution is caused by the dissipation of the fictional and plastic effects.

As the COF increases, the elastic strain energy effect becomes dominant, and the frictional dissipation decreases since most of the contacting area during fretting is in the stick condition (as indicated by ANSYS). Therefore, comparing μ=0.1 and μ=0.3, the work done to the system is larger in case with μ=0.3 initially, but then it becomes smaller as fretting continues. As the COF decrease, the elastic strain energy effect is not dominant. But the friction dissipation decreases as a result of the drop of the COF. Therefore, at a certain interference, there exists a certain ("critical") COF, which produces the largest work dissipation.

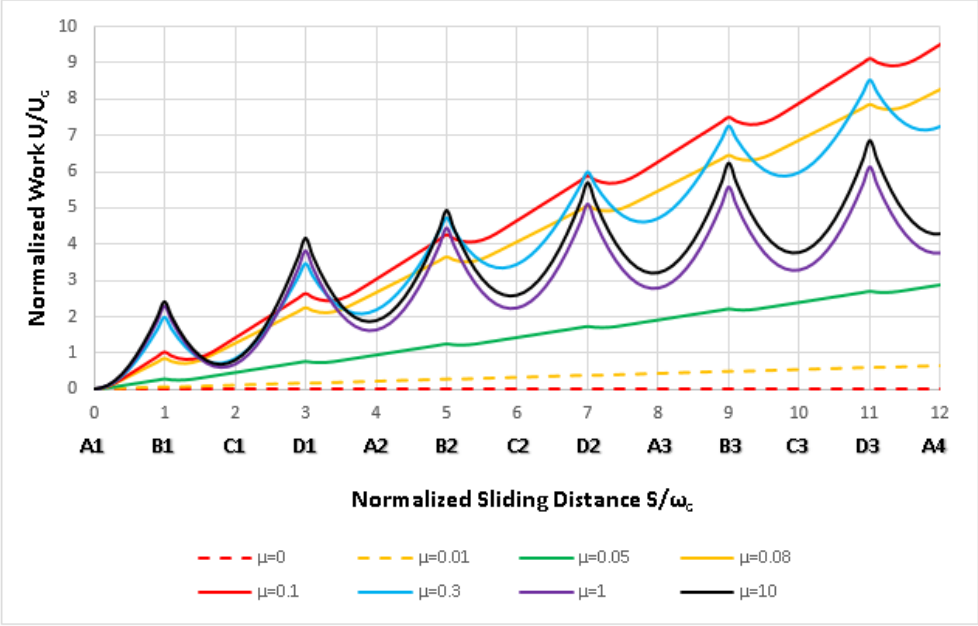

Figure 3-27. The evolution of the total work done to the system at 3*ω_c during three cycles of loading with different COFs for steel/steel

3.2.10 Conclusion

This spherical contact fretting model is between a hemisphere and a flat block. The materials of the two bodies are set to be identical steels with one percent strain hardening based on the elastic modulus. It is a displacement-controlled model with various COFs being applied at the interface. Several conclusions are drawn.

1. The largest von-Mises stress is confined under the contacting surface with small COFs, while with sufficiently large COFs, the largest von-Mises stress shows up at the contacting surfaces and is located at the edge of the contact.

2. With sufficiently large COFs, the large plastic strains form multiple "rings" on the contacting surfaces after the oscillatory fretting motion.

3. Junction growth is found when there is plastic deformation on the surface of the contact. The contacting region is stretched in the direction of the fretting motion.

4. There are depression marks on the surface of the block caused by the fretting motion. There are pileups at the edges of the contact with large COF. Since the magnitude of the oscillatory sliding distance is relatively small, $1*\omega_c$, the pileup phenomenon is not pronounced.

5. The fretting loop of the initial cycles is found. The evolution of the tangential force stabilizes fast with small COFs. The maximum effective COF during the cyclic loading equals to the COF applied to the model after the stabilization. The tangential force is always zero at frictionless contact without the plowing effect, which is due to the sphere being structurally weaker than the block.

6. The work done to the system equals to the enclosed area of the hysteresis curve, which is the evolution of the tangential loading. It corresponds to three kinds of energy: elastic strain energy, plastic strain energy, and frictional energy dissipation. The fluctuating nature of the evolution of the work is caused by the preservation of the elastic strain energy, while the cumulative increase of the effect is caused by the dissipation of the frictional and plastic dissipation. At certain interference, there exists a certain COF, which will yield the largest work done to the system.

3.3 Conclusion

In this chapter, the fretting models between identical materials are built in both 2D plane strain cylindrical and 3D spherical contacts for elasto-plastic regimes. The results for displacement-controlled loading conditions with various COFs are discussed.

For 2D plane strain cylindrical contact, the following results are found. With small COFs, the largest von-Mises stress is confined under the contacting surface. With large COFs, the largest von-Mises stress is located at the edge of the contact. Likewise, the largest plastic strain shows up at the edges, too. It is, therefore, postulated that cracks and fatigue are most likely to initiate and propagate at the contact edges with large COFs, at bulk material under contacting surface with small COFs. Due to the plastic deformation of the surfaces, junction growth is found. The magnitude of the junction growth increases with the COFs, while the rate of the convergence of the growth decreases with the COFs. The behavior of the junction growth is found to agree qualitatively with the experimental results [89]. In the experimental work reported by Brizmer *et al.* [89], where the normal load is kept constant, the contact area increases with the tangential load, and the contact area is

stretched more in the sliding direction, which agrees with the Fig. 3-20 in the current work. The fretting loop (i.e., the development of the tangential force versus fretting motion) for the initial few cycles of loading is likewise found, where the enclosed area indicates the energy loss. The similar types of fretting loop including conditions of partial stick and partial slip (Fig. 3-25), and gross slip (Fig. 3-26) can also be found in the experimental work by Vingsbo *et al.* [6]. Pileup appears with large COFs, which intensify the plastic strain at the contact edges.

For 3D spherical contact, the following results are found. With small COFs, the largest von-Mises stress is confined under the contacting surface. With large COFs, the largest von-Mises stress is located at the edge of the contact. The large plastic strains form multiple "rings" on the contacting surfaces after the oscillatory fretting motion. It is, therefore, postulated that cracks and fatigue are most likely to initiate and propagate at the contact edges with large COFs, at bulk material under contacting surface with small COFs. Depression marks and pileups on the surface of the block are found. The fretting loop of the initial cycles is found. The evolution of the tangential force stabilizes fast with small COFs. The maximum effective COF during the cyclic loading equals to the COF applied to the model after the stabilization. The tangential force is always zero at frictionless contact without the plowing effect, which is due to the sphere being structurally weaker than the block. The work done to the system equals to the enclosed area of the hysteresis curve, which is the evolution of the tangential loading. It corresponds to three kinds of energy: elastic strain energy, plastic strain energy, and frictional energy dissipation. The fluctuating nature of the evolution of the work is caused by the reservation of the elastic strain energy, while the cumulative increase of the effect is caused by the dissipation of the

frictional and plastic dissipation. At certain interference, there exists a certain COF, which will yield the largest work done to the system.

CHAPTER 4. FRETTING BETWEEN DISSIMILAR MATERIAL PAIRS AT ROOM AND HIGH TEMPERATURES

In the previous chapter, the fretting contact between identical materials is analyzed. In this chapter, the fretting contact between dissimilar materials is going to be discussed. The model is the same as the one in the previous chapter, but the materials are different. The distribution of von-Mises stress, plastic strain, junction growth, depression mark on the block, and work done to the system are discussed. The model and results for the 2D case have been published in Ref.[90].

4.1 Plane Strain Cylindrical Fretting Contact

4.1.1 The Cylindrical Contact Model

The models are the same as those in the previous chapter, the displacement-controlled and force-controlled 2D plane strain cylindrical models. However, the material pairs in this chapter are dissimilar material pairs, which are Inconel 617/ Incoloy 800H at 20C and 800C [90]. The material properties are listed in Table 4-1. The yield strength of Incoloy 800H is about half of that of Inconel 617. The parameter C(ν) represents the ratio between the maximum pressure and the maximum von Mises stress in normal elastic contact as given by Green [61]. The elastic-perfectly plastic behavior is used in the FEA.

Table 4-1. Material properties for cylindrical fretting model

Temperature	Material	Elastic Modulus[GPa] E	Yielding Strength[MPa] S_y	Poisson Ratio ν	C(ν)	$C \cdot S_y$ [MPa]
20°C	Inconel 617	211.0	322	0.3	1.795	578
20°C	Incoloy 800H	196.5	150	0.339	1.839	276
800°C	Inconel 617	157.0	290	0.3	1.795	521
800°C	Incoloy 800H	141.3	90	0.394	1.839	170

In an elastic contact regime, the solution of the 2D plane strain cylindrical contact is given by the Hertzian contact model. Under a total load per unit length, *P/L*, the maximum pressure, p_0, is located at the center of the contact [11]:

$$p_0 = \frac{2P}{\pi bL} \tag{4-1}$$

The half-width of the contact, b, is given by:

$$b = \left(\frac{4PR}{\pi LE^{'}} \right)^{\frac{1}{2}} \tag{4-2}$$

where E' is the equivalent elastic modulus is:

$$\frac{1}{E^{'}} = \frac{1-\nu_1^2}{E_1} + \frac{1-\nu_2^2}{E_2} \tag{4-3}$$

Herein, the subscript "1" and "2" represent the cylinder and the block, respectively. The interference of a half cylinder in contact with a block, whose depth is *d*, is derived in Appendix A:

$$\omega = \frac{P}{L}\frac{(1-\nu_1{}^2)}{\pi E_1}\left\{\ln(\frac{4\pi E^{'}R}{P/L})-1\right\} + \frac{P}{L}\frac{(1-\nu_2{}^2)}{\pi E_2}\left\{\ln(\frac{\pi d^2 E^{'}}{RP/L}) - \frac{\nu_2}{(1-\nu_2)}\right\} \tag{4-4}$$

At the onset of yielding $\sigma_{e-\max} = S_y$, for contact between dissimilar materials, the minimum of C_1S_{y1} and C_2S_{y2} determines the maximum contact pressure, p_0, at which the "weaker" material yields first. For cylindrical contact as given by Green [31], C (ν)=1.164+2.975 ν -2.906 ν^2, for ν >0.1938. Hence, at yielding onset, p_o is replaced by the product,

$$CS_y = \min\left\{C_1S_{y1}, C_2S_{y2}\right\} \tag{4-5}$$

to provide the critical parameters. When the material pair is identical, the two bodies yield at the same normal load. When the material pair is different materials, based on Table 3-1, Incoloy 800H is the weaker material that yields first both at 20°C and 800°C. These values are used to calculate the critical half contact width, b_c , and the critical load per unit length, P_c/L , according to [61]:

$$b_c = \frac{2RCS_y}{E'} \tag{4-6}$$

$$\frac{P_c}{L} = \frac{\pi R(CS_y)^2}{E'} \tag{4-7}$$

By subsisting Eq.4-7 into Eq.4-4, the critical interference is:

$$\omega_c = \frac{R(CS_y)^2(1-\nu_1^2)}{E'E_1}\left[2\ln\left(\frac{2E'}{CS_y}\right)-1\right]+\frac{R(CS_y)^2(1-\nu_2^2)}{E'E_2}\left[2\ln\left(\frac{dE'}{RCS_y}\right)-\frac{\nu_2}{1-\nu_2}\right] \tag{4-8}$$

For the material properties listed in Table 3-1 and the depth of the block (d=R) herein, the critical interference, the critical load per unit length, and the critical half contact width are given in Table3-2. The critical values, ω_c, b_c, P_c/L are used to normalize the forthcoming room and high temperature results, respectively.

Table 4-2. The critical values (onset of plasticity) for different material schemes and different temperatures.

Temperature	Cylinder Material	Block Material	Critical Interference ω_c [μm]	Critical Load per Unit Length P_c/L [MN/m]	Critical Half Contact Width b_c [mm]
20°C	Inconel 617	Inconel 800H	35.4	1.05	2.43
800°C	Inconel 617	Inconel 800H	24.5	0.53	2.00

The mesh convergence procedure is the same as that of identical material pairs, which is first done in elastic normal contact, and then done in elastic-plastic fretting contact. For brevity, it is not shown here.

4.1.2 Loading Steps in Cylindrical Contact Model

As shown in Fig.4-1a, the materials of the cylinder/block are assigned to Inconel617/Incoloy800H respectively and designated as Scheme1. Then the materials are exchanged in Scheme2 (Fig.4-1b). The simulations are performed for both schemes at room temperature first, and then for scheme1 at 800°C. Because the fretting damage on the block is of interest here, results of Scheme1 with the weaker material being the block, will be shown in the following. Meanwhile, the results of Sheme2 will help to understand the junction growth.

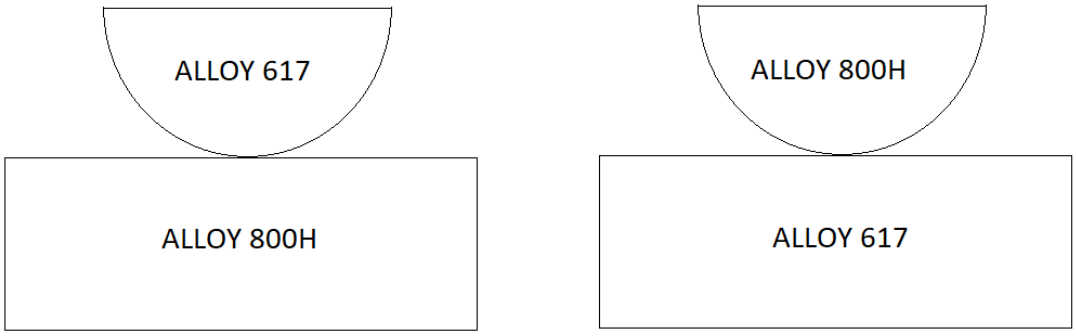

(a) Scheme1 (b) Scheme2

Figure 4-1. Material schemes for the fretting model.

The results of finite element model described above are presented for normalized vertical interference, $\omega^* = \frac{\omega}{\omega_c}$, ranging from 1 (the limit of the elastic regime) to 3 (in the elastic-plastic regime). Two different frictional coefficients are applied, 0.3 and 1. In order to describe the oscillatory horizontal displacement, load steps are used. As shown in Fig.4, Step 0 represents the start of horizontal load just after the vertical interference is applied. Each increment of step represents a sliding distance of $0.1 * \omega_c$. It takes 40 steps to finish one cycle of loading. Due to the computational burden (13 hours for a single simulation on a 3GHz Intel Xeon PC Workstation), the maximum cycle of horizontal displacement investigated in this work is set to three cycles. The following convention of notation is used to signify the location and the cycle number. Points (A,B,C,D) signify $\delta = (0,1,0,-1)\omega_c$, respectively, and n=1,2,3 specify the cycle number. For example, A3 represents the inception of the third cycle, where $\delta = 0 * \omega_c$.

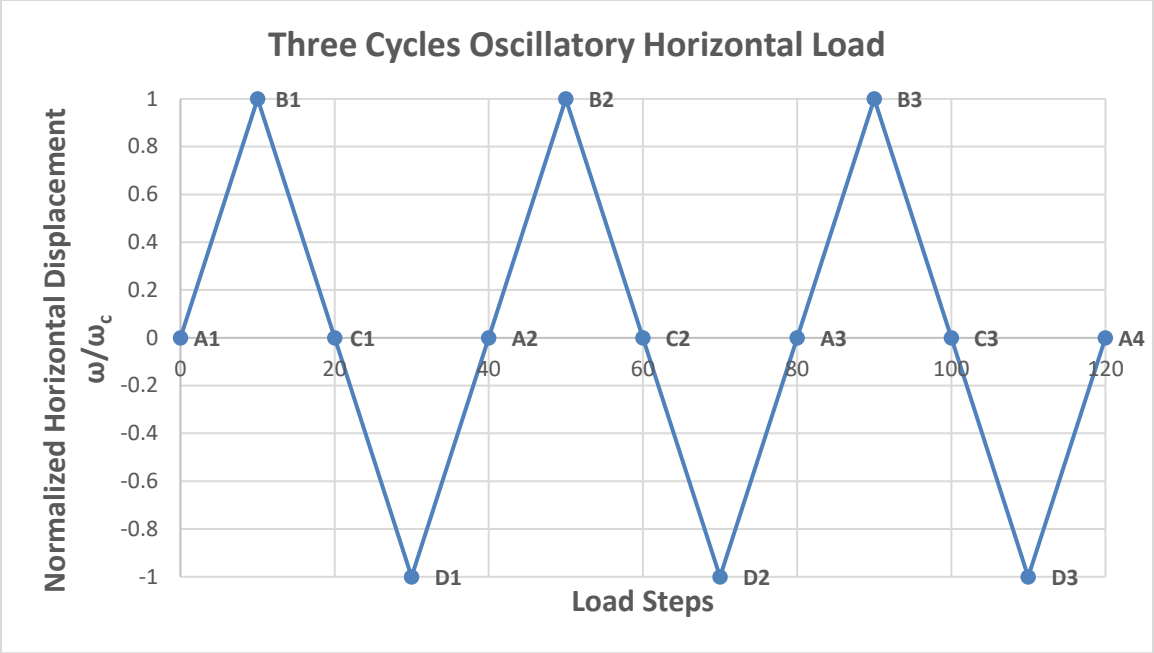

Figure 4-2. Loading stepping of three cycles oscillatory horizontal load.

4.1.3 The Distribution of von-Mises Stresses

Fig.4-3 illustrates the evolution of the von-Mises stresses for Scheme1 at $1*\omega_c$ interference for three cycles of horizontal loading with μ=1, at room temperature of 20℃. After pure normal contact between the cylinder and block is made, i.e., at the inception of the cylinder sliding to the right (location A1 in Fig.4-2), the maximum von-Mises stress in the cylinder and the block reaches S_{y2}=150MPa (see Fig.4-3a), which equals to the yield strength of Incoloy 800H, being the weaker material of the block. The maximum von-Mises stress in the cylinder is 153MPa, which is slightly larger than that in the block (but still smaller than its yield strength of 322MPa). Theoretically, according to Green [61], the maximum von-Mises stress in the cylinder for this case, $\sigma_{emax1}=p_0/C_1$= 153MPa ($p_0=S_{y2}C_2$, as mentioned in Section 4.1.2), agrees well with the FEA results. Then, from position A1, the cylinder

starts to move to the right. Fig.4-3b shows the distribution of the von-Mises stresses when the cylinder reaches the rightmost position (location B1 in Fig.4-2). For the cylinder, even with the tangential force, the material does not yield. Hence, the von-Mises stress keeps increasing where the maximum value reaches 280MPa. For the block, since the von-Mises stress has reached the yield strength after the normal contact, there is no increase in the maximum value, but the plastic area (represented by the orange color in Fig.4-3) gets larger and reaches the surface. As the sliding proceeds back and forth, the region with large von-Mises stresses appears at the two edges of the contact, as shown in Fig.4-3c and Fig.4-3d. Therefore, cracks are expected to initiate and propagate most likely at the two edges of the contact during the fretting motion. For the cylinder, although there is no plastic deformation, the large von-Mises stresses at the two edges of the contact are likely to introduce fretting fatigue. For the block, the cumulative plastic deformations at two edges of the contact are likely to introduce fretting wear and also fretting fatigue.

The maximum von-Mises stress in the cylinder never reaches the yield strength of the Inconel 617 during the three cycles of loading at $1*\omega_c$ interference. Since the maximum value stabilizes after one cycle of loading, the cylinder in this case is presumed to never yield. In order to find the interference at which the cylinder will yield in Scheme1, up to ten critical interferences cases with one cycle of horizontal loading have been simulated. However, the results show that the cylinder never yields. At $7*\omega_c$ interference, the maximum value of the von-Mises stress is 290MPa, which is about 4% increase while the interference increases seven times. As the interference increases to $10*\omega_c$ interference, the maximum von-Mises still stays at 290MPa. It can be explained that the effect of plasticity decreases the rate of the load per unit length growth significantly, with respect to the growth

of the applied interference, as the contact approaches the fully plastic regime. Therefore, it can be postulated that at room temperature for Scheme1, the cylinder of material Inconel 617 is very "strong" or "hard" to yield when it is in contact with block of material Incoloy 800H. Similar results for the block of material Inconel 617 in Scheme2 have been found, but are not reported for brevity.

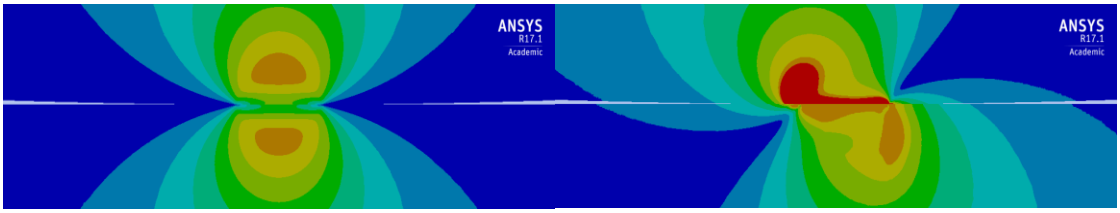

(a) At load step A1 (Shown in Fig.4), max=150MPa

(b) At load step B1, max=270MPa

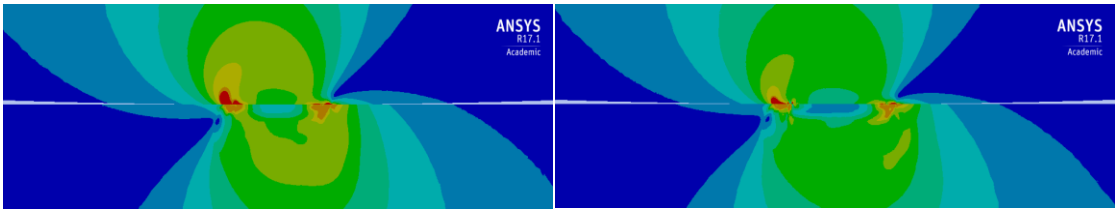

(c) At load step A2, max=250MPa

(d) At load step A4, max=230MPa

Figure 4-3. The distribution of von-Mises stresses at 1*ω_c interference for three cycles of horizontal loading with μ=1 for Scheme1 at 20°C.

4.1.4 The Distribution of Plastic Strain

When the von-Mises stresses in the block of material Incoloy 800H first reach the yield strength and fretting is in the elastic-plastic regime (Scheme1), there are plastic strains in the block which are indicated by the equivalent plastic strain, ε_p. Figure 4-4 shows the distribution of ε_p at the region of contact after three cycles of horizontal loading have completed, at different interferences and COFs. In all the three cases, the maximum ε_p is

located at the two edges of contact on the block, which coincides with the location of the maximum von-Mises stress. That is consistent with the direct correspondence between stress and strain. Because the von-Mises stress in the cylinder does not reach the yield strength, as discussed in Section 4.1.3, there are no plastic strains in it. Hence, all the plastic strains seen in Fig.4-4 are in the block.

Figure 4-4a illustrates the plastic strain distribution at $1* \omega_c$ interference with μ=1. Since there is no plastic strain under surface after the normal loading (only at one point the von-Mises stress reaches the yield strength), the plastic strain is confined near the surface to absorb the work generated by the friction force. As the interference increases to $3* \omega_c$ (Fig.4-4b), the plastic strain distribution changes. Because the region under the surface reaches plasticity in a much larger area (details provided by Jackson and Green [21]), the plastic strain spreads to a deeper and wider region under the surface. Consequently, the larger region absorbs the damage manifested by a deeper depression mark. As a result, the maximum ε_p (located at the edges) is relatively smaller at larger interference. In other words, as the contact produces more permanent damages, there is less plastic strain at the edges, i.e., at the location where the failure, as postulated in Section 4.1.3, is most likely to show up. Evident from the maximum values in Fig.4-4b (μ=1) and Fig.4-4c (μ=0.3), the plastic strain decreases with the drop of the COF, especially at the edges.

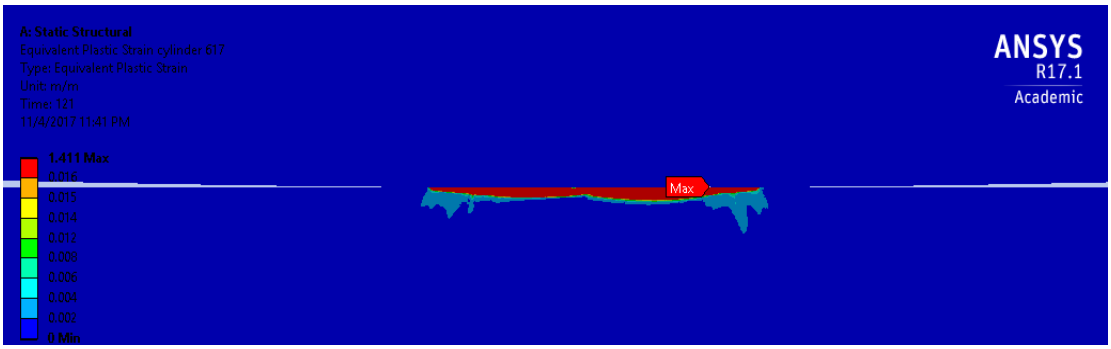

(a) $1 * \omega_c$ interference, μ=1, maximum ε_p=1.41

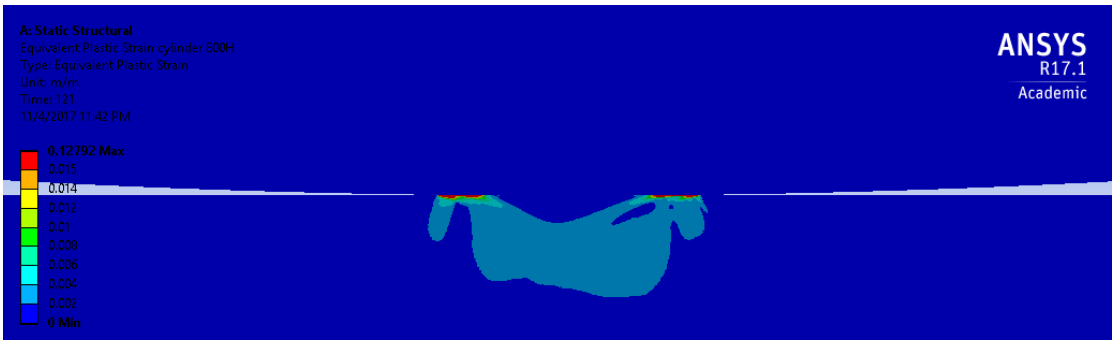

(b) $3 * \omega_c$ interference, μ=1, maximum ε_p=0.12

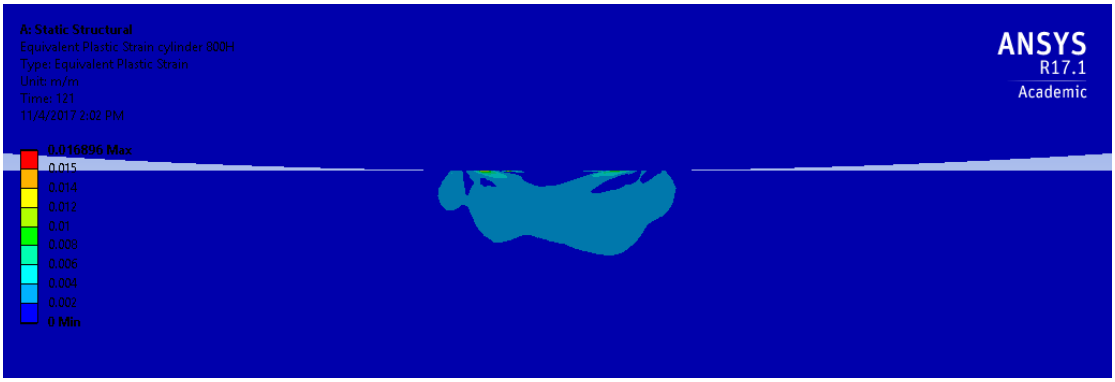

(c) $3 * \omega_c$ interference, μ=0.3, maximum ε_p=0.012

Figure 4-4. The distribution of von-Mises stresses at 1*ω_c interference for three cycles of horizontal loading with μ=1 for Scheme1 at 20°C.

In order to understand the progression of the plastic strain, the distribution of ε_p on the surface of the block after each horizontal loading cycle is investigated. Figure 4-5a shows the evolution of the plastic strain on the surface of the block after three cycles of horizontal loading at $1* \omega_c$ interference with μ=1. The plastic strain keeps increasing after each cycle, and the relatively large value locates near the edges of the contact. Outside the initial contacting area ($|X/b_c|>1$), there are smaller peaks of equivalent plastic strains on each side. These small peaks are caused by the abrupt change of the values of the three normal stresses and shear stress inside and outside the contact area (shown in Fig.4-5b). The abrupt change of the four stresses leads the von-Mises stress to reach another peak, which reaches the yield strength as shown in Fig.4-5b. The peak of the von-Mises stress contributes to the peak of the plastic strain.

The distributions of the plastic strains are asymmetric in Figs.4-4 and 4-5. The plastic strains on the right are always larger than those on the left. That is due to the displacement-controlled loading conditions. The normal load during the fretting motion decreases gradually since the block deforms plastically leading to a reduction in the effective resistance to the vertical interference. The cylinder first moves to the right, which leads to larger plastic strains on the right as it experiences a larger normal load.

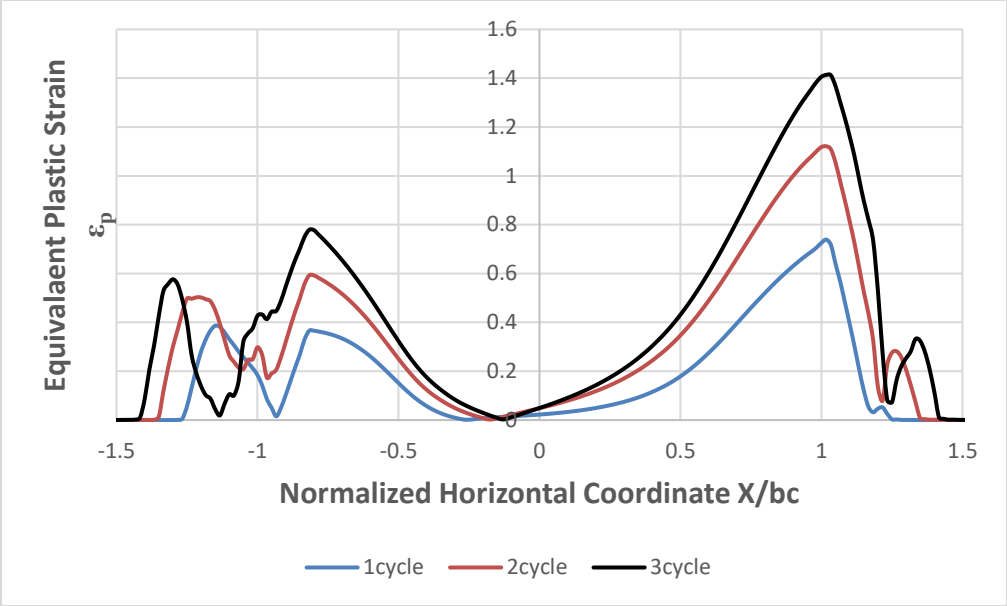

(a) Plastic strain

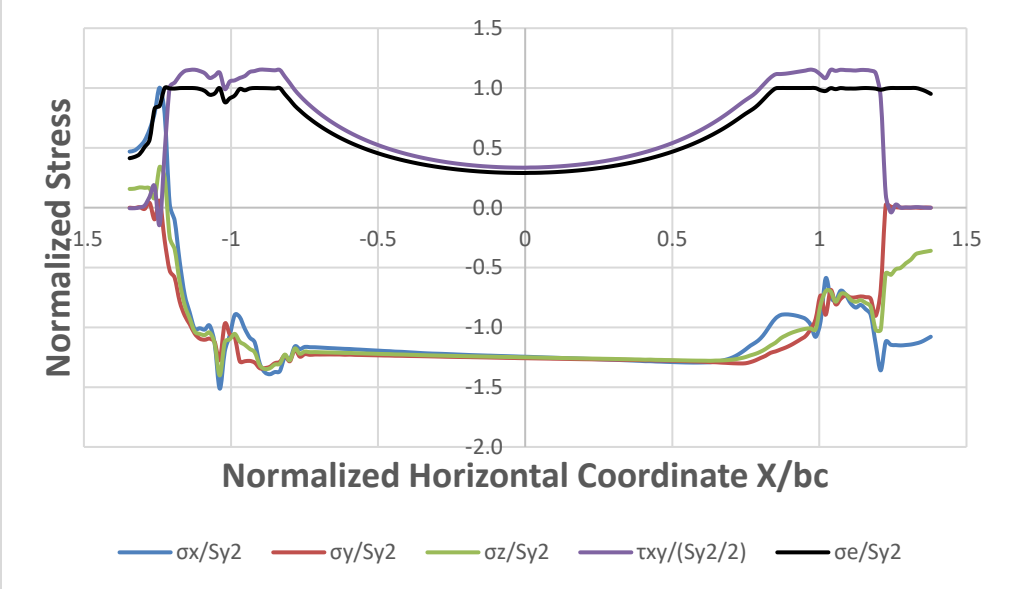

(b) Normal stress and Shear stress

Figure 4-5. The distribution of the equivalent plastic strain, normalized stresses, and shear stress on the contacting surface of the block at 1*ω_c interference with μ=1 for Scheme1.

4.1.5 Junction Growth

Junction growth is the increase of the contacting area, and it is obtained during the fretting motion from FEA code. Figure 4-6 illustrates the evolution of the half contact width during the three cycles of horizontal load at $1* \omega_c$ interference with μ=1 for Scheme1. It shows that the contact width keeps increasing during the three cycles, but it tends to stabilize. The introduction of the tangential force together with the normal load causes plastic deformation on the surface of the contact. The plastic deformation leads to the junction growth. Since the cylinder is also being flattened, the normal force required to keep the constant interference decreases during the fretting motion. With the decrease of the normal force, the tangential force decreases. When the corresponding von-Mises stresses drop under the yield strength, the plastic deformation stabilizes along with the junction growth. The two edges of the contact keep moving outwards during the fretting motion. However, the contributions to the junction growth, $\Delta b=b-b_{A1}$, of the two edges grow at a different rate as it is evident from Figure 4-7, which shows the evolution of the contributions to the growth of the two sides at $1* \omega_c$ interference with μ=1 for both schemes. The variable Δb represents the increase of the absolute value of the horizontal coordinate of the edges of the contact with respect to the values after the pure normal critical interference. For scheme1, the right side contributes more than the left side at the first quarter of the cycle, which means the deformation on the right side of the block is more pronounced. When the cylinder turns to the left, the left side starts to contribute more than the right side. At the end of the first cycle, the contributions of the two sides reach almost the same value. According to the results of the Scheme1, a conclusion could be drawn that the more pronounced junction growth occurs in the same direction of the tangential force

experienced by the surface of the deformed body, i.e. the block. When the materials of the two bodies are exchanged, i.e., Scheme2, the behavior of the junction growth on the two sides reverses, too. In scheme2, the left side contributes more to the growth during the first quarter of the cycle, while the right side starts to contribute more after the cylinder turns to the left. The more pronounced growth is in the same direction of the tangential force experienced by the surface of the cylinder, i.e. the weaker material (Incoloy 800H). The conclusion above is further verified. It is also consistent with the conclusion of Brizmer et al [91] that in the contact between a deformable sphere and a rigid flat under full stick condition, the junction growth is in the same direction of the tangential force experienced by the sphere.

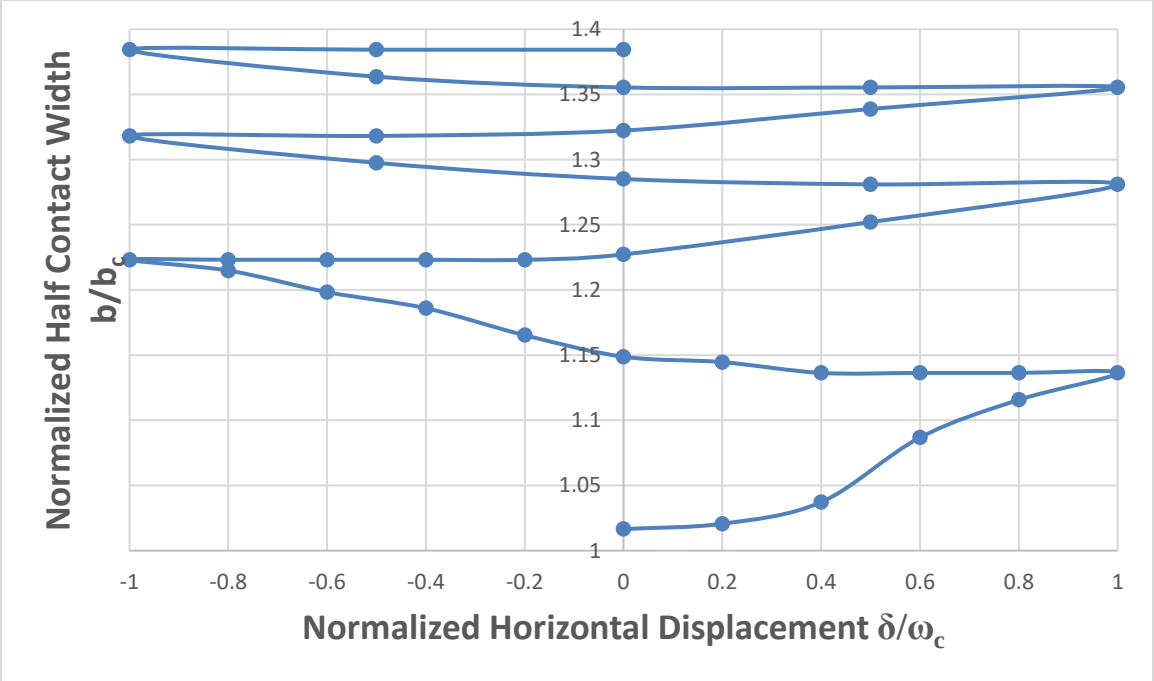

Figure 4-6. The evolution of the junction growth as indicated by the normalized half contact width for three cycles of horizontal load at $1\omega_c$ interference with μ=1 for Scheme1.

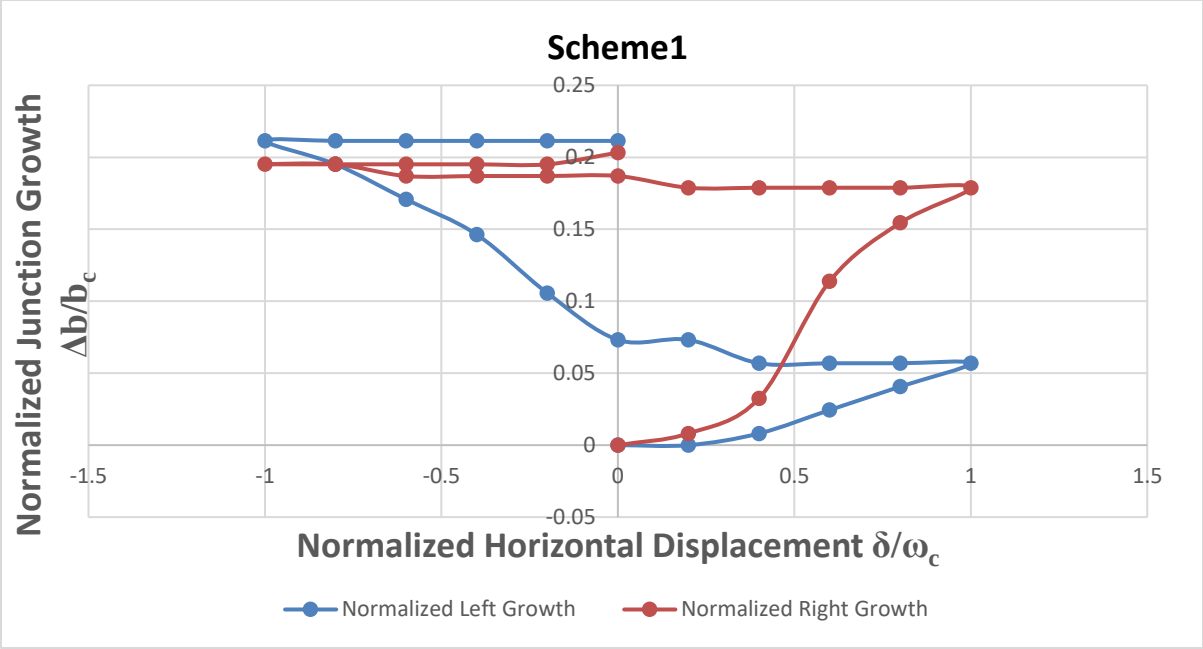

(a) Material Scheme1

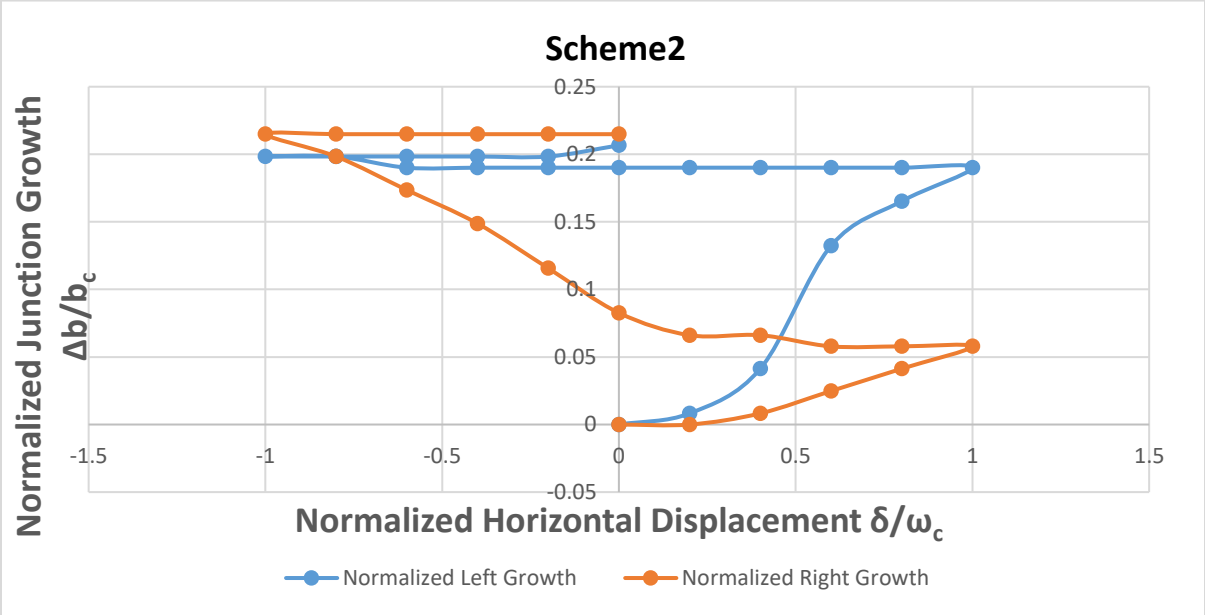

(b) Material Scheme2

Figure 4-7. The junction growth as indicated by the normalized half contact width on the two sides of the contact during the first horizontal cycle at 1*ω_c interference with μ=1 for different material schemes.

4.1.6 The Evolution of Tangential Force per Unit Length

The development of the tangential force per unit length during the fretting motion is recorded. Fig.4-8a depicts the evolution of Q at $1 * \omega_c$ interference with μ=1 for three horizontal loading cycles. That behavior is typically for the initial cycles of the fretting loop according to Walvekar [86]. The enclosed area represents the energy loss caused by the fretting motion under the given COF. As the cycle number increases, the maximum tangential force increases, which can be caused by the cumulative plastic deformation on the surface of the block.

Figure 4-8b illustrates the evolutions of the tangential force during three cycles of loading at $3*\omega_c$ interference with different COFs. When the COF is relatively small (μ=0.1 and 0.2), the loop stabilizes after the first cycle. Additionally, the effective COF (μe=Q/P), stabilizes at the value of the COF applied, μ=0.1 and 0.2, respectively. It is attributed to the full slip contact conditions (as indicated by ANSYS) at the right and left most positions. When the COF increases to μ=0.3, the loop does not stabilize after three cycles, but tends to stabilize after sufficient number of cycles. Therefore, the fretting loop stabilizes at the initial few cycles of loading for small COFs. The larger the COF, the larger of the number of loading cycles that the loop needs to stabilize.

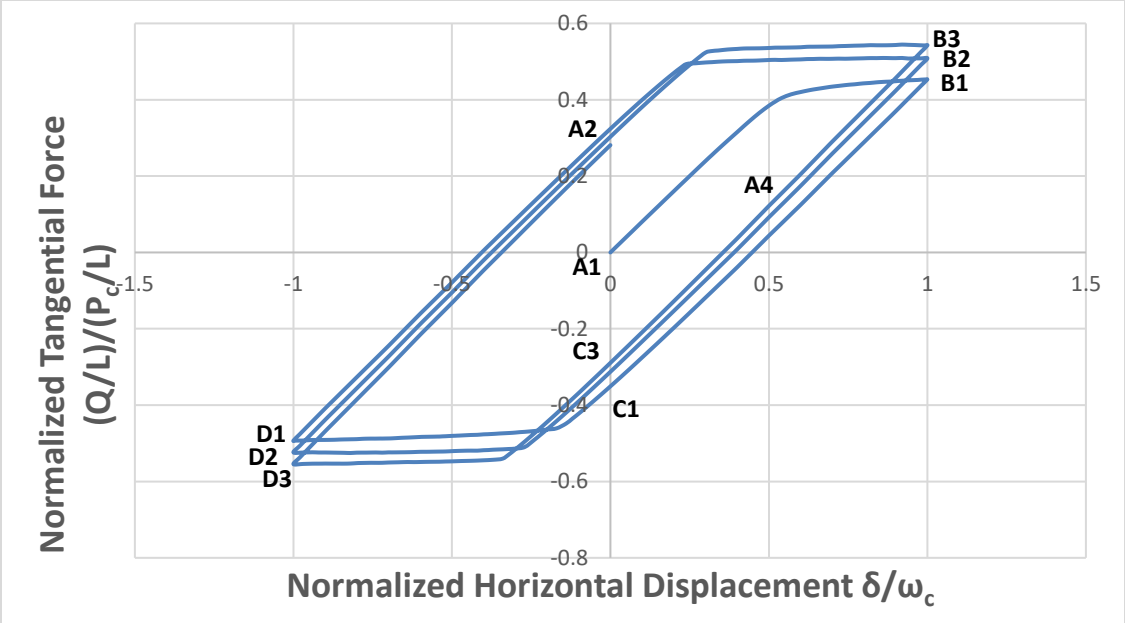

(a) $1* \omega_c$ interference with μ=1

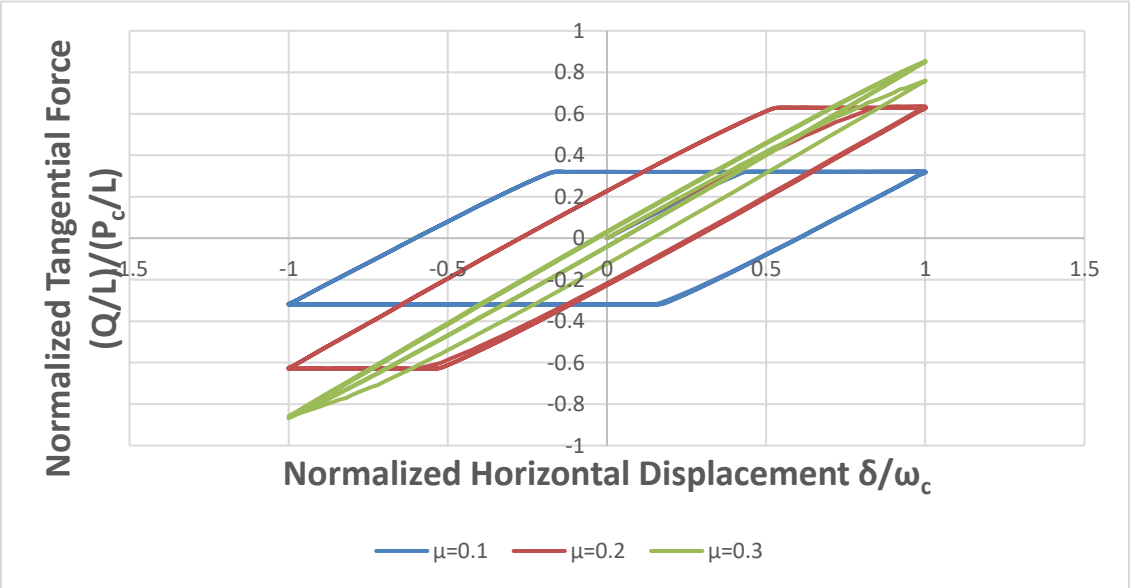

(b) $3* \omega_c$ interference with different COFs

Figure 4-8. The development of the normalized tangential force during three cycles of the horizontal loading for Scheme1.

4.1.7 The Depression marks on the Block

As the fretting motion proceeds, a depression mark is generated on the surface of the flat block. The depression mark can be visualized by the deformed curve of that surface. Fig.4-9 shows the deformed curve at $3* \omega_c$ interference with μ=1 right after the interference is applied for Scheme1. The curve is identical in shape to that of an elastic half-space with line loading, see Fig. 3-11, and as given by Johnson[11]. When the curve near the contact is zoomed in (see the inset in Fig.4-9), the indentation caused by the interference becomes clearly visible. The normalized deformation at the center of the surface of the block is about $1.6* \omega_c$, which is larger than half of the applied interference, $3* \omega_c$. That is caused by the plastic deformation on the block, while the cylinder deforms entirely elastically.

The depression mark grows during the oscillatory horizontal loading. Fig.4-10 depicts the deformed curves of the surface of the contact region at $3* \omega_c$ interference after three cycles of loading with μ=0.3 (under partial slip and partial stick, as indicated in ANSYS) and μ=1 (under full stick, as indicated in ANSYS). For μ=0.3, the depression mark (shown in Fig.4-10) is deeper than the original one (shown in the inset of Fig.4-9) right after the interference is applied. It can be understood by the decrease of the normalized Y-axis of the center of the surface on the block from -0.16 (shown in Fig.4-9) to -0.17. For μ=1, pileup shows up at near the inflection point of the curve. According to the results above, the pileup occurs at the edges of the indentation with a sufficiently large COF, especially in the case of the full stick condition. The abrupt change of the curvature or pileup will further produce the large von-Mises stress and plastic deformation at the corresponding position of the contact.

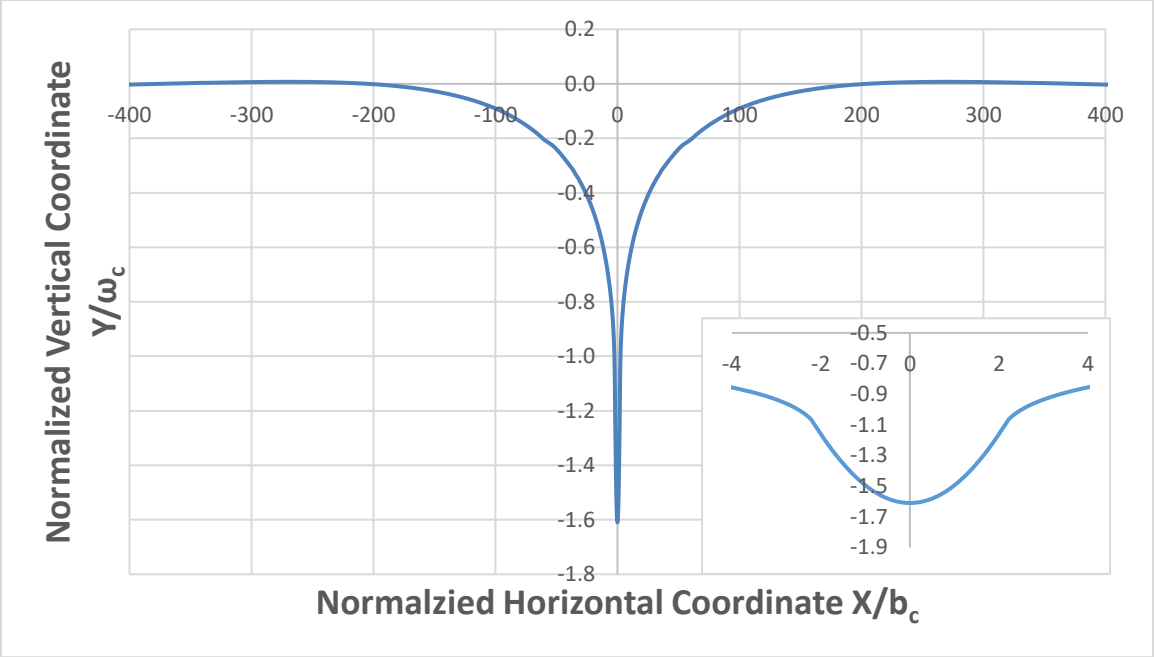

Figure 4-9. The curve of the surface of the block after 3*ω_c interference for Scheme1.

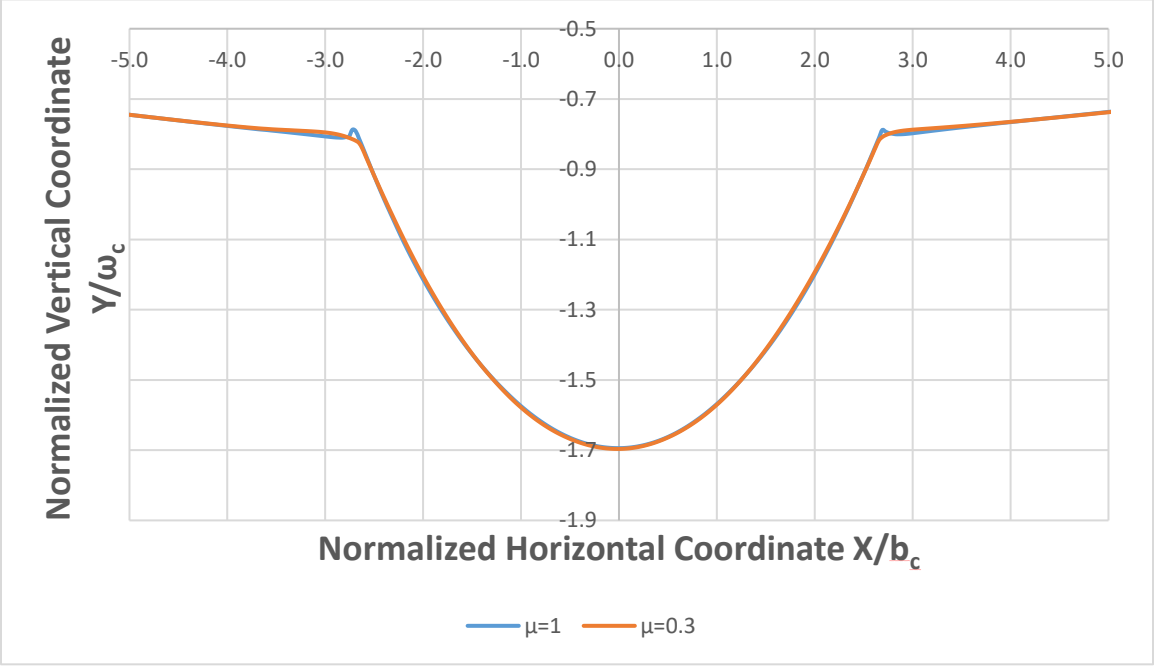

Figure 4-10. The depression marks on the surface of the block at 3*ω_c interference after three cycles of load for Scheme1.

4.1.8 The Influence of the Temperature

The results above are acquired for room temperature 20°C. In this section, results for 800°C are obtained and compared with those for 20°C. Firstly, the absolute horizontal and vertical displacements are kept the same for 20°C and 800°C to show the influence of the temperature. Secondly, the normalized horizontal and vertical displacements for 800°C (ω/ω_{cT} and δ/ω_{cT}) are kept being equal to those for 20°C (ω/ω_c and $\delta/\ \omega_c$) to show the function of normalization.

Table 4-3 shows the results at the two temperatures with the same absolute displacements after one cycle of horizontal displacement with μ=1. With the increase of the temperature, the plastic strain increases because of the decrease of the elastic modulus, E. Meanwhile, the tangential force, normal force, and the maximum von-Mises stress in the cylinder decrease. It is attributed to the decrease of the yield strength of the materials at elevated temperature.

Table 4-3. Different results at 20°C and 800°C after 1*ω_c interference and one cycle of horizontal displacement, whose magnitude is 1*ω_c, with μ=1 for Scheme1.

Temperature	Plastic Strain ε_p	Normalized Tangential Force per Unit Length $(Q/L)/(P_c/L)$	Normalized Normal Force per Unit Length $(P/L)/(P_c/L)$	Normalized Maximum Von-Mises Stress in Cylinder σ_{e1}/S_{y2}
20°C	0.74	0.54	1.14	2.0
800°C	0.83	0.34	0.82	1.4

4.1.9 Conclusion

This section presents a 2D plane strain finite element fretting model of a half cylinder in contact with a block. The materials of the two bodies are Inconel 617 and Incoloy 800H. The fretting model is displacement-controlled, where it is loaded with an interference first, and then a reciprocating horizontal displacement is applied to the top of the half cylinder. Different COFs are used in the model. Several conclusions are drawn.

1.During the oscillatory tangential loading, the two contact edges tend to experience the largest von-Mises stress. It is, therefore, postulated that cracks and fatigue are most likely to initiate and propagate at the contact edges. Between Inconel 617 and Incoloy 800H, the former is “harder” or “stronger,” and in the current investigation it never yields.

2.The largest plastic strains show up at the edges, too. The plastic deformation on the surface of the cylinder is not perfectly symmetric about the origin point, where it is slightly larger on the right, which is the direction of the initial motion. This is attributed to the decreasing normal force necessary to maintain a prescribed interference.

3.Due to the plastic deformation of the surfaces, junction growth is found. The more pronounced growth on the two edges is in the same direction of the tangential force experienced by the surface of the deformed body. This conclusion agrees with the results of Brizmer et al [91] whose model is the contact between a deformable sphere and a rigid flat under full stick condition.

4.The fretting loop (i.e., the development of the tangential force versus fretting motion) for the initial few cycles of loading is found, which is similar to that found experimentally by Courtney-Pratt and Eisner [92].

5.There are abrupt changes of the curvature at the edges of the indentation on the surface. When the COF is large enough to reach the fully stick condition, pileup will appear at the position of the abrupt change.

6.The temperature elevation causes the increase of the plastic strain and the decrease of the tangential force, normal force, and the maximum von-Mises in Inconel 617.

4.2 Spherical Fretting Contact

4.2.1 The Spherical Contact Model

The models are the same as those in the previous chapter, the displacement-controlled and force-controlled 3D spherical contact models. However, the material pairs in this chapter are dissimilar material pairs, which are Inconel 617/ Incoloy 800H at 20C and 800C [90]. The material properties are listed in Table 4-1. The yield strength of Incoloy 800H is about half of that of Inconel 617. The parameter C(ν) represents the ratio between the maximum pressure and the maximum von Mises stress in normal elastic spherical contact as given by Green [61]. Both materials are assumed to possess a 1% strain hardening based on the elastic modulus. That amount of the tangential modulus is verified not to significantly affect the FEA results, yet it improves the convergence times in ANSYS. The code ABAQUS is used too on select cases just to verify result. Adhesion is not considered in this chapter.

Table 4-4. Material properties for spherical fretting model

Temperature	Material	Elastic Modulus[GPa] E	Yielding Strength[MPa] S_y	Poisson Ratio ν	C(ν)	$C \cdot S_y$ [MPa]
20°C	Inconel 617	211.0	322	0.3	1.615	520
20°C	Incoloy 800H	196.5	150	0.339	1.662	249
800°C	Inconel 617	157.0	290	0.3	1.615	468
800°C	Incoloy 800H	141.3	90	0.394	1.662	156

According to Green [61], the ratio between the maximum pressure and the maximum von Mises stress in normal elastic contact is defined by $C(\nu) = p_o / \sigma_{e-\max}$, where

C(ν)=1.30075+0.87825 ν +0.54373 ν^2 . At the onset of yielding, the distortion energy theory asserts that $\sigma_{e-\max} = S_y$. The critical maximum pressure, $P_{0c,}$ is, therefore, replaced by the product $C(\nu)S_y$, to establish critical values via Eq.3-9, Eq3-10, Eq.3-11 and Eq.3-12.

By substituting the material properties of Table 4-2 in Eq.3-9, Eq.3-11, and Eq.3-12, the said critical parameters are obtained, and are listed in Table 4-5. The critical contact area is calculated based on a_c, $A_c=\pi a_c^2$. These critical values are subsequently used to normalize (i.e., generalize) results within this work.

Table 4-5. The critical values (onset of plasticity) for different material schemes and different temperatures.

Temperature	Cylinder Material	Block Material	Critical Interference ω_c [μm]	Critical Load P_c[kN]	Critical Contact Radius a_c [mm]	Critical Contact Area A_c[mm^2]
20°C	Inconel 617	Inconel 800H	5.96	1.556	1.73	9.36
800°C	Inconel 617	Inconel 800H	4.15	0.677	1.44	6.52

The scheme of normalization in this work is achieved by utilizing the normalized interference, namely 1*ω_c, 2*ω_c, 3*ω_c, while keeping the amplitude of the horizontal displacement 1*ω_c constant throughout. It allows the results to be applied to the practical situations both microscopically and macroscopically.

The mesh convergence procedure is the same as that of identical material pairs, which is first done in elastic normal contact, and then done in elastic-plastic fretting contact. For brevity, it is not shown here.

4.2.2 Loading Steps in Spherical Contact Model

As shown in Fig.4-11, load steps are used to impose the oscillatory horizontal displacement and extract results of the intermediate state. Step 0 corresponds to the loading condition where the interference has been just applied while the hemisphere is about to move horizontally. Each cycle of the horizontal displacement is achieved by 40 loading steps. The maximum number of cycles of the oscillatory horizontal displacement is three, because of the vast computational effort (144 hours for a single case on a 4 cores 3GHz PC with a Xeon CPU).

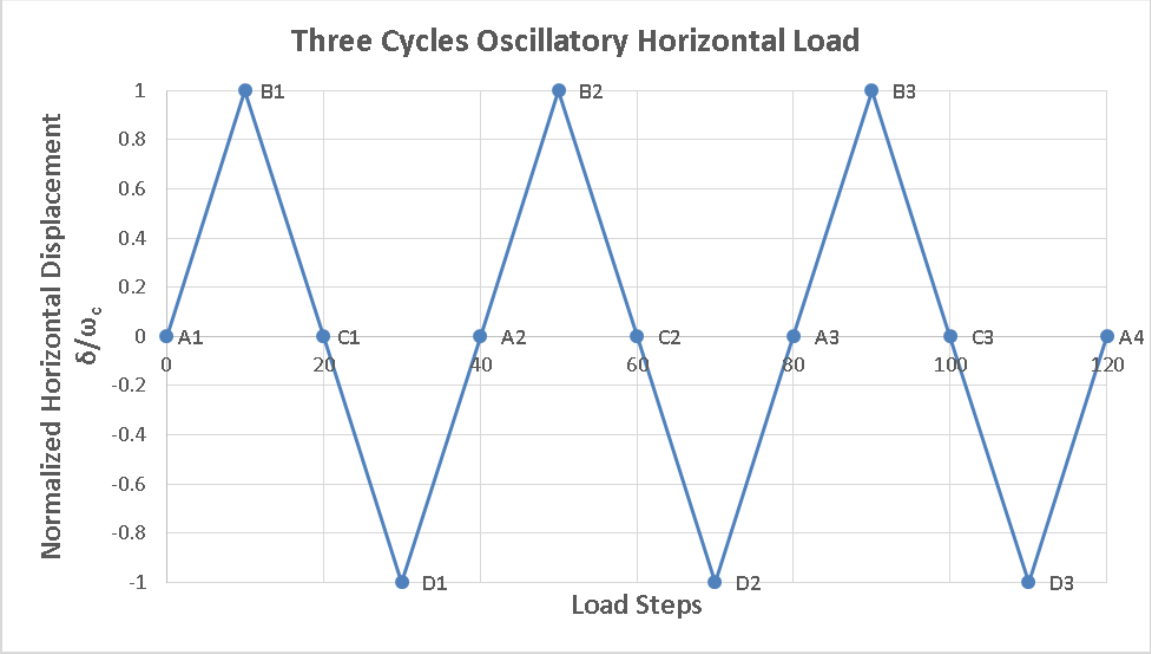

Figure 4-11. Loading stepping of three cycles oscillatory horizontal for plane strain case.

In order to describe the location and the cycle number explicitly, the following convention of notation is utilized. Points (A,B,C,D) represent, respectively, $\delta = (0,1,0,-1)\omega_c$, and the

cycle number is specified by n=1,2,3. For instance, A_2 corresponds to the end of the first cycle, where $\delta=0^* \omega_c$.

The results for dissimilar material pairs are similar to those in identical material pairs. The results shown in this section are used to verify the phenomena found in the identical pair cases.

4.2.3 The Distribution of von-Mises Stresses

During the oscillatory horizontal loading, the contact edges tend to experience the largest von-Mises stress. Figure 4-12 shows the von-Mises distribution at 1*ω_c vertical interference with μ=1. The large von-Mises stresses, represented by the red regions, are always located at the edges of the contact, and form "rings". However, the large von-Mises stresses disappear on the contact surface with low COF, μ=0.3, and appear at the region under the surface. For brevity, the results are not shown.

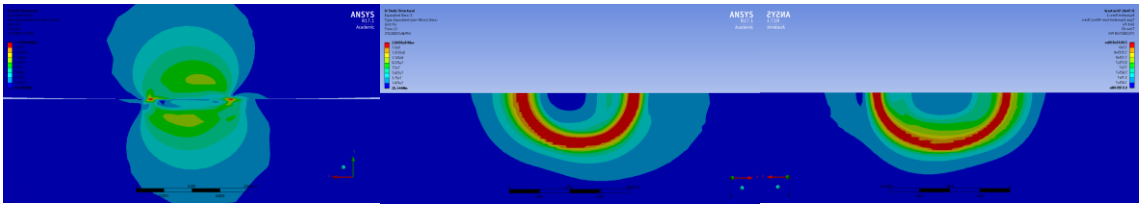

(a) (b) (c)

Figure 4-12. The evolution of von-Mises stresses during three cycles of horizontal loading at 1* ω_c interference with μ=1. (a)Front view at the end of three cycles (b) Top view on the block at the end of the first cycle (c) Top view on the block at the end of the third cycle case.

4.2.4 The Distribution of Plastic Strains

Figure 4-13 shows the plastic strain distribution at $1*\omega_c$ vertical interference with $\mu=1$. During the fretting motion, only the block yields where the plastic strains are generated. As shown in Fig.4-13a, the plastic strains appear closed to the surface of contact, where the two edges experience the largest von-Mises stress. The plastic strains accumulate during the fretting cycles ($\varepsilon_{pmax}=0.025$ after one cycle and $\varepsilon_{pmax}=0.038$ after three cycles). The plastic strain is not found on the contacting surface for the above case when the COF drops to 0.3.

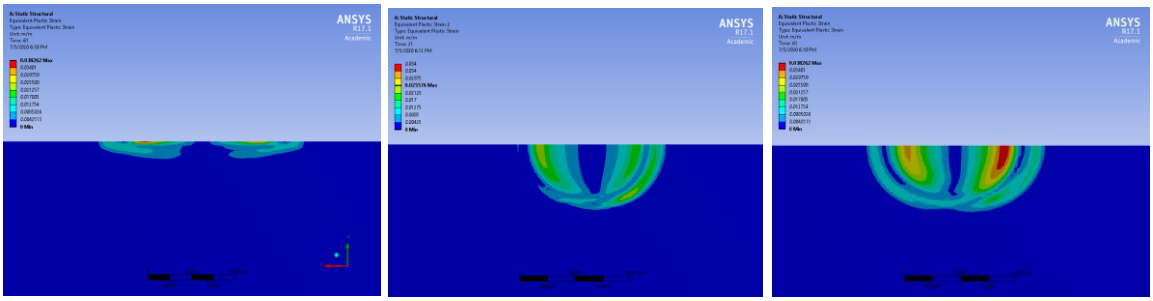

(a) (b) (c)

Figure 4-13. The evolution of equivalent plastic strain during three cycles of horizontal loading at $1*\omega_c$ interference with $\mu=1$. (a)Front view at the end of three cycles (b) Top view on the block at the end of the first cycle (c) Top view on the block at the end of the third cycle.

4.2.5 Junction Growth

Figure 4-14 shows the schematics of the contact region at $1*\omega_c$ with $\mu=1$. The red color represents the region at the loading step A1, i.e., at the beginning of the loading. The blue color represents the region at the loading step A4, i.e., at the end of the three cycles of loading. In the figure, the contact region grows radially. However, the growth in the X

direction is larger than that in the Z direction, which stretches the contact region in the X direction.

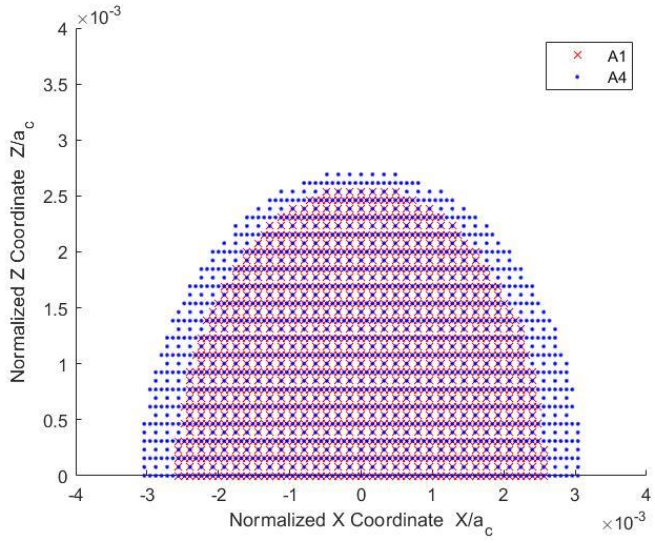

Figure 4-14. The schematics of the contact zone at the beginning (A1) and ending of the three cycles (A4) of loading at 1*ωc with μ=1.

With a sufficient large COF, the pileup appears at the edges of the contact. Figure 4-15 shows the profile of the contacting region of the block after three cycles of horizontal loading while the vertical interference is still maintained at $1*\omega_c$ with μ=1. There are pileups at the edges of the contact. This is due to the plasticity on the surface, introduced by the friction force.

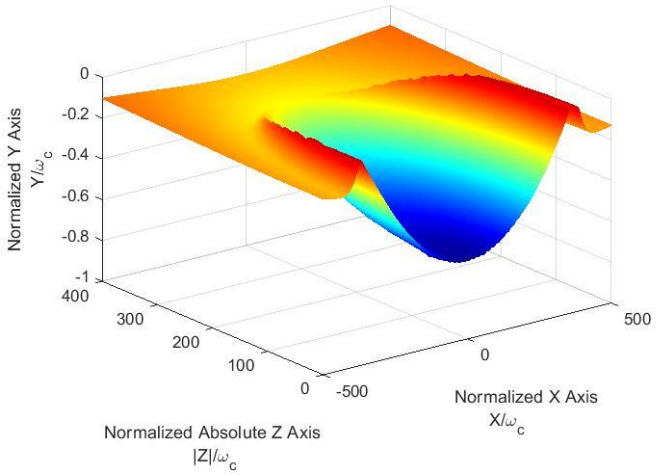

Figure 4-15. The surface profile of the contacting region of the block at 1*ω_c after three cycles of horizontal loading with μ=1.

4.2.6 Conclusion

This section presents a 2D plane strain finite element fretting model of a half cylinder in contact with a block. The materials of the two bodies are Inconel 617 and Incoloy 800H. The fretting model is displacement-controlled, where it is loaded with an interference first, and then a reciprocating horizontal displacement is applied to the top of the half cylinder. The same phenomena appear in both identical and dissimilar material cases:

1.The largest von-Mises stress is confined under the contacting surface with small COFs, while with sufficiently large COFs, the largest von-Mises stress shows up at the contacting surfaces and is located at the edge of the contact.

2.With sufficiently large COFs, the large plastic strains form multiple “rings” on the contacting surfaces after the oscillatory fretting motion.

3.Junction growth is found when there is plastic deformation on the surface of the contact. The contacting region is stretched in the direction of the fretting motion.

4.There are depression marks on the surface of the block caused by the fretting motion. There are pileups at the edges of the contact with large COF. Since the magnitude of the oscillatory sliding distance is relatively small, $1*\omega_c$, the pileup phenomenon is not pronounced.

4.3 Scheme of Normalization

In Chapter 3 and 4, the results are always normalized by the critical values of the corresponding material pairs. In this way, the normalized results may well characterize a range of contact scales (from micro to macro) of various ductile material pairs. The following results are shown to verify the effectiveness of the normalization scheme.

4.3.1 Plane Strain Cylindrical Contact

Figure 4-16 shows the junction growth during one cycle of horizontal displacement at $1*\omega_c$ interference for 20°C and 800°C with the same normalized displacement input and the same COF, μ=1 for Inconel 617/ Incoloy800H. The results are also compared with the normalized junction growth when the two bodies consist of identical steel materials. The evolutions of the normalized contact width for the three cases are essentially the same. Additionally, based on Fig.4-17, the evolutions of the normalized tangential force in the three conditions are also very close. The good agreement of the normalized contact widths and the tangential forces demonstrates the effectiveness of the normalization even though the critical values of the alloys (see Table 4-2) and steel (see Table 3-2) are about an order of magnitude different (where also CS_y is much larger for steel, see Tables 3-1). That means that the normalized results of the fretting model for different material properties are effectively the same when normalized. It is suggested, therefore, that the results in this

work may be applied to the fretting between materials that are different from those investigated in the current work.

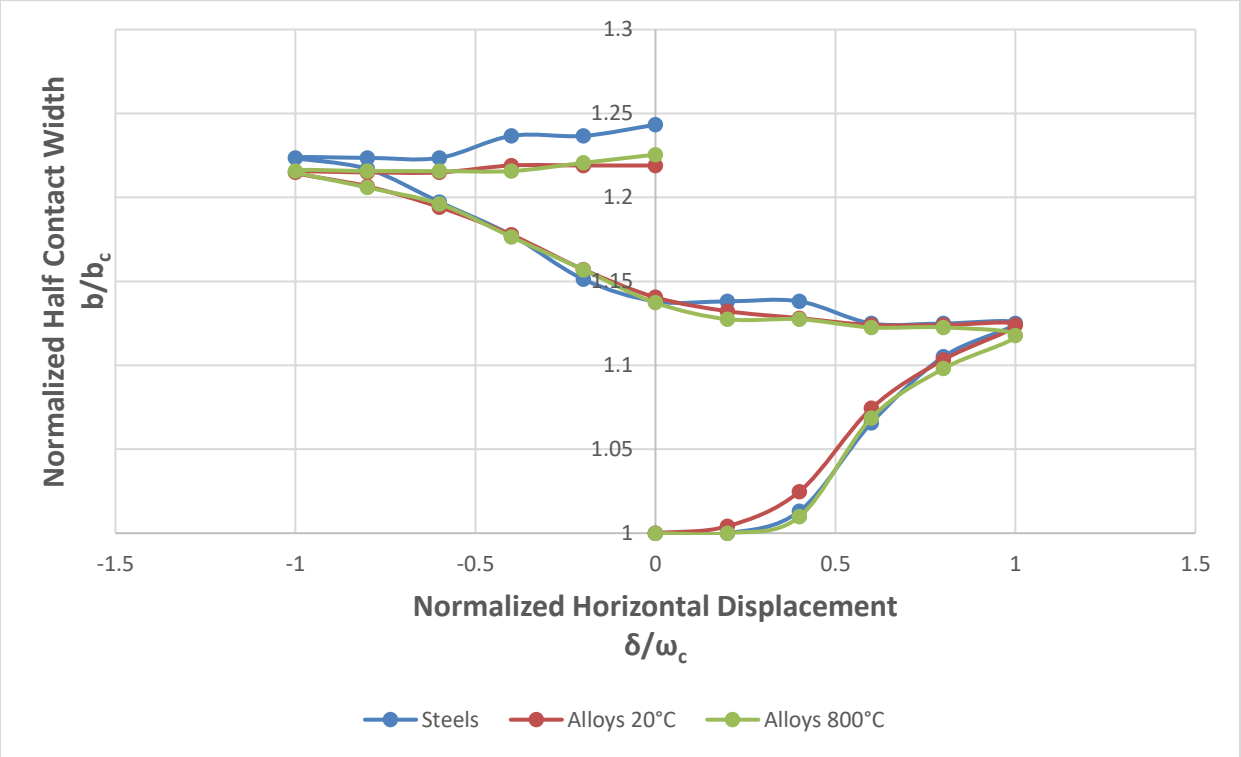

Figure 4-16. The evolution of the junction growth as indicated by the normalized half contact width during one cycle of horizontal displacement at 1*ω_c interference with the same normalized displacement input, μ=1. Note that b_c and ω_c are taken from Table 4-2 corresponding to 20°C or 800°C, or Table 3-2 for the steel case

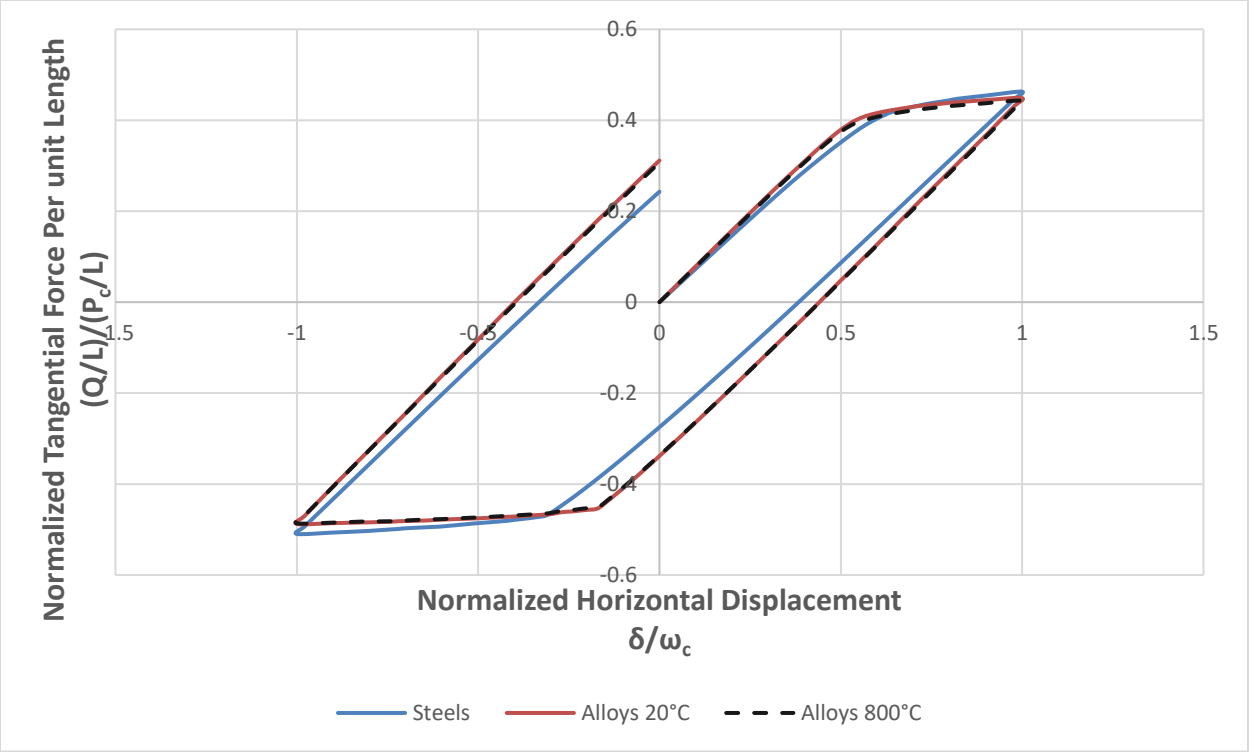

Figure 4-17. The evolution of the normalized tangential force during one cycle of horizontal displacement at 1*ω_c interference with the same normalized displacement input, μ=1. Note that b_c, P_c/L, and ω_c are taken from Table 4-2 corresponding to 20°C or 800°C, or Table 3-2 for the steel case

4.3.2 Spherical Contact

In order to verify the normalization scheme utilized in 3D cases, the normalized results, including the contact area and the tangential force, for steel-on-steel and copper-on-copper contacts are compared in Fig.4-18 and Fig.4-19. It pointed that steel and copper have significantly different material properties and critical values (See Tables 3-4 and 3-5). Figure 4-18 depicts the evolution of the normalized contact area during three cycles of horizontal loading at 1*ω_c with μ=1. Figure 4-19 depicts the evolution of the normalized tangential force under the same conditions as in Fig.4-18. The curves for the steel-on-steel and copper-on-copper contacts are very close. The good agreement demonstrates the

effectiveness of the normalization scheme. That means that the normalized results of the fretting model for different material properties are effectively the same when normalized. In other words, it suggests that the results of this work can be applied to the fretting between materials that may be different from those investigated in the current model.

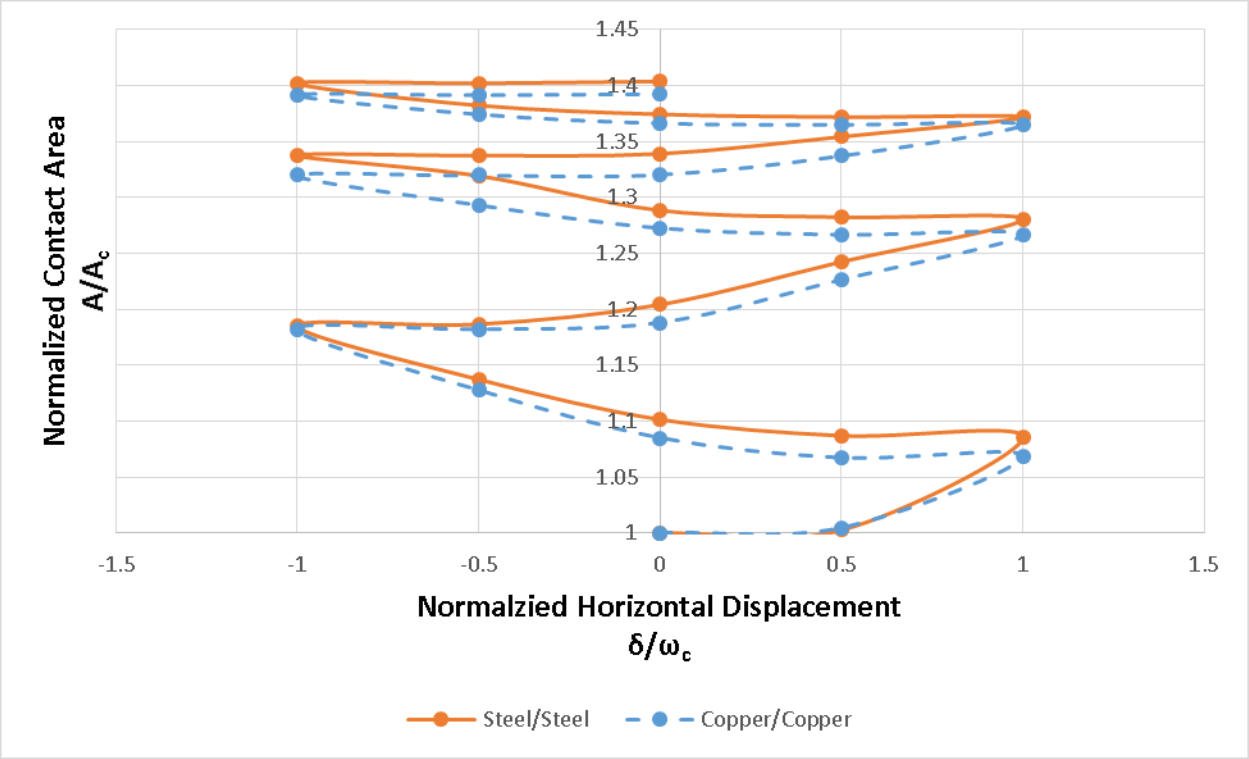

Figure 4-18. The evolution of the normalized contact area during three cycles of horizontal displacement at 1*ω_c interference with the same normalized displacement input, μ=1. Note that A_c and ω_c are taken from Table 3-5 corresponding to steel and copper.

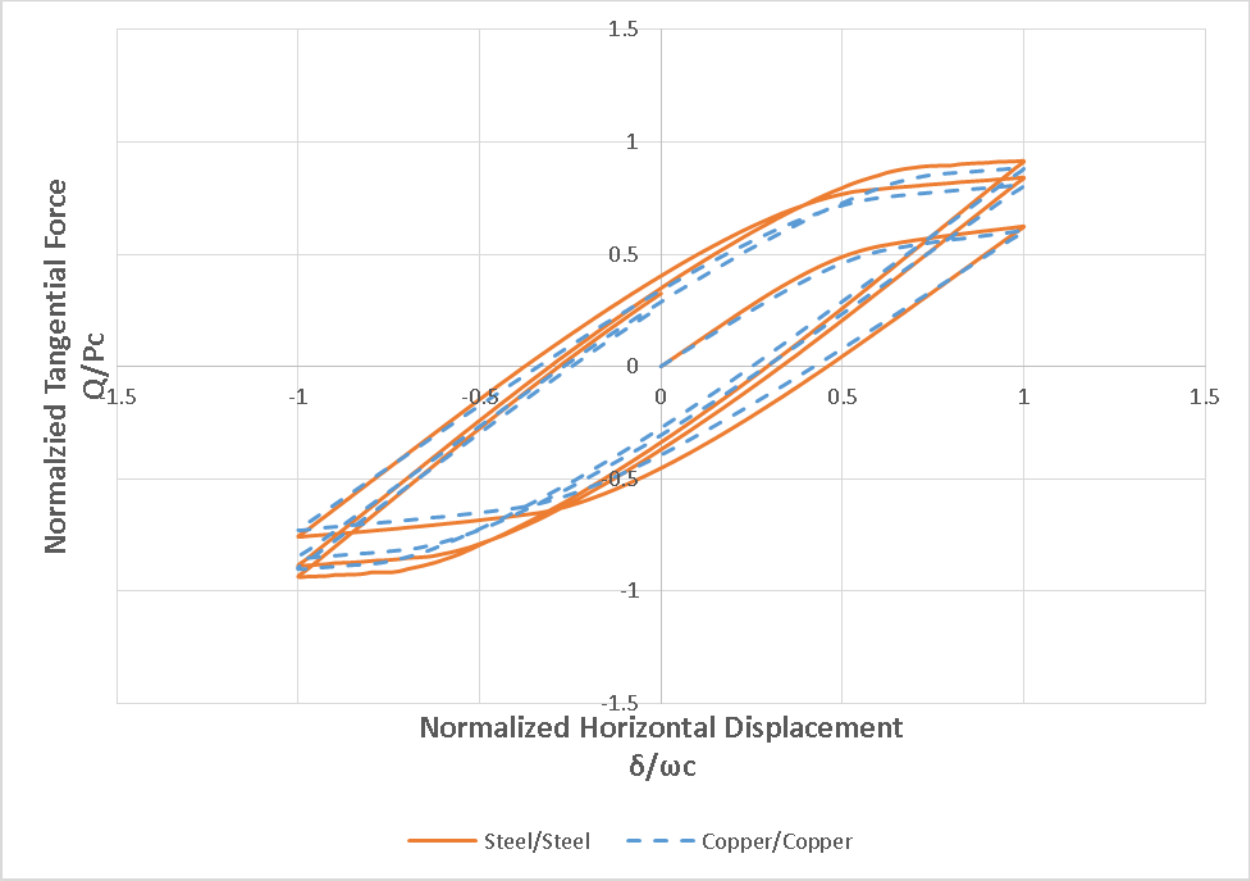

Figure 4-19. The evolution of the tangential force during three cycles of horizontal displacement at 1*ω_c interference with the same normalized displacement input, μ=1. Note that P_c, and ω_c are taken from Table 3-5 corresponding to steel and copper.

4.4 Conclusion

In this chapter, the fretting contact between dissimilar material pairs are investigated in both cylindrical and spherical contacts. The material pairs are set to Inconel 617/ Incoloy 800H at 20C and 800C. The phenomena appear in identical material pair cases (Chapter3) are verified to also appear in dissimilar material pair cases. Besides, there are some unique observations between dissimilar materials.

For results in 2D cylindrical contact, the two contact edges tend to experience the largest von-Mises stress. Between Inconel 617 and Incoloy 800H, the former is “harder” or “stronger,” and in the current investigation it never yielded. Due to the plastic deformation of the surfaces, junction growth is found. The more pronounced growth on the two edges is in the same direction of the tangential force experienced by the surface of the deformed body. This conclusion agrees with the results of Brizmer et al [91] whose model is the contact between a deformable sphere and a rigid flat under full stick condition. The temperature elevation causes the increase of the plastic strain and the decrease of the tangential force, normal force, and the maximum von-Mises in Inconel 617. For results in 3D spherical contact, the largest plastic strain appears at the leading and trailing edges. The pattern of the plastic strain distribution is not “ring-like” in identical material pair cases, since there is plowing effect between dissimilar material pairs.

Additionally, the scheme of normalization is discussed. In Chapter 3 and 4, the results are always normalized by the critical values of the corresponding material pairs. In this way, the normalized results may well characterize a range of contact scales (from micro to macro) of various ductile material pairs. The normalized contact area and normalized tangential traction are compared between different material pairs (steel/steel, copper/copper, Inconel 617/Incoloy 800H at 20C and 800C). The excellent agreement of the normalized results verifies the effectiveness of the normalization scheme.

CHAPTER 5. FRETTING WEAR

In this chapter, the formulation to predict fretting wear (volume removal) under frictional conditions for plane strain line contact and spherical circular contact are found. The materials in contact are set to different material pairs. Various coefficients of friction (COFs) and the Archard Wear Model are applied to the interface. In this chapter, the wear models that take place at the interface are applicable for elastic and elastic-plastic conditions. Wear debris that may be generated at the interface could be trapped in the contact; however, this is not considered here. In the current models, such wear debris are assumed to be expelled out of the contact. Initially, pure elastic conditions are investigated. The theoretical predictions for the wear volume at the end of the partial slip condition in unidirectional sliding contact are compared with the FEA results. After that, the theoretical predictions for the wear volume of a general cycle during the fretting motion is compared with the FEA results. Lastly, the influence of plasticity is discussed. The model and results for the 2D case have been published in Ref. [93].

5.1 Plane Strain Cylindrical Contact Model

This is the first study to develop an empirical formulation to predict fretting wear (volume removal) under frictional conditions for plane–strain line contacts as borne out by the finite element analysis (FEA). The contact is between a deformable half-cylinder rubbing against a deformable flat block. The FEA is guided by detailed physical conceptions, with results that subsequently lead to the methodical modeling of fretting wear. The materials in contact are set first to steel/steel, then to Alloy617/Alloy617, and finally to copper/copper. Various coefficients of friction (COFs) and the Archard Wear Model are applied to the interface.

Initially, pure elastic conditions are investigated. The theoretical predictions for the wear volume at the end of the partial slip condition in unidirectional sliding contact, agree very well with the FEA results. The empirical formulation for the initial gross slip distance is constructed, again revealing results that are in good agreement with those obtained from the FEA for different materials and for various scales. The Timoshenko beam theory and the tangential loading analysis of a half-elastic space are used to approximate the deflection of the half-cylinder and the flat block, respectively. That theory supports well the empirical formulation, matching closely the corresponding FEA results. The empirical formulation of the wear volume for a general cycle under fretting motion is then established. Its results are shown to be valid for different materials and various COFs when compared with the FEA results. Lastly, plasticity is introduced to the model, shown to cause two phenomena, namely junction growth and larger tangential deformations. Wear is shown to either increase or decrease depending on the combined influences of these two phenomena.

5.1.1 The Archard Wear Model

The fretting model in this work is shown in Fig. 5-1. A simulated rigid plate is positioned on top of a half-cylinder that has a radius of R=0.5m, which is in contact with an R×4R block. The elastic modulus of that plate is set large enough (2×10^{10} GPa) to enforce a uniform downward displacement at the interface between the plate and half-cylinder during the fretting motion. That interface is made frictionless, as the rigid plate role is to prevent rotation of the half-cylinder at its upper boundary. The material of the half-cylinder and the flat block is first set to steel/steel, then to Alloy617/Alloy617, and finally to copper/copper. The material properties are listed in Table 5-1. While the Poisson ratios of the chosen materials are very close, the moduli of elasticity and yield strengths are quite distinct.

The fretting loading condition is shown in Fig.5-1. The axes of X and Y are shown where the origin is located at the initial contact point. For brevity, the positive and the negative directions of X axis are designated as “right” and “left”, respectively. The base of the flat block, a, is fixed in both the X and the Y directions (other B.C. will be discussed shortly). A normal force, P, is first applied to the top of the plate, which introduces a vertical interference, ω, designated as the indentation. With the normal force being kept constant, an oscillatory displacement in the X direction, δ, is applied to the top of the half-cylinder. The oscillation magnitude in each cycle is maintained constant. That fretting cycles are identical to those in Chapter 3, but again for brevity, the schematics are omitted here. The loading condition is displacement-controlled in the X direction and force-controlled in the Y direction. In other words, the normal load, P, and the tangential displacement, δ, are inputs, while the interference, ω, and tangential force, Q, are outputs.

An Archard wear model, Eq. 5-1, is used at the contact between the half-cylinder and the block. The wear volume, V, is proportional to the normal force P, sliding distance, S, and inversely proportional to the hardness [21], H[1]. The hardness, H, is assumed to equal to $2.8*S_y$ for each material. The dimensionless wear coefficient K, according to Archard and Hirst [10], is typically between 10^{-2} and 10^{-5} for metallic contacts under unlubricated

1. Eq. (5-1) is used here as Archard intended, regarding hardness as a material property. According to the work by Jackson and Green [12], it has been shown that hardness actually depends not only on the yield strength but also on the deformation. For consistency with Archard original model, however, hardness is used here as if it were a constant material property.

conditions. Without loss of generality, K is set to 10^{-4} in this work[2]. The Archard Wear Model is applied locally (i.e., at each nodal point) at the contact region.

$$V = \frac{KPS}{H} \tag{5-1}$$

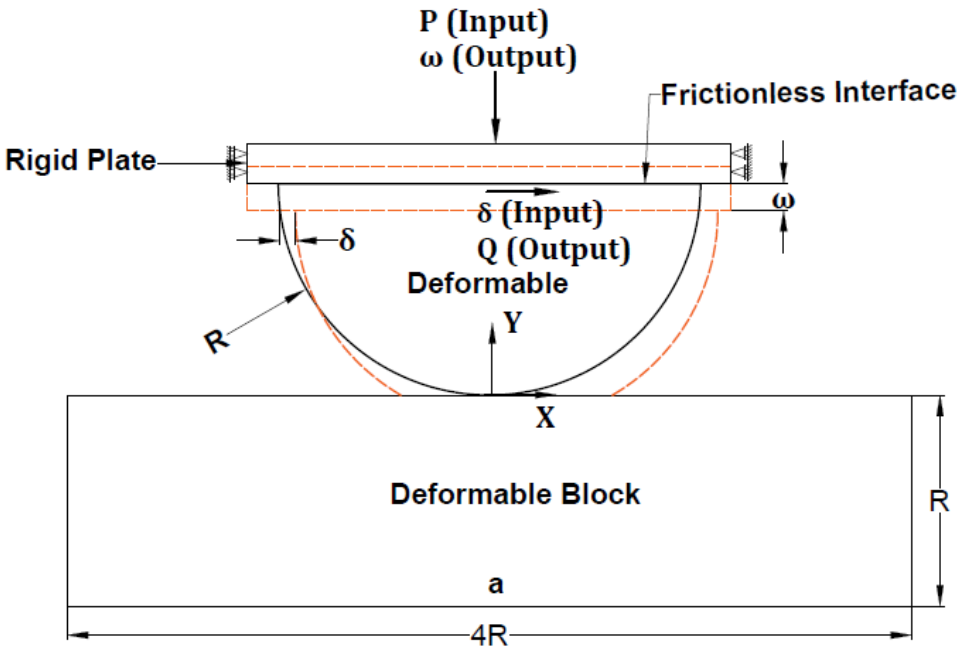

Figure 5-1. The loading condition and dimensions of the cylindrical contact model.

2. A numerical value for K has to be implemented in the FEA code. However, because of normalization, the results are generalized for any value of K.

Table 5-1. The material properties and critical values for three cases [94].

Case	Materials	Elastic Modulus[GPa] E	Yielding Strength[MPa] Sy	Poisson Ratio ν	Critical Interference ω_c [μm]	Critical Load per Unit Length Pc/L [MN/m]	Critical Half Contact Width b_c [mm]
1	Steel	200	911	0.32	927	38.7	14.9
2	Inconel 617	211	322	0.3	144	4.83	5.26
3	Copper	130	331	0.33	328	7.90	8.30

5.1.1.1 Theoretical Equations for Normal Contact

For normal contact of elastic cylinders in plane-strain, the relations between the load per unit length, P/L, the half contact width, b, the maximum contact pressure, p_0, and the pressure distribution, p(x), are given in the following, according to the Hertzian theory of contact [11]:

$$p_0 = \frac{2P}{\pi bL} \tag{5-2}$$

$$b = \left(\frac{4PR}{\pi LE'} \right)^{\frac{1}{2}} \tag{5-3}$$

$$p(x) = p_0 \sqrt{1 - \frac{x^2}{b^2}} \tag{5-4}$$

The symbol ν represents the Poisson ratio, while E' represents the equivalent elastic modulus, given by:

$$\frac{1}{E'} = \frac{1-\nu_1^2}{E_1} + \frac{1-\nu_2^2}{E_2} = \frac{2(1-\nu^2)}{E} \tag{5-5}$$

The symbols, E_1 and E_2, correspond to the elastic moduli of the half-cylinder and the block, respectively, while ν_1 and ν_2 corresponds to the Poisson ratio of the half-cylinder and the

block, respectively. In this work, $E=E_1=E_2$ and $\nu=\nu_1=\nu_2$, since the material properties of the two bodies in contact are set to be identical, with the outcome given in Eq. 5-5.

For the block whose depth equals to the radius of the half-cylinder, d=R=0.5m, the relation between the interference, ω, and the load per unit length, P/L, is derived in Appendix A, Eq. A-8:

$$\omega = \frac{P/L}{2\pi E'}\left\{2\ln\left(\frac{2\pi R E'}{P/L}\right) - \frac{1}{1-\nu}\right\} \tag{5-6}$$

According to Green [61], the ratio between the maximum contact pressure and the maximum von-Mises stress is defined as a parameter, $C=p_0/\sigma_{emax}$. In the elastic contact regime, this parameter is a function of the Poisson's ratio, $C(\nu)=1.164+2.975\nu-2.906\nu^2$, for $\nu>0.1938$. By introducing this ratio, the critical half contact width, b_c, critical load per unit length, P_c/L, and critical interference, ω_c, at the onset of plasticity in the contact, are given by [95]:

$$b_c = \frac{2RCS_y}{E'} \tag{5-7}$$

$$\frac{P_c}{L} = \frac{\pi R(CS_y)^2}{E'} \tag{5-8}$$

$$\omega_c = \frac{R}{2}\left(\frac{CS_y}{E'}\right)^2\left[4\ln\left(\frac{\sqrt{2}E'}{CS_y}\right) - \frac{1}{1-\upsilon}\right] \tag{5-9}$$

By substituting the material properties in Table 5-1 into Eq.5-7, Eq.5-8, and Eq.5-9, the critical values are then calculated and listed alongside. The three cases exhibit critical values that are nearly an order of magnitude different. The critical values in each case are used to normalize the foregoing results. It is also noted that the oscillation amplitudes in all cases are always maintained at $1*\omega_c$, which is listed in Table 5-1.

5.1.1.2 Theoretical Equations for Tangential Contact

Consider the model in Fig.5-1 under a Hertzian pressure, p(x) (Eq. 5-4), caused by a total normal load per unit length, P/L (Eq. 5-2). A constant friction of coefficient (COF), μ, is applied to the contact when sliding takes place. According to Johnson [11], when the tangential traction per unit length, Q/L< μ*(P/L), the interface experiences partial slip conditions. As shown schematically in Figure 5-2, within the contacting region (-b<x<b), the conditions are stick for [-c, c], and slip between [-b, -c] U [c, b], The symbol, c, is called the stick half-width.

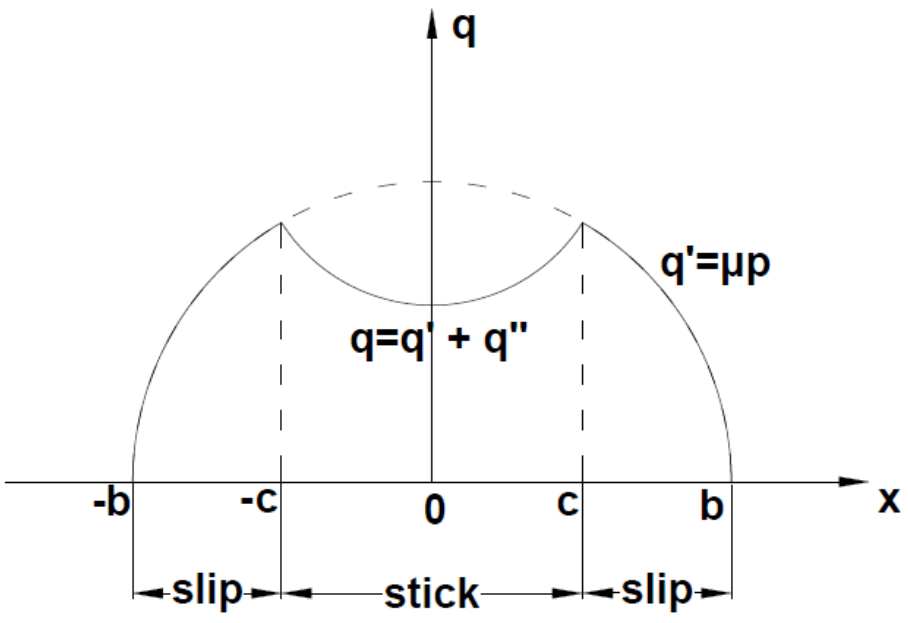

Figure 5-2. The distribution of tangential surface traction of the cylindrical contact under a tangential force, Q/L< μ(P/L).

In the slip region, the tangential traction is q'(x)=μp(x), where p(x) is the Hertzian pressure given by Eq.5-4. If the q'(x) is applied to the entire contact region, [-b, b], there should be

another q’’(x) to achieve the stick status for [-c, c], where all the points in the stick region displace uniformly. The distributions of q’(x) and q’’(x) are given by Johnson [11],

$$q'(x) = \mu p_0 \sqrt{1 - \frac{x^2}{b^2}} \qquad -b < x < b \tag{5-10}$$

$$q''(x) = -\frac{c}{b} \mu p_0 \sqrt{1 - \frac{x^2}{c^2}} \qquad -c < x < c \tag{5-11}$$

Note that q(x)=q’(x) for slip region, and q(x)=q’(x)+q’’(x) for stick region[3]. Clearly, the flat block and the half-cylinder always experience the tangential traction in opposite directions. For instance, if the half-cylinder is forced to the “right” (i.e., the positive X direction), in the coordinates of this model the flat block experiences q’(x) and q’’(x), while the half-cylinder experiences –q’(x) and –q’’(x).

When the tangential force per unit length reaches Q/L= μ(P/L), gross slip starts. The tangential force is maintained at μ(P/L) at the threshold and during gross slip. In other words, the contact status is slip for the entire range [–b, b], while c=0. By taking the two bodies as two half elastic spaces, the tangential displacement on the surface of contact for each body, $\bar{u}(x)$, within contact is given by Johnson [11],

$$\bar{u}(x) = -\frac{(1-\nu^2)\mu p_0}{bE} x^2 \cdot \mathrm{sgn}(q(x)) + C \qquad -b < x < b \tag{5-12}$$

Hence, in the current coordinates, if the half-cylinder is forced to the “right”, the tangential displacement of the half-cylinder, $\bar{u}_1(x)$, and that of the block, $\bar{u}_1(x)$, are, respectively:

3. Note that q(x) has units of stress and is occurring at the interface. It is distinguished from Q/L, which is the tangential force (per unit length) applied at the top of the half-cylinder, see Fig.1.

$$\bar{u}_1(x) = \frac{(1-\nu_1^{\,2})\mu p_0}{bE_1} x^2 + C_1 \qquad -b < x < b \tag{5-13}$$

$$\bar{u}_2(x) = -\frac{(1-\nu_2^{\,2})\mu p_0}{bE_2} x^2 + C_2 \qquad -b < x < b \tag{5-14}$$

Considering the boundary condition that at the initial of gross slip, $\bar{u}_1(0) = \bar{u}_2(0)$, makes the two constants equal, C_1=C_2. The local sliding distance between the half-cylinder and the flat block at the initiation of the gross slip, $s_0(x)$, is then derived by $s_0(x) = \bar{u}_1(x) - \bar{u}_2(x)$. Using the relations, $E=E_1=E_2$ and $\nu=\nu_1=\nu_2$, gives,

$$s_0(x) = \frac{2(1-\nu^2)\mu p_0}{bE} x^2 \tag{5-15}$$

It is again emphasized that this initial gross slip equation is derived for elastic conditions.

5.1.2 Mesh Convergence for Cylindrical Wear Model

Mesh convergence has been done to a displacement-controlled model in Chapter 3. However, since this model is force-controlled in normal direction and displacement-controlled in tangential direction, it is prudent to verify mesh convergence under such conditions just as well.

Element PLANE183 is used to mesh the model in ANSYS 17.1 (a representative of which is shown in Fig. 5-3). Taking the case for steel/steel for instance, there are 58103 elements for the entire model. The size of the refined mesh in the contact area is $8*10^{-4}R$. One hundred contact elements (CONTA172 and TARGE169) on each side of the contact are used to simulate the contact between the half-cylinder and the block. Similar mesh schemes are used to model the other two material cases.

A frictionless contact condition is applied to the interface between the rigid plate and the half-cylinder. The contact between the half-cylinder and the flat block is set to frictionless or frictional to investigate different cases. In the frictional contact cases, a small amount of fake slip is generated in sticking area to calculate tangential traction in ANSYS 17.1, and it is documented by ANSYS [96]. In order to alleviate the influence of this fake slip, the elastic slip tolerance factor is used so as to control the fake slip to be smaller than 1% of the sliding distance applied to the top of the half-cylinder.

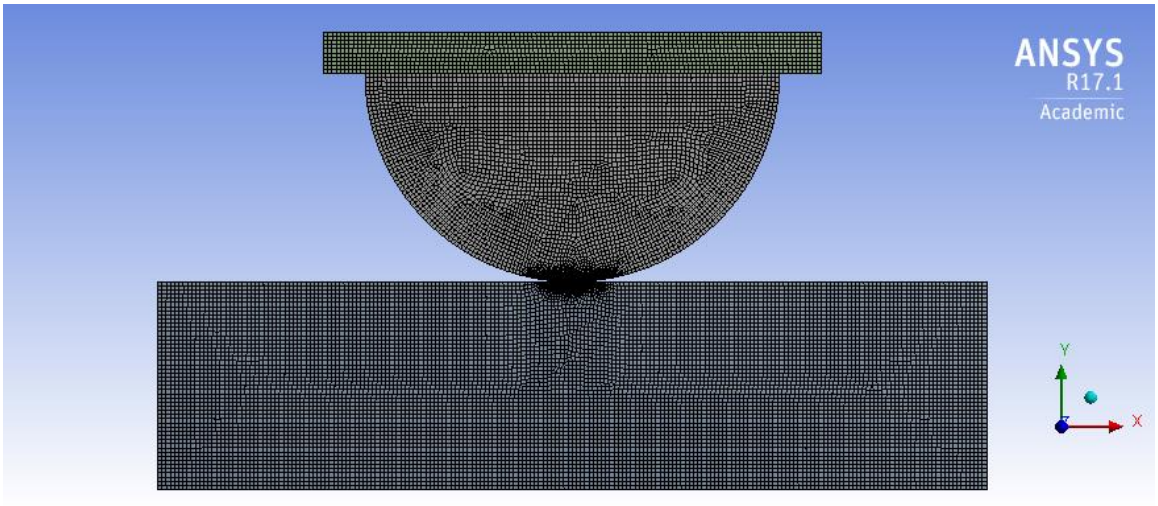

Figure 5-3. The model in ANSYS 17.1.

The results of the mesh convergence for material Case1 (see Table 5-1) is shown in Table 5-2. It is first done to the pure normal elastic contact and frictionless loading. To validate the mesh in FEA, the results from ANSYS are compared with those obtained from theoretical predictions. With an input of normal force per unit length, P/L (ranges from 0.2*Pc/L to 1*Pc/L), the half contact width, b, is calculated by Eq. 5-3, and the interference, ω, is calculated by Eq. 5-6. The maximum contact pressure, p_0, is then derived by Eq. 5-2. The maximum von-Mises stress, $\sigma_{emax}=p_0/C$, is consequently obtained. The theoretical results for Case1 are compared with those from the finite element method (ANSYS 17.1), as shown in Table 5-2. The percentage differences are listed under "%dif" for each of the parameters. Except for the difference of half contact width, b, that is 4.91% under 0.2 P_c due to the relative coarse mesh, all the other differences are below 3%. Table 5-3 shows the results for the case of P*=1, but for frictional loading with μ=0.3, for material Case 1. The half contact width converges to 15.2 mm after the mesh size is reduced to 0.8 mm and below (this is relative to the cylindrical radius of 500 mm). Note (from Table 2) that the theoretical value for the half contact width is 14.88 mm for frictionless contact. Clearly,

further refinement of the mesh is unnecessary, and thus the mesh size of 0.4 mm is mostly adopted. Additionally, the region of contact is safeguarded to always be confined within the refined mesh. Similar mesh convergence processes for the other two material cases have also been done with similar outcomes. The mesh, therefore, can be regarded established for the elastic normal contact.

Table 5-2. Comparisons of contact parameters between theoretical predictions and FEA results for material Case1. The relation, $\sigma_{emax} = p_0/C$, is according to Green [61].

Input	Theoretical Predictions					FEA Results							
P^*	P/L [MN/m]	ω [μm]	b [mm]	p_0 [GPa]	σ_{emax}[GPa]	ω [μm]	%dif	b [mm]	%dif	p_0 [GPa]	%dif	σ_{emax}[GPa]	%dif
0.2	7.75	221	6.65	0.741	0.408	222	0.43	6.98	4.91	0.736	-0.72	0.410	0.56
0.6	23.2	590	11.52	1.28	0.706	591	0.13	11.75	2.00	1.28	-0.39	0.718	1.74
1	38.7	927	14.88	1.66	0.912	929	0.24	14.93	0.36	1.65	-0.16	0.930	2.03

Table 5-3. The half contact width for different mesh sizes in the contact region for a normal load, $P^*=1$, with elastic perfectly plastic model for material Case 1.

Mesh Size in Contact region [mm]	8	4	2	0.8	0.4
Half Contact Width [mm]	16.0	15.7	14.5	15.2	15.2

Now, mesh convergence verification is done also for tangential loading. Under a tangential loading per unit length, $Q/L<\mu*(P/L)$, the contact status is partial slip. At the inception of gross slip, the relative slip distribution (for the situation when the half-cylinder is forced to the right), $s_0(x)$, is given by Eq.5-15. That theoretical result is compared with those obtained from FEA.

Figure 5-4 shows the normalized local sliding distance under $P^*=1$ with $\mu=0.3$ at the inception of the gross slip for different pairs of materials. By inputting the normal load per unit length, P_c/L, the maximum contact pressure, p_0, and the half contact width, b, are obtained by Eqs. 5-2 and 5-3. With the known parameters, p_0, b, E, ν and μ, the sliding distance, $s_0(x)$, is derived by Eq.5-15 and normalized by the critical interference, ω_c. In the FEA model, $P^*=1$ is first applied to the top rigid plate, and then $1*\omega_c$ sliding distance to the "right" is stepwise applied to the top of the half-cylinder (see the stepwise details in [22]). By investigating the contact status during sliding, the gross slip starts at the sliding distance of $0.44*\omega_c$. The local sliding distance, $s_0(x)$, at $0.44*\omega_c$ is then obtained from ANSYS 17.1 as the local sliding distance at inception of the gross slip. The theoretical prediction agrees very well with the FEA results with a maximum difference less than 5% at the edges of the contact for all three cases. Note that Eq.5-15 shows symmetry with respect to x, and the FEA results confirm that behavior. The good agreement also exists for other material cases with different normal loads and different COFs, but for brevity, those results are omitted. With that verification, it is concluded that mesh convergence for elastic contacts is likewise established for tangential loading just as well.

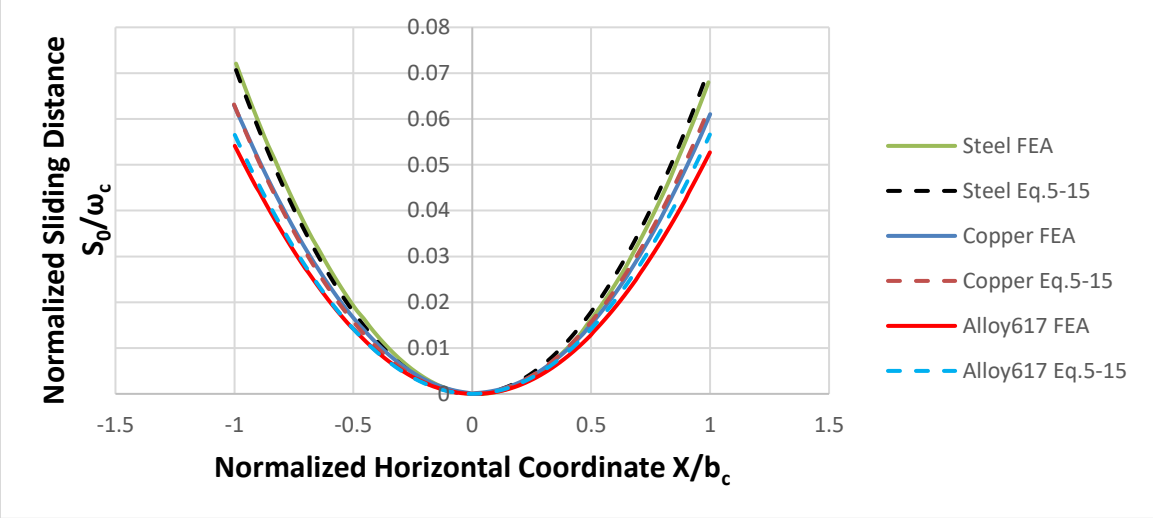

Figure 5-4. The normalized sliding distance at inception of gross slip under $P^*=1$ with $\mu=0.3$ for three material cases.

Note that since there is no closed-form solution for elastic-plastic contacts under the combination of normal and tangential loads, the elements of the mesh are iteratively refined by a factor of two until there is less than one percent difference in the contact width between the iterations.

5.1.3 The initial gross slip distance

In the model of this work, after the normal load P/L is applied, the sliding distance, δ, is applied uniformly to every point on the top of the half-cylinder, as shown in Fig. 5. Before gross slip initiates, the sliding distance, δ, equals to the addition of the deflection of the half-cylinder, δ_1, and the tangential displacement of the stick region, δ_2, while the centerline of the half-cylinder, OA, deforms to O'A'. The deflection of the half-cylinder, δ_1, equals to the deflection of the centerline. The midpoint of the contact region is point, O, which is also the last point in stick just before gross slip starts. The tangential displacement of the stick region, δ_2, equals to the tangential displacement of the midpoint, O, to O', so $\delta_2=\overline{OO'}$.

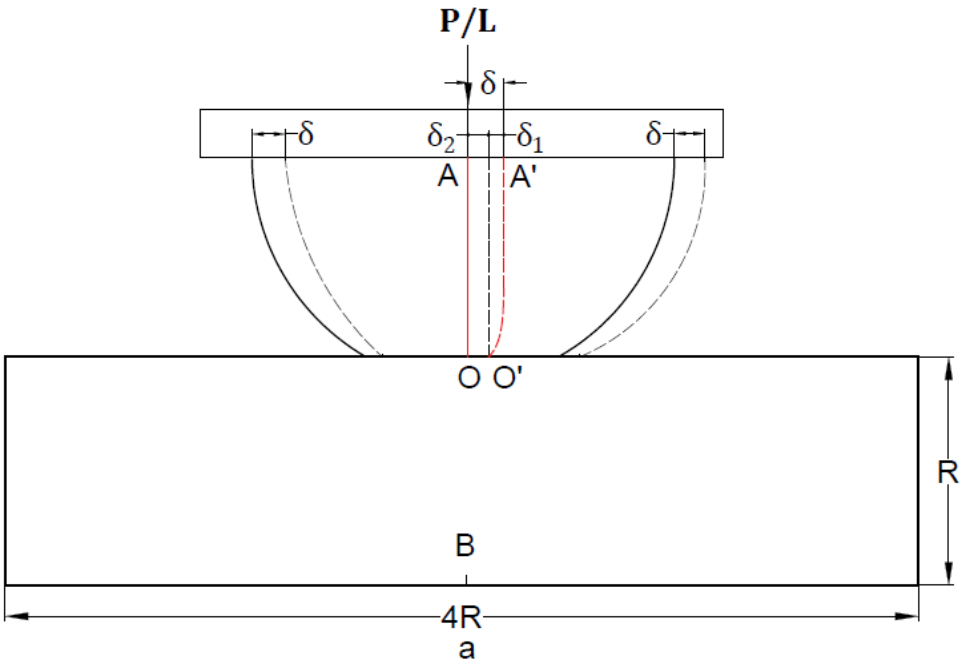

Figure 5-5. The schematic of the sliding distance.

For the frictional contact under partial slip condition, as the sliding distance, δ, increases, the tangential traction, Q/L increases with it. When Q/L=μ(P/L), the onset of gross slip

begins. The corresponding sliding distance is designated to the initial gross slip distance, δ_i. That δ_i varies under different P/L and different COFs. Figure 5-6 shows both the FEA results and theoretical predictions for the evolutions of the normalized initial gross slip distance, δ_i/ω_c, with different P^* and μ for steel/steel. The inset of the figure shows the same results but in linear scale coordinates. The δ_i is shown to be proportional to P/L and μ. A fitting function is found to express δ_i analytically as:

$$\delta_i = 4.78\mu^{1.15}\left(\frac{P/L}{RE}\right)^{0.928} R \tag{5-16}$$

The rationale for this fit form is forthcoming (details are provided below and in the Appendix C).

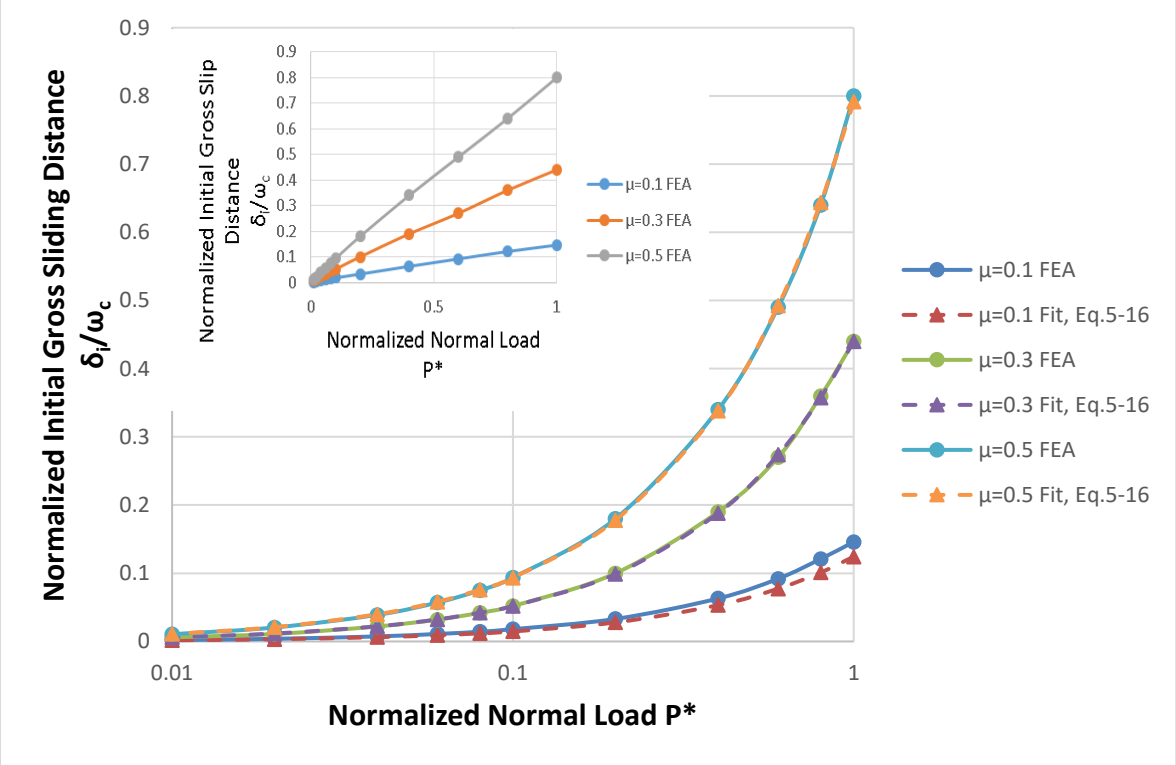

Figure 5-6. The normalized initial gross slip distance under different normalized normal loads with different COFs for the FEA results and fitting functions, Eq.5-16, for steel/steel.

The predicted normalized initial gross slip distance from the fitting function in Eq.5-16 is compared with the results from FEA, as shown in a semi-log scale of Fig.5-6. The normalized load is given in log scale in order to spread the data points at low P^*. The results from the FEA and the fitted function agree well with the maximum difference of less than 5%. Noteworthy, Figure 5-7 shows the dimensional initial gross slip distance under μ=0.3 and different normal loads for three different pairs of material for R=0.5m, and for steel/steel also for three radii R=0.05m, 0.5m, and 5m. The normal load for each material ranges from $0.01*P_c/L$ to $1*P_c/L$. While the three materials are vastly different in material properties as listed in Table1, the results from the FEA and the fitted function agree well with less than 5% difference even when the radii are orders of magnitude different. Therefore, in the foregoing Eq. 5-16 is used to predict the initial gross slip distance.

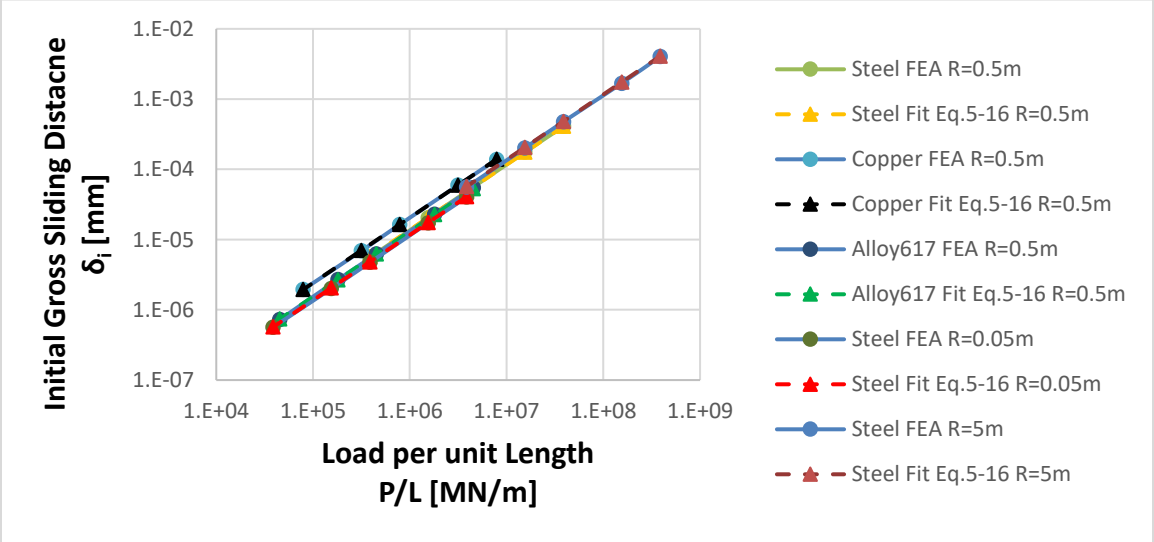

Figure 5-7. The dimensional initial gross slip distance under different normal loads with μ=0.3 for the FEA results and fitting functions results for steel/steel (for R=0.05m, 0.5m and 5m), for Alloy617/Alloy617, and for Cu/Cu (for R=0.5m)

The initial gross slip, δ_i, as given by Eq.5-16, seems nearly linearly proportional to μ and P/L. That is explained in the Appendix C with the Timoshenko beam theory and half-elastic

space loading analysis. The deflection of the half-cylinder, δ_{i1}, where the gross slip initiates is obtained in the Appendix, specifically see Eq. C-8. By nullifying the unknown but small moment on the tips, $M_0/L=0$, the deflection of the half-cylinder can be estimated.

Figure 5-8 shows the deflections of the half-cylinder at the initiation of gross slip from FEA and Eq. C-8 (with M_0/L being neglected as discussed in the Appendix), for $P^*=1$ at three different COFs. While the results from both seem to converge for small COFs, the difference increases with the COFs, which cause larger tangential loads and strains. Recall that the strain-displacement relation in the Timoshenko beam analysis is valid for small strains. Consequently, that is the cause for the discrepancy.

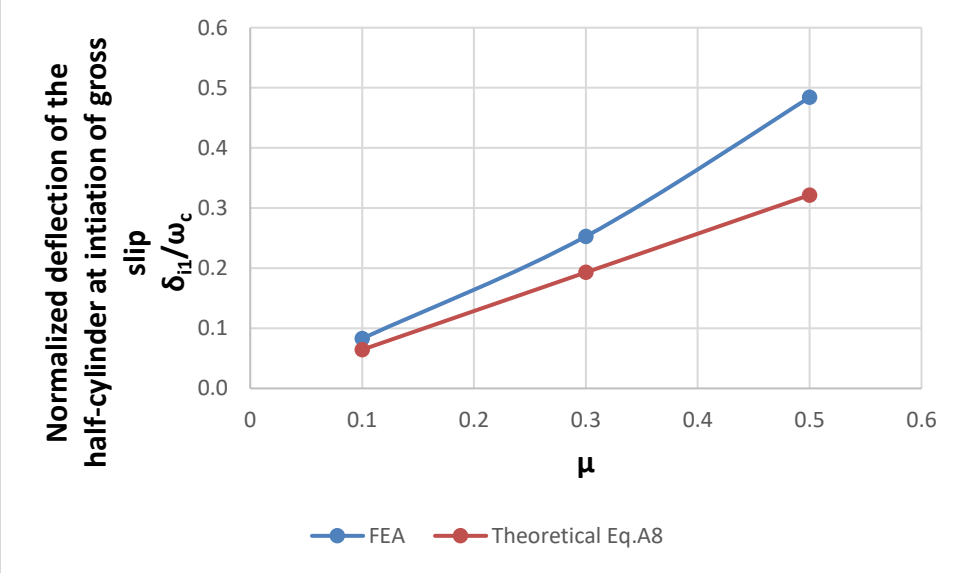

Figure 5-8. The normalized deflections of the half-cylinder at the initiation of gross slip from FEA and Eq. C-8 with for $P^*=1$ at different COFs

The tangential displacement, δ_{i2}, can be estimated by taking the block as a half elastic space and applying the Hertzian distributed tangential traction to the contacting region. The tangential displacement distribution, u(x), on the surface is derived by Eq. C-18. Figure 5-

9 shows the u(x) from FEA and Eq. C-18 at P^*=1 with μ=0.3. The results agree well on the "left" side of the surface with little difference at the contact center. A larger difference appears on the "right" side, since the boundary condition of the right side of the block is free, so the block does not produce sufficient resistance to horizontal deflection. The difference is likewise heightened by ignoring the normal load, p(x), when calculating u(x). Fortunately, though, the tangential displacement, δ_{i2}, is relevant only on the "left" part (x<0) of the surface anyhow. Therefore, the estimation in Eq. C-19 is unaffected by the differences shown in the behavior on the "right" side. Noteworthy, Eq. C-8 and C-19 that estimate δ_{i1} and δ_{i2}, respectively, are nearly linearly proportional to μ and P/L, which provides the rationale for Eq. 5-16. The slight deviation from linearity is caused by the difference in the boundary conditions used in the FEA pitted against the half-space assumption used in the analytical model.

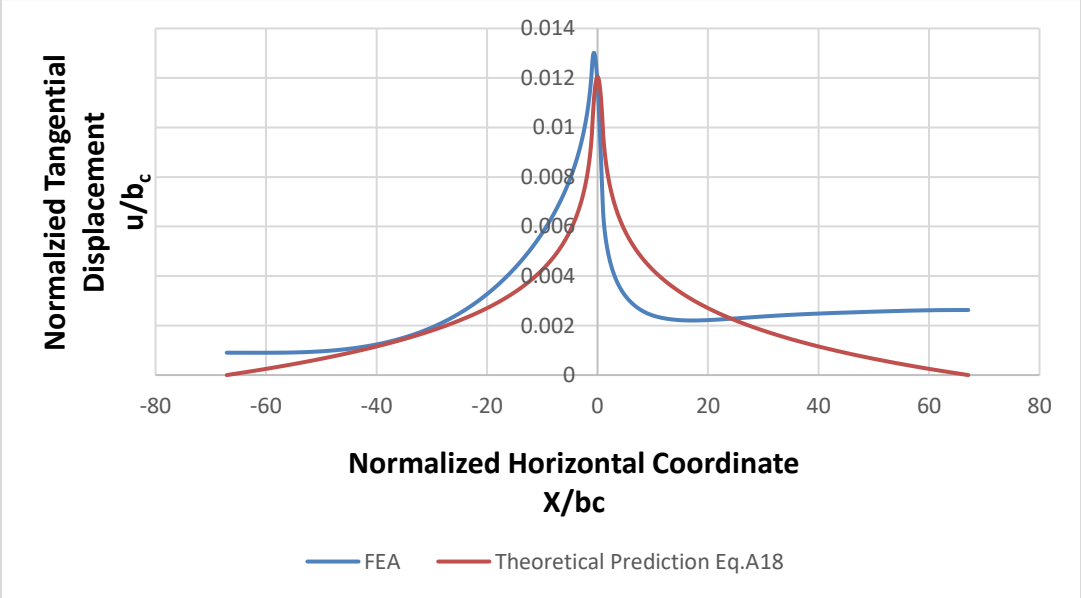

Figure 5-9. The normalized tangential displacement on the surface of the block at P*=1 with μ=0.3 from FEA and half elastic space estimation

5.1.4 The wear volume at initiation of gross sliding

As discussed in section 5.1.1.2, before gross sliding starts, the contact condition is partial slip and partial stick, as shown in Fig. 5-2. The local Archard Wear model is applied to the interface, as given by:

$$v(x) = \frac{K}{H} p(x)s(x) \tag{5-17}$$

Here, only the wear on the half cylinder is considered. The local wear volume per unit area, v(x), is proportional to the dimensionless wear coefficient, K, contact pressure, p(x), and the local sliding distance, s(x), while it is inversely proportional to the hardness, H. Clearly, in reality, wear happens in both the half-cylinder and the block, in which case the wear volume is just twice that of the case for half-cylinder alone, which is true for identical materials being in contact. Had the materials been different, the wear volume would be inversely proportional to the hardness of each material. However, only the wear volume on the half cylinder is reported here. Note that the evolution of the contacting profile due to wear is not considered here because of the low number of cycles. With greater computational power to simulate more cycles, the evolution can be generated.

At the initiation of gross sliding, the local sliding distance is $s(x)=s_0(x)$, as given by Eq. 5-15. The pressure distribution can be approximated by the Hertzian pressure, p(x), as given by Eq. 5-4. The total wear volume at the initiation of gross sliding, V_0, can be derived by integrating Eq. 5-17 over the region in contact:

$$V_0 = \int_{-b}^{b} \frac{K}{H} p(x)s_0(x)dx = \int_{-b}^{b} \frac{K}{H} p_0 \sqrt{1-\frac{x^2}{b^2}} \frac{2(1-\nu^2)\mu p_0}{bE} dx \tag{5-18}$$

The result of the Eq. 5-18 gives the wear volume at the initiation of gross slip, giving:

$$V_0 = \frac{(1-\nu^2)\mu\pi K p_0^2 b^2}{4HE} \tag{5-19}$$

In order to normalize the results, the critical wear volume, V_c, is defined as:

$$V_c = \frac{K_c \omega_c (P_c / L)}{H} \tag{5-20}$$

Herein, the critical wear coefficient is by definition, K_c=1.

Figure 5-10 shows the normalized wear volume at the initiation of gross slip, V_0/V_c, from FEA and Eq. 5-19 at different normal loads and COFs for steel/steel. Since the tangential displacement is applied stepwise, it is hard to pinpoint numerically the initiation of gross slip. However, the two steps changing from partial slip to gross slip are easy to detect. Thus, V_0 in the FEA is decided as the average volume between these two steps. As shown in Fig. 5-10, the results in the FEA and from Eq. 5-19 agree very well with less than 5% difference, which further verifies the theoretical prediction.

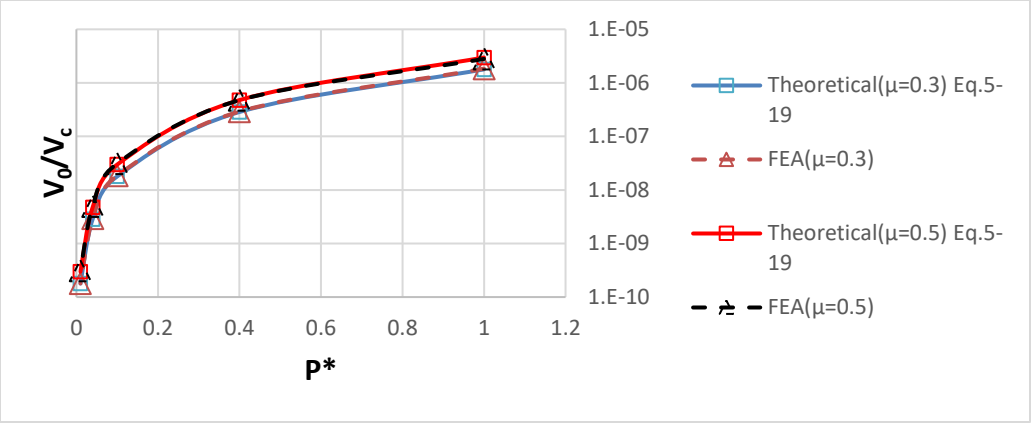

Figure 5-10. The normalized wear volume at the initiation of gross slip, V_0/V_c, from FEA and Eq. 5-19 at different normal loads and COFs with $K=10^{-4}$ for steel/steel.

Figure 5-11 shows the wear volume at the initiation of gross slip, V_0, from FEA and Eq. 5-19 with μ=0.3 now for different material pairs. The normal load for each material ranges from $0.01*P_c/L$ to $1*P_c/L$. The results for the three cases from the FEA and Eq. 5-19 are all in excellent agreement with less than 5% difference, which supports the viability of using Eq. 5-19 for different material pairs.

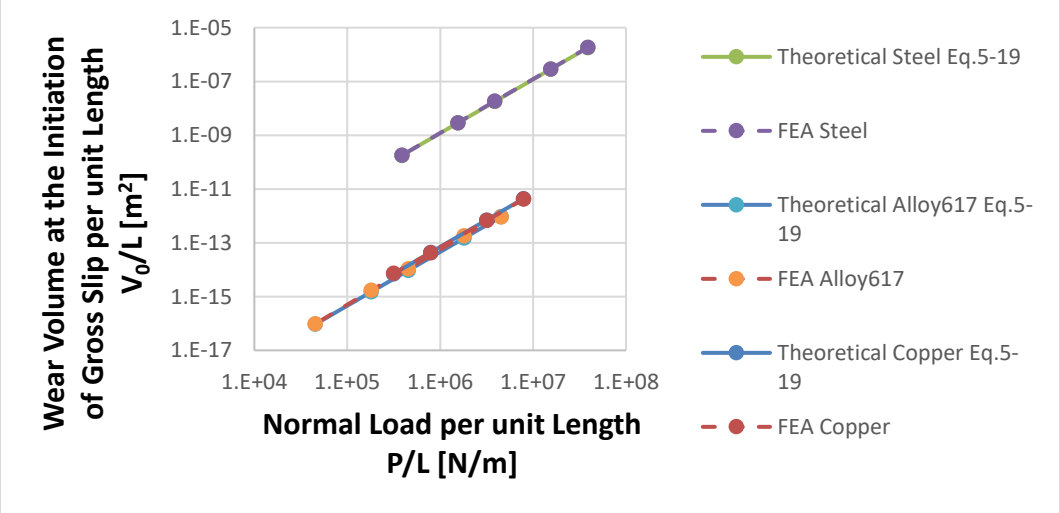

Figure 5-11. The wear volume per unit length at the initiation of gross slip, V_0/L, from FEA and Eq. 5-19 at different normal loads with μ=0.3 for steel/steel, Alloy617/Alloy617, and copper/copper.

5.1.5 Prediction of fretting wear volume under elastic conditions

During the fretting motion, the amplitude of each cycle in the different cases (see Table 5-1) is maintained at $1*\omega_c$. Figure 5-12 shows the typical evolution of wear volume during one cycle of the motion from FEA results at $P^*=1$ with different COFs for steel/steel under elastic conditions. The nominal sliding distance, S_n, represents the cumulative tangential sliding distance applied to the top surface of the half-cylinder, which is different from the local sliding distance at the contact region. It is also different from δ, which is the tangential displacement applied to the top surface of the half-cylinder. For $\mu=0$, the wear volume increases linearly with respect to the nominal sliding distance, and it is a special case for gross slip fretting. For $\mu=0.3$, there are two parts in each direction of sliding (the half-cylinder changes direction at $S_n^*=S_n/\omega_c=1, 3$, etc.). At the beginning, the contact status is partial slip and the wear volume increases slowly. As the half-cylinder displaces further, gross slip starts, and the wear volume increases linearly at the same rate as that in the case of $\mu=0$. For $\mu=1$, the contact status is always partial slip with no gross slip. Thus, the wear volume is thus negligible compared with the other two cases. In this work, the prediction of the wear volume is only done for the case when gross slip condition is reached.

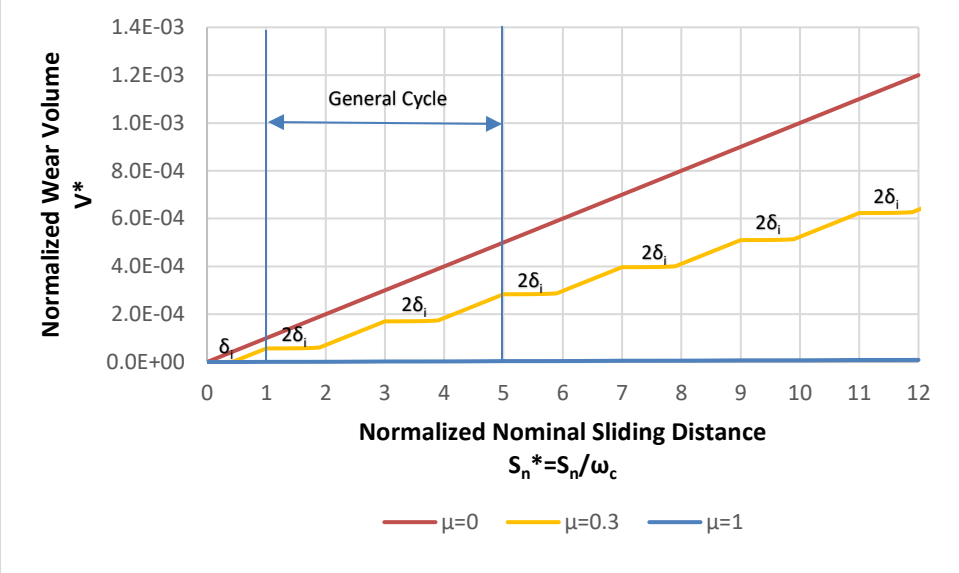

Figure 5-12. The FEA results of the evolution of normalized wear volume during three cycles of fretting motion at P^*=1 for steel/steel in elastic contact.

For the case with μ=0.3 as shown in Fig.5-12, the evolution of the wear volume is periodic after S_n^*=1. Hence, a general cycle is presented in the figure, starting where the half-cylinder is positioned at the rightmost point, i.e., x^*=1 or S_n^*=1, heading back to the leftmost position, i.e., x^*=-1 or S_n^*=5, thus completing a general cycle. Then, the half-cylinder changes motion returning to the rightmost position.

The wear volume for a general cycle is thus analyzed by taking the cycle, S_n^*=1 to 5, for instance. At the beginning of the cycle (S_n^*=1), the half-cylinder is at the rightmost position, x^*=1. Since the half-cylinder is forced to the right before reaching S_n^*=1, its centerline is pre-deflected by a tangential force acting to the right. At the beginning of the cycle, the half-cylinder starts to move to the left. The centerline of the half-cylinder now restores and deforms from the right to the left. As a result, it takes a nominal sliding distance $2\delta_i$ (i.e., $S_n=2\delta_i$) to finish the partial slip condition, with a corresponding wear volume that is $V=2V_0$. As the half-cylinder slides further to the left, gross slip starts, i.e.,

the nominal sliding distance equals to the sliding distance in the contact region, $s(x)=\Delta S_n$. The normalized wear rate, i.e., the slop of the normalized wear volume in Fig. 5-12, for gross slip is:

$$\frac{\Delta V^*}{\Delta S_n^*} = \frac{\int_{-b}^{b} \frac{Kp_0(x)\Delta S_n dx}{H} / \frac{KP_c\omega_c}{H}}{\Delta S_n / \omega_c} = K\frac{\int_{-b}^{b} p_0(x)dx}{P_c} = KP* \qquad (5\text{-}21)$$

Here, $\Delta V^*= \Delta V / V_c$, $\Delta S_n{}^*= \Delta S_n{}^*/\omega_c$.

When the half-cylinder returns back to the right at $x^*=0$ or $S_n{}^*=3$, the second partial slip starts with $V=2V_0$. After that, another gross slip begins with the normalized wear rate given by Eq.5-21. The total wear volume for a general cycle during partial slip condition is thus:

$$V_{partial}^* = 4V_0^* \qquad \delta_i^* < 0.5 \qquad (5\text{-}22)$$

The total normalized nominal sliding distance for the gross slip condition during a general cycle is, $\Delta S_n{}^* =4(1- \delta_i{}^*)$. Then, the total wear volume for the gross slip condition during a general cycle is:

$$V_{slip}^* = \Delta S^* \frac{\Delta V^*}{\Delta S^*} = 4(1-\delta_i^*)KP^* \qquad \delta_i^* < 0.5 \qquad (5\text{-}23)$$

The normalized wear volume for a general cycle of the fretting motion is then the sum of $V^*_{partial}$ and V^*_{slip}:

$$V^* = 4V_0^* + 4(1-\delta_i^*)KP^* \qquad \delta_i^* < 0.5 \qquad (5\text{-}24)$$

If $\delta_i{}^*>0.5$, the partial slip condition will last for the whole cycle, which leads to a very small (negligible) wear volume.

Figure 5-13 shows the normalized wear volume for a general cycle of fretting motion under elastic condition with different normal loads and COFs for steel/steel. The results from FEA and Eq.5-24 agree very well, which further verifies the theoretical predictions. For the case with μ=0.5, the wear volume first increases with the normal load as predicted by the Archard Wear model. However, the wear volume decreases as the normal load further increases, because δ_i^* increases with P^*, which then decreases V^*, as shown in Eq.5-24.

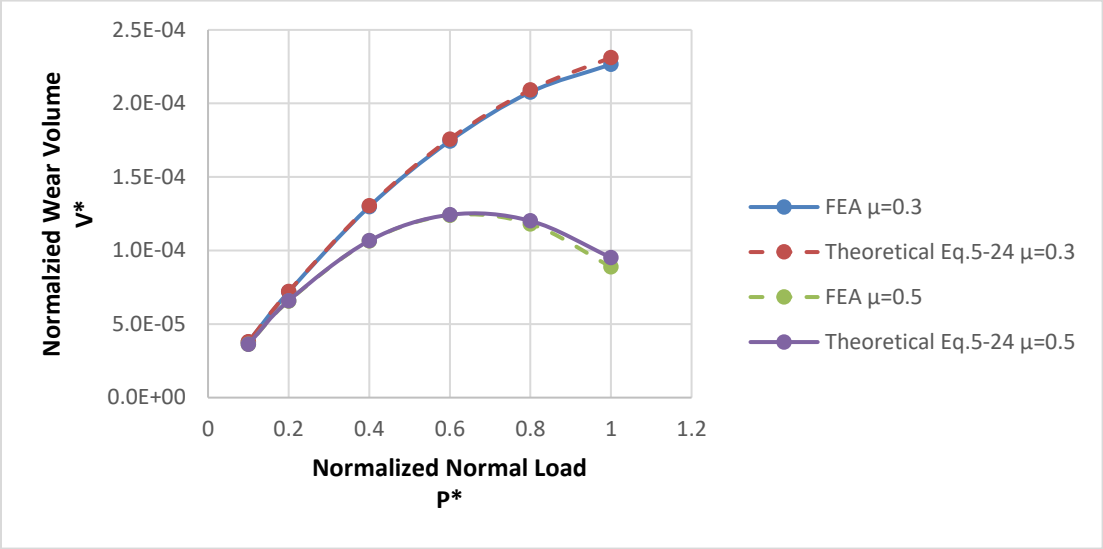

Figure 5-13. The wear volume for a general cycle of fretting motion at elastic condition for different normal loads and COFs, comparing FEA and theoretical predictions for steel/steel (for R=0.5m)

Figure 5-14 shows the results of the wear volume for a general cycle of fretting motion under elastic condition with μ=0.3 under different normal loads, now for three different material cases (see Table 5-1). The results from the FEA and theory are in very good agreement, which further verifies the analytical predictions.

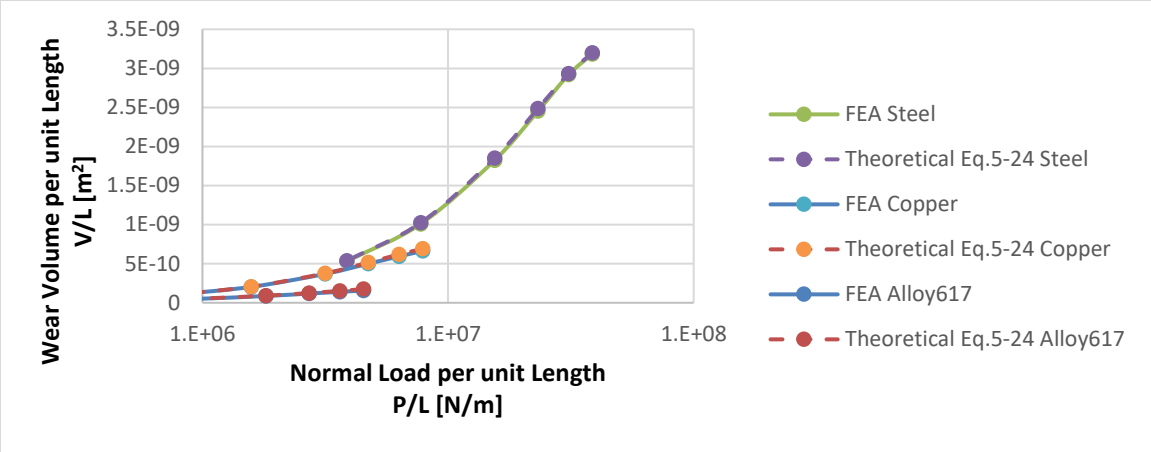

Figure 5-14. The wear volume per unit length for a general cycle of fretting motion at elastic condition with μ=0.3 under different normal loads from FEA and theoretical predictions for steel/steel, Alloy617/Alloy617, and copper/copper (for R=0.5m)

5.1.6 The effect of plasticity

In the previous section, the wear volume is considered for elastic conditions. Here, the elastic perfectly plastic contact model is applied. To find the influence of plasticity on the wear volume, two groups of loading conditions are compared. One is the loading that introduces plasticity, and the other is the same loading but yielding (or plasticity) is disabled (i.e., pure elasticity is open-endedly imposed upon the material in ANSYS 17.1, as it is solved in Section 5.1.3.3). The wear volumes between the elastic and plastic conditions are then compared in Fig. 5-15. Figure 5-15 shows the evolution of wear volume at P^{*}=1 with different COFs under elastic and elasto-plastic conditions. Plasticity appears due to the combined effects of normal and the frictional tangential loadings. The wear volumes under pure elastic conditions are larger than those under elasto-plastic conditions in these two cases. For μ=0.3, there is larger tangential deflection in the elasto-plastic case,

which decreases the gross slip distance and the wear rate during gross slip. Consequently, the wear volume in the elasto-plastic case is smaller. For μ=0.5, the decrease of wear volume in the elasto-plastic condition is dominated by the junction growth effect (see details in [95]). Due to the large COF, higher plastic strains (deformations) are generated at the interface, causing an increase of the contact region, i.e., causing junction growth. The junction growth leads to the partial slip condition at the two limit positions during the fretting motion, which greatly decreases the wear volume.

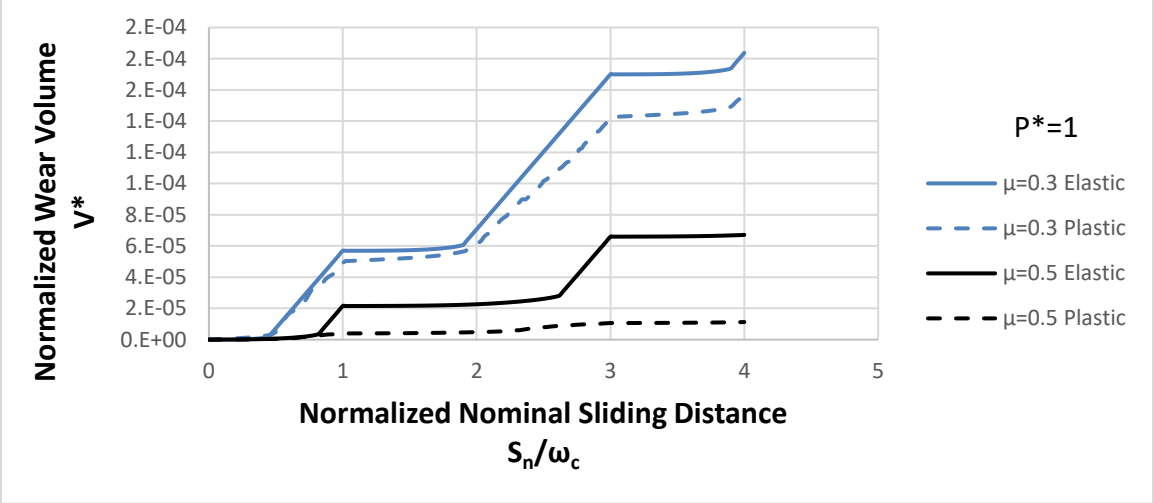

Figure 5-15. The evolution of normalized wear volume at elastic and plastic conditions with different COFs under P^*=1 for steel/steel during one cycle of fretting motion (for R=0.5m).

It should be noted that the wear volumes in elastic cases are not always larger than those in elasto-plastic cases under the same loading conditions. As shown in Fig.5-16, the wear volume at P^*=3 with μ=0.3 is larger in elastic case first, but larger in elasto-plastic case after three-fourth of the cycle that keeps getting larger up to three cycles, which is the largest number of the cycle in the current simulation. Wear is larger in the elastic case first, because plasticity introduces junction growth, which decreases the sliding distance at the

interface with the same amount of nominal sliding distance. It is larger in the elasto-plastic case afterwards because the cross section, A(x), given in Eq. C-3, is getting larger in elasto-plastic contact, which decreases the deflection. Consequently, the sliding distance at the interface is larger with the same amount of nominal sliding distance.

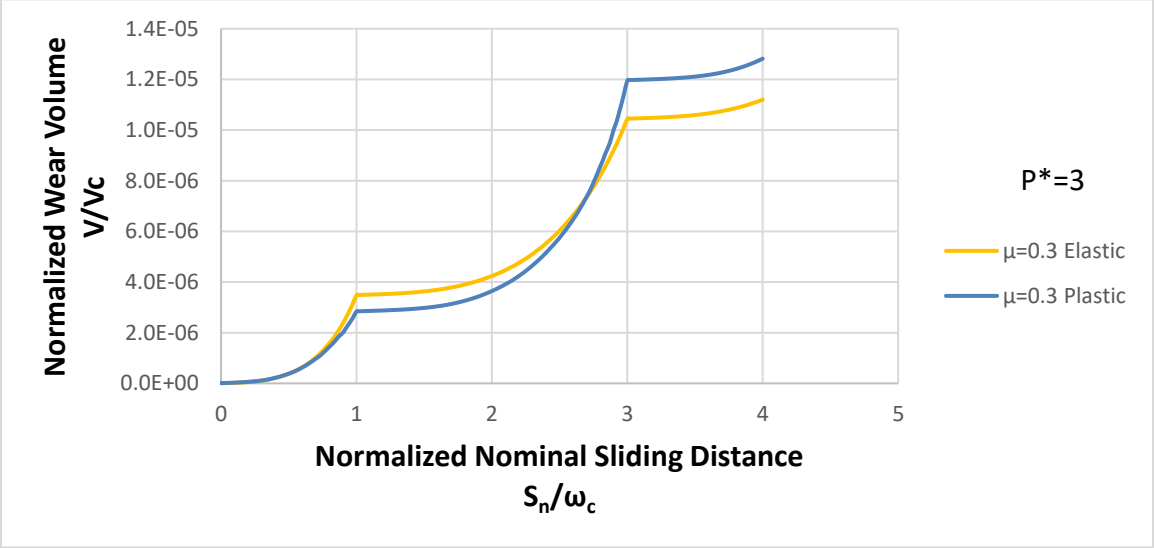

Figure 5-16. The evolution of normalized wear volume at elastic and plastic conditions with μ=0.3 under P^*=3 for steel/steel during one cycle of fretting motion.

5.1.7 Conclusion

A fretting wear model is presented in this work for a cylindrical line contact, under 2D plane strain conditions, for force-controlled in the normal direction and displacement-controlled in the tangential direction. The contact is between identical material pairs. Friction and the Archard wear model are applied at the interface. Three different material pairs are examined by the model. The following are the outcomes:

1.The initial gross slip distance is defined and approximated with the Timoshenko beam theory and line loading of a half elastic space. A fitting function for the initial gross sliding distance is also derived. Both the theoretical approximation and the fitting function agree well with the FEA results.

2. The wear volume at the initiation of the gross slip is derived. Results between the theoretical prediction and FEA are in good agreement.

3. The wear volume under elastic conditions for the first cycle of the fretting motion is derived based on the fitting function of the initial gross sliding distance. The results are in good agreement between the theoretical predictions and the FEA.

4. The effect of the plasticity is analyzed. On one hand, under small normal load plasticity introduces small deflections and junction growth when COFs are large. These two effects decrease the wear volume. On the other hand, under larger normal loads plasticity introduces larger cross sections, which makes the two bodies stiffer to the tangential load. As a result, the deflection decreases, and the wear volume increases.

5.2 Spherical Contact Model

5.2.1 The Archard Wear Model

The model in the spherical wear model is the same as the force-controlled spherical model used in the Chapter 3 and 4. There is a rigid plate on top surface of the hemisphere to keep uniform downward displacement. The interface between the rigid plate and the hemisphere

is set to frictionless. The external normal load is applied on the top surface of the rigid plate, while the reciprocal displacement is applied on the top surface of the hemisphere. The material of the hemisphere and the bottom flat block is first set to the identical material pair: Inconel617/Inconel617, and then set to the dissimilar material pair: Inconel617/Incoloy800H. The material properties are listed in Table 5-4.

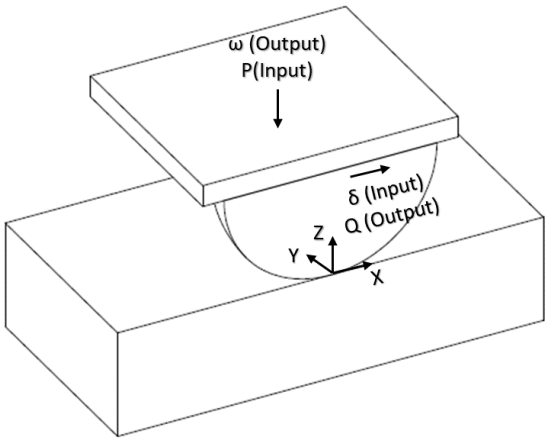

Figure 5-17. Schematic of a ¼ sphere in contact with a flat block for force-controlled steel/steel model.

Table 5-4. The material properties and critical values for two cases [94].

Temperature	Material	Elastic Modulus[GPa] E	Yielding Strength[MPa] S_y	Poisson Ratio ν	C(ν)	$C \cdot S_y$ [MPa]
20°C	Inconel 617	211.0	322	0.3	1.615	520
20°C	Incoloy 800H	196.5	150	0.339	1.662	249

Same as the plane strain cylindrical contact case, an Archard wear model, Eq. 5-24, is used at the contact between the hemisphere and the bottom block. The wear volume, V, is proportional to the normal force P, sliding distance, S, and inversely proportional to the

hardness [21]. The hardness, H, is assumed to equal to 2.8*S_y for each material. The dimensionless wear coefficient K is set to 10^{-4}. The Archard Wear Model is applied locally (i.e., at each nodal point) at the contact region.

$$V = \frac{KPS}{H} \tag{5-24}$$

5.2.1.1 Theoretical Equations for Normal Contact

As derived in Chapter 3, in the regime of static elastic normal contact, the Hertzian theory gives the solution to the 3D spherical contact [11]. The relations between the normal load, P, the contact radius, a, the maximum contact pressure, p_0, the interference, ω, and the pressure distribution, p(r), are given in the following

$$a = \left(\frac{3PR}{4E'}\right)^{\frac{1}{3}} \tag{5-25}$$

$$p_0 = \frac{3P}{2\pi a^2} \tag{5-26}$$

$$\omega = (\frac{\pi p_0}{2E'})^2 R \tag{5-27}$$

$$p(r) = p_0(1-\frac{r^2}{a^2})^{\frac{1}{2}} \tag{5-28}$$

E' is the equivalent elastic modulus:

$$\frac{1}{E'} = \frac{1-\nu_1^2}{E_1} + \frac{1-\nu_2^2}{E_2} \tag{5-29}$$

According to Green [61], the ratio between the maximum pressure and the maximum von Mises stress in normal elastic contact is defined by $C(\nu) = p_o / \sigma_{e-\max}$, where $C(\nu)$=1.30075+0.87825 ν +0.54373 ν^2. The critical contact radius, a_c, the critical load, P_c, the critical interference, ω_c, and the critical elastic strain energy are derive in [61],

$$a_c = \frac{\pi C S_y R}{2E'} \tag{5-30}$$

$$P_c = \frac{(\pi C S_y)^3 R^2}{6E'^2} \tag{5-31}$$

$$\omega_c = \left(\frac{\pi C S_y}{2E'}\right)^2 R \tag{5-32}$$

By substituting the material properties of Table 5-5 in Eq.5-30, Eq.5-31, and Eq.5-32, the said critical parameters are obtained, and are listed in Table 5-5. The critical contact area is calculated based on a_c, $A_c=\pi a_c^2$. These critical values are subsequently used to normalize (i.e., generalize) results within this work.

Table 5-5. The critical values (onset of plasticity) for different material schemes and different temperatures.

Temperature	Cylinder Material	Block Material	Critical Interference ω_c [μm]	Critical Load P_c[kN]	Critical Contact Radius a_c [mm]	Critical Contact Area A_c[mm^2]
20°C	Inconel 617	Inconel 617	24.8	13.472	3.52	38.9
20°C	Inconel 617	Inconel 800H	5.96	1.556	1.73	9.36

5.2.1.2 Theoretical Equations for Tangential Contact

Consider the model in Fig.5-17 under a Hertzian pressure, p(r) (Eq. 5-28), caused by a total normal load, P (Eq. 5-26). A constant friction of coefficient (COF), μ, is applied to the contact when sliding takes place. According to Johnson [11], when the tangential traction, Q< μ*P, the interface experiences partial slip conditions. As shown schematically in Figure

5-18, within the contacting region (-a<x<a), the conditions are stick for [-c, c], and slip between [-a, -c] U [c, a]. The symbol, c, is called the stick half-width.

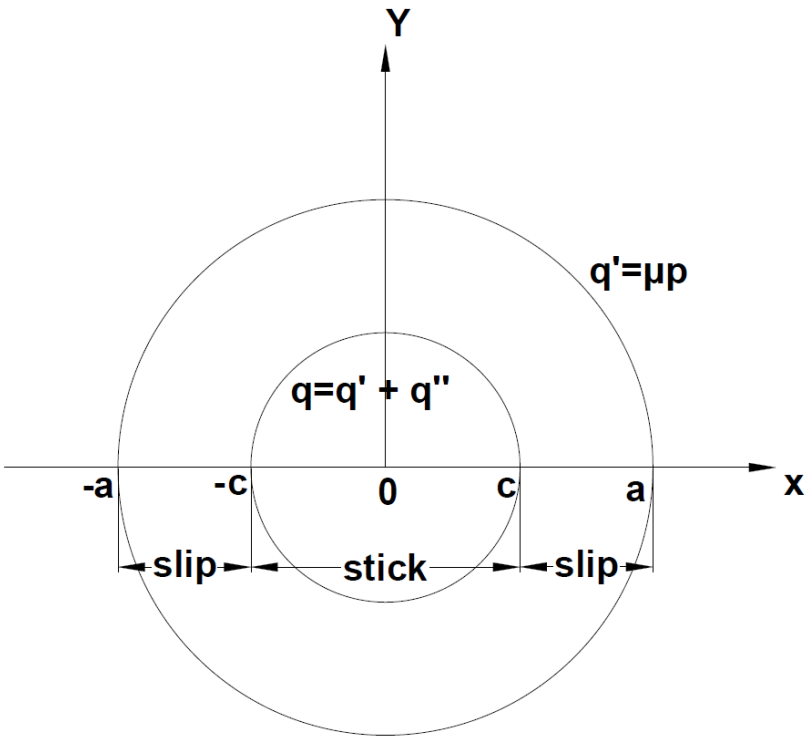

Figure 5-18. The distribution of tangential surface traction of the spherical contact under a tangential force, Q< μP.

In the slip region, the tangential traction is q'(r)=μp(r), where p(r) is the Hertzian pressure given by Eq.5-28. If the q'(r) is applied to the entire contact region, [-c, c], there should be another q''(r) to achieve the stick status for [-c, c], where all the points in the stick region displace uniformly. The distributions of q'(r) and q''(r) are given by Johnson [11],

$$q'(r) = \mu p_0 (1 - \frac{r^2}{a^2})^{\frac{1}{2}} \quad r \le a \tag{5-33}$$

$$q''(r) = -\frac{c}{a}\mu p_0 (1-\frac{r^2}{c^2})^{\frac{1}{2}} \quad r \le c \tag{5-34}$$

Note that q(r)=q'(r) for slip region, and q(r)=q'(r)+q''(r) for stick region. Clearly, the bottom block and the hemisphere always experience the tangential traction in opposite directions. For instance, if the half-cylinder is forced to the "right" (i.e., the positive X direction), in the coordinates of this model the flat block experiences q'(r) and q''(r), while the half-cylinder experiences –q'(r) and –q''(r).

When the tangential force per unit length reaches Q= μP, gross slip starts. In other words, the contact status is slip for the entire range [–a, a], while c=0. The tangential force is maintained at μP at the threshold and during gross slip. By taking the two bodies as two half elastic spaces, the tangential displacement in the X direction on the surface of contact for each body, $\bar{u}_x(x,y)$, within contact is given by Johnson [11],

$$\bar{u}_x = \frac{\pi\mu p_0}{32Ga}\{4(2-\nu)a^2 + (4-\nu)x^2 + (4-3\nu)y^2\} sgn(q(x,y)) \tag{5-35}$$

Where G is the shear modulus of the material, which can be obtained by:

$$G = \frac{E}{2(1+\nu)} \tag{5-36}$$

Hence, in the current coordinates, if the hemisphere is forced to the "right", the tangential displacement of the hemisphere, $\bar{u}_{x1}(x)$, and that of the block, $\bar{u}_{x2}(x)$, are, respectively:

$$\bar{u}_{x1} = -\frac{\pi\mu p_0}{32G_1 a}\{4(2-\nu_1)a^2 + (4-\nu_1)x^2 + (4-3\nu_1)y^2\} \quad r \le a \tag{5-37}$$

$$\bar{u}_{x2} = \frac{\pi\mu p_0}{32G_2 a}\{4(2-\nu_2)a^2 + (4-\nu_2)x^2 + (4-3\nu_2)y^2\} \quad r \le a \tag{5-38}$$

Here, $\bar{u}_{x1}(0,0)$ represents the sliding distance of the last stick point relative to the hemisphere bulk body, while $\bar{u}_{x2}(0,0)$ represents the sliding distance of the last stick point relative to the bottom block bulk body. The local relative sliding distance between the hemisphere and the flat block at the initiation of the gross slip, $s_0(x,y)$, is then derived by

$$s_0(x,y) = (\bar{u}_{x1}(0,0) - \bar{u}_{x1}(x,y)) + (\bar{u}_{x2}(x,y) - \bar{u}_{x2}(0,0)).$$

$$s_0(x,y) = \frac{\pi\mu p_0}{32G_1 a}\{(4-\nu_1)x^2 + (4-3\nu_1)y^2\} + \frac{\pi\mu p_0}{32G_2 a}\{(4-\nu_2)x^2 + (4-3\nu_2)y^2\} \quad (5\text{-}39)$$

For identical material pairs, using the relations, $E=E_1=E_2$ and $\nu=\nu_1=\nu_2$, gives,

$$s_0(x,y) = \frac{\pi\mu p_0}{16Ga}\{(4-\nu)x^2 + (4-3\nu)y^2\} \quad (5\text{-}40)$$

It is again emphasized that this initial gross slip equation is derived for elastic conditions. The mesh convergence procedure of this model in the normal direction Hertzian contact is the same as that in the Chapter 3. The tangential direction mesh convergence can be verified by the comparisons between results from theoretical equations derived in Section 5.2.2 and its corresponding FEA values. For brevity, the mesh convergence procedure for this model is not shown here.

5.2.2 The initial gross slip distance

In the model of this work, after the normal load P is applied, the sliding distance, δ, is applied uniformly to every point on the top of the hemisphere, as shown in Fig. 5-19. Before gross slip initiates, the sliding distance, δ, equals to the addition of tangential displacement of the stick region on the hemisphere, δ_1, and the tangential displacement of the stick region on the bottom block, δ_2, while the centerline of the hemisphere, OA, deforms to O'A'. The midpoint of the contact region is point, O, which is also the last point

in stick just before gross slip starts. The tangential displacement of the stick region, δ_2, equals to the tangential displacement of the midpoint, O, to O', so $\delta_2=\overline{OO'}$.

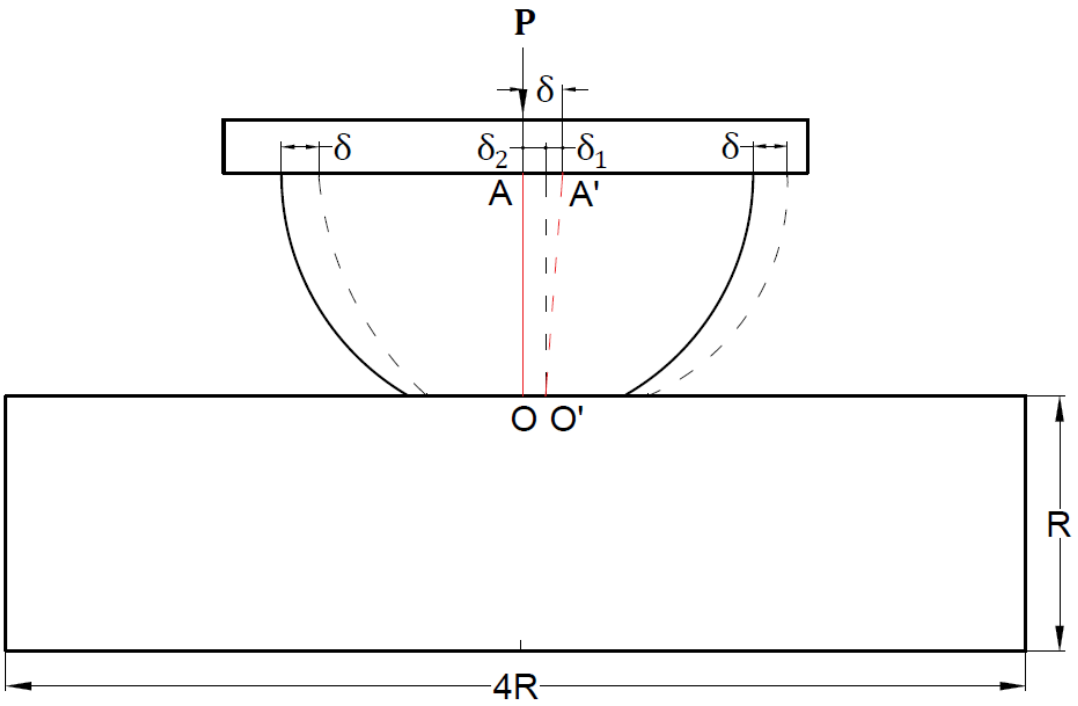

Figure 5-19. The schematic of the sliding distance for the front view of the model.

For the frictional contact under partial slip condition, as the sliding distance, δ, increases, the tangential traction, Q increases with it. When Q=μP, the onset of gross slip begins. The corresponding sliding distance is designated to the initial gross slip distance, δ_i. That δ_i varies under different P/L and different COFs. By taking the two bodies as two elastic space, the tangential displacement of the midpoint can be obtained by Equation 5-35 that:

$$\delta_{i1}=\bar{u}_{x1}(0,0)=\frac{\pi\mu p_0}{32G_1 a}\{4(2-\nu_1)a^2\} \tag{5-39}$$

$$\delta_{i2}=\bar{u}_{x2}(0,0)=\frac{\pi\mu p_0}{32G_2 a}\{4(2-\nu_2)a^2\} \tag{5-40}$$

By adding δ_{i1} and δ_{i2} and substituting Eq. 5-26, the initial gross slip distance can be derived as:

$$\delta_i = \frac{3\mu P}{8a}\{\frac{(2-\nu_1)(1+\nu_1)}{E_1} + \frac{(2-\nu_2)(1+\nu_2)}{E_2}\} \tag{5-41}$$

For identical material pairs, the equation can be further simplified as:

$$\delta_i = \frac{3(2-\nu)(1+\nu)\mu P}{4Ea} \tag{5-42}$$

Figure 5-20 shows the dimensional initial gross slip distance under different normal loads with μ=0.1, 0.3, 0.5 for Inconel 617/Inconel 617. The normal load ranges from 0.01*Pc/L to 1*Pc/L. The results from the FEA and Eq.7 agree well with less than 5% difference.

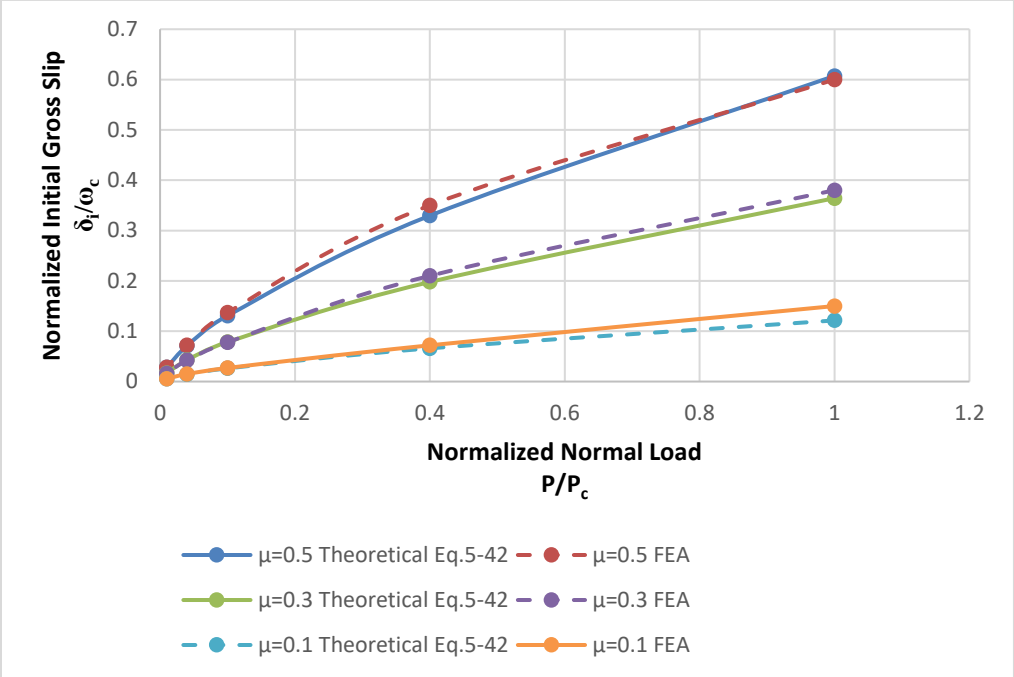

Figure 5-20. The dimensionless initial gross slip distance under different normal loads with μ=0.1, 0.3 and 0.5 for the FEA results and Eq.5-42 results for Inconel 617/Inconel 617

5.2.3 The wear volume at initiation of gross sliding

As discussed in section 5.2.2.1, before gross sliding starts, the contact condition is partial slip and partial stick, as shown in Fig. 5-2. The local Archard Wear model is applied to the interface, as given by:

$$v(x,y) = \frac{K}{H} p(x,y) s_x(x,y) \tag{5-43}$$

Here, only the wear on the hemisphere is considered. The local wear volume per unit area, v(x,y), is proportional to the dimensionless wear coefficient, K, contact pressure, p(x,y), and the local sliding distance, s(x,y), while it is inversely proportional to the hardness, H. Clearly, wear happens in both the half-cylinder and the block, in which case the wear volume is just twice that of the case for half-cylinder alone. This is true for identical materials in contact. Had the materials been different, the wear volume would be inversely proportional to the hardness. Note that the evolution of the contacting profile due to wear is not considered here.

At the initiation of gross sliding, the local sliding distance in the X direction is $s_x(x,y)=s_0(x,y)$, as given by Eq. 5-39. The pressure distribution can be approximated by the Hertzian pressure, p(x), as given by Eq. 5-28. The total wear volume at the initiation of gross sliding, V_0, can be derived by integrating Eq. 5-43 over the region in contact:

$$V_0 = \int_0^a \int_0^{2\pi} \frac{K}{H} p(r,\theta) s_0(r,\theta) r d\theta dr$$

$$= \int_0^a \int_0^{2\pi} \frac{K\mu\pi p_0^2 \sqrt{1-\frac{r^2}{a^2}}}{32aH} \left(\frac{(4-\nu_1)r^2\cos^2\theta + (4-3\nu_1)r^2\sin^2\theta}{G_1} + \frac{(4-\nu_2)r^2\cos^2\theta + (4-3\nu_2)r^2\sin^2\theta)}{G_2} \right) r d\theta dr \quad (5\text{-}44)$$

$$= \frac{K\pi^2\mu p_0^2 a^3}{60H} \left(\frac{2-\nu_1}{G_1} + \frac{2-\nu_2}{G_1} \right)$$

For identical material pair, the wear volume at the initiation of gross slip can be found as:

$$V_0 = \frac{K\pi^2\mu p_0^2 a^3 (2-\nu)}{30HG} \quad (5\text{-}45)$$

In order to normalize the results, the critical wear volume, V_c, is defined as:

$$V_c = \frac{K_c \omega_c P_c}{H} \quad (5\text{-}46)$$

Herein, the critical wear coefficient is by definition, K_c=1.

Figure 5-21 shows the wear volume at the initiation of gross slip, V0, from FEA and Eq. 8 with μ=0.3 now for different material pairs. The normal load for each material ranges from 0.01*Pc/L to 1*Pc/L. The results for the three cases from the FEA and Eq. 5 are all in excellent agreement with less than 5% difference, which supports the viability of using Eq. 5 for different material pairs.

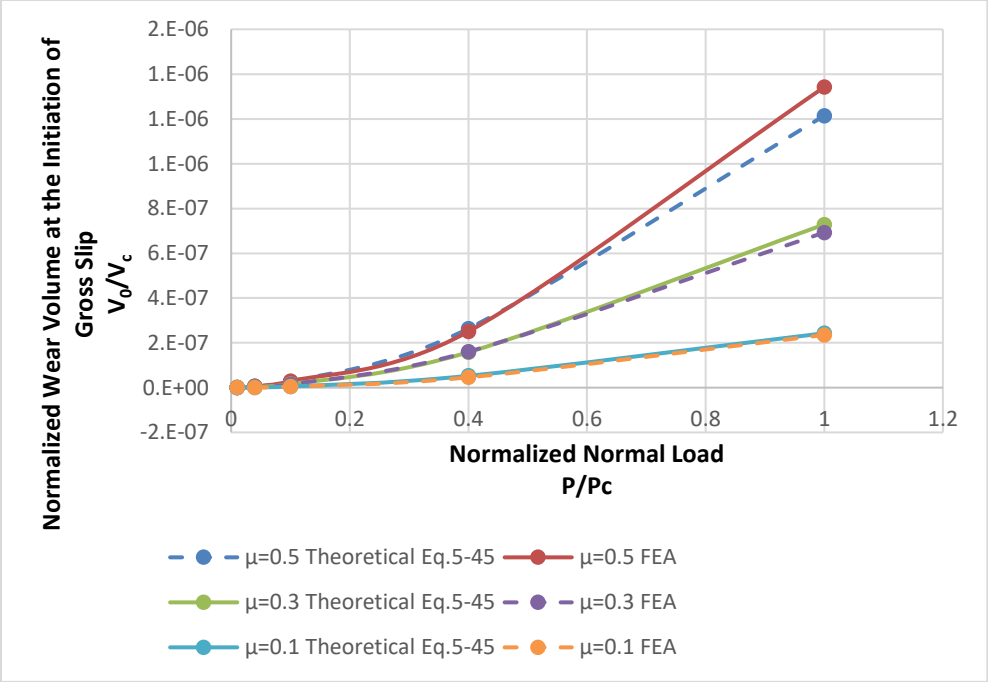

Figure 5-21. The normalized wear volume at the initiation of gross slip, V_0, from FEA and Eq.5-45 at different normal loads with μ=0.1, 0.3 and 0.5 for Inconel 617/Inconel 617.

5.2.4 Prediction of fretting wear volume under elastic conditions

In the spherical contact case, the total wear volume for a general cycle during partial slip condition is the same as that in the 2D case:

$$V^*_{partial} = 4V^*_0 \qquad \delta^*_i < 0.5 \tag{5-47}$$

The total normalized nominal sliding distance for the gross slip condition during a general cycle is, $\Delta S_n^* = 4(1-\delta_i^*)$. Then, the total wear volume for the gross slip condition during a general cycle is:

$$V_{slip}^{*} = \Delta S^{*} \frac{\Delta V^{*}}{\Delta S^{*}} = 4(1-\delta_i^{*})KP^{*} \qquad \delta_i^{*} < 0.5 \tag{5-48}$$

The normalized wear volume for a general cycle of the fretting motion is then the sum of $V^{*}_{partial}$ and V^{*}_{slip}:

$$V^{*} = 4V_0^{*} + 4(1-\delta_i^{*})KP^{*} \qquad \delta_i^{*} < 0.5 \tag{5-49}$$

If $\delta_i^{*}>0.5$, the partial slip condition will last for the whole cycle, which leads to a very small (negligible) wear volume.

Figure 24 shows the results of the wear volume for one cycle of fretting motion under elastic condition with μ=0.1, 0.3 and 0.5 under different normal loads for Inconel 617/Ally617. The results from the FEA and theory are in very good agreement, which verifies the analytical predictions. The difference is relatively large with large COF, which is due to the beam deformation effect. When the COF is large, the friction force is large, which causes the deformation of the hemisphere and block as two beams. As a result, the deformation decreases the actual sliding distance at the interface.

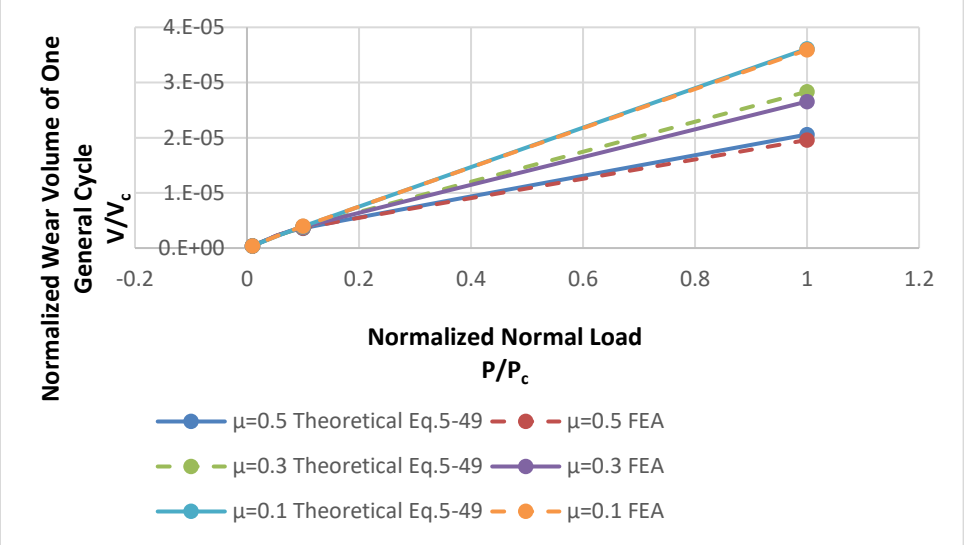

Figure 5-22. The normalized wear volume for a general cycle of fretting motion at elastic condition with μ=0.1, 0.3, and 0.5 under different normal loads from FEA and theoretical predictions (Eq.5-49) for Inconel 617/Inconel 617.

5.2.5 The effect of plasticity

In the previous section, the wear volume is considered for elastic conditions. Here, the elastic perfectly plastic contact model is applied. To find the influence of plasticity on the wear volume, two groups of loading conditions are compared. One is the loading that introduces plasticity, and the other is the same loading but yielding (or plasticity) is disabled (i.e., pure elasticity is open-endedly imposed upon the material in ANSYS 17.1, as it is solved in Section 2.3). The wear volumes between the elastic and plastic conditions are then compared.

Figure 25 shows the wear volume of one general cycle of fretting motion at elastic and plastic conditions with μ=0.3 under different normal loads for dissimilar material pair Inconel 617/Incoloy 800H. The elastic prediction agrees well with the FEA results under elastic condition, while the results under plastic condition is larger than the results in elastic

condition. The increase of the wear volume under plastic condition is due to junction grow effect, which increases the contact area. However, the results between elastic condition and plastic condition are still close to each other.

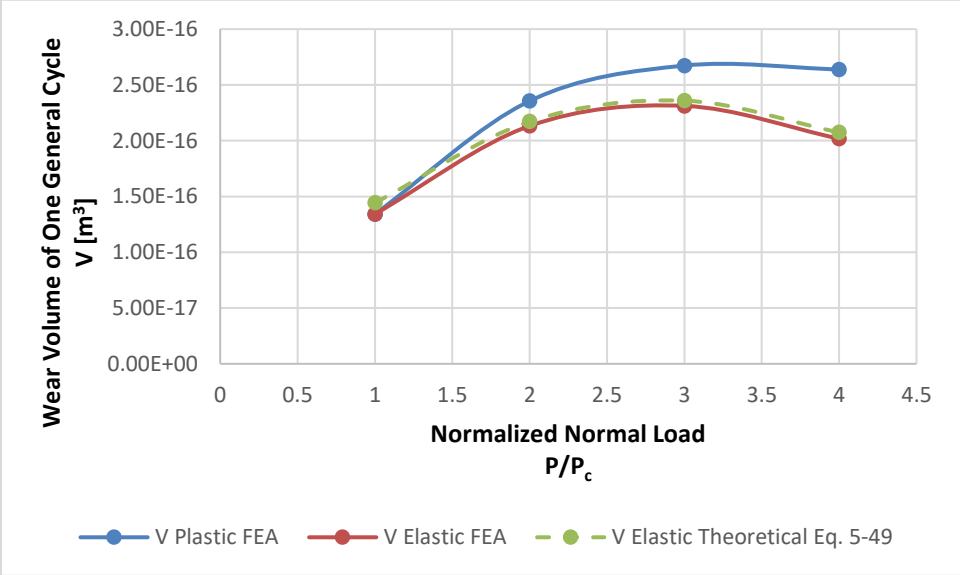

Figure 5-23. The wear volume for a general cycle of fretting motion at elastic and plastic conditions with μ=0.3 under different normal loads from FEA and theoretical elastic predictions (Eq.5-49) for Inconel 617/Incoloy 800H.

5.2.6 Conclusion

In 3D fretting wear model under elastic conditions, the initial gross slip distance, wear volume at the initiation of the gross slip, and wear volume for the one cycle of the fretting motion, are derived. The results are in very good agreement between the theoretical predictions and the FEA. The effect of the plasticity is analyzed. The plasticity introduces junction growth, which increases the wear volume. However, the wear volume between elastic prediction and plastic FEA results are still close.

5.3 Conclusion

In this chapter, the fretting wear model is built in both plane strain cylindrical contact and spherical contact. An Archard wear model is applied at the interface. The contact is only done for identical material pairs in 2D case, since there is an empirical fitting function for initial gross slip distance, which varies for dissimilar material pairs. However, in 3D case, all the equations are derived in analytical solutions. Thus, the spherical contacts are simulated between both identical and dissimilar material pairs.

In 2D fretting model under elastic condition, the initial gross slip distance, wear volume at the initiation of the gross slip, and wear volume for the one cycle of the fretting motion are derived. The results are in very good agreement between the theoretical predictions and the FEA. The effect of plasticity is double edged. On one hand, under small normal load, plasticity introduces small deflections and junction growth when COFs are large. These two effects decrease the wear volume. On the other hand, under larger normal loads plasticity introduces larger cross sections, which makes the two bodies stiffer to the tangential load. As a result, the deflection decreases, and the wear volume increases.

In 3D fretting wear model under elastic conditions, the initial gross slip distance, wear volume at the initiation of the gross slip, and wear volume for the one cycle of the fretting motion are derived. The results are in very good agreement between the theoretical predictions and the FEA. The effect of the plasticity is analyzed. The plasticity introduces junction growth, which increases the wear volume. However, the wear volume between elastic prediction and plastic FEA results are still close.

CHAPTER 6. MITIGATION SCHEME

To mitigate the damage during the fretting motion, two main properties are focused on: plastic strain and wear volume. The plastic strain represents the plastic deformation in the bulk material, which will decrease the life of the component. The wear volume represents the damage at the interface, which will also decrease the life of the component.

6.1 Pre-stress Scheme

As shown in Fig.6-1, in cylindrical contact, before the fretting input (P and δ), the prestressed displacement inputs S_1 and S_2 are applied to two side faces of the bottom block. In this way, the block experiences normal stress in x direction before the fretting load, which, according to definition of von-Mises stress, elevates the hydrostatic situation during the fretting load.

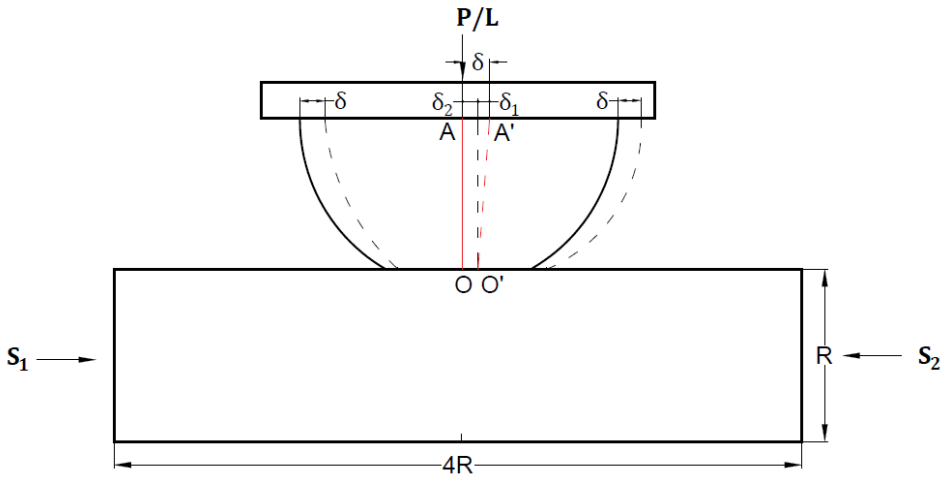

Figure 6-1. The 2D Pre-stress Scheme.

Figure 6-2 shows the distribution of plastic strain at $2P_c$ normal load with different prestress inputs of S_1 and S_2 with μ=0.3 after three cycle of fretting motion. As the prestress input increases from 0 to $6\omega_c$, the plastic strain in the bulk material decreases and then increases. The plastic strain in the bulk material is largest at the centerline when s_1 is small. Thus, the prestress effect elevates the hydrostatic situation, which decreases the plastic strain (Fig.6-2b and Fig.6-2c). There are two reasons for that behavior. Firstly, there is σ_z, which elevates the hydrostatic situation (see Eq. B-1), thus reducing the von-Mises stress. Secondly, the negative σ_x opposes the natural tendency of creating a positive σ_x in the fretting sliding motion, which also reduces the von-Mises stress during sliding. With smaller von-Mises stresses, the corresponding plastic strain is smaller. The compressive pre-stress is envisioned to also suppress any crack initiation and/or growth at the two edges of the fretting contact. However, when s_1 increases, the combined effect of shear stress at the two contact edges and the preloaded stress in x direction starts to dominate in the contribution of plastic strain. Thus, in order to reduce the plastic strain in the bulk material, the prestress input cannot be too small or too large.

Moreover, the application of the prestress aggravates the damage at the interface. As shown in Fig.6-2, the maximum plastic strain always appears at the interface, and it is shown that the maximum plastic strain increases with the prestress input. Since the plastic strain at the interface is a combined effect of frictional shear stress and normal stress, the preloaded stress in the x direction aggravates the shear effect, which increases von Mises stress at the interface.

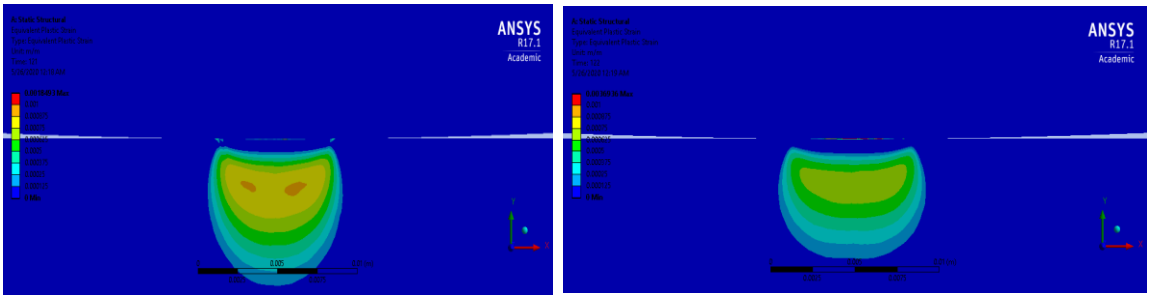

(a) $S_1 = S_2 = 0$ $\varepsilon_{pmax} = 0.0018$ (b) $S_1 = S_2 = 2\omega_c$ $\varepsilon_{pmax} = 0.0037$

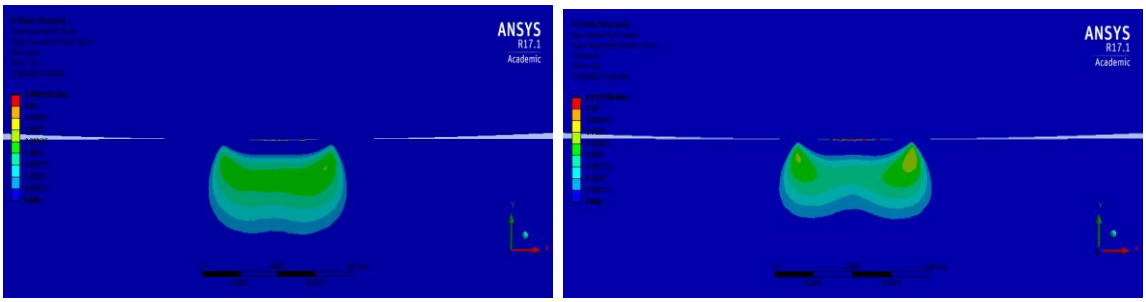

(c) $S_1 = S_2 = 4\omega_c$ $\varepsilon_{pmax} = 0.008$ (d) $S_1 = S_2 = 6\omega_c$ $\varepsilon_{pmax} = 0.015$

Figure 6-2. The distribution of plastic strain at 2Pc normal load with different prestress inputs of S1 and S2 with μ=0.3 after three cycles of fretting motion.

Similar to the 2D case, in the 3D case, the effect of prestress scheme can also be achieved. In the 3D case, the prestresses can be loaded both in the x (left and right) and z (front and back) directions. As shown in Fig.6-3, S_1 and S_2 are inputs in the x direction, while S_3 is in z direction. It should be noted that the front face is kept at z=0 to maintain symmetric condition with respect to X-Y plane.

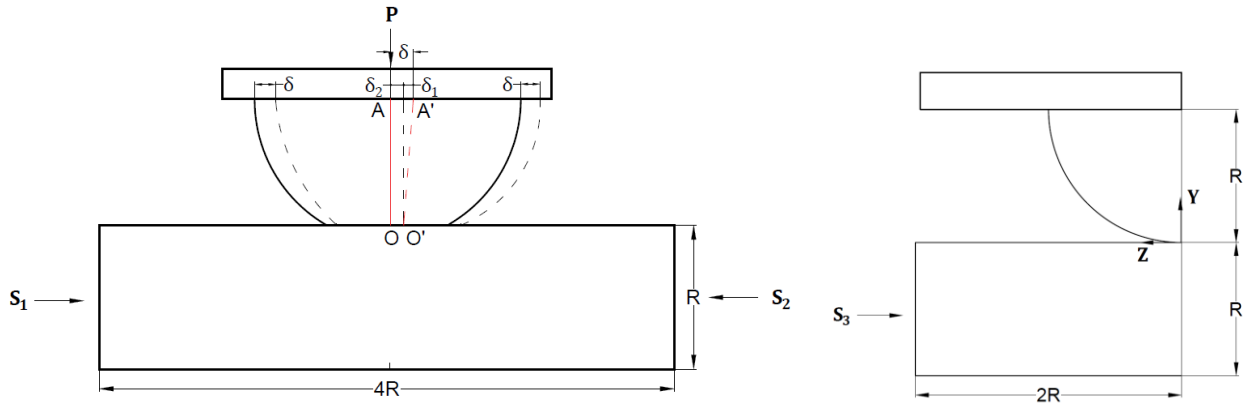

Figure 6-3. The 3D Pre-stress Scheme in X and Z directions.

Figure 6-4 shows the distribution of plastic strain at $1.5P_c$ normal load with different prestress inputs of S_1, S_2, and S_3, with μ=0.3 after three cycles of fretting motion. For the cases with only prestress in x direction (S_3=0), the plastic strain in the bulk material decreases at the centerline when S_1 and S_2 are small (Fig.6-4b), and the plastic strain near the contact edges starts to increase when S_1 and S_2 are large (Fig.6-4c). The application of the prestress in both x and z direction further decreases the plastic strain in the bulk material as shown in Fig.6-4d. However, the plastic strain at the interface in any case with the prestress scheme is larger than that without prestress scheme, which is indicated by the maximum plastic strain.

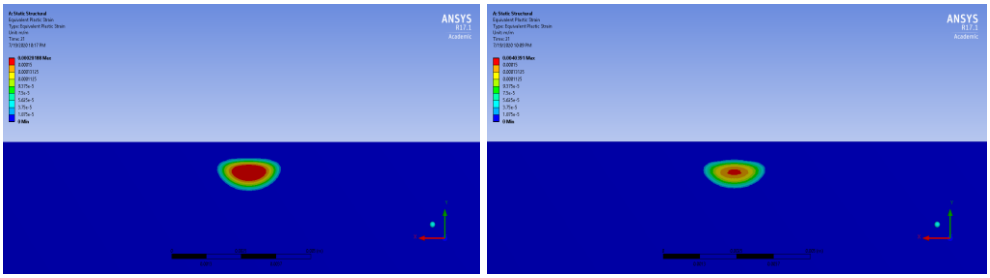

(a) S_1= S_2=0 ε_{pmax} =0.0002 (b) S_1= S_2=1 ω_c ε_{pmax} =0.004

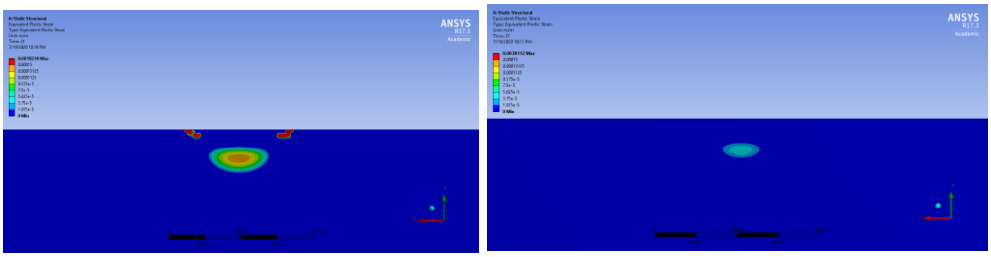

(b) S_1= S_2=1.2 ω_c ε_{pmax} =0.00192 (b) S_1= S_2=1ω_c S_3=2ω_c ε_{pmax} =0.003

Figure 6-4. The distribution of plastic strain at 1.5P_c normal load with different prestress inputs of S_1, S_2, S_3, and S_4, with μ=0.3 after three cycles of fretting motion.

6.2 Wear Volume Mitigation Scheme

In the actual working condition, the normal load can be designed to avoid excessive (or maximum) wear. Suppose that for a certain material pair, the COF is predetermined. As a result, Eq.5-24 (2D) and Eq.5-49 (3D), as derived in this work, can help to determine the worst normal load which would result in the largest wear volume.

As shown in Fig.6-5 and Fig.6-6, the wear volume increases with the normal load first but then it decreases. When the normal load is small, the portion of gross slip is relatively large during the entire range of oscillation. Thus, according to the Archard wear law that the

wear volume is proportional to the normal load, the wear volume for one general cycle increases. When the normal load is large, the portion of stick and partial slip is relatively large during the entire oscillation. Thus, according to the Archard wear law that the wear volume is proportional to the sliding distance, the wear volume for one general cycle decreases.

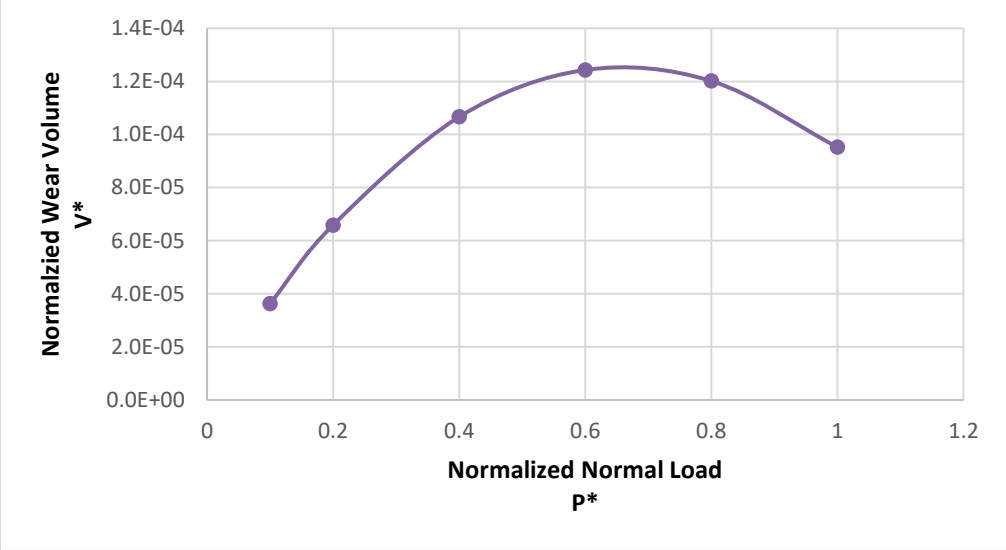

Figure 6-5. Wear volume of one general cycle in 2D cylindrical contact under different normal load with μ=0.5 and 1ω_c fretting magnitude.

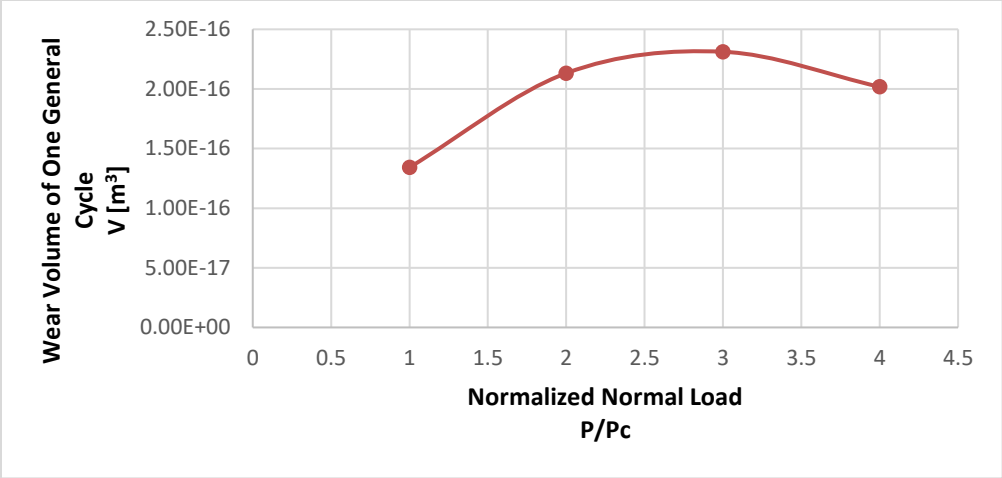

Figure 6-6. Wear volume of one general cycle in 3D spherical contact under different normal load with μ=0.3 and 1ω_c fretting magnitude.

Based on the observation above, the analytical way to obtain the worst normal load, P_w (i.e., the load that causes maximum wear), is to solve the equation dV/dP=0 for P_w. For the 3D case, the dimensionless expression of the wear volume is derived in Eq. 5-49. By taking the derivative of the dimensional expression, the worst normal load, P_w is obtained:

$$P_w = \frac{E_1 E_2 S}{\mu(-E_2\nu_1^2 + E_2\nu_1 - E_1\nu_2^2 + E_1\nu_2 + 2E_1 + 2E_2)} * \sqrt{\frac{6RS(-E_2\nu_1^2 - E_1\nu_2^2 + E_1 + E_2)}{\mu(-E_2\nu_1^2 + E_2\nu_1 - E_1\nu_2^2 + E_1\nu_2 + 2E_1 + 2E_2)}} \tag{6-1}$$

where E_1 and E_2 are elastic moduli, ν_1 and ν_2 are Poisson ratios, μ is COF, R is the equivalent contact radius, and S is the oscillatory sliding magnitude. For similar material pair cases, the P_w can be further simplified to:

$$P_w = \frac{ES}{\mu(-\nu^2 + \nu + 2)} \sqrt{\frac{3RS(\nu - 1)}{2\mu(\nu - 2)}} \tag{6-2}$$

For the 2D case, the dimensionless expression of the wear volume is derived in Eq. 5-24. The worst normal load, P_w, is obtained in a similar manner as above. However, a closed form is not feasible. Hence, P_w can be obtained by solving numerically this equation instead.

$$S - 9.216\mu^{1.15}R\left(\frac{P}{RE}\right)^{0.928} - \frac{2\mu P(\nu^2 - 1)}{\pi E} = 0 \tag{6-3}$$

To verify Eqs. 6-1 to 6-3, the worst normal loads, P_w, that are derived analytically are compared with those obtained numerically for the 2D and 3D cases, Eq.5-24 and Eq. 5-49. The comparison is given in Table 6-1. For instance, in the 3D dissimilar case, the analytical expression for P_w is derived in Eq. 6-1, while the dimensional expression of wear volume is derived by Eq. 5-49. In Eq. 5-49 the expression, V(P), is a function of normal load. Numerically, we find the peak of the wear volume and its location, and hence the worst normal load is obtained. These two P_w numerical values are both 0.0044713 MN. Thus, the analytical expression of P_w is verified. Accordingly based on the results in Table 6-1, Eqs. 6-1, 6-2, and 6-3 are verified.

Table 6-1. The worst normal load P_w table from Eq. 6-1 to Eq. 6-3 and numerically solving dimensional expression of Eq. 5-24 and Eq. 5-49.

	2D (Eq.6-3 and Eq. 5-24)	3D Dissimilar (Eq.6-1 and Eq. 5-49)	3D Similar (Eq.6-2 and Eq. 5-49)
Analytical P_w [MN]	48.446	0.0044713	0.20722
Numerical P_w [MN]	48.445	0.0044713	0.20722

In summary, once the inputs of material properties (E, ν, and μ) and fretting magnitude, S, are determined, P_w can be obtained by Eq. 6-1, Eq. 6-2, or Eq.6-3. From a design point of view, the normal load, P, should be considerably different than P_w, either being much smaller or much larger than the P_w.

6.3 Conclusion

Two mitigation schemes are proposed, prestress scheme and wear volume mitigation scheme. In the prestress scheme, the plastic strain in the bulk material in reduced at appropriate prestress input, and the prestress in both x and z directions can further reduce the plastic strain in 3D case. There are two reasons for that behavior. Firstly, there is σ_z, which elevates the hydrostatic situation, thus reducing the von-Mises stress. Secondly, the negative σ_x opposes the natural tendency of creating a positive σ_x in the fretting sliding motion, which also reduces the von-Mises stress during sliding. With smaller von-Mises stresses, the corresponding plastic strain is smaller. The compressive pre-stress is envisioned to also suppress any crack initiation and/or growth at the two edges of the fretting contact. However, the prestress condition aggravates the plastic strain at the interface both in 2D and 3D cases. For engineering purposes, pre-compressed conditions may be achieved locally at the contact also by shot peening. In the wear volume mitigation scheme, the worst normal load can be solved numerically based on Eq. 6-1, Eq. 6-2, or Eq.6-3. From a designer's point of view, the normal load should be either much less or much larger than the P_w.

CHAPTER 7. SPHERICAL ADHESION FRETTING MODEL

The model in this chapter is developed to investigate the adhesion effects between a deformable hemisphere and a rigid flat surface under fretting conditions. The material for the deformable body is gold (that is commonly used in electrical contacts). The adhesion effect is considered to generate force and traction in the normal and tangential directions. The normal direction adhesion is based on the classic JKR model, while the tangential resistant traction is generated by applying tuned bilinear elastic springs (defined later) at the interface. An effective "friction" emerges via a hysteretic loop as generated by the adhesion effect combined with an oscillatory tangential loading. The model is robust and insensitive to the mesh settings in the FEA. The results include the distribution of von-Mises stress, plastic strains, and the tangential traction. Only pure adhesion effects are applicable at the interface where no other contrived conditions (e.g., "sticking," or a "coefficient of friction") are ever artificially imposed. Also, the emphasis here is on building the model and methodology. While results are indeed presented for a specific material and an application (electric contact), because of the extreme simulation run times, an exhaustive parametric study is not undertaken (that may be left for a future study). Also, wear is currently excluded (but aspects of such modeling can be found in chapter 5 and also in [93]).

7.1 The Adhesion Model

As shown in Fig. 7-1, the fretting arrangement in this work is for a non-conforming contact between a hemisphere and a rigid flat block. The coordinate system X-Y-Z is shown in Fig.7-1, where the origin is located at the center contact point at the bottom of the

hemisphere. The mechanical model is symmetric with respect to the X-Y plane. Hence, to reduce the computational effort, the model is simplified to a quarter sphere pressed against a rigid flat block. Adhesion has effects in both the normal and tangential directions. The Tabor parameter [73] is calculated based on the parameters shown in Table 7-1, $\mu_T=[(16R\gamma^2)/(9E'^2z_0^3)]^{1/3}=31$. The Tabor parameter is much larger than 1, which indicates the contact condition is more suitable for JKR model rather than the DMT model. Thus, in the normal direction, adhesion is based on the JKR model [71]. In the tangential direction, the resistance traction is based on the maximum shear stress theory and the surface free energy. The interface between the hemisphere and the rigid bottom block is set to be frictionless. However, due to the presence of the adhesion effect in tangential direction, tangential traction is generated during the transverse fretting motions.

The loading condition is force-controlled in the Y direction, and displacement-controlled in the X direction. In order to keep a uniform vertical displacement at the top surface of the hemisphere constant, a rigid flat plate is added there. The interface between the top rigid flat plate and the hemisphere is likewise frictionless. An external force, F, is applied at the top surface of the rigid plate. While keeping this external force fixed, a reciprocal horizontal displacement, δ, is applied to the top surface of the hemisphere to simulate the fretting motion.

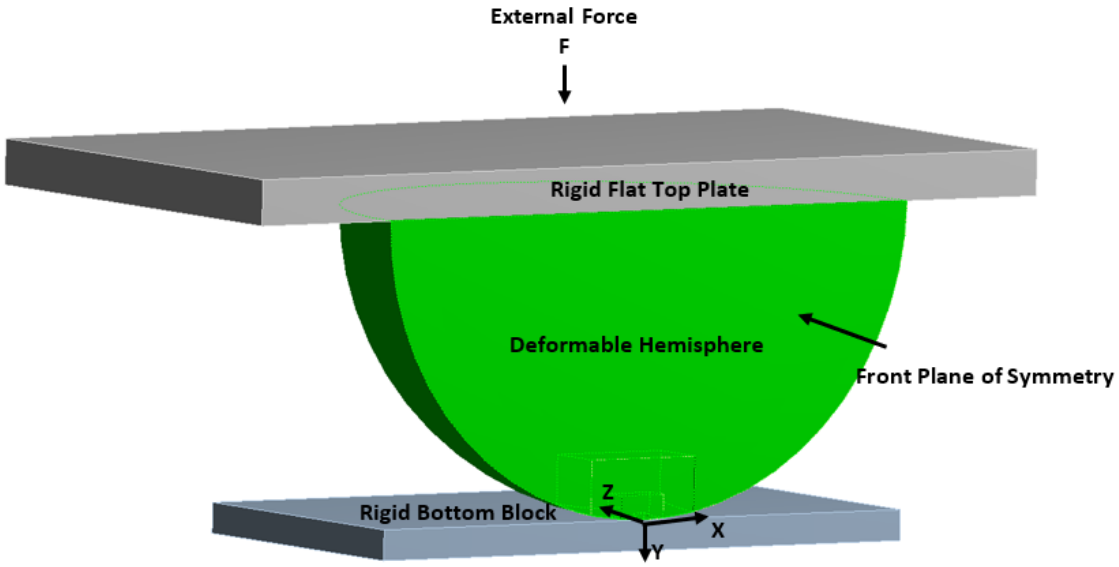

Figure 7-1. Fretting model built in ANSYS 17.1

A reciprocal horizontal displacement, δ, is applied by discrete loading steps at the top of the deformable hemisphere, with a behavior shown in Fig. 7-2. It takes 40 steps to finish one cycle of the fretting motion. The amplitude of the motion is either 15 or 20 nm. The top surface of the hemisphere starts from the state as shown in Fig.7-1, which is designated as position "A" in Fig.7-2. Next, the hemisphere is forced to displace to the furthest position in the positive direction of the X-axis, which is recorded as position "B". Then the hemisphere turns back to the original position, and that is recorded as position "C". As it moves further backwards, the hemisphere reaches the furthest point in the negative position of X-axis, which is recorded as position "D". Finally, the hemisphere turns back to the original position, which previously was designated as point "A." That is the start of the next fretting cycle. So, A_1 indicates the beginning of the first cycle, while A_2 indicates the beginning of the second cycle, etc.

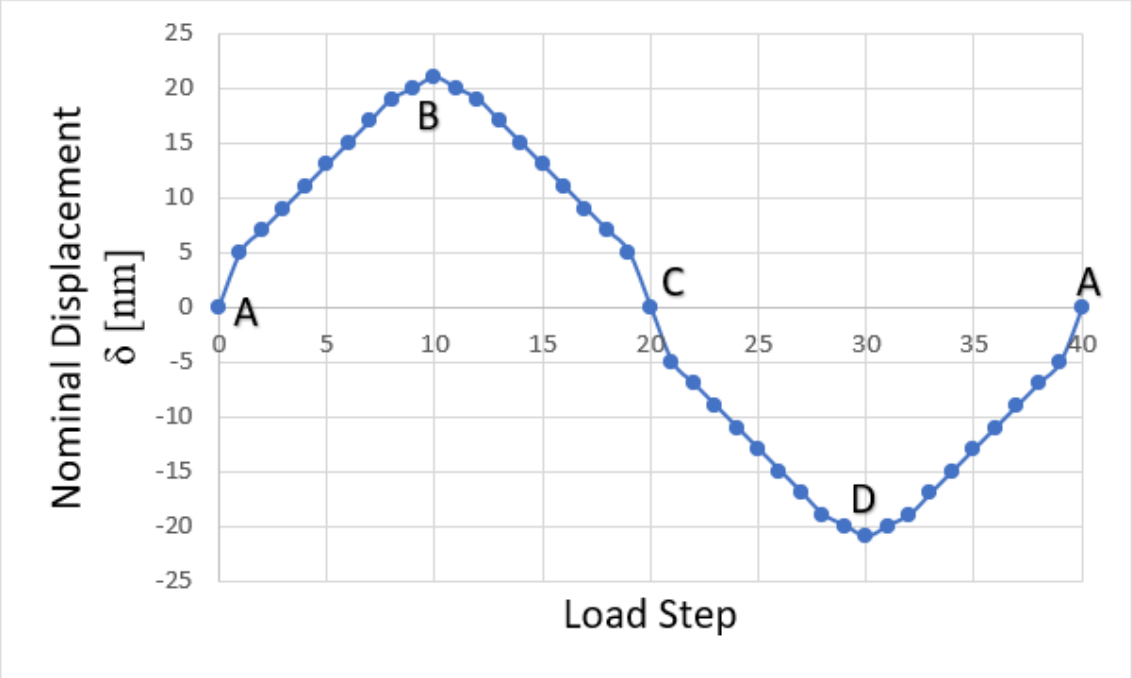

Figure 7-2. Loading steps on the top surface of hemisphere for cycle of fretting motion

According to the JKR model (see [71]) , the external force, F, is related to the other parameters by:

$$F = \frac{4E'a^3}{3R} - \sqrt{8\pi a^3 \Delta\gamma E'} \tag{7-1}$$

The parameters *a* and *R* represent the contact and the hemisphere radii, respectively. The adhesion energy, $\Delta\gamma$, equals to two times of the surface free energy, $\Delta\gamma=2\gamma$. The equivalent elastic modulus, E', is expressed by:

$$\frac{1}{E'} = \frac{1-\nu_1^2}{E_1} + \frac{1-\nu_2^2}{E_2} \tag{7-2}$$

where E_1 and E_2 represent the elastic moduli of the two contacting bodies, and ν_1 and ν_2 represent their Poisson ratios. When the surface free energy is of no practical significance,

setting $\Delta\gamma=0$ in Eq. 7-1 reveals the classical Hertzian solution for a forced normal contact between a hemisphere and a flat. The explicit expression of the contact radius, a, is derived from Eq.7-1 to be:

$$a = [\frac{3R}{4E'}(F + 3\Delta\gamma\pi R + \sqrt{6\Delta\gamma\pi RF + (3\Delta\gamma\pi R)^2})]^{\frac{1}{3}} \tag{7-3}$$

The pressure distribution at the interface is also given by Johnson *et al.* [71]:

$$p(r) = p_{Hertzian} + p_{adhesion} = \frac{2aE'}{\pi R}(1-\frac{r^2}{a^2})^{\frac{1}{2}} - \sqrt{\frac{2\Delta\gamma E'}{\pi a}}(1-\frac{r^2}{a^2})^{-\frac{1}{2}} \tag{7-4a}$$

where specifically,

$$p_{adhesion} = -\sqrt{\frac{2\Delta\gamma E'}{\pi a}}(1-\frac{r^2}{a^2})^{-\frac{1}{2}} \tag{7-4b}$$

The pressure, p(r), consists of a positive Hertzian pressure and a negative adhesion pressure. The positive Hertzian pressure is caused by the elastic deformation of the interface, while the negative adhesion pressure is caused by the adhesion effect in the normal direction.

To include the JKR model in the current finite element model, $p_{adhesion}$ is added in the normal direction nodal-wise. As shown in Fig.7-3a, a local adhesion force is applied to each node at the bottom surface of the sphere. At a certain input of the external force, F, the contact radius, a, is calculated by Equation 7-3. For each node, i, having the coordinates (x_i, y_i), the local radius is $r_i = (x_i^2 + y_i^2)^{1/2}$. By applying the local radius of the node, r_i, the contact radius, a, the material properties, and the geometrical parameters, the negative local adhesion pressure is calculated by Eq.7-4b. Thus, the local adhesion force in the normal

direction can be calculated by the product of local adhesion pressure and the area of the mesh element, ΔA.

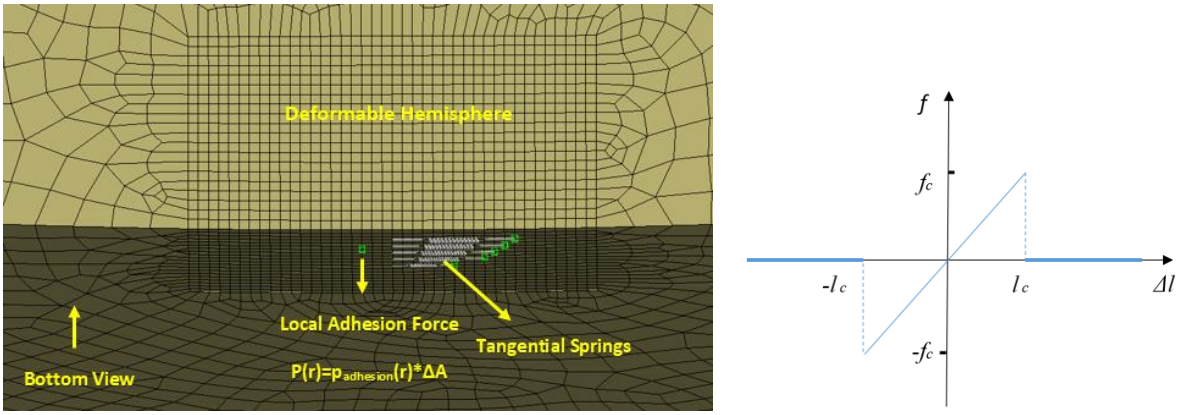

(a) Normal and tangential adhesion effects (b) A bilinear tangential spring

Figure 7-3. Adhesion effects applied at the bottom surface of the sphere.

The effect of tangential resistance can be achieved by applying bilinear springs in the X-direction. As shown in Fig.7-3b, the bilinear spring behaves as a linear spring within the elongation limitation ($-l_c$, l_c), but exerts zero force outside of that range. Principally, the spring "breaks" or "snaps-back" at the limits of $|l_c|$. Therefore, in the model, for each mesh element at the bottom surface of the hemisphere, an interfacial tangential spring is attached. Only elements that are at the contacting interface shall contain bilinear springs; one spring end is linked to a node on the hemisphere, while the other end is linked to an inertial point, i.e., at bottom rigid plate. One spring represents one tangential resisting element. The deactivation of the tangential resistant element is achieved by the "breakage" of the spring (where its internal force "snaps" to zero). The definition of the surface free energy is the energy that is required to create one surface per unit area[97]. Thus, the elastic energy stored in the spring when the spring breaks is equal to the product of the adhesion energy, $\Delta\gamma=2\gamma$ (where two new surfaces are created), and the area of the contact element,

$$\frac{1}{2}kl_c^2 = \Delta A \Delta\gamma \tag{7-5}$$

The parameter, k, represents the tuned spring stiffness, and the parameter, l_c, indicates the corresponding limitation of the elongation at breakage, see Fig.7-3b. The spring "breaks" when the elongation exceeds l_c, at which instant a surface is created by the energy released from the spring. Additionally, the tangential stress of that local element when each spring breaks equals to the shear strength of the material, S_{sy}. The tangential force is then:

$$kl_c = S_{sy}\Delta A \tag{7-6}$$

where based on the Tresca failure criterion, $S_{sy}=S_y/2$, and S_y is the yield strength of the material (in the current case, it is that of gold).

By combining equations 7-5 and 7-6, the stiffness and limitation of the elongation of each spring can be expressed by:

$$l_c = \frac{2\Delta\gamma}{S_{sy}} \tag{7-7}$$

$$k = \frac{S_{sy}{}^2\Delta A}{2\Delta\gamma} \tag{7-8}$$

The material of the sphere is gold [76], properties of which are listed in Table 1. The pull-off force, F=-Fc, is the external force needed to part the adhesive contact (i.e., in the negative y-direction), and is given by [71]:

$$F_c = \frac{3}{2}\Delta\gamma\pi R \tag{7-9}$$

The value of F_c is also provided in Table 7-1. A small strain hardening of 1% of the elastic modulus is used in the finite element simulation to expedite convergence, which is discussed in the following.

Table 7-1. The model geometry, pull off force, and material properties of gold for the model [76].

Parameter	R [mm]	E[GPa]	γ [J/m^2]	S_y [MPa]	ν	Z_0 [nm]	S_{sy} [MPa]	F_c [mN]
Au	1	80	0.5	670	0.42	0.184	335	0.471

7.2 Mesh Convergence for the JKR Model

Figure 7-4 shows the model built using the commercial software ANSYS 17.1. A quadratic 3D solid mesh element is used. The model consists of 125,608 mesh elements. The "no separation/penetration" condition is applied to the interface between the deformable hemisphere and the frictionless rigid top plate. That condition means the two contacting surfaces can freely move relative to each other along their interface, but they cannot penetrate each other or be parted. Likewise, frictionless contact conditions are applied to the interface between the deformable hemisphere and the rigid bottom plate. There, however, adhesion takes effect. A Xeon computer with 32 GB of memory using four threads of parallel computing is used to simulate the fretting cases with a maximum duration case of 97 hours.

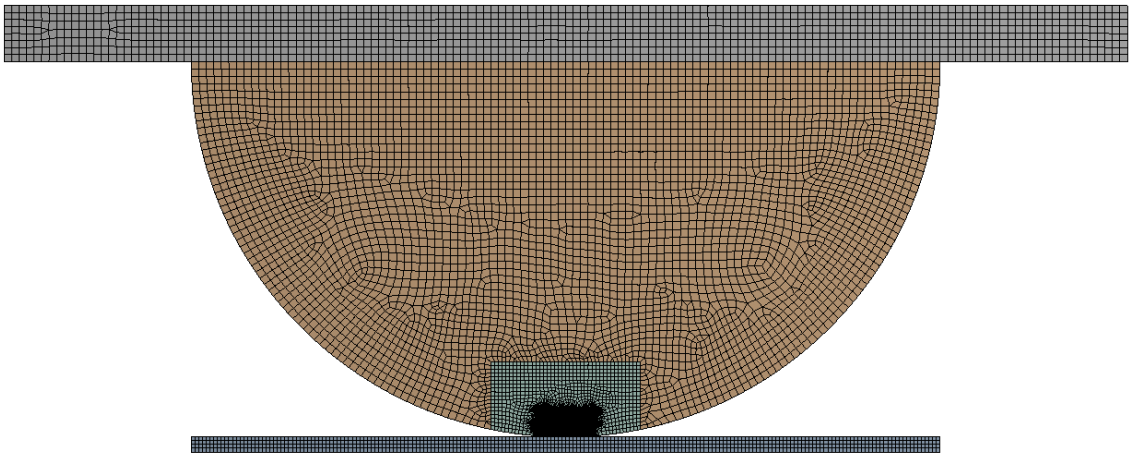

Figure 7-4. The mesh model and its refinement in ANSYS 17.

Convergence of the model is mostly influenced by the number of contact elements at the interface between the deformable hemisphere and the rigid bottom plate. The mesh at the interface had been increased successively until the difference between the contact areas at two mesh refinements is smaller than 2%. As shown in Fig.7-5, the evolution of the contact area increases with the number of contact elements, subject to an external force that equals to the magnitude of pull-off force. Beyond 100 contact elements the changes in the contact area are slight, so it is determined that 400 contact elements (which is used throughout) are adequate.

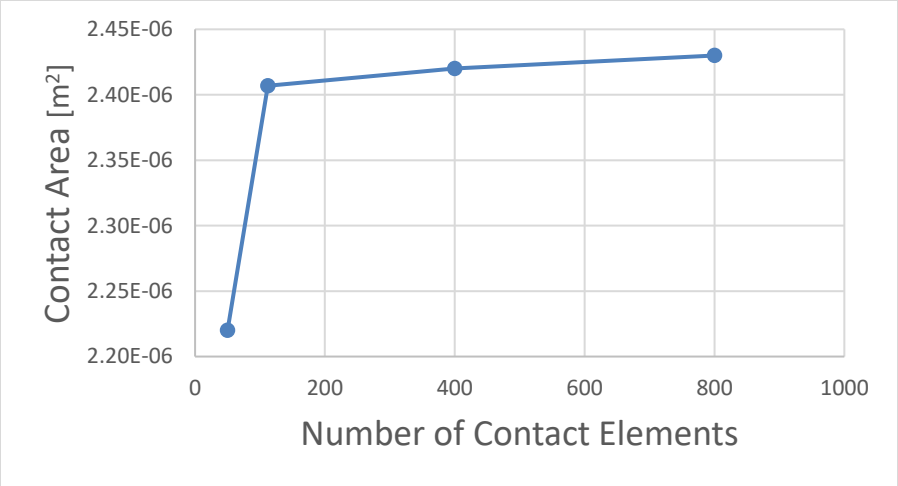

Figure 7-5. The evolution of contact area with different number of contact elements.

By applying the strategy of 400 contact elements, Figure 7-6 shows the theoretical contact radius from Eq.7-3 and the numerical contact radius from FEA as a function of external forces ranging from –Fc to Fc. The difference between the contact radii from the two different methods is less than 3%. The good agreement further indicates that the results at the current meshing level have converged and are satisfactorily accurate.

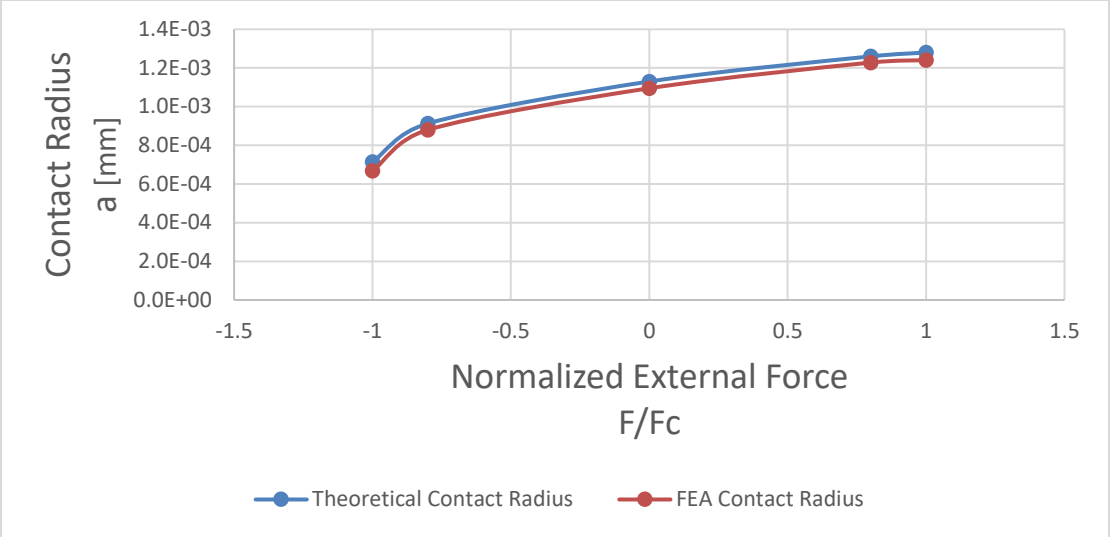

Figure 7-6. The contact radii, a, from Eq.7-3 theoretically and FEA at different normalized external forces, F/F_c

7.3 Results with Only Normal Adhesion

The model is first applied with only normal adhesion, using the classic JKR model and F=0 (i.e., only adhesion is in effect at the contact). The FEA-based JKR model is applied as shown in Fig.7-3a, as described above. Henceforth, if not mentioned specifically otherwise, the additional external normal force is implied to be zero. As given by Equation 7-4, the pressure is positive when the point is close to the center (the local radius, r, is close to zero). The pressure is negative when the point is close to the edge (the local radius, r, is close to the contact radius, a). At the contact edge, the local radius, r, equals to the contact radius, a, which leads to the theoretical pressure to approach a value of negative infinity (as implied by Eq. 7-4). Figure 7-7 shows the pressure distributions at the centerline of the contact (x=0) for both the theoretical JKR model, Eq.7-7, and the finite element model built herein. The results are in very good agreement, except at the center point (z=0) and the edge (z=a). When the point is close to the center, there is an ANSYS programming modeling issue

where a nodal force cannot be assigned to a point at the symmetric front plane. This issue leads to the slight difference at or near z=0. When the point is close to the edge, the theoretical pressure tends to negative infinity. Since the model is discretized by finite mesh elements, the actual value input to the model is also finite, which leads to the difference at or near z=a. In general, however, the pressure distribution shows very good agreement between the theoretical and numerical model, which further verifies the said FEA model.

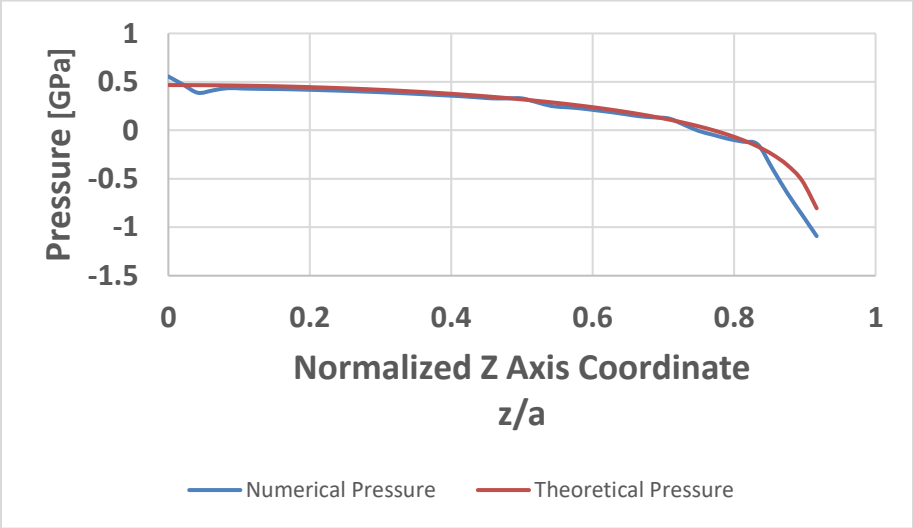

Figure 7-7. The pressure distributions at the centerline (x=0) vs. z for the theoretical JKR and the FEA models for F=0.

The von-Mises stress distribution at the interface is shown in Figure 7-8. Since the magnitude of the negative pressure at the edge is relatively large (theoretically it tends to infinity, see Eq.7-4b), the von-Mises stress is also relatively large at the contacting edges. The regions in red represent points whose stresses are at or slightly larger than the yield stress (because of the small strain hardening), which means that plasticity takes place there. However, for the most part of the interface, the deformation is elastic. This concludes the verification of the model.

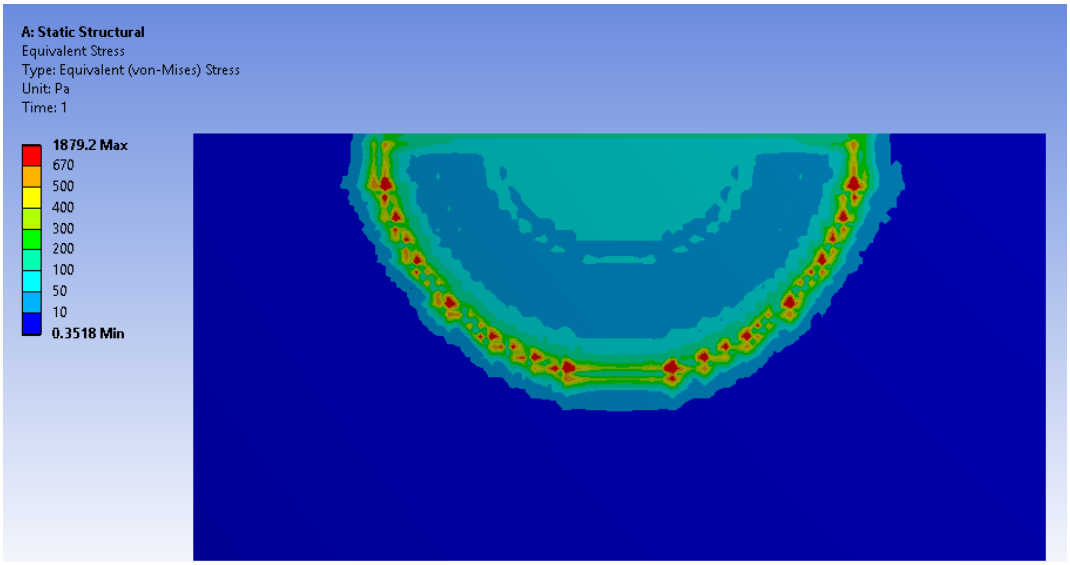

Figure 7-8. Von-Mises distribution for normal direction model.

7.4 Results with Normal Adhesion and Tangential Resistance

First, the hemisphere is subjected to normal adhesion (as is the case in the JKR model). Then tugging in the tangential direction is imposed (the classical JKR model is not applicable when that happens). Tangential resistance is established by the said interfacial bilinear springs as discussed previously in Section 7.2. In this section, the external force is either F=0 or F=Fc. The detachment of the contact element is achieved by the "breakage" of the spring, i.e., its elongation surpassed l_c (see Eq. 7-7). When that happens, the work that is done upon the spring (i.e. strain energy stored) equals to the surface free energy multiplied by the area of the mesh element. The force that the spring exerts equals to the shear strength multiplied by the area of the mesh element. Due to the oscillatory behavior of the fretting motion, the elongation of spring will start to decrease after the hemisphere reaches the rightmost or leftmost position (position B and D in Fig.7-2). After breakage,

when the spring elongation returns to the range (-lc,lc) (Fig. 7-3b), reattachment of the spring takes place.

The nominal tangential displacement, δ, is defined as the transverse displacement applied to the top surface of the hemisphere in the X-direction. Figure 7-9 shows a typical trend of the evolution of the tangential force with the increase of the nominal tangential displacement, δ. For the pure elastic case, with the increase of δ, the spring forces at the interface increase linearly without breakage. Once one of the springs' length reaches the breakage limitation, the spring breaks, which represents the detachment of the local contacting elements. That reduces the number of springs that support the tangential force, causing the force that each spring needs to hold to increase. That generates an avalanche of springs breakage.

However, when plasticity is introduced into the model, as the von-Mises stress reaches the yield strength of the material, the model structure-wise becomes more flexible. The relative displacement at the interface is larger, which allows the springs not to reach the breakage limitation all at the same time. In this situation, some springs break first, while others break later, which makes the springs breakage more gradual. Since the springs do not break simultaneously, the largest tangential traction that the model generates is somewhat smaller than that of the purely elastic case. As shown in Fig.7-9, although the breakage is gradual, the breakage in the elasto-plastic case is still avalanching only when it passes the largest tangential force the springs can support, as determined by the following concept. Assume that all springs break at the same instant at the interface. According to Equations 7-7 and 7-8, the force that each spring generates at breakage limitation, f_c, is:

$$f_c = kl_c = S_{sy}\Delta A \tag{7-10}$$

The total number of springs at the interface is:

$$N = \frac{\pi a^2}{\Delta A} \tag{7-11}$$

Then, the total maximum tangential traction that the springs can generate is:

$$F_{x,\max} = Nf_c = S_{sy}\pi a^2 \tag{7-12}$$

The maximum tangential force, $F_{x,max}$, at zero normal external force based on Eq.7-12 is also shown in Figure 7-9. It is close to the $F_{x,max}$ in the elastic and elasto-plastic case, which further corroborates the model. Additionally, the theoretical F_c should be a physical value for a certain external normal force. In other words, $F_{x,max}$ should not be influenced by the mesh size, the stiffness, or the breakage limitation of the springs. As implied by Eq.7-12, this is indeed true for the current model, as it is apparent from Fig. 7-9.

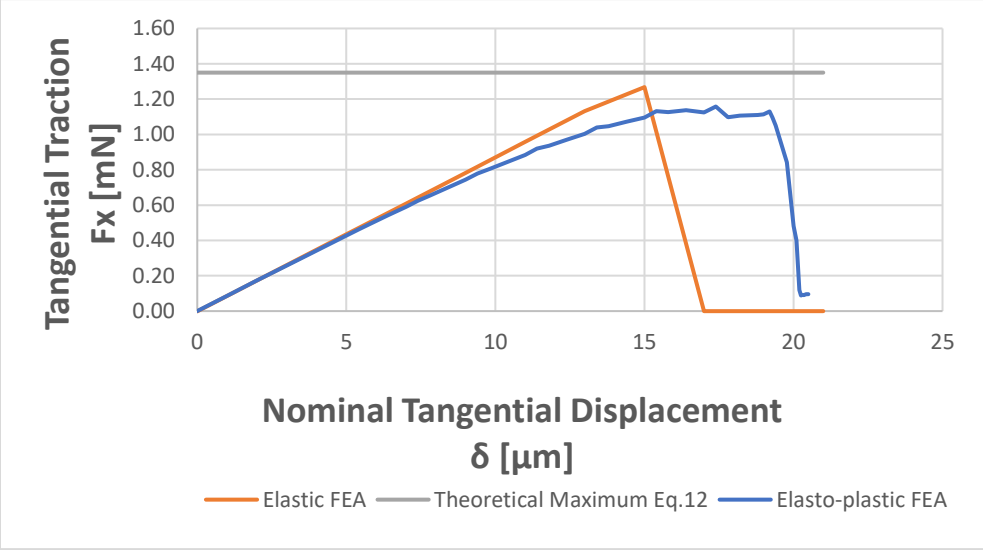

Figure 7-9. The evolution of the tangential force with respect to the nominal tangential displacement during unidirectional sliding.

The tangential resistant traction also affects the distribution of the von-Mises stress. Figure 7-10 shows the distribution of von-Mises stress at the interface just before the breakage of the springs at the interface. The regions in red represent elements where the von-Mises stress is larger than the yield strength of gold (670 MPa). As seen, the von-Mises stress is large over a significant interfacial area indicating plasticity. That is now examined via the equivalent plastic strain, shown in Fig. 7-11.

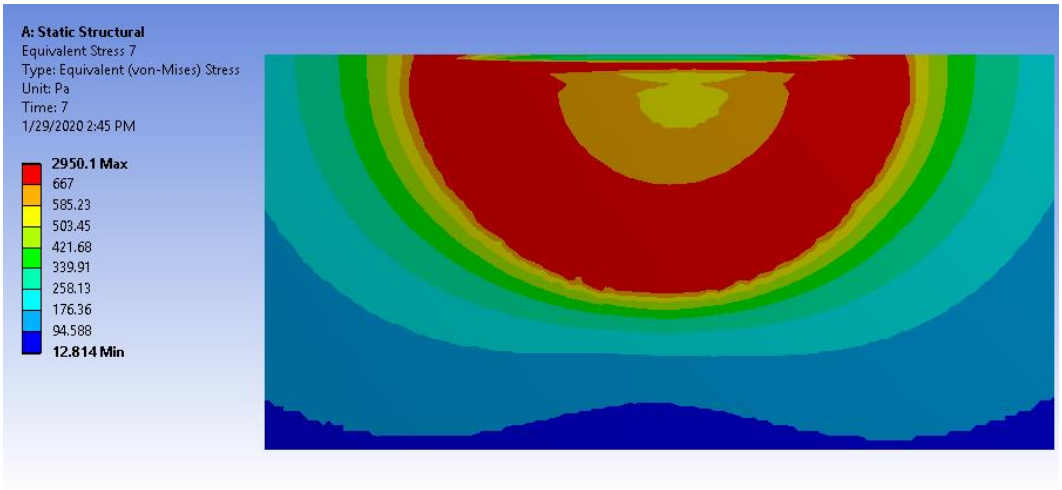

Figure 7-10. The distribution of the von-Mises stress of the hemisphere at the interface (y=0) at the breakage of the springs for the normal and tangential directions adhesion after one cycle of fretting motion. Motion is in the positive X direction, while Z is the transverse direction, F=0, delta=20 nm

Since the tangential resistant traction increases the von-Mises stress at and near the contacting edges, larger equivalent plastic strains are present there, too. Figure 7-11 shows the distribution of the equivalent plastic strains at the interface after one cycle of fretting motion. The magnitude of the tangential displacement is 20nm that guarantees to be large enough so that the hemisphere passes the position where all the springs break. While the classical normal direction JKR model only generates plasticity within a tiny part at the contacting edges, the combination of the normal and tangential direction adhesion model

generates plastic strains that nearly encompass the entire interface. This behavior occurs also when the external normal load takes any value in the range between -Fc and Fc. Thus, normal adhesion and tangential resistance produce an interface that is predominantly in the elasto-plastic state.

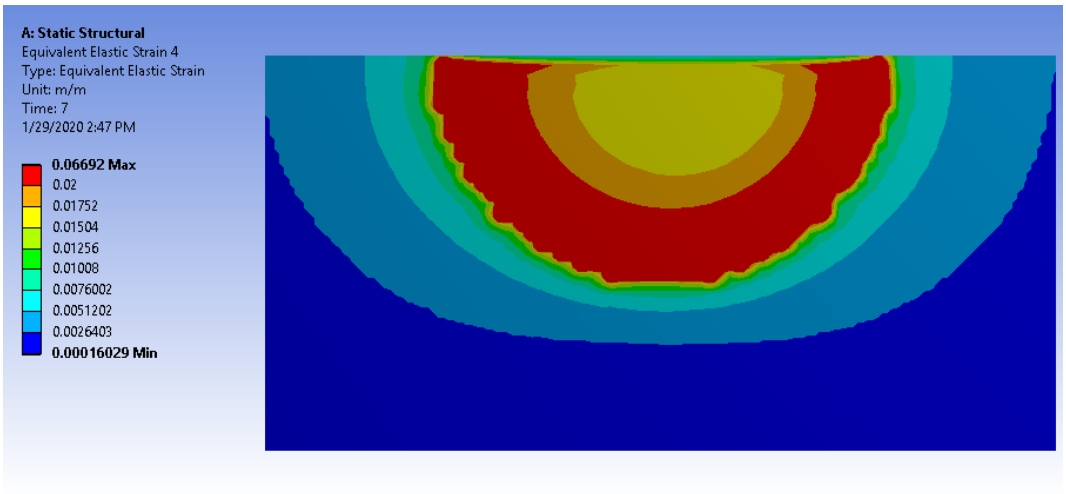

Figure 7-11. The distribution of the equivalent plastic strain after one cycle of fretting motion including normal and tangential directions adhesion effects

When the fretting cyclic tangential displacement is applied to the top surface of the sphere, there are two types of fretting loops. On the one hand, when the maximum nominal displacement is small (less than 15 nm as shown in Fig. 7-9), the springs do not break, and the evolution of the tangential force does not produce a large energy loss. On the other hand, when the maximum nominal displacement is large (larger than 20 nm, also see Fig. 7-9) the springs break, and the evolution of the tangential force does produce a large energy loss. This is discussed next.

Figure 7-12 shows the evolution of the tangential force at an external normal force $F=F_c$ for two cycles of fretting motion with a relatively small fretting displacement magnitude

of 15 nm. Since the no spring ever breaks, the shape of the fretting loop is similar to that in full stick conditions, as described in [98]. The small energy loss is due to the dissipation of plastic strain energy. An effective COF based on the definition from Green [99] is introduced here:

$$\mu_{eff} = \frac{U_{net}}{\int F_y dx} = \frac{\int F_x dx}{\int F_y dx} \tag{7-13}$$

where U_{net} represents the net energy loss during the fretting cycles, and F_y represents the normal external force. U_{net} is calculated by numerical quadrature. The calculated COF is μ_{eff}=0.23 for the case of 15nm oscillation amplitude.

At a relatively larger fretting oscillation amplitude, say of 20 nm, the springs do break, and the evolution of the tangential force generates large energy losses. Figure 7-13 shows the evolution of the tangential force also at an external normal force of $F=F_c$ for two cycle of fretting motions with the said larger fretting oscillation amplitude of 20 nm. At the very beginning, the hemisphere moves in the positive X direction. The tangential force increases with the nominal displacement applied to the top surface of the hemisphere. After the springs break at the interface, the tangential force decreases sharply to a very small value but not to zero due to the elastic resistance caused by the indentation, which is restored. As the hemisphere turns back in the negative X direction, the lengths of the springs drop and tangential adhesion is reinstated, causing the reattachment of the two surfaces. Thus, the tangential forces increase somewhat with the retracted motion. As the hemisphere approaches the original center point, some of the springs change status from stretched to compressed, and thus the tangential forces decrease again. For the hysteretic loop shown in Fig. 7-12, the calculated COF is μ_{eff}=0.70 for the case of 20nm oscillation amplitude.

Note that the fretting loop in Fig. 7-13 is not similar to that in gross slip conditions for models without adhesion [84]. The variation is caused by the spring's detachment and reattachment mechanism used in the current model. Herein, there is no application of a "coefficient of friction;" adhesive detachment or reattachment happens only when the elongation is out of or returns to the range ($-l_c$,l_c), respectively. In other models that apply some arbitrary "constant" COF, the friction force that is generated [84], along with the fretting loops, correspond only to those arbitrarily postulated COFs.

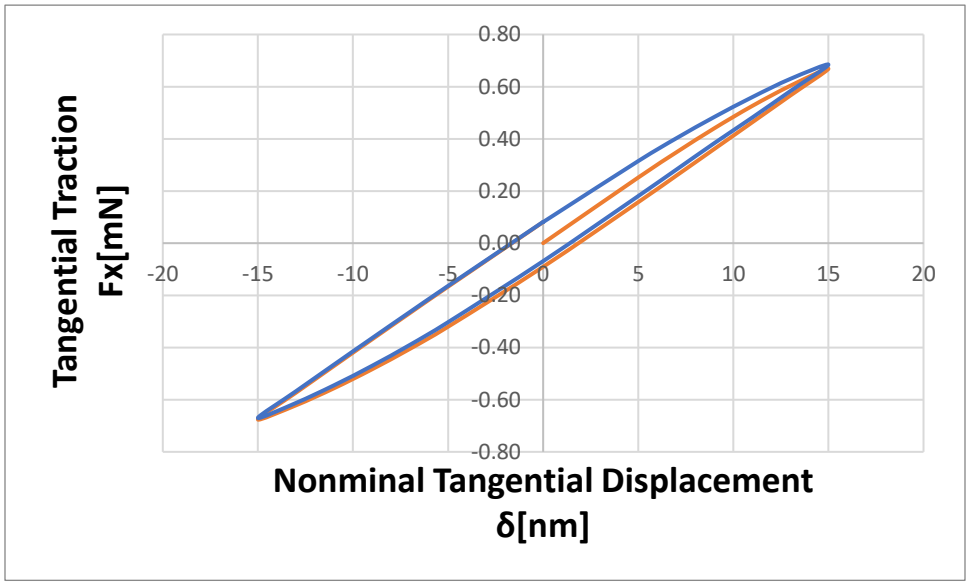

Figure 7-12. The evolution of the tangential force at 1Fc external normal force for two cycle of fretting motion with a smaller fretting displacement magnitude of 15 nm (1st cycle=orange, 2nd cycle=blue).

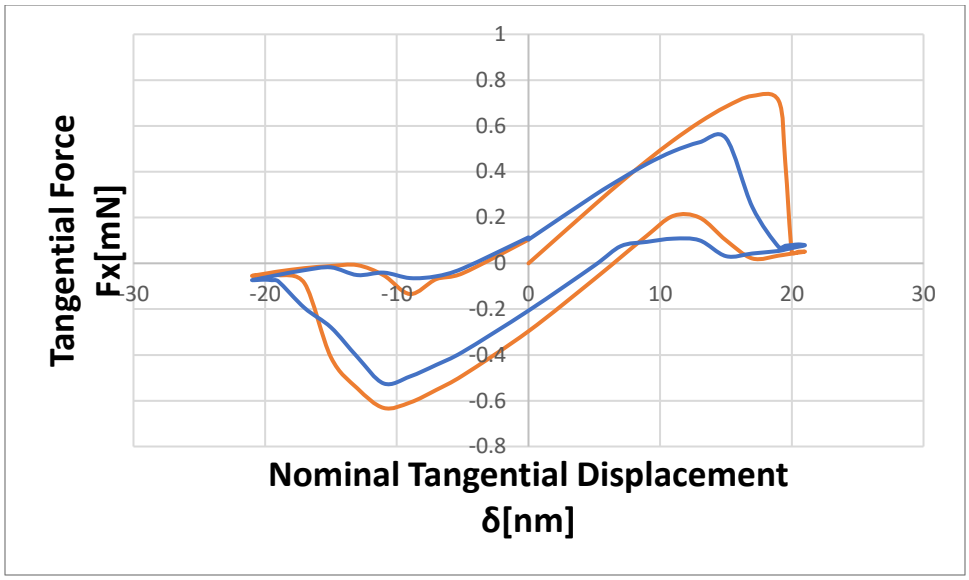

Figure 7-13. The evolution of the tangential force at 1Fc external normal force for two cycles of fretting motion with a larger fretting displacement magnitude of 20 nm (1st cycle=orange, 2nd cycle=blue).

7.5 Comparisons between Adhesion and Non-Adhesion Models

To understand further the mechanism of the adhesion model used in this work, the distribution of the von-Mises stresses, the equivalent plastic strains, and the evolution of the tangential resistant forces are compared now using three different models for an oscillation amplitude of 15 nm (no spring breakage, i.e., adhesion is steadfastly in effect):

Modal A. This is precisely the model described throughout this work: The model includes JKR adhesion in the normal direction, but with tangential resistance by means of bilinear springs.

Modal B. The model is with JKR adhesion in the normal direction and frictional contact in the tangential direction. The coefficient of friction (COF), however, is always set sufficiently large (COF=10) to cause and maintain full stick conditions.

Modal C. The model is a pure Hertizan contact model in the normal direction and a frictional contact in the tangential direction. Again, the COF is always set sufficiently large to cause and maintain full stick condition. While no adhesion is applied here, the normal external force is increased to maintain the same contact area as those in models A and B.

As indicated the COF in frictional contact is set to be large enough to maintain full stick in model B and C, but in model A, no COF is applied at all. In model A adhesion resistance to sliding is done by the tangential bilinear springs until their avalanching break. The results just right before that breakage (i.e., contact condition change from full stick to gross slip) are compared herein. The input of the nominal tangential displacement on the top surface of the hemisphere are maintained the same for all three models. Model C with the same external normal load is not considered, because its contact area is tiny, and the results are trivial.

Figure 7-14 shows the distribution of the von-Mises stress at the bottom interface of the hemisphere for the three models. For Model A, the largest von-Mises stress is located at the edges due to the infinite normal pressure as implied by the JKR model. For Model B, the largest von-Mises is also located at the edges. The stresses in Model B are larger at the center compared to A, because of the full stick condition, as effectively model B possesses structurally a higher stiffness than the bilinear springs (in Model A). It is thus capable of transmitting an increased tangential load under the same tangential displacement input. For Model C, the stress distribution is typical of a full stick Hertzian contact. The region in red is where the von-Mises stress reaches the yield strength to indicate plasticity. The area of plasticity in Model C is considerably larger than those in models A and B.

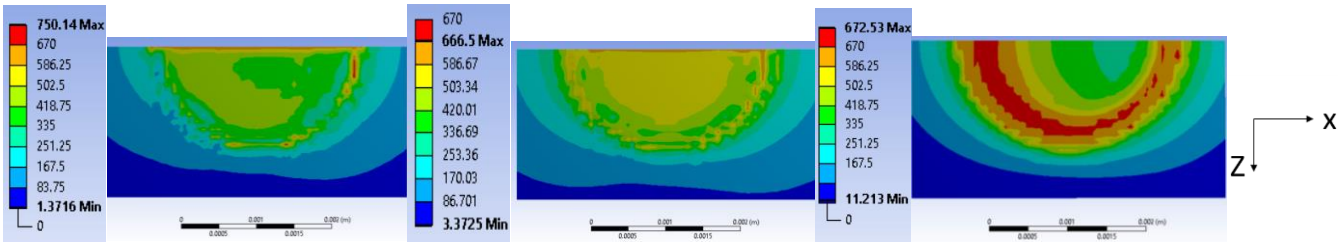

(A) (B) (C)

Figure 7-14. Bottom view. The distribution of the von-Mises stress at the bottom interface of the hemisphere (y=0) having the same tangential displacement to the right (but just before the breakage of springs in model (A) for all three models.

Although the distributions of the von-Mises stress at the bottom surface of the hemisphere are different in the three models, the distributions are somewhat similar for the front surface, i.e., the XY plane where at z=0 (see definitions in Fig. 7-1). Figure 7-15 shows the distributions of the von-Mises stress under the same condition for the front view for the three models. The large von-Mises stresses are located at the region near the interface, and the von-Mises stresses spread to a larger area to the "left) side than that on the "right," because the direction of the (reactive) tangential force is in the negative x direction (i.e., to the "left") when the hemisphere is forced in the positive x direction (or, to the "right").

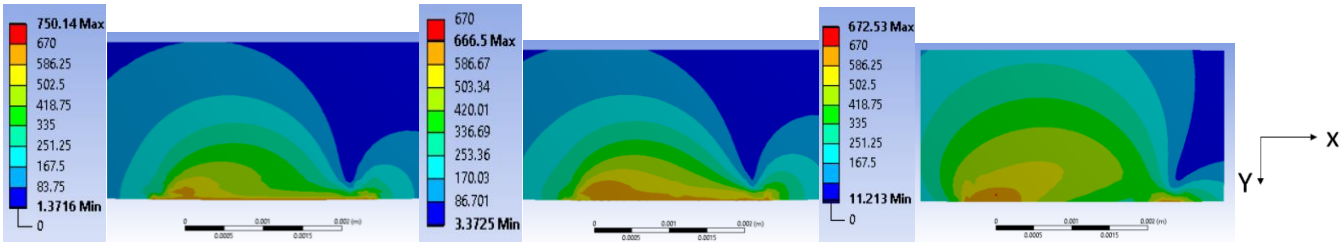

(A) (B) (C)

Figure 7-15. Front view. The distribution of the von-Mises stress at the front surface (XY plane and z=0) of the hemisphere having the same tangential displacement to the right (but just before the breakage of springs in model A) for all three models.

Figure 7-16 shows the distribution of the equivalent plastic strains at the bottom of the sphere for three models. For Model A, the plastic deformation is mainly due to the JKR model producing infinite pressure at the contact edges. For Model B, since the tangential load is larger (as seen in Fig. 7-15), the plastic strain is therefore larger than model A. For Model C, plasticity (i.e., the von-Mises stress reaching the yield strength) does not show up after normal contact, since there is no JKR pressure. During the fretting motion, plastic strain appears at the very beginning, at point A_1 (see Fig.7-2) for Models A and B, while the plastic strain appears later between points A_1 and B_1 for Model C. The later appearance of plastic strain in Model C causes a smaller spread region than the other two.

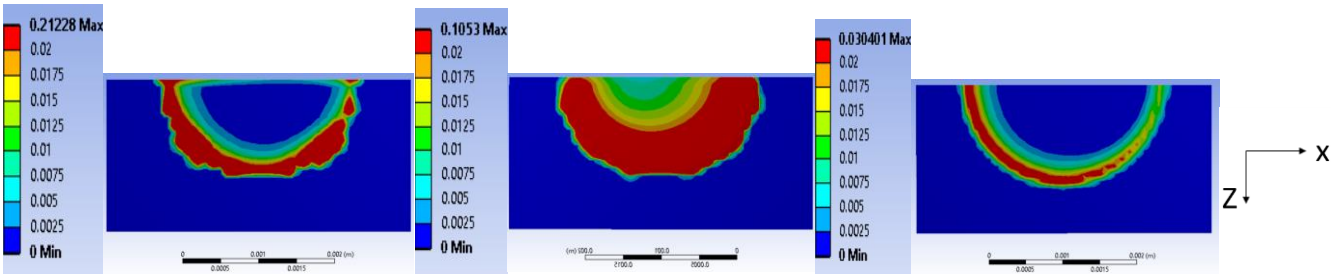

(A) (B) (C)

Figure 7-16. The distribution of the equivalent plastic strains at the bottom of the hemisphere at the same tangential displacement to the right (before the breakage of springs in model (A) for three models.

Figure 7-17 shows the tangential force evolutions during one cycle of fretting loading for the three models (recall that all models have a smaller oscillation amplitude of 15 nm). All three tangential force evolutions are typical for fretting loop of full stick conditions. However, the slopes of the fretting loop are different. For model A, the elastic bilinear springs at the interface have the least effective stiffness. The large plastic deformation at the contact edges of JKR model also decreases the tangential resistance. Thus, it has the smallest slope or inclination. For model C, it is in a full stick condition with no JKR

pressure, which produces the largest effective structural stiffness. Thus, it has the largest slope. Model B is a transition model between models A and C, where the structural stiffness of model B is in between.

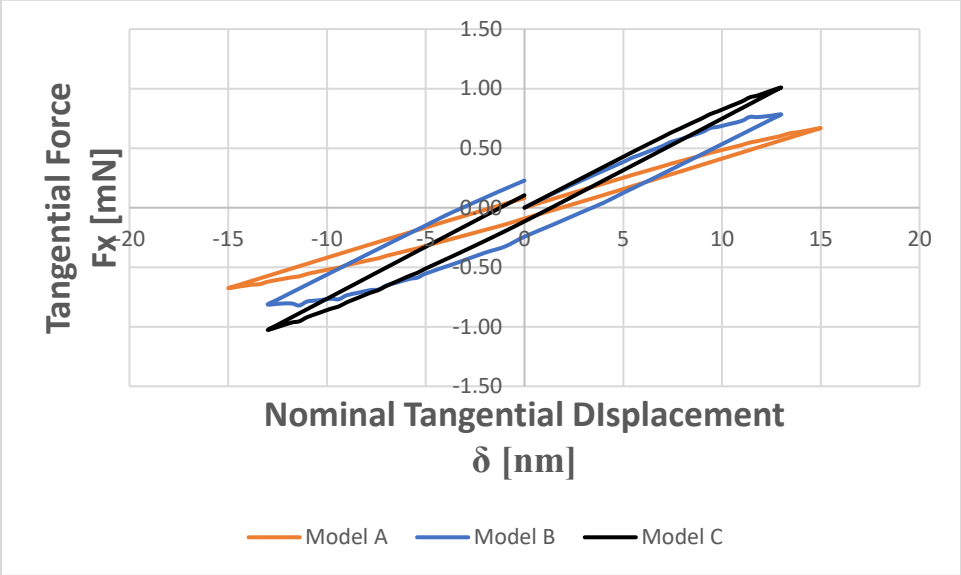

Figure 7-17. The evolution of the tangential force during one cycle of fretting load for three models.

In conclusion, up to the point where the bilinear spring in the adhesion model A do not break, that model exhibits von-Mises stresses distribution, plastic strain distributions (see Fig.7-16), and fretting loops (see Fig. 7-17) similar to the full stick contact model C. The plastic damage is more concentrated in this model A due to the infinite JKR pressure. The contact system is less stiff in this model A due to the smaller tangential resistance of the interfacial bilinear springs.

7.6 Conclusion

The work in this chapter builds a comprehensive adhesion model that incorporates adhesive tangential resisting traction between a deformable hemisphere and a rigid plate. The normal direction load is based on the classical JKR model. However, the tangential adhesive resistance is based on the definition of shear strength and surface free energy. The model is built using the FEA commercial code ANSYS, with bilinear elastic springs and nodal forces applied at the interface. The material for the deformable hemisphere is gold. Several conclusions are drawn:

1.The robust adhesion model in the tangential direction is not influenced by the mesh and the spring settings.

2.The detachment of the adhesive bond of the two contacting surfaces is achieved by the breakage of the bilinear springs at the interface. The breakage of the springs is avalanching in both elastic and plastic conditions but is somewhat more gradual with the latter. When the two surfaces are about to detach, the vast part of the contact region deforms plastically.

3.There are two types of fretting loop depending on the magnitude of the oscillatory tangential displacement. At small fretting amplitudes, the fretting loop is similar to that of full stick conditions (as if the contacting model has an interfacial friction force that is exceedingly large). At large fretting amplitudes, the fretting loop generates large energy losses, while the fretting loop is dissimilar than those created by gross slip conditions.

4.The adhesion model in this work exhibits similar patterns in von-Mises stress distribution, plastic strains distribution, and fretting loops as the full stick contact models

up to the point of breakage. The plastic strain is larger in JKR pressure than that in pure Hertzian model. The contact system is less stiff in this model due to the tangential resisting springs added at the interface.

CHAPTER 8. CLOSURE

8.1 Conclusions

This work uses the FEA to study fretting in tribological contacts. A numerical model enables the investigation of fretting between identical and dissimilar materials with and without wear. Many of the results are confirmed theoretically whenever possible. Based on the FEA and analytical results, two mitigation methods to reduce fretting damage are proposed. In addition, a novel fretting adhesion model is built, where a constant artificial COF is replaced with the effects of adhesion.

Firstly, this work provides systematic results for the stress-strain analysis, junction growth, fretting loop, and depression marks on the bottom body for different material pairs. The results are normalized, which are verified to be effective to be applied to different dimensions (microscopically and macroscopically). It helps understand the mechanisms of fretting wear and fretting fatigue.

For 2D plane strain cylindrical contact between identical material pairs, the following results are found. With small COFs, the largest von-Mises stress is confined under the contacting surface. With large COFs, the largest von-Mises stress is located at the edge of the contact. Likewise, the largest plastic strain shows up at the edges, too. It is, therefore, postulated that cracks and fatigue are most likely to initiate and propagate at the contact edges with large COFs, at bulk material under contacting surface with small COFs. Due to the plastic deformation of the surfaces, junction growth is found. The magnitude of the junction growth increases with the COFs, while the rate of the convergence of the growth

decreases with the COFs. The fretting loop (i.e., the development of the tangential force versus fretting motion) for the initial few cycles of loading is likewise found, where the enclosed area indicates the energy loss. Pileup appears with large COFs, which intensify the plastic strain at the contact edges.

For 3D spherical contact between identical material pairs, the following results are found. With small COFs, the largest von-Mises stress is confined under the contacting surface. With large COFs, the largest von-Mises stress is located at the edge of the contact. The large plastic strains form multiple “rings” on the contacting surfaces after the oscillatory fretting motion. It is, therefore, postulated that cracks and fatigue are most likely to initiate and propagate at the contact edges with large COFs, at bulk material under contacting surface with small COFs. Depression marks and pileups on the surface of the block are found. The fretting loop of the initial cycles is found. The evolution of the tangential force stabilizes fast with small COFs. The maximum effective COF during the cyclic loading equals to the COF applied to the model after the stabilization. The tangential force is always zero at frictionless contact without the plowing effect, which is due to the sphere being structurally weaker than the block. The work done to the system equals to the enclosed area of the hysteresis curve, which is the evolution of the tangential loading. It corresponds to three kinds of energy: elastic strain energy, plastic strain energy, and frictional energy dissipation. The fluctuating nature of the evolution of the work is caused by the reservation of the elastic strain energy, while the cumulative increase of the effect is caused by the dissipation of the frictional and plastic dissipation. At certain interference, there exists a certain COF, which will yield the largest work done to the system.

The unique findings for dissimilar material pairs are later found. For results in 2D cylindrical contact, between Inconel 617 and Incoloy 800H, the former is “harder” or “stronger,” and in the current investigation it never yielded. Due to the plastic deformation of the surfaces, junction growth is found. The more pronounced growth on the two edges is in the same direction of the tangential force experienced by the surface of the deformed body. The temperature elevation causes the increase of the plastic strain and the decrease of the tangential force, normal force, and the maximum von-Mises in Inconel 617. For results in 3D spherical contact, the largest plastic strain appears at the leading and trailing edges. The pattern of the plastic strain distribution is not “ring-like” in identical material pair cases because plowing takes place between dissimilar material pairs.

Secondly, a notable contribution of this work is building the fretting wear model and its corresponding analytical solutions. In 2D fretting model under elastic condition, the initial gross slip distance, wear volume at the initiation of the gross slip, and wear volume for the one cycle of the fretting motion are derived. The results are in very good agreement between the theoretical predictions and the FEA. The effect of plasticity is double edged. On one hand, under small normal load, plasticity introduces small deflections and junction growth when COFs are large. These two effects decrease the wear volume. On the other hand, under larger normal loads plasticity introduces larger cross sections, which makes the two bodies stiffer to the tangential load. As a result, the deflection decreases, and the wear volume increases.

In 3D fretting wear model under elastic conditions, the initial gross slip distance, wear volume at the initiation of the gross slip, and wear volume for the one cycle of the fretting motion are derived. The results are in very good agreement between the theoretical

predictions and the FEA. The effect of the plasticity is analyzed. The plasticity introduces junction growth, which increases the wear volume. However, the wear volume between elastic prediction and plastic FEA results are still close.

Thirdly, two mitigation schemes are proposed, prestress scheme and wear volume mitigation scheme. In the prestress scheme, the plastic strain in the bulk material in reduced at appropriate prestress input, and the prestress in both x and z directions can further reduce the plastic strain in 3D case. There are two reasons for that behavior. Firstly, there is σ_z, which elevates the hydrostatic situation, thus reducing the von-Mises stress. Secondly, the negative σ_x opposes the natural tendency of creating a positive σ_x in the fretting sliding motion, which also reduces the von-Mises stress during sliding. With smaller von-Mises stresses, the corresponding plastic strain is smaller. The compressive pre-stress is envisioned to also suppress any crack initiation and/or growth at the two edges of the fretting contact. However, the prestress condition aggravates the plastic strain at the interface both in 2D and 3D cases. In the wear volume mitigation scheme, the worst normal load can be solved numerically based on Eq. 6-1, Eq. 6-2, or Eq.6-3. From a designer's point of view, the normal load should be either much less or much larger than the P_w.

Lastly, a tentative fretting adhesion model is built, where the COF is replaced with effect of adhesion. For the first time, it builds a comprehensive adhesion model for frictional contact considering both the normal and tangential direction adhesion effects. The normal direction adhesion contact is based on the classic JKR model. The tangential resistance is based on the definition of the shear strength and the surface free energy. It helps to replace the artificial COF with the effect of adhesion, which is a giant leap in the FEA frictional contact modelling. The model is built using the FEA commercial code ANSYS, with

bilinear elastic springs and nodal forces applied at the interface. The material for the deformable hemisphere is gold. The robust adhesion model in the tangential direction is not influenced by the mesh and the spring settings. The detachment of the adhesive bond of the two contacting surfaces is achieved by the breakage of the bilinear springs at the interface. The breakage of the springs is avalanching in both elastic and plastic conditions but is somewhat more gradual with the latter. When the two surfaces are about to detach, the vast part of the contact region deforms plastically.

There are two types of fretting loop depending on the magnitude of the oscillatory tangential displacement. At small fretting amplitudes, the fretting loop is similar to that of full stick conditions (as if the contacting model has an interfacial friction force that is exceedingly large). At large fretting amplitudes, the fretting loop generates large energy losses, while the fretting loop is dissimilar than those created by gross slip conditions.

The adhesion model in this work exhibits similar patterns in von-Mises stress distribution, plastic strains distribution, and fretting loops as the full stick contact models up to the point of breakage. The plastic strain is larger in JKR pressure than that in pure Hertzian model. The contact system is less stiff in this model due to the tangential resisting springs added at the interface.

8.2 Future Work

The novel adhesion model that is built in the current work can be expanded to include wear. In the novel adhesion model, the frictional resistance is determined by material properties, surface free energy and shear strength without the need to guess a synthetic COF. That would advance the state of the art because all previous FEA models are based on such an

artificial COF that produces translational resistance to motion. An effective COF can, of course, be calculated posthumously to match experimental results. An adhesion-based wear model, as built in chapter 5, would produce untainted results for the wear process.

In this current work, the model is built between smooth surfaces with non-adaptive wear. The non-adaptive wear model does not consider the changes of the surface profile during the fretting process. In the future, it would be worthy to investigate the fretting between rough surface with an adaptive wear model. The FEA method is capable to model the irregular surface profile, which would be very difficult or even unachievable analytically. An additional difficulty that will have to be overcome is that typical fretting cycles tend to be in the thousands along with a surface profile that constantly changes. A corresponding adaptive FEA will have to be implemented. In other words, the adaptive fretting wear model will need to accommodate thousands or more cycles. Mixed regime will have to be investigated, where the contact status during fretting would change from partial slip at the beginning of fretting to gross slip at the end of fretting. As indicated by the work of Zhou et al. [29], this regime is the most dangerous in fretting. Therefore, it is meaningful to investigate this phenomenon based on the proposed FEA model.

APPEDICES

A. Derivation of Equations in Plane Strain Contact

This appendix can be found in Ref. [83]. The interference of a half cylinder in contact with a block is derived below where the dependence of the results on the size of the block is investigated. According to Johnson [11] (taken from p. 130, and shown in Fig.A-1a), the elastic compression of a cylinder in contact with two elastic bodies is obtained. The compression of the upper part of the cylinder O_1C is:

$$\delta_1 = \frac{P}{L}\frac{(1-\nu^2)}{\pi E}\left\{2\ln(4R/b_1)-1\right\} \tag{A-1}$$

Where, the half contact width b_1 is calculated according to the Hertzian theory:

$$b^2_1 = 4PR/(\pi L E_1^*) \tag{A-2}$$

Here, E_1^* is the composite modulus of the upper body and the cylinder:

$$\frac{1}{E_1^*} = \frac{1-\nu_1^2}{E_1} + \frac{1-\nu^2}{E} \tag{A-3}$$

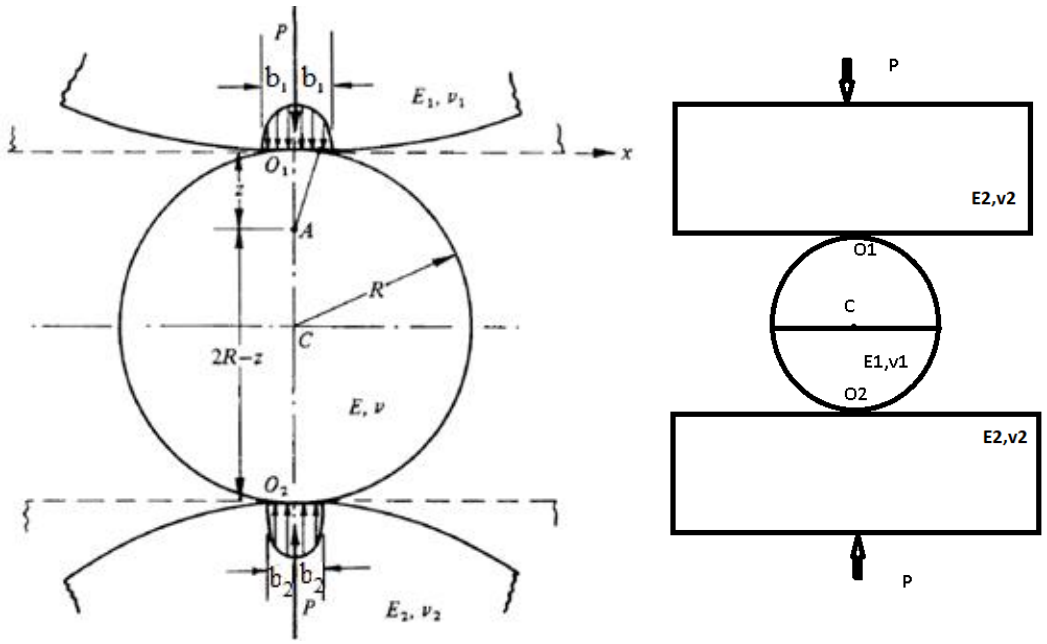

(a) The model in *Contact Mechanics* by Johnson (p. 130) herein

(b) The equivalent model of the compression of the half cylinder

Figure A-1. The contact model to derive the compression of the elastic cylinder in contact with an elastic block

The model of interest in this work is that of a half cylinder in contact with a block. For that we use the equivalent model shown in Fig.A-1b. The horizontal axis of the half cylinder (passing through point C) is prescribed to have a vertical displacement, ω, which is defined as the interference. That interference consists of two parts, the compression of the half cylinder, ω_1, and the compression under the centerline of the block, ω_2. For ω_1, Eq. A-1 yields the compression of the lower half cylinder:

$$\omega_1 = \frac{P}{L}\frac{(1-\nu_1^2)}{\pi E_1}\left\{2\ln(4R/b)-1\right\} \tag{A-4}$$

Where, b is the half contact width between the cylinder and the block. The parameters E_1, ν_1, and R belong to the half cylinder. For ω_2, according to Johnson [11], the compression

under the centerline of the block is equal to the compression of a half-space under the load of the Hertzian pressure relative to a point at a depth, d. Hence,

$$\omega_2 = \frac{P}{L}\frac{(1-\nu_2^{\,2})}{\pi E_2}\left\{2\ln(2d/b) - \nu_2/(1-\nu_2)\right\} \tag{A-5}$$

The interference is then the addition of Eqs. A-5 and A-6:

$$\omega = \frac{P}{L}\frac{(1-\nu_1^{\,2})}{\pi E_1}\left\{2\ln(4R/b) - 1\right\} + \frac{P}{L}\frac{(1-\nu_2^{\,2})}{\pi E_2}\left\{2\ln(2d/b) - \nu_2/(1-\nu_2)\right\} \tag{A-6}$$

For contact case between dissimilar materials, by substituting Eqs. A-2 and A-3 into Eq. A-6, the interference simplifies to:

$$\omega = \frac{P}{L}\frac{(1-\nu_1^{\,2})}{\pi E_1}\left\{\ln(\frac{4\pi E' R}{P/L}) - 1\right\} + \frac{P}{L}\frac{(1-\nu_2^{\,2})}{\pi E_2}\left\{\ln(\frac{\pi d^2 E'}{RP/L}) - \frac{\nu_2}{(1-\nu_2)}\right\} \tag{A-7}$$

For contact case between identical materials, $\nu_1 = \nu_2 = \nu$, $E_1 = E_2 = E$, and d=R. Eq. A-7 simplifies to:

$$\omega = \frac{P/L}{2\pi E'}\left\{2\ln(\frac{2\pi R E'}{P/L}) - \frac{1}{1-\nu}\right\} \tag{A-8}$$

To verify the assumption of viewing the block as a half-elastic space, different dimensions of the block have been used to compare FEA results with theoretical predictions, where %dif, as given in Table A-1, indicates the relative percentage difference between them. According to the table, the FEA results agree very well with the results calculated according to Eqs. A-5 to A-8, when the depth varies from 0.5R to 4R. When the depth is 0.25R, however, the maximum von-Mises stress predicted by the FEA has a somewhat larger deviation from the theoretical value (7.99%). While that indicates that the boundary conditions applied on the block start to affect the stress distribution in the area of the

contact, the other differences are still quite low. So, a block of depth, d, that equals to R can clearly be regarded as a half-elastic space. Indeed, in this work, all reported results are specifically given for that case of d=R. Moreover, the nondimensionalized results in this work, can safely be applied to blocks with depths that are about 0.5R or larger. That proposition conforms to the classical Saint-Venant's Principle, which reassures that the critical interferences between two cylinders, as derived by Eq. A-1 in the reference by Green [32], and the one derived herein for the contact of a half-cylinder against a block in Eq. A-8, match closely with a mere 5% difference.

Table A-1. Comparison of the critical values between theoretical predictions and FEA results for a half-cylinder of radius is R, in contact with a 4dxd block, of depth, d. The ratio d/R is varied from 0.25R to 4R. The equation $C^*S_y=p_{oc}$ is according to Green [61]. Herein, R=0.5m, $\nu_1=\nu_2=0.32$, $E_1=E_2=200$GPa, $S_y=0.9115$GPa.

Theoretical Predictions						FEA Results							
d/R	ω_c [mm]	b_c [mm]	P_c/L [MN/m]	p_{0c} [GPa]	$\sigma_{emax[GPa]}$	b_c [mm]	% dif	P_c/L [MN/m]	%dif	p_{0c} [GPa]	%dif	$\sigma_{emax[GPa]}$	%dif
0.25	0.7732	14.88	38.73	1.657	0.9115	14.60	-1.86	37.14	-4.11	1.625	-1.94	0.9842	7.99
0.5	0.8499	14.88	38.73	1.657	0.9115	14.84	-0.28	37.80	-2.41	1.636	-1.28	0.9361	2.71
1	0.9266	14.88	38.73	1.657	0.9115	15.20	2.17	38.56	-0.43	1.645	-0.75	0.9122	0.08
2	1.0033	14.88	38.73	1.657	0.9115	14.80	-0.52	37.52	-3.12	1.625	-1.94	0.9108	-0.07
4	1.0800	14.88	38.73	1.657	0.9115	15.20	2.17	37.88	-2.20	1.623	-2.08	0.9089	-0.28

B. Boundary Condition Influence

The results herein are taken from Ref. [83]. In the plane strain line contact case, the boundary condition on the four sides of the block are shown to influence the results. Different boundary conditions are tested for the displacement-controlled model. The same effect is also found in the force-controlled results. However, in spherical point contact, the boundary condition effects are found negligible, and therefore are not introduced here.

As shown in Table B-1, several different types of boundary conditions applied on the four sides of the block are now investigated. The four sides of the block, a_1, a_2, s_1, and s_2, are consistent with Fig. 3-1. In all six types, the midpoint M on the bottom side a_1 is fixed in the X and the Y direction to ensure the relative motion between the half cylinder and the block. The top of the block is always free. The Symbol "+" means the side is fixed in the corresponding direction. Type0 represents the boundary condition where all the results in chapter 3 and 4 are generated, where the bottom side a_1 is fixed in the X and the Y direction. In Type1, the boundary condition of the bottom side a_1 is changed relative to Type0 to be free in the X direction. In Type2, the boundary conditions of the two sides s_1 and s_2 are changed to be fixed in the X direction relative to Type1. In Type3, the boundary conditions of the two sides s_1 and s_2 are changed to displace $1 * \omega_c$ to the right and left, respectively, again relative to Type1. The magnitude of that displacement is changed to be $2 * \omega_c$ and $3 * \omega_c$ in Type4 and Tpye5, respectively.

Table B-2. Different types of boundary conditions on the four edges of the block (shown in Fig.1a). "+" represents the edge is fixed in the corresponding direction. Blank represents the edge is free in the corresponding direction. Edge a_2 is always free while the midpoint M on the edge a_1 is always fixed in both the X and the Y direction.

Type	a_1		s_1		s_2	
	X	Y	X	Y	X	Y
0	+	+				
1		+				
2		+	+		+	
3		+	$+1\omega_c$		$-1\omega_c$	
4		+	$+2\omega_c$		$-2\omega_c$	
5		+	$+3\omega_c$		$-3\omega_c$	

The displacements on the two sides, s_1 and s_2, generate pre-stresses in the compressed block. Considering the effect of Poisson ratio, the top side of the block a_2 will displace Δy upwards according to the following. In plane strain, the constitutive equation is:

$$\begin{Bmatrix} \sigma_x \\ \sigma_y \\ \sigma_z \\ \tau_{xy} \end{Bmatrix} = \frac{E}{(1+\nu)(1-2\upsilon)} \begin{bmatrix} 1-\nu & \nu & 0 \\ \nu & 1-\nu & 0 \\ \nu & \nu & 0 \\ 0 & 0 & \dfrac{1-2\nu}{2} \end{bmatrix} \begin{Bmatrix} \varepsilon_x \\ \varepsilon_y \\ \gamma_{xy} \end{Bmatrix} \qquad \text{(B-1)}$$

According to Eq. B-1, the normal stress in the Y direction can be expressed as:

$$\sigma_y = \frac{E}{(1+\nu)(1-2\upsilon)}[\nu\varepsilon_x + (1-\nu)\varepsilon_y] \tag{B-2}$$

However, $\sigma_y = 0$, before the cylinder is compressed downwards, since the top side is set free. Using the condition that the compressive displacement, Δx, is applied on both sides of the block, s_1 and s_2, but in opposite directions, the normal strain in the X direction is compressive:

$$\varepsilon_x = -\frac{\Delta x}{2R} \tag{B-3}$$

According to Eq. B-2 and B-3, the normal strain in the Y direction is:

$$\varepsilon_y = \frac{\nu}{1-\nu}\frac{\Delta x}{2R} \tag{B-4}$$

Using the definition of the normal strain in the Y direction:

$$\varepsilon_y = \frac{\Delta y}{R} \tag{B-5}$$

The displacement of the top side, a_2, is therefore:

$$\Delta y = \frac{\nu}{1-\nu}\frac{\Delta x}{2} \tag{B-6}$$

In order to compare the results of the pre-stressed cases with those of the original cases, Δy must be taken into consideration. If ω is always the interference imposed, as it is the case with no pre-stress, then the interference in the pre-stressed case is:

$$\omega' = \omega - \Delta y \tag{B-7}$$

Figure B-1 shows the junction growth results of the first quarter of the loading cycle at $1*\omega_c$ interference with $\mu=1$, for different types of boundary conditions. It is obvious that

the boundary conditions vary the development of the junction growth. Notably, in Type1, the two sides are free to displace laterally outwards in the X direction. After the interference is applied, it is equivalent to stretching the block instead of compressing. Therefore, there is a trend of increased junction growth among Typ1, Type2, and Type4. In other words, the junction growth increases with the compressive displacement on the two sides (from negative to zero to positive). Additionally, Type0 junction growth is similar to Type2, because the bottom of the block being fixed in the X direction in Type0 introduces a similar effect of the two sides being fixed in the Y direction in Type2. These two conditions characterize most closely the block as a half-elastic space.

Figure B-2 illustrates the equivalent plastic strain on the upper surface of the block after one cycle of loading at $1*\omega_c$ interference with $\mu=1$ under different types of boundary conditions. It is shown that the plastic strain is larger in Type0 than in any type with a pre-stress, and it is the smallest in Type5 with two sides displacing $3*\omega_c$ laterally inwards. Therefore, the pre-stress can reduce the plastic strain on the surface, where the plastic strain decreases with a larger pre-stress. There are two reasons for that behavior. Firstly, there is σ_z , which elevates the hydrostatic stress (see Eq.B-1), thus reducing the von-Mises stress. Secondly, the negative σ_x opposes the natural tendency of creating a positive σ_x in the fretting sliding motion, which also reduces the von-Mises stress during sliding. With smaller von-Mises stresses, the corresponding plastic strain is smaller. The compressive pre-stress is envisioned to also suppress any crack initiation and/or growth at the two edges of the fretting contact.

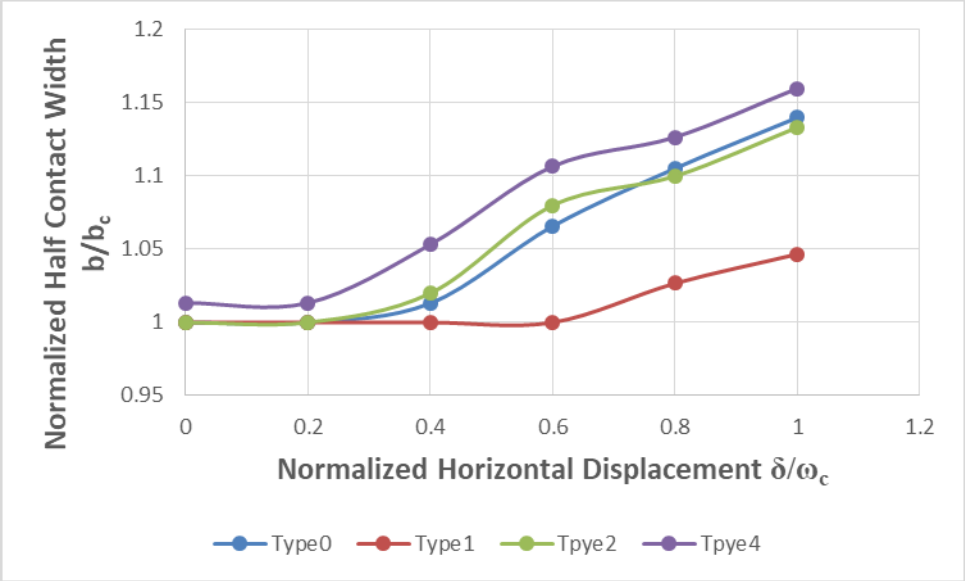

Figure B-1. The junction growth results of the first quarter of the loading cycle at $1*\omega_c$ interference with $\mu=1$ in different types of boundary conditions.

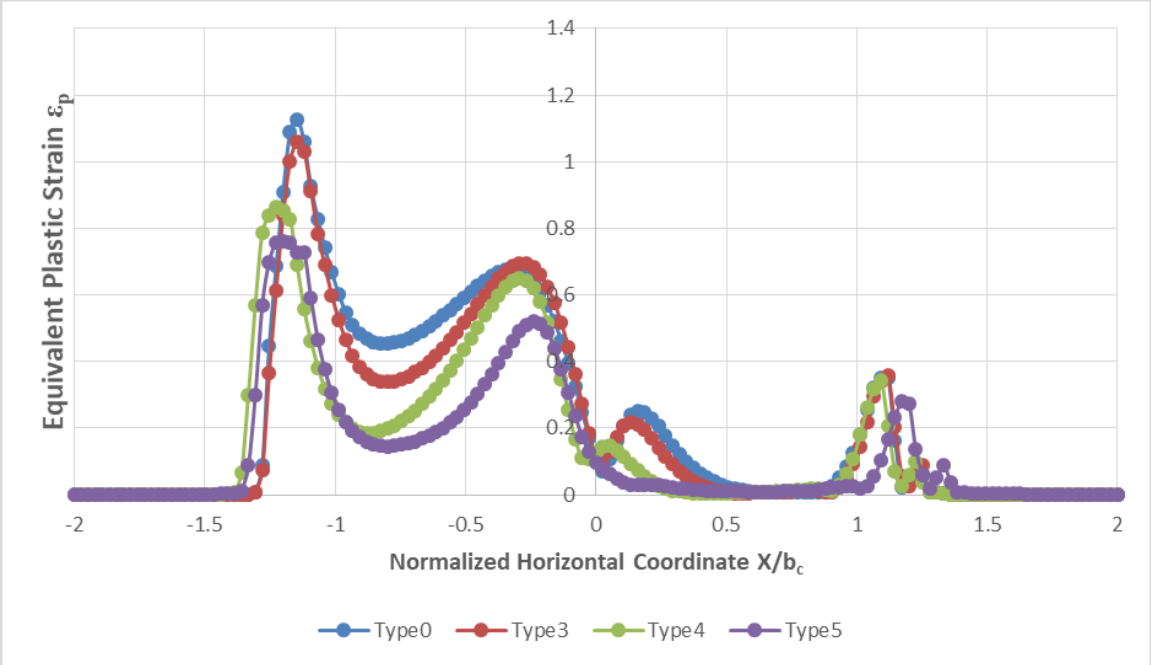

Figure B-2. The distribution of equivalent plastic strain on the surface of the block after one cycle of loading at $1*\omega_c$ interference with $\mu=1$ in different types of boundary conditions.

In conclusion, the boundary conditions of the block sides do influence the fretting results including contact width and equivalent plastic strain. However, the results between different boundary condition cases are found within 10% difference, and the trends are similar. Thus, only the boundary condition of Type 0 is utilized to perform the simulation, which will give behavior tendencies of the fretting damage mechanisms.

C. Timoshenko Beam Approximation for Plane Strain Contact

The initial gross sliding distance for elastic contacts can be estimated by regarding the half-cylinder as a Timoshenko beam[4] while assuming the block as a half elastic space. The loading condition of the half-cylinder is shown in Fig.C-1, when gross slip initiates, i.e., when $Q/L=\mu(P/L)$. In addition to Q/L, there is also a moment per unit length, M_0/L, acting about the tip of the half-cylinder. This moment, M_0/L, is caused by the curvature of the contacting surface, and the local tangential traction $\mu p(x)$ (as shown in Fig. C-1b). This moment is directly related to μ and P/L. The moment distribution, M(x)/L, the second moment of area, I(x)/L, and the cross-section area, A(x)/L, are given, respectively, by:

$$\frac{M(x)}{L} = \mu \frac{P}{L}(R-x) + \frac{M_0}{L} \tag{C-1}$$

$$\frac{I(x)}{L} = \frac{2}{3}(R^2 - x^2)^{\frac{3}{2}} \tag{C-2}$$

$$\frac{A(x)}{L} = 2(R^2 - x^2)^{\frac{1}{2}} \tag{C-3}$$

According to the Timoshenko beam theory [100], the angle of rotation of the mid-surface is defined as ϕ. The derivative of ϕ is determined by M(x)/L and I(x)/L according to:

[4] The Timoshenko beam is appropriate for thick or short beams, since it accounts for shear deformation and rotational bending effects.

$$\frac{M(x)}{L} = -E\frac{I(x)}{L}\frac{d\varphi}{dx} \tag{C-4}$$

By integrating Eq. C-4 with the boundary condition, ϕ=0 at x=0, the distribution of ϕ is expressed as:

$$\varphi(x) = \frac{3}{2}\frac{\mu P}{REL}\left[\frac{R-(1+\frac{M_0}{\mu RP})x}{\sqrt{R^2-x^2}}-1\right] \tag{C-5}$$

According to the Timoshenko beam theory [100], the derivative of the deflection of half-cylinder, Δ, is related to ϕ by:

$$\frac{d\Delta}{dx} = \varphi - \frac{1}{kAG}\frac{d}{dx}(EI\frac{d\varphi}{dx}) \tag{C-6}$$

By substituting ϕ(x) from Eq. C-5 into Eq. C-6, the distribution of deflection of the half-cylinder, Δ, can be solved by integrating Eq. C-6 with the boundary condition, Δ=0 at x=0. The expression of Δ(x) is thus:

$$\begin{aligned}\Delta(x) = {} & \frac{3}{2}\frac{\mu P}{EL}[\arcsin(\frac{x}{R})+(1+\frac{M_0}{\mu RP})\frac{\sqrt{R^2-x^2}-R}{R}-\frac{x}{R}] \\ & -\frac{\mu P}{2kGL}\arcsin(\frac{x}{R})\end{aligned} \tag{C-7}$$

The deflection of the half-cylinder at the initiation of gross slip, δ_{i1}, can be estimated by taking the deflection of the tip of the beam, δ_{i1}= Δ(R). That is given by:

$$\delta_{i1} = |\Delta(R)| = [\frac{3\mu P}{4EL}(4-\pi)+\frac{3M_0}{2EL}+\frac{\pi\mu P}{4kGL}] \tag{C-8}$$

Here, the Timoshenko shear coefficient, k, for rectangular cross section is taken according to Cowper [101], as:

$$k = \frac{10(1+\nu)}{12+11\nu} \tag{C-9}$$

and the shear modulus, G, is given by:

$$G = \frac{E}{2(1+\nu)} \tag{C-10}$$

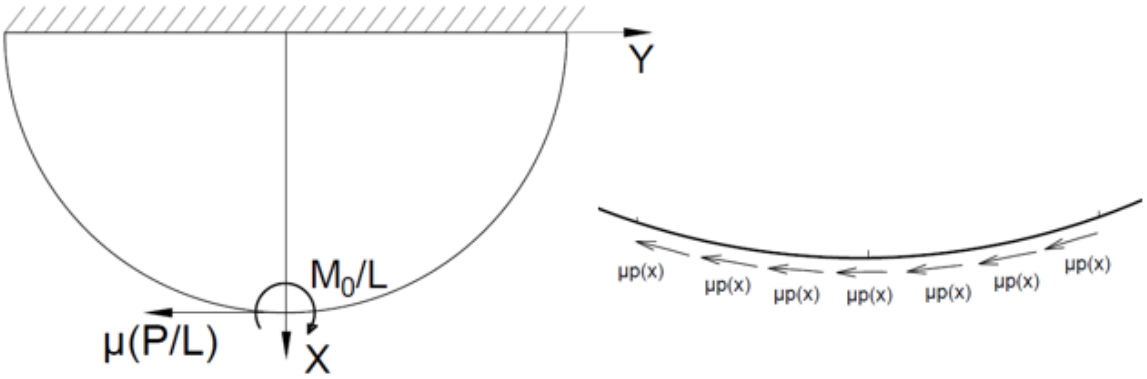

(a) (b)

Figure C-1 (a) The loading condition of the half-cylinder as a Timoshenko beam at slip onset (b) Zoomed in contact region

The influence of the moment, M_0/L, on δ_{i1} is analyzed in now the following. The moment is maximum when the half-cylinder is undeformed (the curvature of the tip is maximum, as if the normal load does not deform the tip of the half-cylinder). Hence, the maximum moment, M_0/L, can be estimated using Fig. C-2. The contact region, $-b<x<b$, is confined to a corresponding angle range, $-\theta_0< \theta<\theta_0$, where θ_0 is given by:

$$\theta_0 = \arcsin\frac{b}{R} \tag{C-11}$$

The local frictional force in this region is q(x)=μp(x). The arm of the force is represented by the length of $\overline{OC}$ in Fig.C-2, and is given by:

$$\overline{OC} = 2R\sin^2\frac{\theta}{2} \tag{C-12}$$

The moment on the tip of the half-cylinder, M_0/L, can be estimated by integrating the product of the local friction force and the arm of the force:

$$M_0 / L = \int_{-b}^{b} \mu p(x) 2R\sin^2\frac{\theta}{2} dx = \int_{-\theta_0}^{\theta_0} 2\mu p_0 \sqrt{1-(\frac{R\sin\theta}{b})^2} R^2 \sin^2\frac{\theta}{2} d\theta \tag{C-13}$$

In the case where θ is small, which agrees with the conditions here (θ~0.01 rad), Eq. C-13 can be simplified as:

$$M_0 / L = \frac{\mu\pi p_0 b^3}{16R} \tag{C-14}$$

According to the above estimation, the deflection of half-cylinder caused by the M_0/L is found to be less than 0.1% of the total deflection for different material cases and different normal loads with different COFs. Therefore, the moment on the tip of the half-cylinder, M_0/L, can largely be ignored in the foregoing.

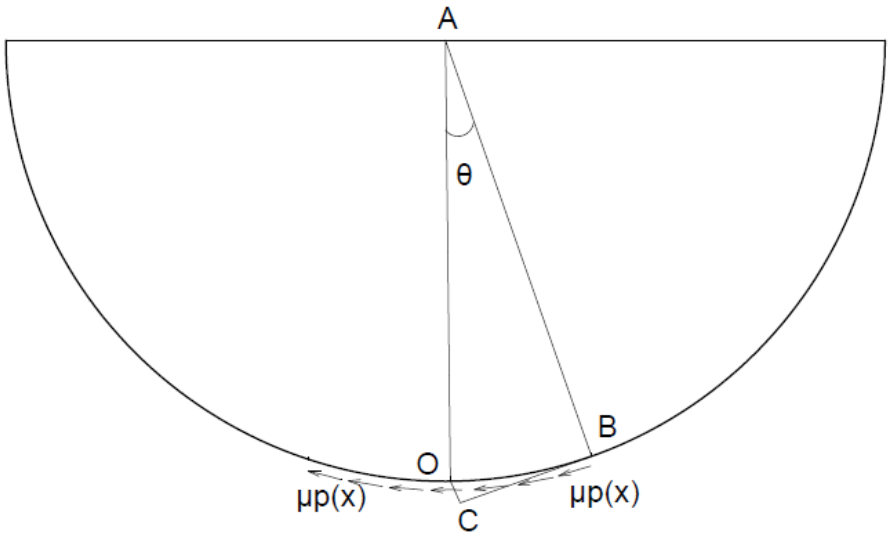

Figure C-2 The schematic of the loading condition for estimation of the moment on the tip of the half-cylinder, M_0/L.

The tangential displacement of the stick region, δ_{i2}, can be estimated by assuming the block to be a half elastic space, and applying the Hertzian tangential traction, q(x), to the surface. At the initiation of gross slip, the local tangential traction in the contact region approaches q(x)=μp(x) within the contact region, [-b, b] (see Fig.5-2), and it is given by

$$q(x) = \mu p_0 \sqrt{1 - \frac{x^2}{b^2}} \quad -b \le x \le b \tag{C-15}$$

According to Johnson [11], for a half elastic space, the derivative of the displacement on the surface of a half elastic space is determined by the distributed tangential traction.

$$\int_{-b}^{b} \frac{\mu p_0}{b} \frac{\sqrt{b^2 - s^2}}{x - s} ds = -\frac{\pi E}{2(1-\nu^2)} \frac{du}{dx} \tag{C-16}$$

The integrations of left-hand side of Eq. C-16 are distinct for the regions inside and outside the contact region, thus

$$\frac{du}{dx}=\begin{Bmatrix} -\frac{2(1-\nu^2)\mu p_0}{bE}(x+\sqrt{x^2-b^2}) & (-\infty,-b) \\ -\frac{2(1-\nu^2)\mu p_0}{bE}x & (-b,b) \\ -\frac{2(1-\nu^2)\mu p_0}{bE}(x-\sqrt{x^2-b^2}) & (b,+\infty) \end{Bmatrix} \quad \text{(C-17)}$$

Consequently, the tangential displacement on the surface, u, can be obtained by integrating Eq. C-17. Here, we take the initial center of the contact as the datum, i.e., u(0)=0. Then u(x) can be derived to give:

$$u=\begin{Bmatrix} -\frac{(1-\nu^2)\mu p_0}{bE}(x^2+x\sqrt{x^2-b^2}-b^2\ln\frac{-x-\sqrt{x^2-b^2}}{b}) & (-\infty,-b) \\ -\frac{(1-\nu^2)\mu p_0}{bE}x^2 & (-b,b) \\ -\frac{(1-\nu^2)\mu p_0}{bE}(x^2-x\sqrt{x^2-b^2}+b^2\ln\frac{x+\sqrt{x^2-b^2}}{b}) & (b,+\infty) \end{Bmatrix} \quad \text{(C-18)}$$

Note the similitude of Eq. C-18 for (-b, b) and Eq. C-15. The displacement of the stick region, δ_{i2}, at initiation of gross slip can be estimated by taking the difference between the u(x) at the leftmost position (x=-2R) and the center of the contact (x=0). Thus, the estimation of δ_{i2} is, δ_{i2}=u (0)-u (-2R), giving:

$$\delta_{i2}=\frac{(1-\nu^2)\mu p_0}{bE}(4R^2-2R\sqrt{4R^2-b^2}-b^2\ln\frac{2R-\sqrt{4R^2-b^2}}{b}) \quad \text{(C-19)}$$

If the contact width is much smaller than the radius, b<<R, Eq. C-19 can be approximated while also using Eq. 3-1 for p_0 to finally result in:

$$\delta_{i2}=\frac{(1-\nu^2)\mu P}{\pi EL}(1-2\ln\frac{b}{4R}) \quad \text{(C-20)}$$

This result shows a linear relation with respect to μ, and nearly linear with respect to P/L (the nonlinearity is caused by the term ln (b/4R), where by Eq. 3-2, b is a function of P/L).

REFERENCES

[1] Varenberg, M., Etsion, I., and Halperin, G., 2004, "Slip index: a new unified approach to fretting," Tribology Letters, 17(3), pp. 569-573.

[2] Li, G., Ding, S., Bao, M., and Sun, H., 2017, "Effect of actively managed thermal-loading in optimal design of an aeroengine turbine disk," International Communications in Heat and Mass Transfer, 81, pp. 257-268.

[3] Yang, Q., Zhou, W., Gai, P., Zhang, X., Fu, X., Chen, G., and Li, Z., 2017, "Investigation on the fretting fatigue behaviors of Ti-6Al-4V dovetail joint specimens treated with shot-peening," Wear, 372, pp. 81-90.

[4] Shi, L., Wei, D.-s., Wang, Y.-r., Tian, A.-m., and Li, D., 2016, "An investigation of fretting fatigue in a circular arc dovetail assembly," International Journal of Fatigue, 82, pp. 226-237.

[5] Chan, K. S., Enright, M. P., Moody, J. P., Golden, P. J., Chandra, R., and Pentz, A. C., 2010, "Residual stress profiles for mitigating fretting fatigue in gas turbine engine disks," International Journal of Fatigue, 32(5), pp. 815-823.

[6] Vingsbo, O., and Söderberg, S., 1988, "On fretting maps," Wear, 126(2), pp. 131-147.

[7] Mei, J. N., Xue, F., Huang, L., Wang, Z. X., Zhang, G. D., Shu, G. G., Li, J. S., and Fu, H. Z., 2013, "Finite Element Analysis of Fretting Wear for Nuclear Inconel 690 Alloy," Advanced Materials Research, 772, pp. 77-82.

[8] Shiozawa, S., Fujikawa, S., Iyoku, T., Kunitomi, K., and Tachibana, Y., 2004, "Overview of HTTR design features," Nuclear Engineering and Design, 233(1-3), pp. 11-21.

[9] Dostal, V., Hejzlar, P., and Driscoll, M. J., 2006, "High-performance supercritical carbon dioxide cycle for next-generation nuclear reactors," Nuclear Technology, 154(3), pp. 265-282.

[10] Archard, J., and Hirst, W., 1956, "The wear of metals under unlubricated conditions," Proc. R. Soc. Lond. A, 236(1206), pp. 397-410.

[11] Johnson, K. L., and Johnson, K. L., 1987, Contact mechanics, Cambridge university press.

[12] Cattaneo, C., 1938, "Sul contatto di due corpi elastici: distribuzione locale degli sforzi," Rend. Accad. Naz. Lincei, 27(6), pp. 342-348.

[13] Mindlin, R., 1949, "Compliance of elastic bodies in contact," J. appl. Mech., 16, pp. 259-268.

[14] Goodman, L., and Hamilton, G., 1966, "The stress field created by a circular sliding contact," J. appl. Mech, 33, pp. 371-376.

[15] Adams, G. G., 2014, "Stick, partial slip and sliding in the plane strain micro contact of two elastic bodies," Royal Society open science, 1(3), p. 140363.

[16] Popov, V. L., and Heß, M., 2015, Method of dimensionality reduction in contact mechanics and friction, Springer.

[17] Courtney-Pratt, J., and Eisner, E., 1957, "The effect of a tangential force on the contact of metallic bodies," Proceedings of the royal society of london a: mathematical, physical and engineering sciences, 238(1215), pp. 529-550.

[18] Parker, R., and Hatch, D., 1950, "The static coefficient of friction and the area of contact," Proceedings of the Physical Society. Section B, 63(3), p. 185.

[19] Tabor, D., 1959, "Junction growth in metallic friction: the role of combined stresses and surface contamination," Proceedings of the Royal Society of London A: Mathematical, Physical and Engineering Sciences, 251(1266), pp. 378-393.

[20] Kogut, L. E., I, 2002, "Elastic–plastic contact analysis of a sphere and a rigid flat," ASME J. Appl. Mech, 69(5), pp. 657-662.

[21] Jackson, R. L., and Green, I., 2005, "A finite element study of elasto-plastic hemispherical contact against a rigid flat," Transactions of the ASME-F-Journal of Tribology, 127(2), pp. 343-354.

[22] Tsukizoe, T., and Hisakado, T., 1968, "On the Mechanism of Contact Between Metal Surfaces: Part 2—The Real Area and the Number of the Contact Points," Journal of Lubrication Technology, 90(1), pp. 81-88.

[23] Sharma, A., and Jackson, R. L., 2017, "A Finite Element Study of an Elasto-Plastic Disk or Cylindrical Contact Against a Rigid Flat in Plane Stress with Bilinear Hardening," Tribology Letters, 65(3), p. 112.

[24] Brizmer, V., Kligerman, Y., and Etsion, I., 2007, "A model for junction growth of a spherical contact under full stick condition," ASME Trans., Journal of Tribology, 129(4), pp. 783-790.

[25] Chang, L., and Zhang, H., 2007, "A mathematical model for frictional elastic-plastic sphere-on-flat contacts at sliding incipient," Journal of Applied Mechanics, 74(1), pp. 100-106.

[26] Holmberg, K., Laukkanen, A., Ronkainen, H., Wallin, K., Varjus, S., and Koskinen, J., 2006, "Tribological contact analysis of a rigid ball sliding on a hard coated surface: Part

I: Modelling stresses and strains," Surface and Coatings Technology, 200(12-13), pp. 3793-3809.

[27] Boucly, V., NÄŠlias, D., and Green, I., 2007, "Modeling of the rolling and sliding contact between two asperities," Journal of tribology, 129(2), pp. 235-245.

[28] Tomlinson, G., Thorpe, P., and Gough, H., 1939, "An investigation of the fretting corrosion of closely fitting surfaces," Proceedings of the Institution of Mechanical Engineers, 141(1), pp. 223-249.

[29] Zhou, Z., and Vincent, L., 1995, "Mixed fretting regime," Wear, 181, pp. 531-536.

[30] Zhou, Z., Nakazawa, K., Zhu, M., Maruyama, N., Kapsa, P., and Vincent, L., 2006, "Progress in fretting maps," Tribology International, 39(10), pp. 1068-1073.

[31] Waterhouse, R., 1984, "Fretting wear," Wear, 100(1-3), pp. 107-118.

[32] McColl, I., Ding, J., and Leen, S., 2004, "Finite element simulation and experimental validation of fretting wear," Wear, 256(11-12), pp. 1114-1127.

[33] Fouvry, S., Kapsa, P., Zahouani, H., and Vincent, L., 1997, "Wear analysis in fretting of hard coatings through a dissipated energy concept," Wear, 203, pp. 393-403.

[34] Blanchard, P., Colombie, C., Pellerin, V., Fayeulle, S., and Vincent, L., 1991, "Material effects in fretting wear: application to iron, titanium, and aluminum alloys," Metallurgical Transactions A, 22(7), pp. 1535-1544.

[35] Waterhouse, R., 1992, "Fretting fatigue," International materials reviews, 37(1), pp. 77-98.

[36] Hills, D. A., 1994, "Mechanics of fretting fatigue," Wear, 175(1-2), pp. 107-113.

[37] Szolwinski, M. P., and Farris, T. N., 1996, "Mechanics of fretting fatigue crack formation," Wear, 198(1-2), pp. 93-107.

[38] Fouvry, S., Kapsa, P., and Vincent, L., 1996, "Quantification of fretting damage," Wear, 200(1-2), pp. 186-205.

[39] Neu, R. W., Pape, J. A., and Swalla, D. R., 2000, "Methodologies for linking nucleation and propagation approaches for predicting life under fretting fatigue," Fretting fatigue: current technology and practices, ASTM International.

[40] Leonard, B. D., Sadeghi, F., Evans, R. D., Doll, G. L., and Shiller, P. J., 2009, "Fretting of WC/aC: H and Cr2N coatings under grease-lubricated and unlubricated conditions," Tribology Transactions, 53(1), pp. 145-153.

[41] Leonard, B. D., Sadeghi, F., Shinde, S., and Mittelbach, M., 2012, "A novel modular fretting wear test rig," Wear, 274, pp. 313-325.

[42] Warhadpande, A., Leonard, B., and Sadeghi, F., 2008, "Effects of fretting wear on rolling contact fatigue life of M50 bearing steel," Proceedings of the Institution of Mechanical Engineers, Part J: Journal of Engineering Tribology, 222(2), pp. 69-80.

[43] Zhu, M., Zhou, Z., Kapsa, P., and Vincent, L., 2001, "Radial fretting fatigue damage of surface coatings," Wear, 250(1-12), pp. 650-657.

[44] Xu, J., Zhu, M., Zhou, Z., Kapsa, P., and Vincent, L., 2003, "An investigation on fretting wear life of bonded MoS2 solid lubricant coatings in complex conditions," Wear, 255(1-6), pp. 253-258.

[45] Kim, D.-G., and Lee, Y.-Z., 2001, "Experimental investigation on sliding and fretting wear of steam generator tube materials," Wear, 250(1-12), pp. 673-680.

[46] Kim, I.-S., Hong, J.-K., Kim, H.-N., and Jang, K.-S., "Wear Behavior of Steam Generator Tubes in Nuclear Power Plant Operating Condition," Proc. Transactions of the 17th International Conference on Structural Mechanics in Reactor Technology (SMiRT 17), Prague, Czech Republic, pp. D04-05.

[47] Zhang, X.-Y., Liu, J.-H., Cai, Z.-B., Peng, J.-F., Zhu, M.-H., and Ren, P.-D., 2017, "Experimental Study of the Fretting Wear Behavior of Incoloy 800 Alloy at High Temperature," Tribology Transactions, pp. 1-10.

[48] Hoeppner, D., Adibnazari, S., and Moesser, M. W., 1994, "Literature Review and Preliminary Studies of Fretting and Fretting Fatigue Including Special Applications to Aircraft Joints," UTAH UNIV SALT LAKE CITY DEPT OF MECHANICAL ENGINEERING.

[49] Mohrbacher, H., Celis, J.-P., and Roos, J., 1995, "Laboratory testing of displacement and load induced fretting," Tribology international, 28(5), pp. 269-278.

[50] Brandt, J., Charron, K., Zhao, L., MacDonald, S., and Medley, J., 2011, "Commissioning of a displacement-controlled knee wear simulator and exploration of some issues related to the lubricant," Proceedings of the Institution of Mechanical Engineers, Part H: Journal of Engineering in Medicine, 225(8), pp. 736-752.

[51] Johnson, T., Laurent, M., Yao, J., and Gilbertson, L., 2001, "The effect of displacement control input parameters on tibiofemoral prosthetic knee wear," Wear, 250(1), pp. 222-226.

[52] Lanovaz, J., and Ellis, R., 2008, "Dynamic simulation of a displacement-controlled total knee replacement wear tester," Proceedings of the Institution of Mechanical Engineers, Part H: Journal of Engineering in Medicine, 222(5), pp. 669-681.

[53] Shigley, J. E., 1972, "Mechanical engineering design."

[54] Jiang, Y., Zhang, M., Park, T.-W., and Lee, C.-H., 2004, "An experimental study of self-loosening of bolted joints," Journal of mechanical design, 126(5), pp. 925-931.

[55] Kenny, P., and Johnson, S., 1976, "An investigation of the abrasive wear of mineral-cutting tools," Wear, 36(3), pp. 337-361.

[56] Benhamena, A., Talha, A., Benseddiq, N., Amrouche, A., Mesmacque, G., and Benguediab, M., 2010, "Effect of clamping force on fretting fatigue behaviour of bolted assemblies: Case of couple steel–aluminium," Materials Science and Engineering: A, 527(23), pp. 6413-6421.

[57] Antler, M., 1985, "Survey of contact fretting in electrical connectors," IEEE Transactions on components, hybrids, and manufacturing technology, 8(1), pp. 87-104.

[58] Huq, M., Butaye, C., and Celis, J.-P., 2000, "An innovative system for fretting wear testing under oscillating normal force," Journal of Materials Research, 15(7), pp. 1591-1599.

[59] Gupta, V., Bastias, P., Hahn, G. T., and Rubin, C. A., 1993, "Elasto-plastic finite-element analysis of 2-D rolling-plus-sliding contact with temperature-dependent bearing steel material properties," Wear, 169(2), pp. 251-256.

[60] Ghosh, A., Leonard, B., and Sadeghi, F., 2013, "A stress based damage mechanics model to simulate fretting wear of Hertzian line contact in partial slip," Wear, 307(1), pp. 87-99.

[61] Green, I., 2005, "Poisson ratio effects and critical valus in spherical and cylindrical Hertzian contacts," Applied Mechanics and Engineering, 10(3), p. 451.

[62] Zolotarevskiy, V., Kligerman, Y., and Etsion, I., 2011, "Elastic–plastic spherical contact under cyclic tangential loading in pre-sliding," Wear, 270(11-12), pp. 888-894.

[63] Shi, X., Wu, A., Zhu, C., and Qu, S., 2013, "Effects of load configuration on partial slip contact between an elastic · plastic sphere and a rigid flat," Tribology International, 61, pp. 120-128.

[64] Olsson, H., Åström, K. J., De Wit, C. C., Gäfvert, M., and Lischinsky, P., 1998, "Friction models and friction compensation," Eur. J. Control, 4(3), pp. 176-195.

[65] Johnson, K., 1997, "Adhesion and friction between a smooth elastic spherical asperity and a plane surface," Proceedings of the Royal Society of London. Series A: Mathematical, Physical and Engineering Sciences, 453(1956), pp. 163-179.

[66] Bowden, F. P., Bowden, F. P., and Tabor, D., 2001, The friction and lubrication of solids, Oxford university press.

[67] Keller, D., 1963, "Adhesion between solid metals," Wear, 6(5), pp. 353-365.

[68] Buckley, D. H., 1977, "The metal-to-metal interface and its effect on adhesion and friction," Plenary and Invited Lectures, Elsevier, pp. 37-54.

[69] Burwell, J., and Strang, C., 1952, "On the empirical law of adhesive wear," Journal of Applied Physics, 23(1), pp. 18-28.

[70] Dessureautt, M., and Spelt, J., 1997, "Observations of fatigue crack initiation and propagation in an epoxy adhesive," International Journal of Adhesion and Adhesives, 17(3), pp. 183-195.

[71] Johnson, K. L., Kendall, K., and Roberts, A., 1971, "Surface energy and the contact of elastic solids," Proceedings of the royal society of London. A. mathematical and physical sciences, 324(1558), pp. 301-313.

[72] Derjaguin, B. V., Muller, V. M., and Toporov, Y. P., 1975, "Effect of contact deformations on the adhesion of particles," Journal of Colloid and interface science, 53(2), pp. 314-326.

[73] Tabor, D., 1977, "Surface forces and surface interactions," Plenary and invited lectures, Elsevier, pp. 3-14.

[74] Maugis, D., 1992, "Adhesion of spheres: the JKR-DMT transition using a Dugdale model," Journal of colloid and interface science, 150(1), pp. 243-269.

[75] Li, L., Song, W., Xu, M., Ovcharenko, A., and Zhang, G., 2015, "Atomistic insights into the loading–unloading of an adhesive contact: a rigid sphere indenting a copper substrate," Computational Materials Science, 98, pp. 105-111.

[76] Du, Y., Chen, L., McGruer, N. E., Adams, G. G., and Etsion, I., 2007, "A finite element model of loading and unloading of an asperity contact with adhesion and plasticity," Journal of colloid and interface science, 312(2), pp. 522-528.

[77] Yoshizawa, H., Chen, Y. L., and Israelachvili, J., 1993, "Fundamental mechanisms of interfacial friction. 1. Relation between adhesion and friction," The Journal of Physical Chemistry, 97(16), pp. 4128-4140.

[78] Binnig, G., Quate, C. F., and Gerber, C., 1986, "Atomic force microscope," Physical review letters, 56(9), p. 930.

[79] Carpick, R. W., and Salmeron, M., 1997, "Scratching the surface: Fundamental investigations of tribology with atomic force microscopy," Chemical reviews, 97(4), pp. 1163-1194.

[80] Lantz, M., O'shea, S., Welland, M., and Johnson, K., 1997, "Atomic-force-microscope study of contact area and friction on NbSe 2," Physical Review B, 55(16), p. 10776.

[81] Wei, Z., Wang, C., and Bai, C., 2001, "Investigation of nanoscale frictional contact by friction force microscopy," Langmuir, 17(13), pp. 3945-3951.

[82] Popov, V. L., Lyashenko, I. A., and Filippov, A. E., 2017, "Influence of tangential displacement on the adhesion strength of a contact between a parabolic profile and an elastic half-space," Royal Society Open Science, 4(8), p. 161010.

[83] Yang, H., and Green, I., 2018, "An elastoplastic finite element study of displacement-controlled fretting in a plane-strain cylindrical contact," Journal of Tribology, 140(4).

[84] Yang, H., and Green, I., 2019, "Analysis of Displacement-Controlled Fretting Between a Hemisphere and a Flat Block in Elasto-Plastic Contacts," Journal of Tribology, 141(3).

[85] Jackson, R. L., and Green, I., 2005, "A finite element study of elasto-plastic hemispherical contact against a rigid flat," J. Trib., 127(2), pp. 343-354.

[86] Walvekar, A. A., Leonard, B. D., Sadeghi, F., Jalalahmadi, B., and Bolander, N., 2014, "An experimental study and fatigue damage model for fretting fatigue," Tribology International, 79, pp. 183-196.

[87] Tabor, D., 1959, "Junction growth in metallic friction: the role of combined stresses and surface contamination," Proceedings of the Royal Society of London. Series A. Mathematical and Physical Sciences, 251(1266), pp. 378-393.

[88] Peterson, M. B., and Winer, W. O., 1980, Wear control handbook, American Society of Mechanical Engineers.

[89] Brizmer, V., Kligerman, Y., and Etsion, I., 2007, "A model for junction growth of a spherical contact under full stick condition."

[90] Yang, H., and Green, I., 2019, "A fretting finite element investigation of a plane-strain cylindrical contact of Inconel 617/Incoloy 800H at room and high temperatures," Proceedings of the Institution of Mechanical Engineers, Part J: Journal of Engineering Tribology, 233(4), pp. 553-569.

[91] Brizmer, V., Kligerman, Y., and Etsion, I., 2007, "A model for junction growth of a spherical contact under full stick condition," Journal of Tribology, 129(4), pp. 783-790.

[92] Courtney-Pratt, J., and Eisner, E., "The effect of a tangential force on the contact of metallic bodies," Proc. Proceedings of the royal society of london a: mathematical, physical and engineering sciences, The Royal Society, pp. 529-550.

[93] Yang, H., and Green, I., 2019, "Fretting Wear Modeling of Cylindrical Line Contact in Plane-Strain Borne by the Finite Element Method," Journal of Applied Mechanics, 86(6).

[94] METALS, S., 2008, "PRODUCT HANDBOOK OF HIGHPERFORMANCE NICKEL ALLOYS,"Product Handbook.

[95] Yang, H., and Green, I., 2018, "An Elasto-plastic finite element study of displacement-controlled fretting in a plane-strain cylindrical contact," ASME Trans., Journal of Tribology, 041401-1-041401-11.

[96] ANSYS®SAS IP, I., Release 17.0, Help System, Mechanical APDL Contact Technology Guide, ANSYS, Inc.

[97] Knothe, K., 2011, "CONTACT MECHANICS AND FRICTION: PHYSICAL PRINCIPLES AND APPLICATIONS," SAGE Publications Sage UK: London, England.

[98] Yang, H., and Green, I., 2019, "Analysis of Displacement-Controlled Fretting Between a Hemisphere and a Flat Block in Elasto-Plastic Contacts," Journal of Tribology, 141(3), p. 031401.

[99] Green, I., 2018, "An elastic-plastic finite element analysis of two interfering hemispheres sliding in frictionless contact," Physical Science International Journal, pp. 1-34.

[100] Timoshenko, S. P., 1921, "On the correction for shear of the differential equation for transverse vibrations of prismatic bars," The London, Edinburgh, and Dublin Philosophical Magazine and Journal of Science, 41(245), pp. 744-746.

[101] Cowper, G., 1966, "The shear coefficient in Timoshenko's beam theory," Journal of applied mechanics, 33(2), pp. 335-340.